N°d'ordre NNT :2016LYSEI098

THESE de DOCTORAT DE L'UNIVERSITE DE LYON
opérée au sein de
INSA de Lyon

Ecole Doctorale ED 162
Ecole doctorale des Sciences pour l'Ingénieur de Lyon: Mécanique, Energétique, Génie Civil, Acoustique (MEGA)

Spécialité de doctorat :
Génie Mécanique

Soutenue publiquement le 21/10/2016, par :
Vincent Strubel

Particle Entrapment in EHD Contacts - Aerospace Applications

Devant le jury composé de :

Dellacorte, Christopher	Docteur / NASA	Rapporteur
Dwyer-Joyce, Rob	Professeur / Université de Sheffield	Rapporteur
Fillot, Nicolas	HDR / INSA-Lyon	Directeur
Mondelin, Alexandre	Docteur / SKF Aerospace	Examinateur
Tanguy, Anne	Professeure / INSA-Lyon	Examinatrice
Ville, Fabrice	Professeur / INSA-Lyon	Co-directeur

Département FEDORA – INSA Lyon - Ecoles Doctorales – Quinquennal 2016-2020

SIGLE	ECOLE DOCTORALE	NOM ET COORDONNEES DU RESPONSABLE
CHIMIE	**CHIMIE DE LYON** **http://www.edchimie-lyon.fr** Sec : Renée EL MELHEM Bat Blaise Pascal 3e etage secretariat@edchimie-lyon.fr Insa : R. GOURDON	M. Stéphane DANIELE Institut de Recherches sur la Catalyse et l'Environnement de Lyon IRCELYON-UMR 5256 Équipe CDFA 2 avenue Albert Einstein 69626 Villeurbanne cedex directeur@edchimie-lyon.fr
E.E.A.	**ELECTRONIQUE, ELECTROTECHNIQUE, AUTOMATIQUE** **http://edeea.ec-lyon.fr** Sec : M.C. HAVGOUDOUKIAN Ecole-Doctorale.eea@ec-lyon.fr	M. Gérard SCORLETTI Ecole Centrale de Lyon 36 avenue Guy de Collongue 69134 ECULLY Tél : 04.72.18 60.97 Fax : 04 78 43 37 17 Gerard.scorletti@ec-lyon.fr
E2M2	**EVOLUTION, ECOSYSTEME, MICROBIOLOGIE, MODELISATION** **http://e2m2.universite-lyon.fr** Sec : Safia AIT CHALAL Bat Darwin - UCB Lyon 1 04.72.43.28.91 Insa : H. CHARLES Safia.ait-chalal@univ-lyon1.fr	Mme Gudrun BORNETTE CNRS UMR 5023 LEHNA Université Claude Bernard Lyon 1 Bât Forel 43 bd du 11 novembre 1918 69622 VILLEURBANNE Cédex Tél : 06.07.53.89.13 e2m2@ univ-lyon1.fr
EDISS	**INTERDISCIPLINAIRE SCIENCESSANTE** http://www.ediss-lyon.fr Sec : Safia AIT CHALAL Hôpital Louis Pradel - Bron 04 72 68 49 09 Insa : M. LAGARDE Safia.ait-chalal@univ-lyon1.fr	Mme Emmanuelle CANET-SOULAS INSERM U1060, CarMeN lab, Univ. Lyon 1 Bâtiment IMBL 11 avenue Jean Capelle INSA de Lyon 696621 Villeurbanne Tél : 04.72.68.49.09 Fax :04 72 68 49 16 Emmanuelle.canet@univ-lyon1.fr
INFOMATHS	**INFORMATIQUE ET MATHEMATIQUES** **http://infomaths.univ-lyon1.fr** Sec :Renée EL MELHEM Bat Blaise Pascal 3e etage infomaths@univ-lyon1.fr	Mme Sylvie CALABRETTO LIRIS – INSA de Lyon Bat Blaise Pascal 7 avenue Jean Capelle 69622 VILLEURBANNE Cedex Tél : 04.72. 43. 80. 46 Fax 04 72 43 16 87 Sylvie.calabretto@insa-lyon.fr
Matériaux	**MATERIAUX DE LYON** **http://ed34.universite-lyon.fr** Sec : M. LABOUNE PM : 71.70 –Fax : 87.12 Bat. Saint Exupéry Ed.materiaux@insa-lyon.fr	M. Jean-Yves BUFFIERE INSA de Lyon MATEIS Bâtiment Saint Exupéry 7 avenue Jean Capelle 69621 VILLEURBANNE Cedex Tél : 04.72.43 71.70 Fax 04 72 43 85 28 Ed.materiaux@insa-lyon.fr
MEGA	**MECANIQUE, ENERGETIQUE, GENIE CIVIL, ACOUSTIQUE http://mega.universite-lyon.fr** Sec : M. LABOUNE PM : 71.70 –Fax : 87.12 Bat. Saint Exupéry mega@insa-lyon.fr	M. Philippe BOISSE INSA de Lyon Laboratoire LAMCOS Bâtiment Jacquard 25 bis avenue Jean Capelle 69621 VILLEURBANNE Cedex Tél : 04.72 .43.71.70 Fax : 04 72 43 72 37 Philippe.boisse@insa-lyon.fr
ScSo	**ScSo*** **http://recherche.univ-lyon2.fr/scso/** Sec : Viviane POLSINELLI Brigitte DUBOIS Insa : J.Y. TOUSSAINT viviane.polsinelli@univ-lyon2.fr	Mme Isabelle VON BUELTZINGLOEWEN Université Lyon 2 86 rue Pasteur 69365 LYON Cedex 07 Tél : 04.78.77.23.86 Fax : 04.37.28.04.48

*ScSo : Histoire, Géographie, Aménagement, Urbanisme, Archéologie, Science politique, Sociologie, Anthropologie

Remerciements

Je tiens à remercier mes directeurs de thèse, Nicolas Fillot et Fabrice Ville qui m'ont offert l'opportunité de réaliser cette thèse au LaMCoS. Cette thèse ayant été réalisée dans le cadre de la chaire SKF – Fondation INSA de Lyon, « Lubricated Interfaces for the Future », je tiens à remercier les deux porteurs de la chaire, Philippe Vergne et Guillermo Morales-Espejel. Enfin je tenais à remercier l'équipe de SKF Aerospace à Valence avec qui j'ai eu la chance de travailler, et plus particulièrement Yves Maheo et Alexandre Mondelin pour leur accompagnement. Tous, m'ont permis au cours de ces 3 ans de grandir et de m'épanouir autant professionnellement que personnellement. Au cours des nombreuses réunions, séminaires et congrès auxquels j'ai pu participer, j'ai pu non seulement discuter de mes travaux avec de nombreuses personnes aux compétences scientifiques avancées mais aussi cultiver le plaisir d'échanger simplement sur les habitudes culturelles et sociales de chacun.

Merci à mes deux rapporteurs de thèse, Christopher Dellacorte et Rob Dwyer-Joyce d'avoir pris le temps de relire et juger ce travail et à Anne Tanguy d'avoir accepté d'examiner ce travail.

J'adresse un sincère remerciement à Serge Simoens et Mahmoud El Hajem du laboratoire LMFA pour leur confiance et leur aide dans la réalisation des essais à l'aide de la technique μ-PIV. Cela me permet aussi de remercier toute l'équipe du LMFA et ses doctorants qui ont pris du temps pour m'expliquer leurs méthodes de travail. Au LaMCoS, on a beaucoup de collègues mais aussi beaucoup d'amis alors je remercie en premiers lieux mes deux acolytes de bureau, Nicolas Voeltzel et Jean-David Wheeler. Sans eux la thèse aurait été bien plus longue et surtout bien moins drôle. Je remercie notre coach sportif et couteau-suisse Lionel Lafarge, Nathalie Bousharain et Nicolas Devaux pour leurs précieuses aides sur les manips. En parlant de manips, tout ce travail n'aurait pas cette saveur sans l'aide de Vincent Baudin et surtout Jérôme Cavoret. Pour leur aide logistique, je tiens à remercier Emmanuel Montero et Sophie De Oliveira.

Ayant eu la chance de faire partie de deux équipes TMI et SMC, je remercie l'ensemble des personnes avec qui j'ai pu discuter et échanger tant sur le point scientifique que de la vie en générale, je pense plus particulièrement aux doctorants avec qui j'ai partagé beaucoup de temps au labo mais surtout à côté que ce soit dans les bars ou sur les terrasses des uns et des autres, alors merci dans le désordre à Stéphane, Phansté, Sayed, Nina, Pierre, Arnaud, Pauline, Serigne, Romain, Martin, Guillaume, Jérôme, Grégoire, Charlotte, Nicolas, Matthieu, Marion, Eymard, Serge, Komla, Pierrick, Maria, Julian, Marie, Jacopo, Eric, Fabien, Dimitri, Thomas, Giovanna, Amina, Hassan, Davide, Charly, Mirela, Bogdan, et j'espère n'oublier personne auquel cas je m'en excuse. Il y a aussi les permanents avec qui j'ai passé de très bons moments, merci à Michal, Aurélien, David, Claire, Lionel et Mathieu. En dehors du LaMCoS, d'autres m'ont apporté leur aide à un moment où à un autre, je voulais remercier Yann Marchesse, Michel Fillon et l'équipe de Poitiers.

Merci à tous mes amis de longues et moins longues dates pour leur soutien, les amis de Wettelsa, les amis de prépa, de Karlinsa, et de l'ambassade d'Alsace à Lyon, vous avez été un vrai soutien ! Enfin comment ne pas remercier la famille, elle qui supporte toutes les sautes d'humeur, alors merci à mon papa pour ses conseils, ma maman pour sa patience et ses gâteaux, Laure et François pour leur présence et enfin à Isabelle avec qui j'ai choisi de partager ma vie.

Foreword

This work results from a collaboration between the laboratory of Contact and Structure Mechanics (LaMCoS – INSA de Lyon, France) and the bearing company SKF. It was funded by the industrial research chair SKF-Foundation INSA de Lyon "Lubricated Interfaces for the Future". The PhD took place in the doctoral school MEGA (Mechanics, Energetics, Civil Engineering, Acoustics).

Supervisors	LaMCoS	*Nicolas FILLOT* *Fabrice VILLE*
Reviewers	University of Sheffield (UK)	*Rob DWYER-JOYCE*
	National Aeronautics and Space Administration (USA)	*Christopher DELLACORTE*
SKF Aerospace	Research Director	*Yves MAHEO* *Alexandre MONDELIN*
Industrial chair "Lubricated Interfaces for the Future"	Research Director (CNRS)	*Philippe VERGNE*
	Senior Scientist (SKF ERC)	*Guillermo MORALES-ESPEJEL*

A special acknowledgement is addressed to Serge Simoens and Mahmoud El Hajem from LMFA lab for their help to perform the μ-PIV tests.

Abstract

Contact lubrication is essential in a wide range of mechanical systems like rolling element bearings (REBs). A minimum quantity of clean lubricant all along the bearing life is necessary but difficult to ensure. In fact, lubricants contain inevitably wear debris or external particles, like dust. Carried by the lubricant in the vicinity of elastohydrodynamic (EHD) contacts, particles can be entrapped with disastrous consequences for contacting surfaces. Entrapment of micrometric particles in submicrometric contacting gaps means irreversible damages for the surfaces. Damages weaken the surfaces and reduce significantly the REBs lifetime. The goal of this work is to analyze the critical particle entrainments in the contact inlet. Entrapment of steel spherical particles was investigated from the numerical and experimental point of view. Firstly, the phenomenology of entrapment was explored with a new experimental method based on Particle Image Velocimetry (PIV) technique installed on a tribometer. It enabled the evaluation of velocity profiles in the contact inlet and the tracking of particles within EHD contacts. Secondly, a numerical modelling of the inlet flow for EHD contacts, including the particle tracking, was developed. Finally, tests on a twin-disc machine with a controlled level of well-defined contamination were conducted to validate previous conclusions. A first set of results showed that particle entrapment is highly dependent on the lubricant velocity profile. Depending on contact geometry, from point to wide elliptical contacts, different entrapment probability were revealed. Surprisingly, increasing contact width with wide elliptical contacts leads to a drop of entrapped particles. It was demonstrated that this phenomenon is due to backflows occurring upstream from these contacts. Introducing a hybrid pair of contacting materials (silicon nitride–steel), dents on the surfaces due to entrapped particles were explored. It has been confirmed that silicon nitride surface offers a real ability to resist to indentation. It was also noticed that the entrapment probability for silicon nitride–steel contacts is equivalent to a steel–steel one.

Keywords: *Particle entrapment, elliptical contacts, silicon nitride–steel, elliptical, numerical modelling, twin-disc machine, tribometer, PIV-technique*

Résumé

Une lubrification suffisante est essentielle au bon fonctionnement des mécanismes et/ou composants comme par exemple les paliers à roulement. Par contre, les lubrifiants contiennent souvent des débris d'usure ou des polluants extérieurs. Ces particules micrométriques peuvent pénétrer des contacts d'épaisseur inférieure au micromètre induisant des empruntes ou indents pouvant conduire à des endommagements irréversibles pour les surfaces en contact. L'objet de ce travail est l'étude du piégeage de polluants solides à l'aide de particules sphériques d'acier, d'un point de vue théorique, numérique et expérimental. Dans un premier temps, une étude phénoménologique a été proposée à l'aide d'une nouvelle méthode expérimentale basée sur la technique PIV combinée à un tribomètre bille/disque. Les trajectoires des polluants à l'entrée du contact ont pu ainsi être identifiées. En parallèle, un modèle numérique d'écoulement du lubrifiant a été développé pour permettre l'évaluation des conditions menant au piégeage ou non de particules. Finalement, des expériences sur une machine bi-disques en conditions de lubrification polluée contrôlée ont permis de valider les tendances observées pour le piégeage. Une première série de résultats a montré que le piégeage de contaminants est fortement dépendant du profil de vitesse du lubrifiant. Un taux de piégeage très hétérogène a été observé sur des contacts avec une ellipticité transverse à l'écoulement variable. De manière surprenante, malgré une augmentation de la largeur de contact, une forte diminution du nombre de particules piégées a été observée dans des contacts elliptiques. Il a été démontré que cette diminution pouvait être imputée à la présence d'importants reflux de lubrifiant dans les contacts elliptiques larges. L'étude de contacts hybrides, nitrure de silicium–acier, a montré une bonne résistance à l'indentation du nitrure de silicium. Il est à noter que les contacts hybrides présentent des niveaux de piégeage similaire à un contact tout acier.

Mots-clés : *Piégeage de polluants, contacts elliptiques, nitrure de silicium–acier, modèle numérique, machine bi-disques, tribomètre bille/disque, technique PIV*

Table of contents

Foreword 5

Abstract 9

Résumé 9

Table of contents i

List of figures iii

List of tables ix

Nomenclature xi

Dimensionless numbers xiii

Abbreviations xiii

Résumé étendu xvii

General Introduction 3

Chapter 1 State of the art 7

1.1 Introduction 9

1.2 REB basics 9

1.2.1 Aerospace applications 9

1.2.2 Hybrid REBs 10

1.2.3 Lubrication 12

1.3 Lubricant contamination: a constant challenge 14

1.3.1 Origin of solid contamination and entrapment mechanisms 14

1.3.2 Contamination in EHD contacts 16

1.3.3 REB life prediction in presence of contamination 19

1.4 Summary and objectives of the work 20

Chapter 2 Numerical model and experimental devices 23

2.1 Introduction 25

2.2 Numerical model 26

2.2.1 Fluid flow formulation at the EHD contact inlet 26

2.2.2 Formalism for the particle motion 36

2.3 Experimental techniques 43

2.3.1 Twin-disc machine and contamination test rig 43

2.3.2 Ball-on-disc machine with fluorescence technique 48

2.4 Conclusion 57
Chapter 3 Particle entrapment in circular contacts 59
3.1 Introduction 61
3.2 Particle entrapment visualization using fluorescence technique 61
3.2.1 Entrapment visualization 61
3.2.2 Velocity vectors mapping 65
3.3 Particle release position and operating conditions influence 67
3.3.1 Rolling speed influence 71
3.3.2 Load influence 73
3.4 Influence of the particle size and nature 75
3.5 Contact inlet analysis 80
3.6 Conclusion 85
Chapter 4 Towards entrapment in more realistic contacts 87
4.1 Introduction 89
4.2 Particle entrapment in hybrid contacts 90
4.2.1 Twin-disc tests with hybrid discs 90
4.2.2 Surface analysis after tests 93
4.3 Effect of the geometrical configuration 96
4.3.1 Twin-disc tests with elliptical contacts 96
4.3.2 Visualization of lubricant flows in elliptical EHD contacts 102
4.4 Effect of Slide-to-Roll ratio 105
4.5 Conclusion 110
General Conclusions and Prospects 113
General Conclusions 115
Prospects 116
Appendices 119
References 131
Scientific contributions 141

List of figures

Figure 0-1: Particules d'acier, de carbures de bore et de cendres de volcans xix
Figure 0-2: Définition du domaine 3D d'écoulement xxi
Figure 0-3 : Domaine fluide et conditions aux limites xxiii
Figure 0-4 : Résumé du modèle de couplage fluide-particule xxiv
Figure 0-5 : Machine bi-disques et banc de pollution xxv
Figure 0-6 : Machine bille-disque et outils de visualisation (microscope et caméra) xxvi
Figure 0-7 : banc d'essais bille-disque avec système de visualisation PIV xxviii
Figure 0-8 : Visualisation du piégeage d'une particule d'acier M50 mélangée à des pigments fluorescents dans un contact faiblement chargé (10 N) à faible vitesse de roulement (5 mm/s) avec un objectif x10 xxix
Figure 0-9 : Dimensions de l'indent suite au piégeage d'une particule d'acier AISI M50 entre une surface en acier AISI 52100 et une surface en Si3N4 xxxi
Figure 0-10 : Nombre de marques d'indentations (correspondant aux nombres de particules piégées) au sein de différents contacts elliptiques pour des contacts acier-acier (moyenne sur 3 tests et 2 tests pour le contact circulaire et les contacts elliptiques, respectivement) en condition de lubrification polluée (concentration de polluants en solution 10 mg/l) xxxii
Figure 0-11 : Lignes de courant pour une ligne de fluide entrant dans le domaine à x = -2.4 mm, Δy = 200 µm, z = 10 µm, pour un contact circulaire (k = 1) et elliptique (k = 1.6) xxxiii
Figure 0-12 : Visualisation de l'écoulement dans un contact circulaire et elliptique avec les conditions de contact de 5 mm/s – 10 N et 5 mm/s – 50 N, respectivement xxxiv
Figure 1-1: Example of different kinds of REBs 9
Figure 1-2: Aircraft engine REBs 10
Figure 1-3: Hybrid Si_3N_4-steel REB 11
Figure 1-4: Stribeck curve with different lubrication regimes 13
Figure 1-5: (left) hydrodynamic lubrication with undeformed bodies and (right) elastohydrodynamic lubrication with deformed bodies 13
Figure 1-6: Three different examples of particles 15
Figure 1-7: Particle entrapment visualization through interferometric method [17] 17
Figure 1-8: Predictive trajectories for 20 µm-thick particles released upstream from an EHL contact (inspired by [20]) 18
Figure 1-9: Spalling due to rolling contact fatigue [31] (initiated by an artificial dent made by a Rockwell indenter) 19
Figure 2-1: EHL contact with two-bodies or an equivalent geomerty 26
Figure 2-2: Definition of the 3D flow domain 28
Figure 2-3: Comparison of the film thickness and pressure profiles along the centerline obtained from the resolution of the Reynolds equation and the Navier-Stokes equations for a steel–steel circular contact (600 N – 22 m/s) 29
Figure 2-4: Fluid domain and boundary conditions 30
Figure 2-5: Critical meniscus position for different operating conditions for a steel–steel circular contact (R_x = 17.5mm) 31

Figure 2-6: Entrapment width (EW) for different spherical particles of 10 and 40 μm 32
Figure 2-7: Dimensionless EW for different particle sizes: 10, 20, 30 and 40 μm, and different normal loads within a steel-steel circular contact (R_x = 17.5 mm)..... 32
Figure 2-8: Velocity field for a steel–steel contact, equivalent radius of 17.5mm, with EHL parameters: 600 N – 22 m/s – 60 °C..... 35
Figure 2-9: Pressure field for a steel–steel contact, equivalent radius of 17.5mm, with EHL parameters: 600 N – 22 m/s – 60 °C..... 36
Figure 2-10: Different fluid-particle couplings (inspired by [103])..... 37
Figure 2-11: Reynolds number function of the relative speed between the particle and the surrounding fluid velocity for different particle diameters..... 39
Figure 2-12: Evolution of the drag coefficient with Reynolds number (inspired from [105])..... 40
Figure 2-13: Sketch of the particle-flow model and the forces at play..... 41
Figure 2-14: Wall particle interaction and entrapment criterion..... 42
Figure 2-15: Simulations of two released particles, with one entrapped (red) and one bypassing (blue)..... 42
Figure 2-16: Twin-disc machine and device for studying particle entrapment..... 43
Figure 2-17: (a) Unsieved M50-steel powder observed with SEM, (b) Sieved particles in the range 10–20 μm (c) and in the range 32–40 μm observed with optical microscope..... 46
Figure 2-18: Entrapment area and indentation features..... 47
Figure 2-19: Dent on steel surface and related profile in an all-steel case..... 48
Figure 2-20: Typical film thickness distribution for a steel–glass dynamical contact with a 26N-load and 2.5 m/s rolling speed..... 49
Figure 2-21: Ball-on-disc tribometer composed of tribological part (ball-on-disc device) and an observation device (microscope and related camera)..... 50
Figure 2-22: Size distribution of the rhodamine tracers composing the red fire fluo paint provided by Lefranc et Bourgeois®..... 52
Figure 2-23: Ball-on-disc test-rig coupled with PIV system composed of an illumination source/guidance stick/recording device..... 53
Figure 2-24: Ball-on-disc machine coupled with the PIV system..... 54
Figure 2-25: Principle of synchronized pulsed lasers..... 55
Figure 2-26: Sequential illumination of the fluid domain for performing particle tracking..... 55
Figure 2-27: Principle of the PIV analysis [127]..... 56
Figure 3-1: Rhodamine particles from Lefranc & Bourgeois® (paint red fire fluo) mixed with sieved M50 steel particles (in the range 32–40 μm) observed with an optical microscope..... 62
Figure 3-2: Visualization of particle entrapment in a steel-glass contact (5 mm/s; 10N; optical x10 objective -field size of 1.805 x 1.820 mm): - (a, left) film thickness distribution obtained with numerical model; (a, right) picture of the contact - (b) series of 6 successive pictures taken between t = 0 s and t = 0.33 s..... 63
Figure 3-3: Section view of an EHD contact with process leading to particle entrapment..... 64
Figure 3-4: Mapping of the mean velocity field from a PIV analysis for a circular steel-glass contact with operating conditions: 0.005 m/s – 10 N..... 66

Figure 3-5: Mapping of the mean velocity field from a PIV analysis for a circular steel-glass contact with operating conditions: 0.5 m/s – 10 N 66
Figure 3-6: a) Side view of the fluid domain (illustration of the numerical fluid domain (striped area)); b) Front view of the release plane at RP_x = -6*a* (release positions at the inlet boundary) . 68
Figure 3-7: Mapping of particle entrapment according to release positions across the film thickness for steel–steel equivalent contact considering a 40 μm particle and using the conditions in Table 3-2 (striped red circles represent the farthest positions from the surfaces and the symmetry plane for which the particles are entrapped) 69
Figure 3-8: Streamlines for a fluid flow entering the domain at x = -2.4 mm, y =-5 μm and Δz = h_{in} = 164 μm (across the film thickness) upstream from a steel–steel contact (striped red circles represent the farthest positions from the surfaces and the symmetry plane for which the particles are entrapped) 70
Figure 3-9: Mapping of particle entrapment according to release position across the film thickness for a symmetrical two-body steel–steel contact considering a 40 μm particle and using the conditions in Table 3-2 (striped red circles represent the farthest positions from the surfaces and the symmetry plane for which the particles are entrapped) 71
Figure 3-10: Mapping of particle entrapment for different mean rolling speeds (18 – 22 – 30 m/s) within a two-body symmetrical steel–steel contact using the conditions in Table 3-2 (striped red circles represent the farthest positions from the surfaces and the symmetry plane for which the particles are entrapped) 72
Figure 3-11: Size of the fluid domain for the entrapment calculations using different loads 73
Figure 3-12: Mapping of particle entrapment for different contacting loads (300 – 600 – 1200 N) within a two-body symmetrical steel–steel contacts using the conditions of Table 3-2 (striped red circles represent the farthest positions from the surfaces and the symmetry plane for which the particles are entrapped) 74
Figure 3-13: Particle-size effect on entrapment with a large particle (40 μm) and a small one (10 μm) within a steel-steel contact (operating conditions in Table 3-2) 75
Figure 3-14: Mapping of particle entrapment according to particle size (10, 20 and 40 μm) within a two-body symmetrical steel–steel contacts using the conditions in Table 3-2 76
Figure 3-15: Surface of a steel disc after a twin-disc test with a controlled level of contaminants of different sizes (10-20 and 32–40 μm) within a steel-steel contact 78
Figure 3-16: Particle-mass effect with a steel and a sand particle released at the same position within a steel-steel contact 78
Figure 3-17: Evolution of the Stokes number within confined gaps of various thicknesses considering different steel particles from 10 to 40 μm, for a fixed viscosity of the fluid: 12 mPa·s and constant relative particle speed: 3 m/s 79
Figure 3-18: Side view of an EHD circular contact with lubricant streamlines leading to particle entrapment or bypass 80
Figure 3-19: Schematic section view of an EHD circular contact with velocity profiles of the lubricant across the film thickness at different abscissa 82
Figure 3-20: Fluid velocity profile across the dimensionless film thickness 83

Figure 3-21: Fluid velocity profiles across the film thickness for three different mean rolling speed (18 – 22 – 30 m/s) for a same applied load equal to 600 N 84
Figure 4-1: Number of dents (corresponding to the number of entrapped particles) for experiments (dispersion established after 3 successive tests) with (left) all-steel and (right) Si_3N_4–steel contacting surfaces using a unique range of contaminants (32–40 μm), see conditions Table 4-1 91
Figure 4-2: Mapping of particle entrapment according to release position across the film thickness for (left) an all-steel contact and (right) a Si_3N_4–steel one considering a 40 μm particle with the conditions in Table 4-2 92
Figure 4-3: Number of dents (corresponding to the number of entrapped particles) for experiments with all-steel contacting surfaces and Si_3N_4–steel ones (left) with a constant load (dispersion established after 3 successive tests) and (right) with a constant Hertzian surface (1 test) using a unique range of contaminants (32–40 μm) with conditions in Table 4-2 93
Figure 4-4: Scenario of the particle and surface deformations 94
Figure 4-5: Profiles of two representative dents made on all-steel contact by a steel particle in the range 32–40 μm 94
Figure 4-6: Profiles of two representative dents made on a Si_3N_4-steel contact by a steel particle in the range 32–40 μm 95
Figure 4-7: Different contacts existing in REBs [135] 96
Figure 4-8: Section view and EW for a circular (k = 1) and an elliptical contact configuration (k = 1.6) 97
Figure 4-9: Number of dents (corresponding to the number of entrapped particles) in different contacts for steel–steel contacts under pure rolling condition with 10 mg/l contamination (particles 32–40 μm) and conditions of Table 4-1 98
Figure 4-10: Streamlines for a fluid line entering the domain at x = -2.4 mm, Δy = 200 μm, z = 10 μm, for a circular contact (k = 1) and conditions of Table 4-1 99
Figure 4-11: Streamlines for a fluid line entering the domain at x = -2.4 mm, Δy = 200 μm, z = 10 μm, for an elliptical contact (k = 1.6) and conditions of Table 4-1 100
Figure 4-12: Streamlines for a fluid line entering the domain at x = -2.4 mm, Δy = 200 μm, z = 10 μm, for an elliptical contact (k = 2.5) and conditions of Table 4-1 100
Figure 4-13: Particle trajectories within a circular contact (top) and an elliptical one (bottom) for the same upstream release position: RP_x = -2400 μm, RP_y = -10 μm and RP_z = 20 μm 101
Figure 4-14: Visualization of the fluid flow upstream a steel–glass circular contact with k = 1 (5 mm/s – 10 N) 103
Figure 4-15: Visualization of the fluid flow upstream a steel–glass elliptical contact with k = 3.5 (5 mm/s – 50 N) 103
Figure 4-16: Visualization of the fluid flow upstream a steel–glass elliptical contact with k = 8 (5 mm/s – 50 N) 104
Figure 4-17: Entrapment features after rolling–sliding tests in the steel–steel configuration (600N – 22 m/s – SRR=12%) (a): embedded particles, (b): dents left by entrapped particles 105
Figure 4-18: Stages of the indentation process during a rolling–sliding test: (A) the particle is trapped between the surfaces, (B) the particle is squeezed and sheared in the contact, (C) the

particle is expelled from the contact and the dents caused by entrapment remains on the discs surfaces 106
Figure 4-19: Number of dents for different steel–steel twin-disc experiments in pure rolling and in rolling–sliding conditions (SRR=12%) for different configurations: circular (k=1) and elliptical (k=1.6 and 2.5) contacts with conditions of Table 4-1 107
Figure 4-20: Number of dents on the steel disc for two different twin-disc experiments with SRR = 12 % within a hybrid Si_3N_4–steel circular contact with the steel disc moving faster and (left) with the Si_3N_4 disc moving faster (right) with conditions of Table 4-1 with 11 mg/l of contaminants 108
Figure 4-21: Resulting steel disc surfaces with embedded particles observed in both steel–steel and Si_3N_4–steel contacts with SRR=12% with conditions of Table 4-1 with 11 mg/l of contaminants 109
Figure 4-22: Marks observed on a Si_3N_4 disc after a rolling-sliding test within a hybrid Si_3N_4–steel contact (600N – SRR=12% – 60°C – 5min) 110
Figure A-1: Full-scale test of volcano particle intake performed by NASA [145] 121
Figure A-2: SEM pictures of the volcano ashes (from El Misti volcano, Peru and from Fuji Mount, Japan) and Energy-dispersive X-ray spectroscopy (EDX) analysis revealing the ash compositions 122
Figure A-3: Indentation marks left on the steel surface after a twin-disc test with a steel–steel contact with the operating conditions: 600 N – 22 m/s – 60 °C – 5 min 123
Figure A-4: Indentation marks left on steel counterfaces after two different twin-disc tests with a hybrid Si_3N_4–steel couple of contacting materials with the operating conditions: 600 N – 22 m/s – 60 °C – 5 min and two types of particles dispersed in the lubricant (boron carbide – left and El Misti volcano ashes – right) 124
Figure B-1: Mapping of the velocity vectors using the experimental ball-on-disc set-up with a PIV analysis 125
Figure B-2: Mapping of the velocity vectors using the numerical simulations 126
Figure B-3: Comparison of the velocity vector mapping for the experimental ball-on-disc machine and using the numerical simulation for a circular glass–steel contact with following operating conditions: 10 N applied load and 0.5 m/s rolling speed 126
Figure D-1: Number of dents (corresponding to the number of entrapped particles) for different pure rolling experiments, with steel–steel and Si_3N_4–steel contacting discs for different contact configurations: k=1, k=1.6 and 2.5 with 10 mg/l contamination and conditions of Table 4-1. 129

List of tables

Table 1-1: Contaminant origin in aeronautical REBs according [13,14] 15
Table 2-1: WLF parameter for the MIL-L-23699 lubricant [30] 33
Table 2-2: Properties of the contacting discs 44
Table 2-3: Different geometries and related parameters resulting for steel-steel contact 44
Table 2-4: Properties of lubricant Nycobase 5750 in comparison to lubricant MIL-L-23699 45
Table 2-5: Properties of the rotating counterparts of the ball-on-disc machine 50
Table 2-6: Different geometries and related parameters resulting from the contact between a steel ball or a steel barrel and a glass disc 51
Table 2-7: Size of the observed fluid domain with the different microscope objectives 54
Table 2-8: Correlation between rolling speed and synchronization time 57
Table 2-9: Range of parameters for the EHD contacts simulated with the different numerical/ experimental tools 57
Table 3-1: Contact parameters for particle entrapment tests 61
Table 3-2: Operating conditions and contact parameters for a steel-steel contact 68
Table 3-3: Contact parameters for the simulated contact conditions 73
Table 3-4: Parameters and results of entrapment tests carried out on the twin-disc tests with particles of different sizes: 10–20 and 32–40 μm 77
Table 3-5: Flow of lubricant in the Hertzian contact for three different loads (300 – 600 – 1200 N) using the conditions of Table 3-2 81
Table 4-1: Operating conditions for tests performed with the twin-disc machine and the ball-on-disc tribometer 89
Table 4-2: Contact parameters for an all-steel contact and a hybrid one (600 N) 90
Table 4-3: Parameters for the different contact configurations tested on the twin-disc machine for operating conditions in Table 4-1 97
Table 4-4: Contact parameters obtained with a steel ball or steel barrel and a glass disc on the ball-on-disc machine 102
Table 4-5: Dent dimensions (in pure rolling and rolling–sliding conditions) for steel–steel and Si_3N_4–steel contacts with conditions of Table 4-1 106
Table A-1: Pair of contacting materials for twin-disc tests performed with volcano ashes with the following operating conditions: 600 N – 22 m/s – 60 °C – 5 min 122

Nomenclature

a	Hertzian radius or semi-minor axis	[m]
A_1	WLF parameter for Yasutomi and new Yasutomi correlation	[°C]
A_2	WLF parameter for Yasutomi and new Yasutomi correlation	[1/GPa]
b	Semi-major axis	[m]
B_1	WLF parameter for Yasutomi correlation	[-]
B_2	WLF parameter for Yasutomi correlation	[1/GPa]
C	Concentration of particles in solution	[mg/l]
C_1	WLF parameter for Yasutomi and new Yasutomi correlation	[-]
C_2	WLF parameter for Yasutomi and new Yasutomi correlation	[°C]
C_D	Drag coefficient	[-]
d_p	Particle diameter	[m]
E_i	Young modulus	[Pa]
f	Frequency	[Hz]
$\boldsymbol{F_B}$	Buoyancy force	[N]
$\boldsymbol{F_D}$	Drag forces	[N]
$\boldsymbol{F_{fr,i}}$	Friction forces	[N]
$\boldsymbol{F_G}$	Gravity force	[N]
$\boldsymbol{F_i}$	On particle acting forces	[N]
$\boldsymbol{F_{N,i}}$	Normal forces	[N]
$\boldsymbol{F_S}$	Stokes force	[N]
$\boldsymbol{g}$	Gravity vector	[m/s^2]
h	Film thickness	[m]
h_c	Central film thickness	[m]
h_{in}	Inlet film thickness	[m]
$\boldsymbol{\bar{I}}$	Identity matrix	[-]
K_1	Constant of the Poiseuille term	[m/s]
k	Ellipticity ratio	[-]
m_p	Particle mass	[kg]
$n_{ent,part}$	Number of entrapped particles	[-]
$\boldsymbol{n}$	Normal vector to the boundary	[-]
$N_{pix,X}$	Number of pixels of the camera along x	[-]
p	Pressure	[Pa]
P_{atm}	Atmospheric pressure	[Pa]
$P_{Reynolds}$	Pressure obtained by the resolution of the Reynolds equation	[Pa]
P_H	Hertzian pressure	[Pa]
$Q_{contact}$	Flow in the contact	[m^3/s]
R_a	Roughness, arithmetic average	[m]
R_p	Particle radius	[m]
R_x , R_y	Curvature radii	[m]
RP_x	Release position along x-axis	[m]

RP_y	Release position along y-axis	[m]
RP_z	Release position along z-axis	[m]
t	Duration of contaminated lubrication	[s]
T	Temperature	[°C]
T_g	Glass temperature	[°C]
T_S	Sequential time	[s]
u	Fluid velocity along x	[m/s]
$\boldsymbol{U_f}$	Fluid velocity vector	[m/s]
$\boldsymbol{U_m}$	Mean rolling speed: $(U_1+U_2)/2$	[m/s]
U_r	Relative particle speed to the surrounding fluid	[m/s]
U_1	Rolling speed of the lower contacting solid	[m/s]
U_2	Rolling speed of the upper contacting solid	[m/s]
v	Fluid velocity along y	[m/s]
v_p	Particle speed	[m/s]
$\boldsymbol{v_p}$	Particle velocity vector before interaction with a wall	[m/s]
$\boldsymbol{v'_p}$	Particle velocity vector after interaction with a wall	[m/s]
V_p	Particle volume (spherical particle: $4/3\Pi R_p^3$)	[m^3]
w	Fluid velocity along z	[m/s]
W	Load	[N]
x	Coordinate parallel to rolling direction	[m]
$\boldsymbol{x_p}$	Particle position vector	[m]
X	Dimensionless coordinate along x	[-]
X_c	Critical meniscus position	[m]
y	Coordinate normal to rolling direction	[m]
z	Coordinate across film thickness	[m]
Z	Dimensionless coordinate along z (dimensionless thickness)	[-]
$\boldsymbol{z}$	Direction vector along z	[m]
Δ_C	Size of the Couette dominated zone	[m]
Δ_P	Size of the Poiseuille dominated zone	[m]
Δt	Synchronization time	[s]
ΔX	size of the camera image in the x-direction	[m]
ΔY	size of the camera image in the y-direction	[m]
μ	Viscosity	[Pa.s]
μ_g	Glass transition viscosity	[Pa.s]
ν_i	Poisson ratio	[-]
ϱ_f	Fluid density	[kg/m^3]
ϱ_p	Particle density	[kg/m^3]
ϱ_{sand}	Sand density	[kg/m^3]
ϱ_{steel}	Steel density	[kg/m^3]
ω_i	Rotational speed	[rpm]

Dimensionless numbers

M	Moes parameter	$M = \frac{W}{E_{eq}R^2}\left(\frac{\mu(U_1+U_2)}{E_{eq}R}\right)^{-3/4}$
Re	Reynolds number	$Re = \frac{U_r d_p \varrho_f}{\mu}$
St	Stokes number	$St = \frac{\varrho_p d_p^2 U_r}{18\mu h}$

Abbreviations

AISI	American Iron and Steel Institute
Al_2O_3	Aluminum oxide
B_4C	Boron carbide
CARB	Compact Aligning Roller Bearings
CFD	Computational Fluid Dynamics
CRB	Cylindrical Roller Bearings
DDL	Degré de Liberté
DGBB	Deep Groove Ball Bearings
DLM	Distributed Lagrange Multiplier
DoF	Degree of Freedom
EDX	Energy-Dispersive X-ray spectroscopy
EHD	ElastoHydrodynamic
EHL	ElastoHydrodynamic Lubrication
EW	Entrapment width
FEM	Finite Element Method
FWHM	Full Width at Half Maximum
HL	Hydrodynamic Lubrication
HR	Rockwell Hardness
HV	Vickers Hardness
IFTS	Institut de la Filtration et des Techniques Séparatives
INSA	National Institute of Applied Sciences
ISO	International Organization for Standardization
LaMCoS	Contact and Structure Mechanics Laboratory
MD	Molecular Dynamics
MEB	Microscope Electronique à Balayage
NASA	National Aeronautics and Space Administration
NS	Navier-Stokes

Nd:YAG	Neodymium-doped Yttrium Aluminium Garnet
OEM	Original Equipment Manufacturer
PIV	Particle Image Velocimetry
REBs	Rolling Element Bearings
RCF	Rolling Contact Fatigue
SEM	Scanning Electron Microscope
SiC	Silicon carbide
Si_3N_4	Silicon nitride
SRR	Slide-to-Roll Ratio
TiO_2	Titanium dioxide
TRL	Technology Readiness Level
VII	Viscosity Index Improver
ZrO_2	Zirconium dioxide

Résumé étendu

Résumé étendu

Ce manuscrit de thèse ayant été rédigé en anglais, un résumé étendu des travaux et des principaux résultats est proposé en français.

a. Introduction

Beaucoup de roulements sont présents dans les mécanismes rotatifs. La demande est telle que la production mondiale atteint aujourd'hui plus de 5000 roulements par seconde. Des roulements de toutes tailles et de tous types couvrent une très large plage d'applications, allant des micro-mécanismes embarqués aux appareillages de très grandes dimensions tels que les grandes roues de parcs d'attractions.

La plupart de ces roulements sont lubrifiés. Le lubrifiant intervient dans les contacts élastohydrodynamiques (EHD). Il a pour mission de séparer les surfaces en évitant l'usure et en diminuant le frottement. Or il est possible que des polluants solides soient transportés au sein de ces contacts. La question principale de cette étude est de savoir quel entrainement critique est susceptible de guider de telles particules dans les contacts et de mener à leurs piégeages. Le piégeage peut alors causer un endommagement des surfaces et un risque de défaillance prématurée pour l'ensemble du système. Les recherches actuelles visent à introduire de nouveaux matériaux, plus durs, plus à même de résister aux conditions extrêmes imposées dans les contacts EHD. Ainsi la présence de particules au voisinage des contacts peut difficilement être évitée mais les phénomènes critiques menant au piégeage doivent être mieux maitrisés.

Le **chapitre 1** présente les bases de la lubrification dans les roulements et les défis rencontrés dans l'élaboration du roulement de demain. Un état de l'art permet de mettre en lumière les principales avancées réalisées sur l'analyse de la présence de contaminants solides au sein de contacts EHD.

Pour identifier les phénomènes critiques du piégeage de particules, des méthodes originales d'investigation ont été développées dans cette thèse. Les techniques numériques et expérimentales qui ont permis l'étude de ce problème sont présentées dans le **chapitre 2.**

Une analyse séquentielle a été mise en place. Le **chapitre 3** présente une étude phénoménologique de la contamination particulaire dans un contact circulaire. Il donne les paramètres généraux qui conduisent au piégeage, tels que les propriétés de la particule (taille, nature) et les paramètres du contact (charge, vitesse de roulement).

Une extension à des cas plus réalistes est réalisée dans le **chapitre 4**. Les contacts hybrides nitrure de silicium (Si_3N_4)–acier, les contacts elliptiques ainsi que des contacts avec roulement–glissement sont étudiés.

b. Etat de l'art

La grande variété des contacts lubrifiés que l'on retrouve dans les roulements se confronte au problème de contamination par des particules solides (débris d'usure, poussières, etc.).

Dans le cadre de cette étude, l'application visée est un roulement d'arbre principal au sein d'un turbopropulseur. Ces roulements doivent répondre à la fois à de fortes exigences en terme de fiabilité et à de nouvelles règles de conception allégée.

Ces roulements sont généralement conçus entièrement en acier, pour répondre aux conditions extrêmes de fonctionnement telles que de hautes vitesses de rotation, des hautes températures de fonctionnement ou une lubrification contaminée. Aujourd'hui de nouveaux matériaux sont envisagés tels que le nitrure de silicium (Si_3N_4) choisi pour ses propriétés à la fois de dureté renforcée (HRC>60), de faible densité (3260 kg/m^3) et ses bonnes propriétés en terme de résistance électrique, thermique et à la corrosion.

L'utilisation du Si_3N_4 dans les roulements est envisagé au travers de son association avec un acier standard dans un roulement hybride où les éléments roulants sont en Si_3N_4 et les bagues en acier. De nombreuses études tant au niveau des performances matériaux [1–4] que des performances tribologiques [5–10] ont été menées conjointement pour mettre en évidence les possibilités offertes par cette combinaison de matériaux.

Le challenge imposé par la présence de contaminants dans des contacts lubrifiés est d'autant plus important que la contamination peut être aussi diverse et variée (Figure 0-1) que le types d'applications pour lesquels sont prévus ces roulements. Cette contamination peut être intrinsèque au lubrifiant (voir les relevés ferrographiques sur des huiles neuves [11,12]), provenir de l'environnement extérieure lors du survol d'un désert par exemple, ou encore être générés lors de rodage des pièces à la mise en route du mécanisme [13,14].

Hunt proposa ainsi une catégorisation de ces types de particules en plusieurs sous catégories en fonction de leurs types :

- de source externe ou interne
- due à l'usinage, le montage, le rodage ou l'usure
- due à l'environnement (grains de sables, cendres de volcans, suies de combustion)
- de leur nature, ductile ou fragile

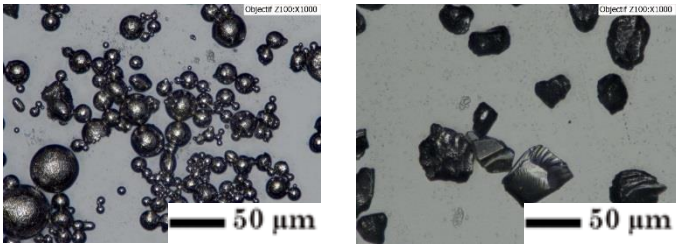

(gauche) particules d'acier M50 et (droite) de carbures de bore (microscope optique)

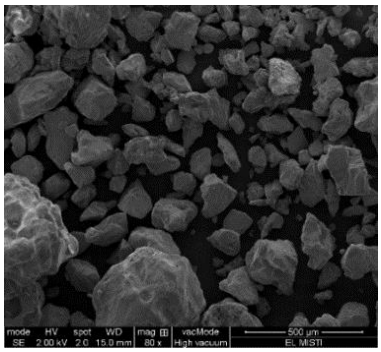

Cendres de volcans (MEB)

Figure 0-1: Particules d'acier, de carbures de bore et de cendres de volcans

Dans les années 70, Fitzsimmons et Clevenger [15] réalisèrent les premiers tests en lubrification polluée sur des bancs de roulements. Ces essais montrèrent rapidement que la nature et la taille des particules conduisent à des endommagements totalement différents. Il apparut ainsi que des particules micrométriques peuvent entrer et se faire piéger dans des confinements sub-micrométriques [16].

De nombreux chercheurs ont alors observé, analysé et quantifié le piégeage de contaminants solides au sein de contacts lubrifiés. Dans les années 90, Cann et al. [17] implémentèrent la technique d'interférométrie combiné à une machine bille sur disque pour observer le phénomène de piégeage. Ville et Nélias [18] et Dwyer-Joyce et Heymer [19] focalisèrent leur travail respectif sur les analyses qualitatives et quantitatives des profils d'indentation résultants du piégeage de particules. Sur deux dispositifs différents, une machine bi-disques ou un dispositif bille sur disque, ils quantifièrent le taux de piégeage en fonction des paramètres des particules polluantes (taille, nature) et des conditions opératoires (vitesse de roulement, taux de glissement et charge).

Nikas [20–23] entreprit pour la première fois une modélisation numérique du piégeage de contaminants. Au travers de l'implémentation des différentes forces pouvant agir sur une particule en suspension dans le lubrifiant, il retrouva un ensemble d'observations expérimentales telles que la plus faible probabilité de piégeage de petites particules.

Les perspectives promises à la technologie de roulements hybrides entrainèrent aussi la mise en place d'une série d'étude sur l'impact de l'utilisation d'un couple hybride de matériaux en régime de

lubrification polluée. Kahlman et Hutchings [24] notamment mirent en évidence la meilleure résistance des surfaces céramiques à toute forme d'indentation.

La compréhension des verrous phénoménologiques donnant lieu au piégeage de particules est une nécessité visant à améliorer de manière générale la durée de vie du roulement et donc du mécanisme. Les lois de prédiction probabilistiques successivement proposées par Lundberg-Palmgren [25], Harris [26] puis Zaretsky et al. [27] ont montrées leurs limites et nécessitent aujourd'hui d'être basées sur des études déterministes. C'est au travers de recherches sur des conditions de fonctionnement le plus large possible telles que l'influence de différents types d'acier, des régimes de lubrification ou de la présence de contaminants solides que pourra être de mieux en mieux maîtrisée la durée de vie des roulements.

c. Développement d'outils d'investigations

Bien qu'il n'existe pas aujourd'hui de bancs d'essais entièrement consacrés ou dédiés à l'étude du piégeage dans les roulements ou de formules analytiques permettant de prédire le taux de piégeage exacte de contaminants solides en environnement polluée. On peut combiner à la fois les moyens numériques et expérimentaux pour l'étude du piégeage de particules.

c1. Simulations numériques

Ecoulement du fluide en entrée d'un contact EHD

Le piégeage de contaminants résulte du transport de particules solides par le lubrifiant au sein du contact. Ainsi, il s'agit de comprendre comment un entrainement critique de ces particules par le lubrifiant mène à leur piégeage. Ici, on choisit donc de découpler l'analyse de la circulation du lubrifiant de celle de la dynamique des polluants solides.

Ce lubrifiant est présent tout autour et dans la zone hertzienne du contact EHD. Les hypothèses de films minces sont posées et l'équation de Reynolds est résolue de manière couplée à l'élasticité des solides [28,29].

L'épaisseur de film est exprimée en fonction de deux rayons équivalents dans les deux directions du contact (notées x et y par la suite). L'élasticité des solides est résolue sur un solide équivalent caractérisé par 2 coefficients d'élasticité équivalents E_{eq}, ν_{eq}. La résolution de l'équation de Reynolds donne les profils de pression et d'épaisseur de lubrifiant. Le champ 3D complet des vitesses est ensuite obtenu à l'aide de la résolution des équations de Navier-Stokes dans le domaine fluide 3D (Figure 0-2) qui se trouve en amont du contact, où l'épaisseur de film est plus grande.

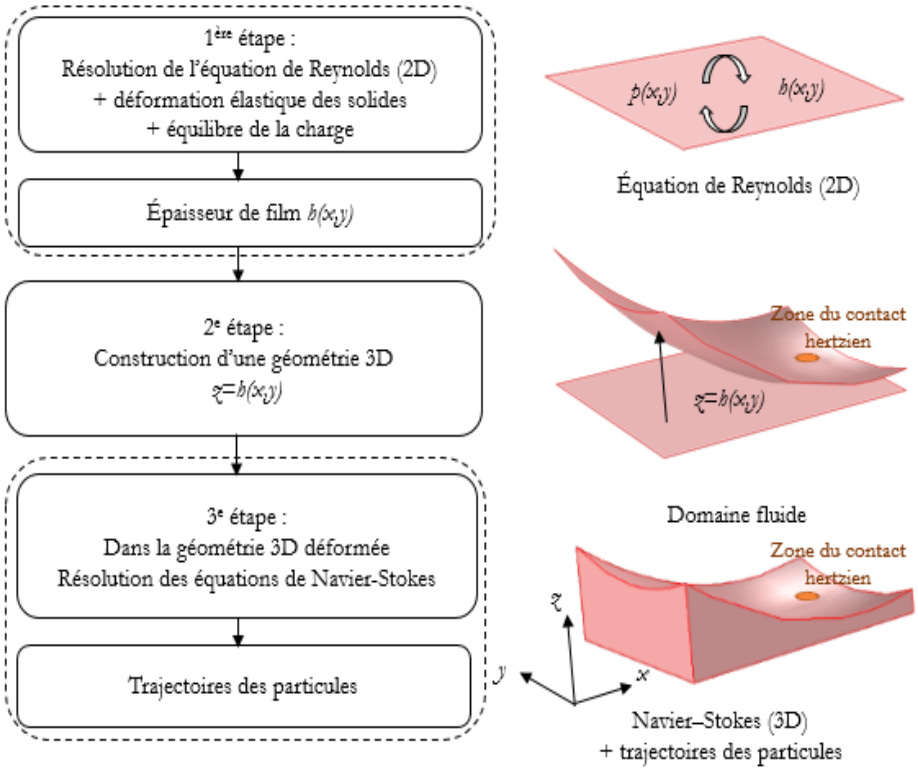

Figure 0-2: Définition du domaine 3D d'écoulement

Dans le cadre de cette étude, focalisée sur des applications aéro-spatiales, un modèle de lubrifiant aéronautique, basé sur le travail de Vergne et Nélias [30] est utilisé. Les paramètres rhéologiques de la loi WLF sont utilisés pour définir le comportement de la viscosité du lubrifiant et la loi de Dowson-Higginson définit l'évolution de la densité en fonction de la pression.

La définition des frontières du domaine fluide est directement dépendante des conditions opératoires que l'on cherche à évaluer. Dans ce travail, on considèrera les conditions suivantes :

- Rayons de courbures équivalents : 10–20 mm
- Vitesses linéaires de roulement : jusqu'à 30 m/s
- Pressions de contacts hertziens : jusqu'à 2 GPa

Le piégeage se déroule en amont du contact. Un plan de symétrie dans le sens principal de l'écoulement est postulé (Figure 0-3 – (i)). La frontière d'entrée (Figure 0-3 – (ii)) c'est-à-dire la localisation du ménisque d'huile en amont du contact doit être définie avec soin. Comme les hypothèses de lubrification complète sont considérées, on suppose ici que cette frontière est localisée 3 fois plus loin que la position critique du ménisque X_C qui correspond au passage d'un régime de lubrification complète à un régime de lubrification sous-alimentée. L'écoulement du lubrifiant ne doit pas dépendre de la position du bord latéral du domaine (Figure 0-3 – (iii)) qui devra donc se trouver

suffisamment loin de l'axe central. La frontière de sortie (Figure 0-3 – (iv)) est située aux alentours de la zone centrale du contact. Une particule la franchissant est soit piégée dans le contact soit dévié définitivement.

Les conditions aux limites des équations de Navier-Stokes sont définies comme suit, le long des différentes frontières du domaine (Figure 0-3) :

$$\begin{aligned} &\text{(i)}: \ \boldsymbol{U_f} \cdot \boldsymbol{n} = 0 \\ &\text{(ii) et (iii)}: P = P_{atm} \text{ and } \left(\nabla \boldsymbol{U_f} + \nabla \boldsymbol{U_f}^T\right) \cdot \boldsymbol{n} = 0 \\ &\text{(iv)}: P = P_{Reynolds} \end{aligned} \qquad (0\text{-}1)$$

avec $\boldsymbol{n}$ le vecteur normal à la surface, $\boldsymbol{U_f}$ le vecteur vitesse du fluide, P la pression, P_{atm} la pression atmosphérique et $P_{Reynolds}$ la pression calculée sur la frontière de sortie par la résolution de l'équation de Reynolds couplée à l'élasticité des solides.

Sur les bords inférieurs et supérieurs du domaine fluide des conditions de non-glissement sont imposées :

(v) Bord inférieur

$$\begin{Bmatrix} u \\ v \\ w \end{Bmatrix} = \begin{Bmatrix} U_1 \\ 0 \\ 0 \end{Bmatrix} \qquad (0\text{-}2)$$

(vi) Bord supérieur

$$\begin{Bmatrix} u \\ v \\ w \end{Bmatrix} = \begin{Bmatrix} (R_x - z)\omega \\ 0 \\ x\omega \end{Bmatrix} \qquad (0\text{-}3)$$

avec $U_2=R_x\omega$, la vitesse linéaire de la surface supérieure au point de contact, R_x le rayon de courbure selon x et ω la vitesse de rotation.

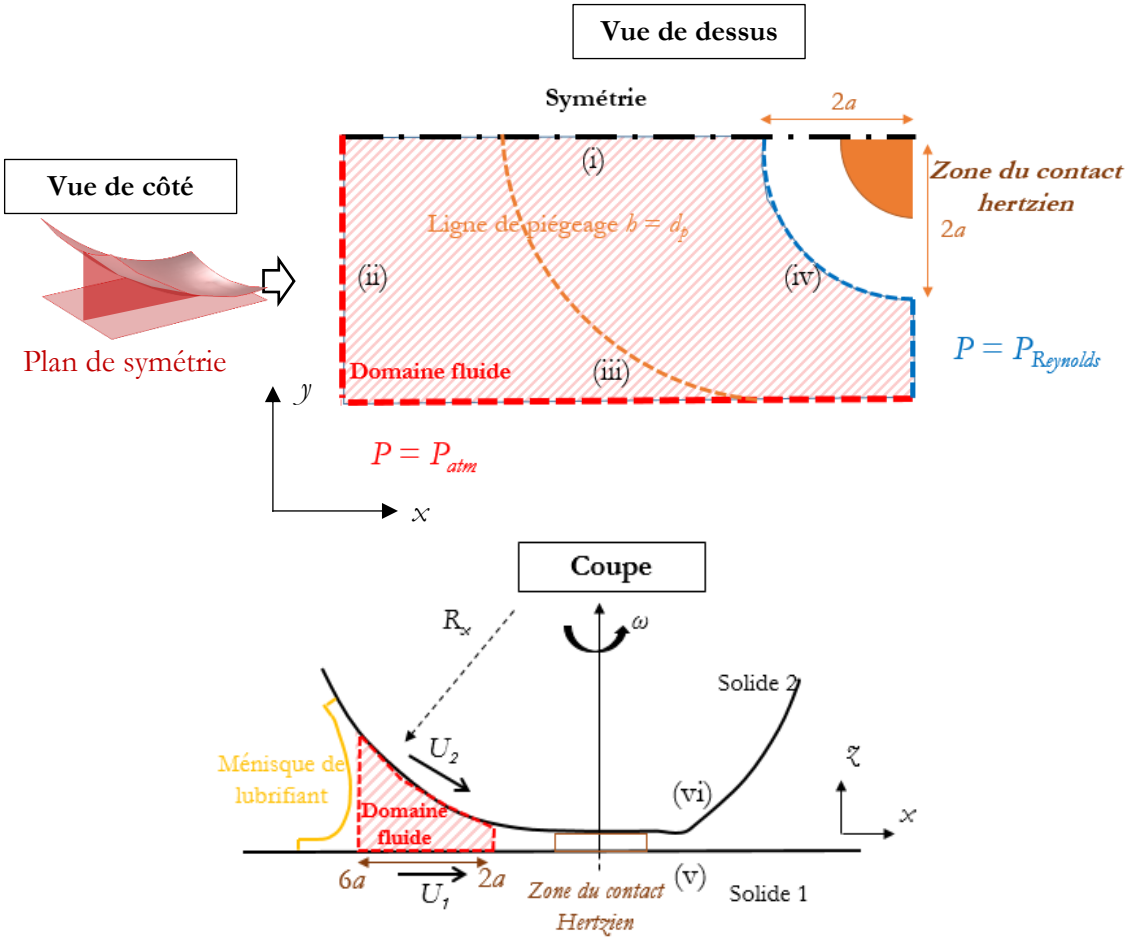

Figure 0-3 : Domaine fluide et conditions aux limites

Suivi de contaminants solides

Le domaine d'étude étant défini et le champ de vitesse dans le lubrifiant pouvant être calculé, on s'intéresse à l'étude de contaminants solides transportés par le lubrifiant.

Le choix d'un couplage faible fluide-particule est proposé dans le cadre de cette étude. Il est justifié par l'hypothèse de considérer une seule particule à la fois. Par sa faible taille, son interaction avec le domaine fluide est faible et on peut considérer que l'effet du passage d'une seule particule sur le champ de vitesse du fluide est négligeable.

La trajectoire de la particule est calculée en résolvant la loi de la dynamique d'un corps rigide de Newton. Un ensemble de 3 forces agit sur la particule : son poids, $\boldsymbol{F_G}$, la poussée d'Archimède, $\boldsymbol{F_B}$, et les forces de trainée, $\boldsymbol{F_D}$, qui proviennent de l'écoulement du lubrifiant (Figure 0-4).

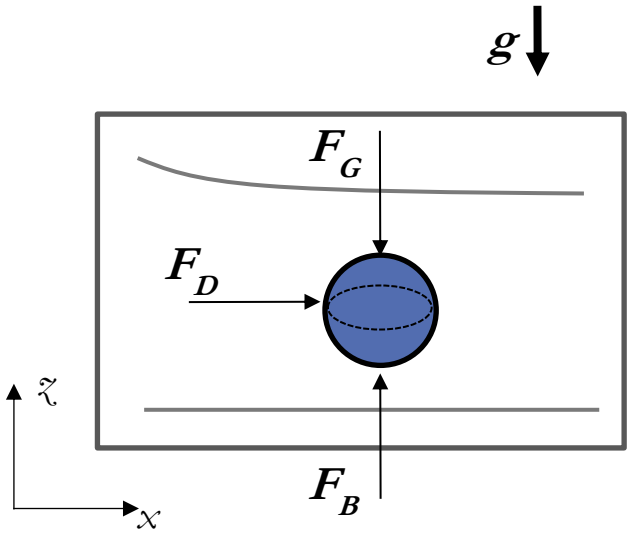

$$F_D = \frac{3\mu Re C_D}{4\varrho_p d_p^2} m_p \left(U_f - v_p\right)$$

$$F_G = -\varrho_p V_p g$$

$$F_B = \varrho_f V_p g$$

Figure 0-4 : Résumé du modèle de couplage fluide-particule

Des simulations numériques peuvent donc être menées en considérant différentes charges, vitesses de roulement, taux de glissement, géométries des solides en contact, propriétés de particules (nature, taille) et des positions de lâcher différentes.

c2. Machine bi-disques avec banc de pollution

Le premier banc d'essais vise à reproduire les conditions de contacts fortement chargées avec hautes vitesses de roulements telles qu'on peut les trouver au sein de roulements aéronautiques. C'est une machine en configuration bi-disques [31], constituée de deux disques contrôlés par 2 électro-broches indépendantes et d'un système de mise en charge hydraulique. La machine est lubrifiée avec une huile, ester de base (Nycobase 5750) et peut être alimentée en régime de lubrification contaminée à l'aide d'un système appelé banc de pollution, comme représentée sur la Figure 0-5.

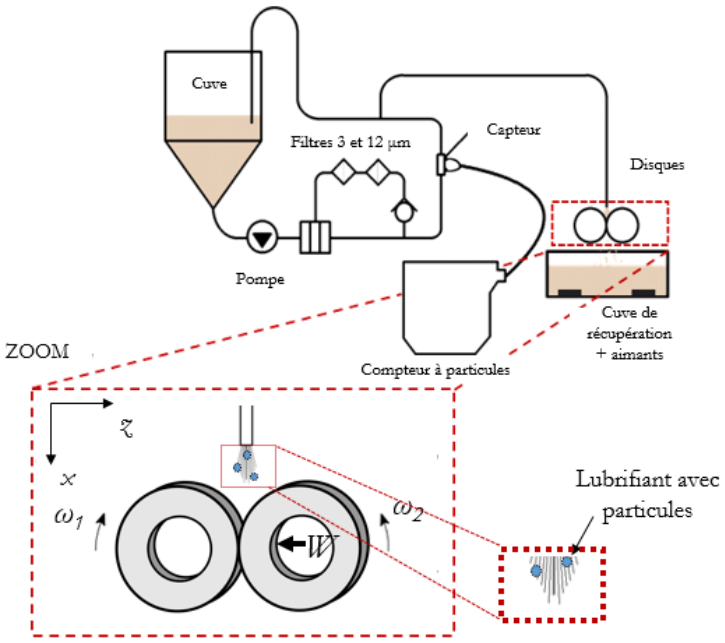

Figure 0-5 : Machine bi-disques et banc de pollution

Les 2 disques présentent à leurs surfaces de contact (tranches) différents rayons de courbures R_x et R_y. L'association d'un disque cylindrique (i.e. avec un rayon R_y infini) avec un disque bombé permet de reproduire des contacts ponctuels avec une aire de contact à ellipticité variable. Le rayon R_x est le même pour tous les disques et vaut 35 mm, le rayon, R_y varie entre 17.5 (contact circulaire), 35, 70, 200 mm (et ∞ pour le cas cylindrique).

Différents matériaux sont utilisés dans cette étude, des disques en acier AISI 52100 pour les disques bombés de rayons de courbures R_y 17.5 et 200 mm, AISI M50 pour les disques de courbures R_y 35 et 70 mm. Les disques cylindriques dans le cas des contacts hybrides sont en nitrure de silicium (Si_3N_4). Les disques sont polis jusqu'à obtenir une rugosité arithmétique (R_a) de 0.05 µm.

Le banc de pollution est un dispositif en boucle fermée constituée d'un compteur à particules commerciale fournie par la société UCC®, de 2 filtres de 3 et 12 µm pour nettoyer l'huile une fois l'essai terminé et d'une pompe permettant la circulation du lubrifiant. Une dérivation de ce banc permet de le relier à la machine bi-disques et ainsi de réaliser des essais en régime de lubrification polluée avec un contrôle sur la nature de la contamination (concentration, distribution en taille des particules, etc.). Les tests de cette étude ont été réalisés avec des particules d'acier AISI M50 tamisées avec des diamètres de 32-40 µm et 10-20 µm.

Chaque particule piégée en acier ductile est supposée être responsable d'une unique marque d'indentation sur les disques roulants. On peut ainsi quantifier le taux de piégeage de contaminants par un comptage précis des marques d'indentation après essai à l'aide d'un microscope optique.

c3. Machine bille-disque avec technique de visualisation par fluorescence

Machine et matériel

La question de la capacité d'observation du piégeage aux abords du contact est posée. Les techniques expérimentales de visualisation en mécanique des fluides sont aujourd'hui adaptées à des micro-écoulements, et l'utilisation de particules fluorescentes offrent la possibilité de visualisation in-situ dans un banc d'essais, appelé communément tribomètre. Ici, le tribomètre est une machine bille-disque développée en interne [32], qui permet de reproduire des contacts roulants sur une large plage de vitesses (0.005-6 m/s) et avec différents matériaux (éprouvettes interchangeables).

Cette machine conçue initialement pour des essais en frottement ou des mesures interférométriques d'épaisseur de film peut aussi servir à réaliser des essais de visualisation d'écoulement du fluide en se focalisant sur une zone en amont du contact hertzien comme représentée sur la Figure 0-6.

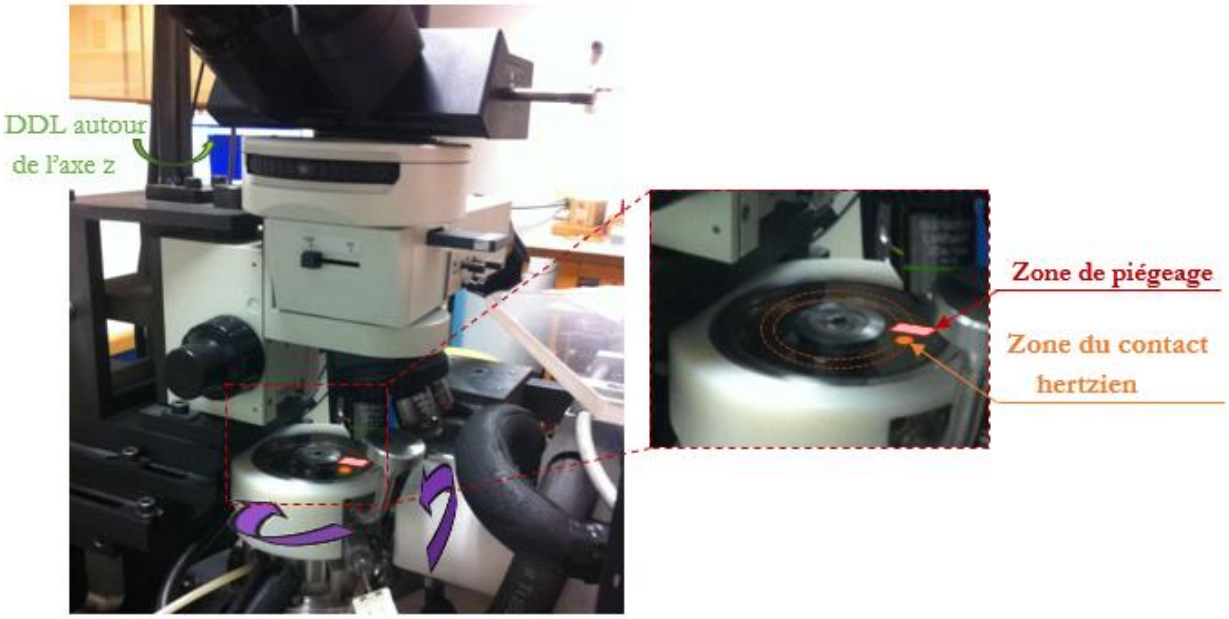

Figure 0-6 : Machine bille-disque et outils de visualisation (microscope et caméra)

Des mesures in-situ nécessitent que l'un des solides soit transparent. Dans cette étude on considère le couple composé d'une éprouvette en acier AISI 52100 et d'un disque en verre Pyrex®. Des éprouvettes sphériques et rouleaux en acier permettent de modéliser différents contacts ponctuels avec une ellipticité variable. Trois types d'éprouvettes avec un couple de rayons de courbures (R_x,R_y) suivants sont utilisées.

Type de contact	Circulaire	Elliptique	
R_x [mm]	12.7	13.1	13
R_y [mm]	12.7	84.2	330
a [µm]	124	151	115
b [µm]	124	513	920
k	1.00	3.46	8.02

Tableau 0-1 : Différentes éprouvettes utilisées sur la machine bille-disque

L'huile utilisée pour lubrifier le contact est une huile commerciale, la Shell T9 de viscosité 12 mPa.s et de densité 875 kg/m^3 à 20°C.

Triplet (traceurs/source/moyen d'acquisition)

L'utilisation de la technique de visualisation par fluorescence nécessite l'utilisation d'un « triplet matériel » constitué de traceurs adaptés pour le fluide analysé, d'un moyen d'éclairement de la zone d'étude et d'un système d'acquisition de l'image. Les particules choisies sont des pigments de peinture fluorescente fournie par la société Lefranc & Bourgeois®, la peinture rouge feu. Cette peinture est constituée de pigments fluorescents encapsulés dans un copolymère de mélamine-formaldéhyde-sulfonamide de distribution centrée en 6 µm.

La densité de ces pigments est de 1080 kg/m^3 à 20°C, ce qui permet de faire de chaque particule un traceur pour le fluide.

Deux lasers pulsés Nd :YAG fournies par la société Quantel® (532 nm, 150 mJ) assure l'éclairage du lubrifiant et un bras optique permet de guider la lumière laser jusqu'au-dessus du disque (Figure 0-7).

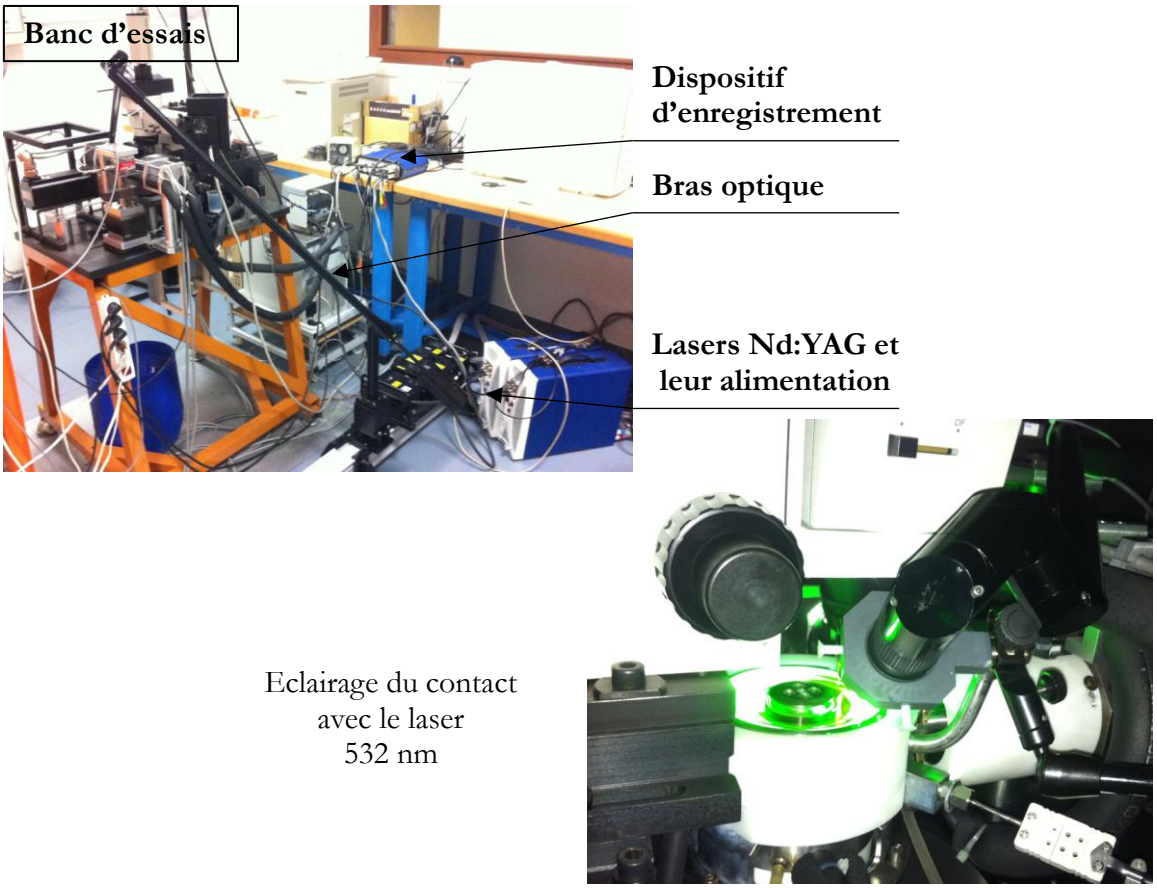

Figure 0-7 : banc d'essais bille-disque avec système de visualisation PIV

Finalement une caméra, Megaplus ES 1.0 avec 1008 x 1018 pixels est utilisée pour enregistrer le mouvement des particules fluorescentes après le passage au travers d'un filtre passe-bande FB-570-10. Ce dernier permet de ne laisser passer que la lumière d'émission de la fluorescence induite sans être perturbé par le bruit d'éclairage incident ou toute autre source provenant de l'environnement.

d. Etude du piégeage dans un contact circulaire

Le domaine d'étude se focalise sur un contact EHD et la zone environnante où le lubrifiant est présent.

Le but de ce chapitre est d'analyser qualitativement les risques de piégeage de contaminants solides. Tout d'abord, des résultats de visualisation du phénomène de piégeage par la technique fluorescente sont présentés et permettent une nouvelle approche des mécanismes menant au piégeage de particules. On prend ensuite l'étude d'un cas idéal de contact ponctuel et circulaire (600 N – 22 m/s) comme référence. On étudie la probabilité de piégeage par rapport à des paramètres de conditions initiales relatives à sa position et vitesse d'entrée dans le lubrifiant et intrinsèques à la particule telles que sa taille et sa nature. Les conditions opératoires sont ensuite étudiées.

La visualisation directe à l'aide de la fluorescence est une technique d'observation qui permet le suivi du piégeage de la particule. Le mélange de particules d'acier avec de la peinture fluorescente permet de rendre observable les particules qui sont transportés dans le ménisque de lubrifiant. Par adhésion des pigments de rhodamine sur la couche supérieure de la particule, on peut observer le piégeage de la particule à faible vitesse de roulement.

Une comparaison du champ d'épaisseur de lubrifiant déterminée par la résolution de l'équation de Reynolds peut être superposée aux images de la caméra pour estimer la zone de piégeage de la particule et ainsi corréler la déformation de la particule à l'épaisseur de lubrifiant. La Figure 0-8 représente 3 images successives de la caméra à une fréquence d'acquisition de 15 Hz. Les indications h = 32 et 40 µm (lignes pointillées) qui correspondent aux tailles minimale et maximale des particules d'acier est donnée à titre indicatif. La zone de Hertz est représentée un cercle hachuré.

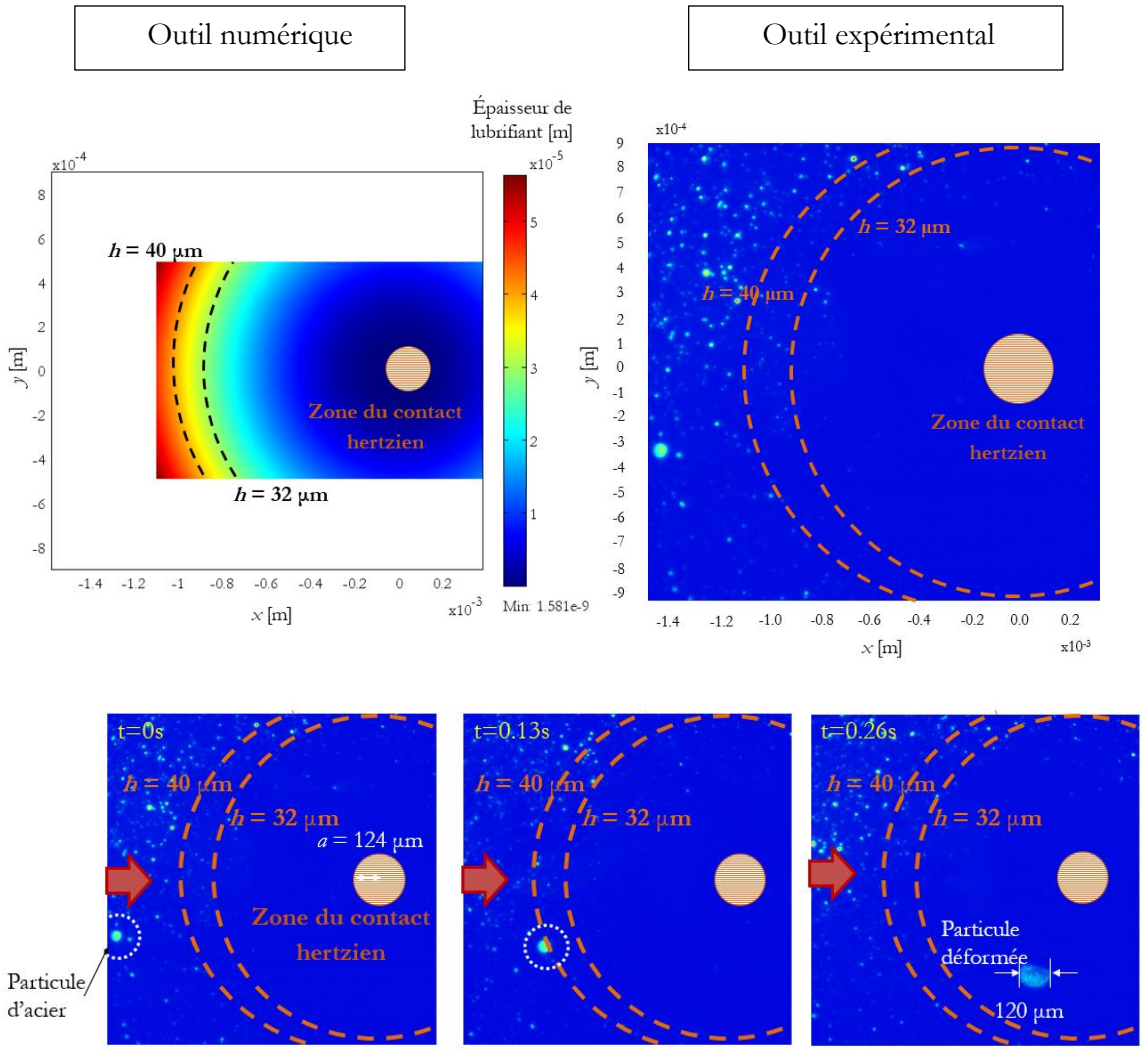

Figure 0-8 : Visualisation du piégeage d'une particule d'acier M50 mélangée à des pigments fluorescents dans un contact faiblement chargé (10 N) à faible vitesse de roulement (5 mm/s) avec un objectif x10

L'instant du piégeage de la particule apparait clairement sur ces 3 clichés successifs. D'une part on peut discriminer la particule d'acier des pigments de rhodamine (en moyenne 5 à 6 fois plus petits) et on observe le début du piégeage une fois la ligne des 40 µm traversée. La taille finale de la particule (son volume) est en corrélation avec l'épaisseur de lubrifiant considéré.

La technique PIV permet aussi de tracer des champs de vitesses au sein du lubrifiant dans le cas d'un contact circulaire.

Les cas critiques menant au piégeage de particules sont ensuite étudiés. La position d'entrée dans le contact, aussi appelé « position de lâcher », influence grandement la probabilité pour une particule de se faire piégée ou non. D'après le modèle numérique les particules lâchées le long de la ligne centrale du contact et proches des parois du domaine fluide sont les plus susceptible de rentrer dans le contact.

La confrontation de résultats issus de simulations numériques et d'essais sur la machines bi-disques a montré que des particules plus grosses ou plus lourdes sont plus assujetties à des effets d'inertie. Elles sont donc guidées plus facilement au sein du contact, conformément aux observations faites notamment par Dwyer-Joyce et Heymer [19].

Les conditions opératoires du contact impactant directement la forme du confinement et la vitesse d'entrainement du fluide, elles sont tout naturellement reliées au piégeage de particules. On observe ainsi que parallèlement, des vitesses de roulement et des charges plus importantes augmentent le risque de piégeage. Une discussion sur l'influence du profil de vitesse du lubrifiant en entrée du contact est proposée. Elle aboutit à une formulation générale du profil de vitesse parabolique en fonction de la vitesse de roulement pour tout type de contact en lubrification pleine. Ce modèle analytique explique les taux de piégeage accrus à plus haute vitesse de roulement et à charge plus importante.

e. Vers le piégeage dans des contacts plus réalistes

Différents types de matériaux en contact sont considérés acier–acier et céramique–acier. Bien que le taux de piégeage se révèle très peu dépendant des différents types de contacts, les mécanismes d'indentations apparaissent bien différents. Ces derniers sont liés à l'interaction avec les solides en mouvement. Dans un contact acier-céramique, la surface céramique ne subit pas d'endommagement contrairement à la contreface en acier (Figure 0-9).

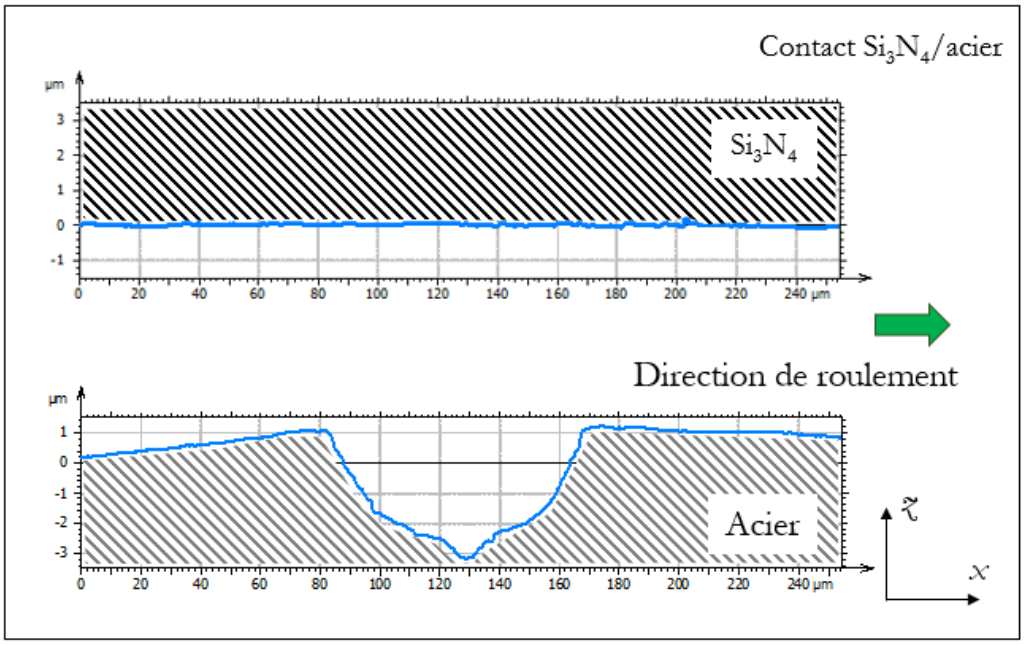

Figure 0-9 : Dimensions de l'indent suite au piégeage d'une particule d'acier AISI M50 entre une surface en acier AISI 52100 et une surface en Si3N4

Pour les mêmes conditions de fonctionnement, les marques d'indentation sur les disques acier dans un contact hybride sont inévitablement plus profondes que dans un contact tout acier. Ceci pose la question de la durée de vie de ces roulements de nouvelle génération.

L'influence de la géométrie des éprouvettes sur le piégeage de contaminants solides est étudiée. En partant de tests réalisés sur la machine bi-disques (600 N–22 m/s) en régime de lubrification polluée, il a été établit que des contacts elliptiques larges entrainent un piégeage moins important que des contacts circulaires équivalents. Cette observation est apparue tout d'abord contre-intuitive, puisque la largeur de piégeage est plus importante lorsque l'ellipticité augmente (Tableau 0-2 et Figure 0-10).

	Circulaire	Elliptique		
R_x [mm]	17.5	17.5	17.5	17.5
R_y [mm]	17.5	35	70	200
$k=b/a$	1.00	1.59	2.50	4.88
Largeur de piégeage pour des particules de 32 µm [mm]	2.324	3.28	4.6	7.58

Tableau 0-2 : Largeur de piégeage pour différentes configurations de contact elliptique testés sur la machine bi-disques avec les conditions (600 N – 22 m/s)

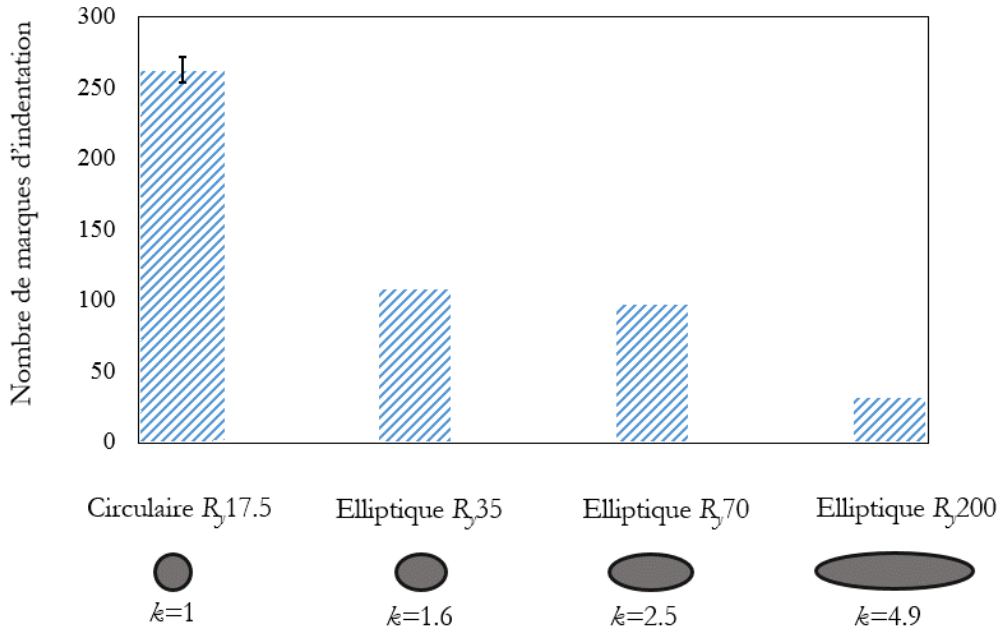

Figure 0-10 : Nombre de marques d'indentations (correspondant aux nombres de particules piégées) au sein de différents contacts elliptiques pour des contacts acier-acier (moyenne sur 3 tests et 2 tests pour le contact circulaire et les contacts elliptiques, respectivement) en condition de lubrification polluée (concentration de polluants en solution 10 mg/l)

Il a donc été postulé que cette diminution du nombre de particules piégées dans le contact est directement liée aux débits de lubrifiant en amont du contact. Cette hypothèse a été validée par des simulations numériques réalisées sur les 4 types de contacts testés expérimentalement. Des reflux d'intensité croissante ont ainsi été mis en évidence lorsque la largeur de la zone hertzienne croit, voir Figure 0-11.

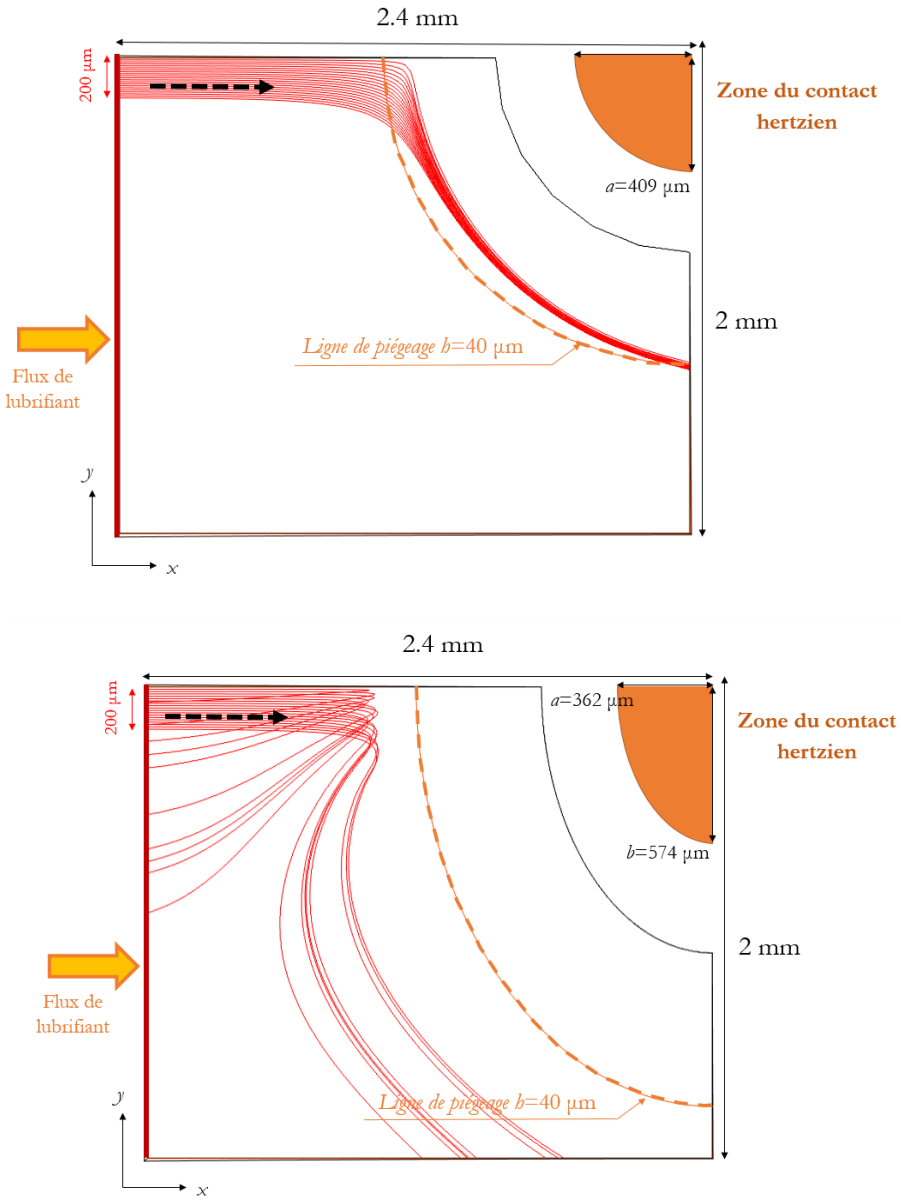

Figure 0-11 : Lignes de courant pour une ligne de fluide entrant dans le domaine à x = -2.4 mm, Δy = 200 µm, z = 10 µm, pour un contact circulaire (k = 1) et elliptique (k = 1.6)

Ces reflux de lubrifiant en amont du contact représentent une barrière à surpasser pour un polluant solide avant d'être capturé par le contact. L'utilisation de traceurs fluorescents dans le dispositif bille-disque avec différents types d'éprouvettes sphériques ou tonneaux a permis de valider la présence de ces reflux au sein de contacts elliptiques larges. La Figure 0-12 représente les observations des écoulements de lubrifiant en amont des contacts circulaires et elliptiques. L'indication h = 6 µm (ligne pointillée) qui correspond à la taille moyenne des particules de rhodamine est donnée à titre indicatif. La zone hertzienne du contact est représentée par un cercle ou une ellipse hachuré(e).

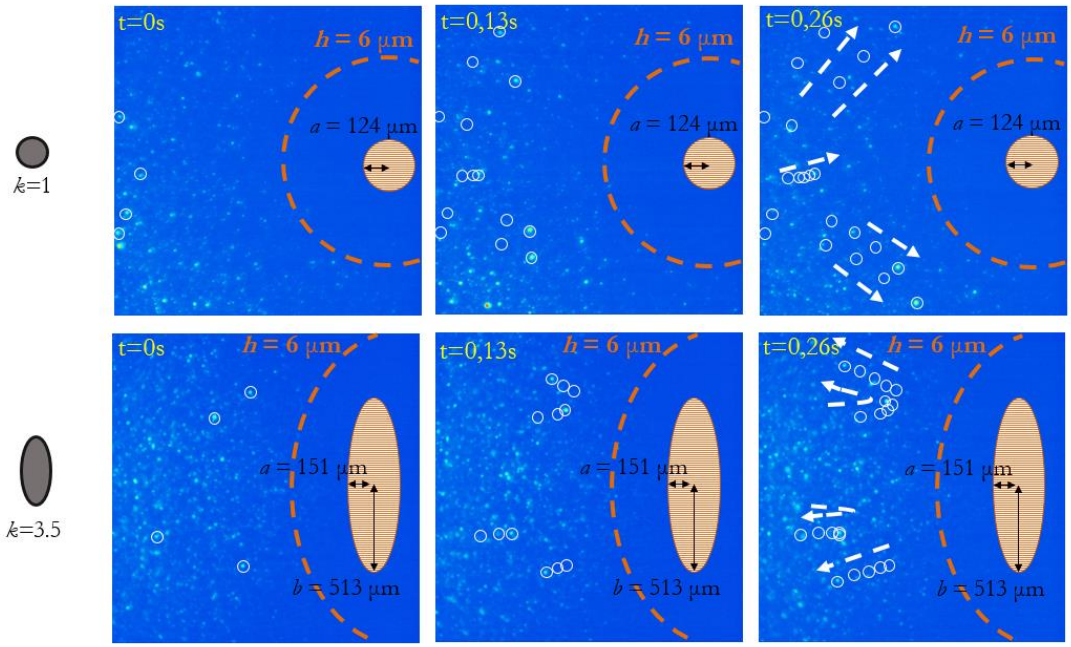

Figure 0-12 : Visualisation de l'écoulement dans un contact circulaire et elliptique avec les conditions de contact de 5 mm/s – 10 N et 5 mm/s – 50 N, respectivement

Enfin, le taux de piégeage de particules solides s'est montré très peu dépendant des conditions de glissement. En revanche, les mécanismes de piégeage sont bien différents. Ainsi, dans un contact avec glissement, les particules se trouvent incrustées et « tartinées » dans le contact alors qu'elles étaient simplement écrasées et rejetées en roulement pur.

f. Conclusion générale

A ce jour, la présence de polluants solides dans les contacts lubrifiés est inévitable. Des filtres trop fins engendrant trop de pertes de puissance, les roulementiers envisagent l'utilisation de matériaux plus à même de faire face aux problèmes de la pollution solide.

La double approche utilisant à la fois, un outil numérique et des tests expérimentaux permet d'étudier qualitativement les phénomènes. Elle permet de plus de mener une étude quantitative sur les conditions de piégeage liées :

- aux propriétés du polluant (taille, nature) ;
- aux conditions du contact (vitesse de roulement, charge appliquée, matériaux en contact, rayons de courbure des solides en contacts, glissement).

L'analyse des différents tests expérimentaux et des simulations numériques ont ainsi permis de trouver les résultats suivants.

- Le piégeage de polluants solides peut être observé à l'aide de la technique de visualisation par fluorescence induite. A l'aide de cette technique, il est possible de suivre en direct le transport, le piégeage et même la déformation de la particule dans un contact acier-verre.
- L'entrainement de contaminants solides est fortement lié à la position d'entrée de la particule dans le contact. Ainsi il a été montré que plus la particule est lâchée proche de la ligne centrale du contact et proche des solides en mouvement et plus elle est susceptible d'être transportée jusque dans la zone du contact.
- Des particules plus lourdes et/ou plus grosses subissent plus d'effets d'inertie et sont piégées plus facilement dans le contact.
- Augmenter la vitesse de roulement d'un contact EHD augmente la probabilité de piégeage de contaminants solides.
- Augmenter la charge d'un contact EHD revient à augmenter la largeur de piégeage du contact et donc à augmenter la probabilité de piégeage de polluants.
- La probabilité de piégeage de contaminants solides n'est que très peu affectée par l'utilisation d'un couple hybride de matériaux (Si_3N_4-acier) ou par des conditions de glissement puisque ces deux types de conditions particulières n'affectent pas ou très peu la géométrie du contact en comparaison d'un contact acier-acier en roulement pur.
- Pour les contacts elliptiques, augmenter la largeur du contact EHD de manière transverse à l'écoulement fait diminuer la probabilité de piégeage de contaminants solides. En effet, considérer un contact à ellipticité croissante revient à considérer un contact avec plus de reflux et donc une barrière supplémentaire au piégeage dans la zone du contact.
- Les faciès des marques d'indentation laissés sur les disques en acier sont bien différents lorsque l'on considère différentes conditions cinématiques de contact. Dans le cas de contacts avec roulement/glissement de nombreuses particules se retrouvent ainsi collées sur les surfaces au lieu d'être éjectées. Dans les contacts hybrides (Si_3N_4-acier), la contreface en acier est bien plus abîmée par les phénomènes d'indentation puisque la surface en Si_3N_4 est non déformée.
- Enfin, on peut dire que l'effet de la géométrie des solides domine sur tous les autres effets liés aux matériaux ou aux conditions de fonctionnement. En effet lors des essais combinés (étude de l'ellipticité avec du SRR ou étude de l'ellipticité avec différents matériaux), les contacts elliptiques larges montrent invariablement un piégeage de contaminants solides plus faible qu'au sein d'un contact circulaire de même rayon de courbure principal.

Ce dernier point illustre particulièrement bien la complémentarité des approches mises en œuvre.

- Dans un premier temps, des essais sur la machine bi-disques ont mis en évidence un piégeage réduit du nombre de polluants solides dans un contact EHD large.
- Une validation numérique a permis de conforter l'hypothèse d'un lien étroit existant entre non-piégeage de polluants et existence de reflux.
- Enfin, la visualisation de ces reflux a été possible à l'aide de la technique de visualisation par fluorescence induite en comparant l'écoulement au sein de contact respectivement bille-plan et tonneau-plan.

Toutes ces données numériques et expérimentales permettent donc de donner une lumière nouvelle sur le piégeage de polluants solides et souligne la nécessité de comprendre ce phénomène complexe pour assurer une conception efficace des roulements du futur.

Particle Entrapment in EHD Contacts – Aerospace Applications

General Introduction

In 2001, 500 rolling element bearings (REBs) were produced each second worldwide [33]. Today some studies evaluate the production to 157.7 billion REBs yearly (about 5000 sets each second). From millimetric size bearings used in spy drones to 2m-diameter bearings supporting Ferris wheels (like the 168-meter tall wheel of the Las Vegas High Roller), REBs have to ensure the rotational motion. Simultaneously they have to be power-efficient, adaptable and robust. The reliability can be challenged by the environmental conditions where lubricated REBs can be used. From bike chain-sets to turbofan main-shafts REBs, the lubrication must be maintained under any operating conditions. REBs as parts of complex systems are in permanent interactions with environment. It is difficult to affirm whether contamination particles will be carried into the critical zones of REBs. But, the presence of hard, solid particles in the vicinity of elastohydrodynamic (EHD) contacts, characterized by submicrometric gaps, may cause irreversible damages for the contacting surfaces. A wide number of studies reported premature failures due to rolling contact fatigue phenomena, initiated by indentation of the surfaces by solid contaminants. Hence entrapment is nowadays a major concern for bearings manufacturers as it significantly reduces the REBs lifetime. Remaining questions are set on the way particles are driven in the contact inlet.

This work investigates the particle entrapment in EHD contacts for aerospace applications. These REBs need both a high reliability and low weight designs that is why current researches are performed towards robust and lighter REBs. The hybrid silicon nitride (Si_3N_4)–steel REBs, composed of Si_3N_4 rolling elements and steel rings, opened new prospects on more efficient EHD contacts. The aim of this work is to analyze particle entrapment in EHD contacts with respect to the flow of lubricant in which particles are carried. This study proposes a dual approach based on both numerical simulations of particle entrapment and experimental tests under contaminated lubrication.

Chapter 1 presents the basics of lubrication in REBs and current industrial challenges. A state of the art is then proposed which concerns the previous work on particle entrapment in lubricated contacts. This review aims at giving an insight of the encountered issues, the proposed solutions and the remaining opened questions that characterize the phenomenon of particle entrapment in both steel–steel and Si_3N_4 ball–steel contacts.

The experimental techniques and the methodologies for numerical simulations used throughout this work are exposed in **chapter 2**. The presentation of the numerical tool is divided in two parts. One is dedicated to the presentation of the model for lubricant flow and the other one is dedicated to the model for the trajectories of suspended particles. Two experimental test-rigs used for the analysis of entrapment phenomena are presented with their dedicated particle-related devices: a pollution test-rig combined with a twin-disc machine and a Particle Image Velocimetry (PIV) device adapted on a ball-on-disc machine.

An investigation of the particle entrapment phenomena in classical all-steel contacts is proposed in **chapter 3**. The phenomenology of the entrapment mechanism was first analyzed through observations with the PIV technique in a glass-steel configuration. Then, by using a dual analysis with both twin-disc tests and numerical simulations, the influence of various parameters on particle

entrapment is investigated. The effects of different initial conditions, intrinsic particle properties (size, nature) and contact parameters (load, rolling speed) are analyzed.

On this basis, the work extends towards industrial EHD contacts. The effects of different contacting materials, several geometries (elliptical contacts) and rolling–sliding conditions are presented in **chapter 4**. The corroboration of the numerical and experimental tools allowed to self-validate this dual approach. Hence, tests revealing entrapment probability obtained with the twin-disc machine are compared with entrapment simulations. In-situ observations on the ball-on-disc machine are compared with numerical simulations.

Chapter 1 State of the art

1.1 Introduction

REBs are composed of two rings separated by rolling elements (balls, rollers, etc.), themselves held within cages. They support loads and reduce friction in rotating mechanisms. In most applications, one of the rings is fixed to the housing and the other one to a shaft. These components are lubricated and the presence of lubricant ensures surfaces separation, load transmission, speed accommodation, cooling-down of the contacting solids and debris removal. The lubricant can be either oil or grease according to applications, environment and operating conditions of the REBs. Seals can be added to prevent any lubricant leakage and avoid contaminants to enter. To answer the many demands from Original Equipment Manufacturers (OEM), engineers have developed several geometries: needle roller bearings, compact aligning roller bearings (CARB), deep groove ball bearings (DGBB), and many others (see Figure 1-1).

Figure 1-1: Example of different kinds of REBs

In this chapter, first, some REBs basics are presented concerning aerospace applications, hybrid REBs (ceramic–steel materials) and contact lubrication. Then, a focus on lubricant contamination and especially the impact of debris-like particles is made regarding literature. Finally the objectives of the present study are defined.

1.2 REB basics

1.2.1 Aerospace applications

A typical example of aerospace applications are REBs equipping the main-shaft of an aircraft engines, Figure 1-2.

Figure 1-2: Aircraft engine REBs

Generally, made of steel and working under extreme operating conditions, REBs are subjected to high rotating speeds (10^6 Ndm – Ndm = rotational speed (r/min) x pitch diameter (mm) [34]), high temperatures (greater than 150°C for long operation [35]) and contaminated lubrication [36]. These operating conditions require improvements by the implementation of efficient cooling-systems, high resistive materials for REBs or the use of smaller lubricant filters.

In the last twenty years, many aeronautical manufacturers have focused their attention on the use of hybrid ceramic-steel REBs, increasing reliability and reducing weight. Originally intended for military aircraft [37], the beneficial use of this technology in high rotating machinery tools was demonstrated [38]. Thus, their use in the wider airplane industry is expected. Moreover they can be lubricated by kerosene [39].

1.2.2 Hybrid REBs

Hybrid ceramic–steel REBs, consisting of steel inner and outer rings with ceramic rolling elements, are among the combinations developed by bearing manufacturers. Different kinds of ceramics**,** such as hot pressed silicon carbide (SiC) [40], aluminum oxides (Al_2O_3) [40], zirconia (ZrO_2) [41] and finally silicon nitride (Si_3N_4) compounds [42–44] have been tested over the last fifty years for various applications. However, only Si_3N_4 rolling elements (Figure 1-3) seem to offer sufficient lifetime and reliability [10,42,45–47].

Figure 1-3: Hybrid Si_3N_4-steel REB

Despite an actual non-negligible cost penalty, hybrid Si_3N_4–steel REBs offer many advantages compared to steel–steel ones:

- a higher hardness: Si_3N_4 hardness is larger than the one of conventional steel used in aeronautical applications [7,24,48]. Thus a larger resistance to solid contamination is expected as the indentation process is governed by the hardness difference between surfaces and particles, as demonstrated by Hamer et al. [49] or mentioned by Wang et al. [2];
- a lower density: density of silicon nitride is about 40 % lower than the steel one. This is one way of saving fuel consumption through lighter REBs, as expressed by Tonicello et al. [1];
- a better resistance to electrical and thermal solicitations [3] which enables operation in severe environments;
- a higher corrosion resistance as explained by Niizeki [4] in his review of ceramic bearings for special environments.

Tribological performance of Si_3N_4 used with steel counterfaces was evaluated both numerically and experimentally. Some illustrations are given below.

- The recent numerical works of Kaneta et al. [5] and Savio et al. [6] aimed at underlining the specific properties using a hybrid couple of materials, especially the low friction. Kaneta et al. showed that thermal effects caused by sliding conditions lead to very thin films in Si_3N_4–steel contacts which could significantly reduce the friction. Savio et al., by a multiscale approach, revealed that a specific wall slip can occur, leading to a change in film thickness and therefore a drop in friction.
- For spatial applications, both full-ceramic or hybrid ceramic-steel configurations proved to resist lubrication interruptions and therefore exhibit a good behavior in mixed lubrication regimes, as recalled by different authors [4,44].
- Lakshminarayanan et al. [7] and Kalin et al. [8] in the mid-nineties, conducted experiments to characterize the impact of using ceramic parts in ball bearings on wear. Their main result was to emphasize the importance of ceramic roughness on steel counterface wear. Nevertheless it was noticed that even if the ceramic surface was undamaged, the rougher the ceramic surface is, the more damaged the steel counterface is. Kalin et al., using fretting tests to study the wear of Si_3N_4 balls against AISI 52100 rods, distinguished different stages in the wear process depending on the fretting amplitude and the lubrication regime. When passing from a

moderate fretting process to a more intense one a transition from high to low wear was observed, resulting from the formation of a protective layer. Novak et al. [9], using the same process with relatively small fretting velocities (0.0042–0.042 m/s), extended the research of Kalin et al. [8] on the wear occurring in lubricated ceramic-steel contact. They characterized the difference with the non-lubricated case by analyzing the tribochemical wear mechanisms and found two orders of magnitude lower coefficient of friction for the lubricated case.

However, ceramic is known to be a fragile material which is certainly the main issue to overcome before an implementation at large scale. Works performed during the last twenty years revealed that Si_3N_4 fails in fatigue spalling or delamination mode [50], similarly to conventional steels. On this basis, wear tests and failure analyses were performed to determine the reliability of this material. It was underlined that failure modes are highly related to material porosity [50,51] and that the reported defects are due to sintering micrometric voids leading to 6.7 lower life compared to steel.

Technology readiness level (TRL) of hybrid REBs is near to prototype demonstration in main-shaft applications and needs to follow a maturing process before being used systematically. This process relies on further improvements of the Si_3N_4 material but also on the validation of tribological performances under realistic conditions.

1.2.3 Lubrication

Three different regimes described on the Stribeck curve (Figure 1-4) exist:

- boundary lubrication, if surface roughnesses are larger than the film thickness, it results in load carrying by asperities and solid–solid friction;
- mixed lubrication, load is partly carried by the asperities and by the confined lubrication medium;
- full-film lubrication, load is entirely carried by the confined lubricant with a film thickness larger than roughnesses.

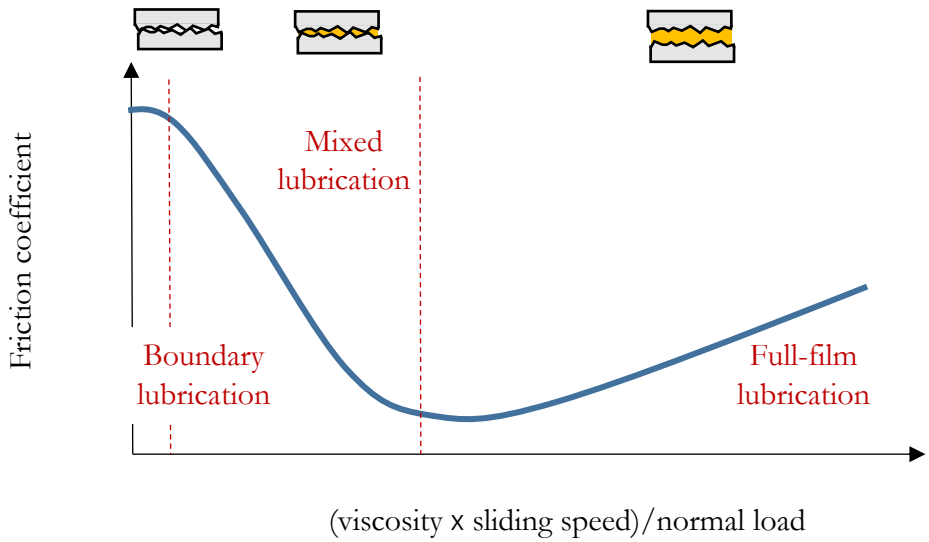

Figure 1-4: Stribeck curve with different lubrication regimes

In the present study, only full-film lubricated contacts will be considered. It is consistent with roughness of REB components which is very low (~ few hundreds nm) compared to generated film thicknesses (~ µm) [52] and with jet lubrication systems used in aerospace REBs that provide a large amount of lubricant [34].

Two non-conforming geometries impose high pressure and thus deformation of contacting bodies. As long as the deformation is smaller than the lubricant film thickness separating the solids, lubrication is called Hydrodynamic (HL) otherwise ElastoHydrodynamic (EHL), Figure 1-5.

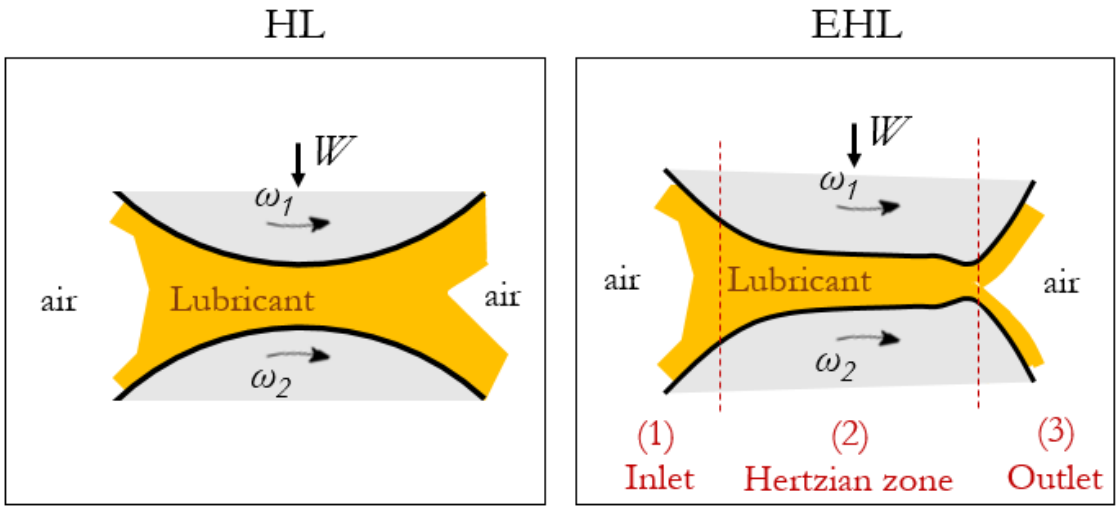

Figure 1-5: (left) hydrodynamic lubrication with undeformed bodies and (right) elastohydrodynamic lubrication with deformed bodies

Lubricated contacts in REBs operate generally in the EHD regime. Within an EHD contact there are three distinctive zones:

- (1) contact inlet, the lubricant is dragged into the contacting gap downstream from the air/lubricant inlet meniscus. The convergent geometry leads to the build-up of both pressure and film thickness through hydrodynamic effects and exhibits lubricant piezo-viscous properties;
- (2) hertzian zone, high pressures are responsible for solid deformations and load is carried by the film thickness as the fluid is highly viscous;
- (3) contact outlet, after the constriction caused by the flow conservation, another lubricant/air meniscus is formed. The solid surfaces show a divergent where the lubricant is expelled at low viscosity and high velocity.

Reliability of EHD contacts depends on the supply of enough clean lubricant. Conditions leading solid particles into EHD contacts will be at the heart of this study. The next section proposes an insight of solid contamination problems in lubricated REBs.

1.3 Lubricant contamination: a constant challenge

REBs are keystones for many mechanical transmissions but they can also remain the *Achilles heels* of the system. A failure of a REB often means a major dysfunction of the mechanism. If any external particle or debris penetrates the lubricated contact, the surfaces are possibly affected and become irreversibly damaged.

Nowadays, high speed machineries lubricated with low viscosity oils, operate with very thin lubricating films, and sub-micrometer gaps face particles of several micrometers. Very fine filters are not the solution as they generate pressure drops and power losses. They also necessitate a time-consuming maintenance process, which explains why the less filters as possible are used and thus why contamination by particles cannot be fully avoided.

1.3.1 Origin of solid contamination and entrapment mechanisms

The contamination can be inherent to the mechanism, due to the lubricant supply for example, or can come from external sources, like sand contamination for an aircraft flying over the desert as well as volcano ashes in the extreme case of an overflight nearby a volcano eruption (Appendix A).

Some other contamination processes are much more time-dependent. Indeed, during the functioning of a high-stressed mechanism containing many EHD contacts involving high pressures, a wide range of grinding dust or abraded materials from the contacting surfaces are produced. For example, initial roughness peaks due to machining are run-in and released in the lubricant during operation as well as spalling flakes generated by rolling contact fatigue.

The type of particles present in mechanism were indexed in the works of Akl et al. [13] and Nélias [14]. They found metallic particles as well as carbides, mineral compositions and oxides, as expressed in Table 1-1.

Internal source	**Machining, mounting**	**Operating (Running-in, Wear, damaging process)**
	Metallic particles (Fe, Cu, Al, …)	
	Carbides (B_4C, SiC, …)	Metallic oxides and sulfides
External source	**Lubrication**	**Exceptional environment**
	Oil or grease components (additives, anti-wear, VII - Vicosity Index Improver-polymers, etc.), dust	Mineral (Si, Ti, Mg, Ca, K,…) Sand particles or volcano ashes

Table 1-1: Contaminant origin in aeronautical REBs according [13,14]

Hunt [53] proposed a classification in seven different classes with particles from sub-micrometer to millimeters in size, and with varying forms:

- spherical particles (fused metallic wear)
- ovoidal particles (external dust)
- cobbled particles (metallic particles coming from surface fatigue)
- platelets and spalling particles (due to setting up or normal use)
- shaving and flake particles (coming from the machining process)
- rollers (shaving and spalling particles together)
- fiber particles (generally non-metallic particles from polluted atmosphere)

Figure 1-6 shows three different types of particles: M50 steel spherical particles, boron carbides particles or volcano ashes.

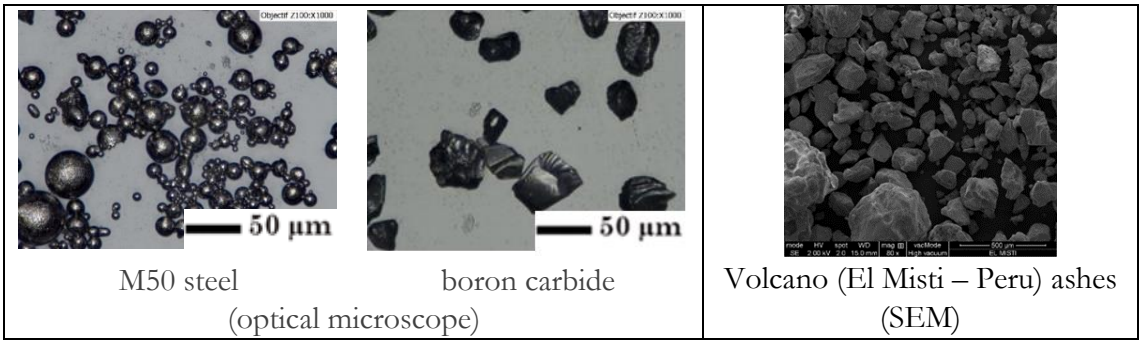

Figure 1-6: Three different examples of particles

The M50 steel spherical particles are commonly used as "models" of ductile contaminants, as their entrapment behavior is well known and easy to quantify: the particles deform under the high pressures

of EHD contacts and cause an indentation mark or dent on the contacting surfaces [19,54]. Boron carbide particles were used to characterize entrapment of hard and fragile particles [54] (see also Appendix A) and volcano ashes, here collected on slopes of El Misti volcano (Peru), represent external solid particles that may penetrate the lubricant loop system.

Depending on the nature of particles (ductile, brittle, fragile, etc.) and contact parameters (geometry - cylindrical, circular or elliptical, operating conditions -rolling/sliding velocities, loads, materials of contacting bodies, etc.), a particle behaves differently once entrapped in the EHD contact [55] (see also Appendix A).

Hence, in presence of so various solid contaminants and diverse kinds of contacting gaps, entrapment mechanisms are numerous. The next section aims at presenting a panel of previous works dealing with contamination problems in EHD contacts.

1.3.2 Contamination in EHD contacts

Historically, engineering community faced with the question of contaminants in REBs, undertook tests with full-scale bearings lubricated with a contaminated lubricant for establishing the impact of such lubrication on the REBs lifetime. In the seventies, Fitzsimmons and Clevenger [15] evaluated the impact of the presence of contaminants on wear in tapered roller bearings; in particular they characterized the influence of nature, size, concentration and hardness of particles on the damaging processes. They showed that large and hard particles generated more damages to the surfaces than small and soft particles. Cusano and Sliney [56,57], in the eighties, studied the dynamic behavior of two contaminants in solution, graphite and molybdenum powder, seen at this time as possible friction reducers. For the first time, it was established that the operating conditions (pure rolling, pure sliding or rolling–sliding conditions) directly influence the flow of particles within a contact. For example, under pure sliding conditions, they observed that an accumulation of particles at very low speeds (0.0021 m/s) may occur at the contact inlet which may at some point leads to oil starvation.

Other studies were performed on tribometers mimicking circular contacts in order to identify the indentation process and influent parameters. Wan and Spikes [16], using high speed photomicrography, focused on the fact that very large particles (up to 50–60 μm) can enter a submicron confinement. It was the first analysis of the flattening of solid particles. They also established that particle entrapment is responsible of a modification of film thickness distribution in the Hertzian zone using optical interferometry, developed in the sixties by Kirk [58] and Gohar and Cameron [59]. In the nineties, Cann et al. [17] used interferometric techniques, combined with a silica coating on the transparent disc to visualize particle entrapment through film thickness measurements. The presence of a foreign particle in the contact area is thus determined once the fluid escaped from the interface between the entrapped particle and the disc, which is characterized by an uncolored interference fringe. The addition of the coating also allowed to detect and characterize the size of the dent caused by such a particle by observing the disc after the tests. Figure 1-7 shows two successive pictures of the entrapment of iron particles. This visualization method was a first attempt to observe

directly particle entrapment but was restricted to low rolling speeds (0.005 m/s) and observation on steel–glass configuration.

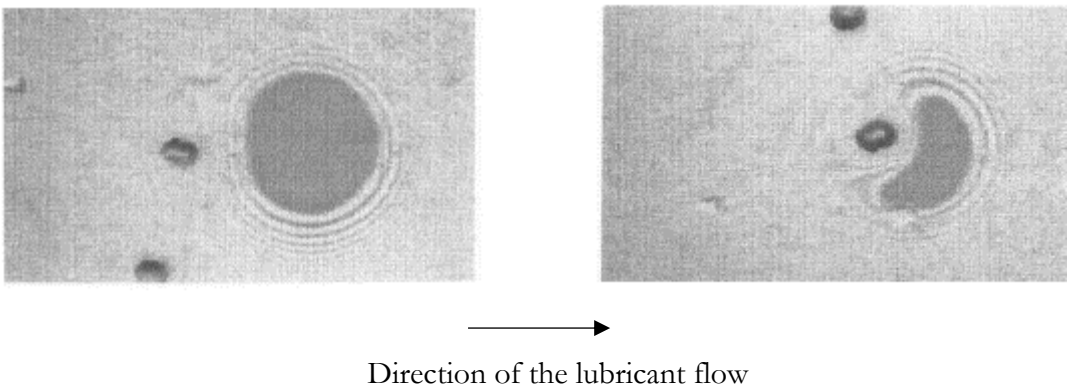

Figure 1-7: Particle entrapment visualization through interferometric method [17]

Experiments under a wide range of operating conditions (load, speed, Slide-to-Roll ratio, temperature, etc.) and with different types of particles (ductile and brittle ones as ceramic particles) were also conducted on an oil jet lubricated twin disc machine [18] and on a ball-on-disc test rig (ball dipped in an oil bath) [19]. The particle entrapment was evaluated in a same way counting the dents left by contaminant particles. Results show that the dent geometry depends on the size and nature of particles but that load does not have any influence. Moreover, in the specific case of pure rolling condition, higher entrainment speed seems to reduce particle entrapment probability [19,56,57]. It was also demonstrated that it is more difficult for small particles to be entrapped than for large ones. It can be also concluded that damage caused by particles is different according their nature, from indentation marks caused by ductile particles to abrasive wear which occurs in presence of small brittle particles [55]. For the last particles, it was showed that rolling elements (generally harder than the raceways) suffer from a higher abrasive wear, as particles remain held in soft surfaces while scratching the hard ones [60]. The previous mentioned experimental studies were carried out under different operating conditions leading to different particle entrapment ratio: i) experiments, carried out in a top-down lubrication configuration and performed at high rotating speeds [54], show that the concentration of particles inside the EHD contact is the same as in the surrounding; ii) on the contrary, experiments like that of Dwyer-Joyce and Heymer [19], using a ball-on-disc test rig with dip lubrication can lead to various concentration of particles.

More recently, Underwood [61] proposed an experimental set-up to measure the temperature of particles passing through an EHD contact by infrared mapping. Particle entrapment can be recorded and a significant temperature increase happens when a particle is sheared and deformed in the contact. Some limitations due to the shutter time of the camera were however observed and limited the study to very low rolling speed experiments.

For the first time, in the beginning of the twenty-first century, Nikas [20–23] undertook to numerically consider particle entrapment. By implementing the different forces acting on particles in

the vicinity of an EHD contact, he performed numerical simulations of particle trajectories leading to entrapment. The model allowed to establish criteria for particle entrapment or particle rejection considering the balance between fluid forces and friction forces acting on suspended particles. The model, despite considering a simplified Stokes' flow, allowed to reproduce and confirm several previous experimental observations, like the lower probability of entrapment of small particles or the contact inlet accumulation under sliding conditions. He also noticed the effect of backflows and stagnation points on the particles' motion. Figure 1-8 reports one of the performed numerical simulations. It appears that only particles released upstream from the contact center are driven towards the contact zone. All the particles released sufficiently off-axis are bypassing the critical zone of entrapment.

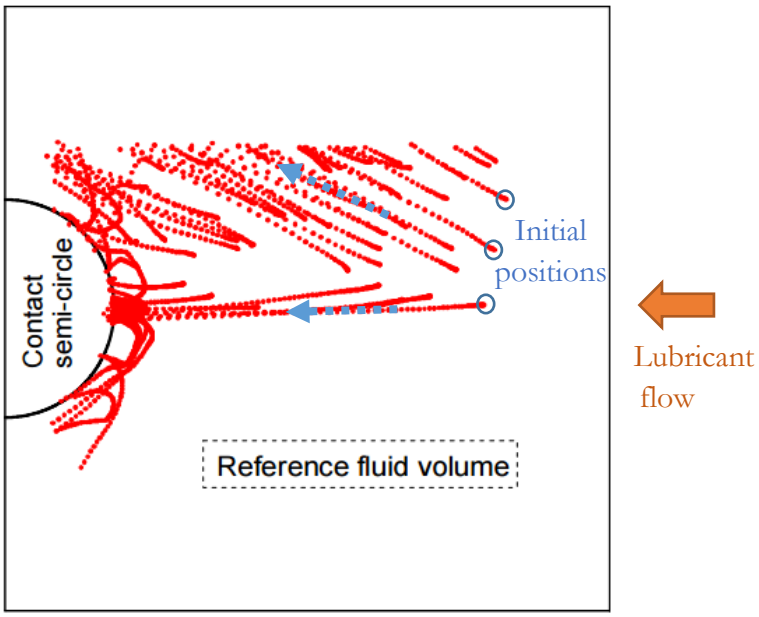

Figure 1-8: Predictive trajectories for 20 µm-thick particles released upstream from an EHL contact (inspired by [20])

Kang and Sadeghi [62] also numerically investigated the entrainment of ellipsoidal particles in EHD contacts assuming that the main forces responsible for entrapment are oriented in the direction of the lubricant flow. They underlined the link between entrapment of debris-like particles and the thickness of a pressure induced backflow region. They showed that particles being in the backflow region are not likely to be entrapped in the contact zone. Recently, a further numerical model was proposed by Twist [63], using a Distributed Lagrange Multiplier (DLM) method for solving the fluid-solid interaction as well as particle/particle interactions in order to describe the flow of dense particle suspensions. She confirmed that high concentration of contaminants can lead to an accumulation of particles at the contact inlet with oil starvation risk.

Finally, it is also of main interest to analyze the behavior of dented surfaces inside the contact as they are responsible for rolling contact fatigue (RCF). On one hand, observations reveal that the film thickness "bump" caused by the dent, induces higher pressures and reduces lifetime. This is directly

influenced by operating conditions [64]. On the other hand, fatigue tests establish that the dent slope plays a crucial role on the lifespan [17],[18],[65],[66],[67].

All these experimental observations and numerical investigations were conducted for classical steel–steel or steel–glass contacts. The development of hybrid bearings induced new tests with specific material combination. Influence of particle entrapment on lifetime of a grease-lubricated hybrid Si_3N_4–steel bearing (with Si_3N_4 balls) was characterized [24]. The main results were that the ceramic balls suffered no wear in comparison to the steel balls.

According to literature, it appears that entrapment mechanism is dependent on intrinsic particle properties (nature, size) and on operating conditions (load, rolling speed, slide-to-roll ratio). The use of different contacting materials proves to affect the resulting indentation marks left by entrapped particles. The aim of the next section is to present models of bearings life predictions in presence of solid contamination.

1.3.3 REB life prediction in presence of contamination

Particle entrapment causes premature fatigue failures (Figure 1-9), and reduces bearing lifetime.

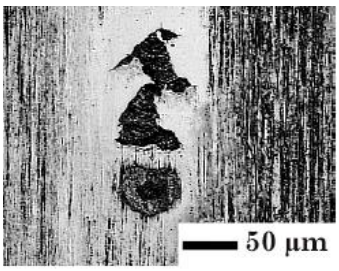

Figure 1-9: Spalling due to rolling contact fatigue [31]
(initiated by an artificial dent made by a Rockwell indenter)

The original theory provided by Lundberg and Palmgren [25] in the fifties set the basis for predicting REB life. Based on the Weibull statistical distribution applied to the Hertzian stressed volume, it aimed at quantifying the lifetime reduction without considering any damage process or any contact features (dents, inclusions, roughness, interaction with the lubricant). Later Ioannides and Harris [73] or Zaretsky et al. [27] introduced a fatigue-limiting stress and generalized the basis to a wider range of materials and conditions (steel cleanliness, lubrication regimes, etc.). It appeared that these probabilistic methods lack of physical bases and that deterministic models were needed for a better estimation of the bearings life in presence of contaminant particles.

Loewenthal and Moyer [74] first estimated bearing service life reduction in presence of contamination. They also underlined filtering influence demonstrating a doubling of lifetime for DGBBs without and with filtration. More recently a reduction in some cases to 1/100 of the relative life was estimated [75]. Mitamura and Murakami [76], aiming at developing an alternative steel (NSJ2-steel) to the conventional AISI 52100 steel, performed fatigue tests under contaminated lubrication.

Particles with hardness varying between HV 370 and 1200 and size between 25 and 100 μm were used. At equivalent particle size, the harder the particles, the shorter the lifetime. Hence, lubricant cleanliness is a key factor for enhancing the bearings lifetime, as underlined later by Nikas [20].

In the beginning of the nineties, Sayles et al. [77] reviewed the effects of particulate contamination on bearing lifetime. They concluded that fatigue prediction has to be approached with an identification of the residual stresses that meet the over-rolling stress field. Thus, investigations on materials with more realistic topologies (presence of dents, roughness, heterogeneities, etc.) revealed to be essential to estimate the bearing lifetime. Bearing lifetime in presence of defects caused by artificial indentation of contacting surfaces was experimentally investigated [78]. It was shown that fatigue lifetime prediction must take into account the deformed dent geometry and that the service life is directly linked to the stressed volume. Regarding REB life as a function of its geometry and operating conditions, numerical dent severity analyses underlined that contact ellipticity can affect the pressure perturbations induced by the dent [79].

Since two decades, significant efforts have been done in the development of deterministic predictive models. Quantitative relationships in order to develop a set of prediction tools are proposed [80]. Based on parametric studies with different indent slopes and different indentation area densities, these models enabled to estimate a life reduction factor which match well with experimental fatigue tests. Recently, Morales and Gabelli [81] proposed a complete model, from the entrapment of particles to the related indentation within EHD contacts. They used data from the literature to validate results obtained with an elastic-plastic semi-analytical model. They were able to predict, with a good agreement, the number of indentations for spherical debris under pure rolling conditions. Other predictive models use measured dent geometry and density to compute reliable data for predicting the reduction of surface lifespan [82].

Predicting the lifetime of a mechanism is the ultimate purpose of each product designer. It was shown here that the lifetime of REBs is strongly linked with particle entrapment in lubricated contacts.

1.4 Summary and objectives of the work

Debris-like particles are inevitably entrained in EHD contacts found in aerospace applications. Previous studies evaluated the consequences of solid contaminant presence in different configurations.

To find out the mechanisms leading to particle entrapment, the present study proposes to focus on the critical entrainment of solid contaminants towards EHD contacts. Hence, a focus will be done on a single EHD contact, and more precisely on the contact inlet. Under different operating conditions the behavior of solid contaminants carried by the lubricant will be analyzed first qualitatively and then quantitatively.

The goals of this work is to get a new insight on the critical entrainment of contaminants within EHD contacts, to understand how particles are entrapped, how they create surface dents and to evaluate the impact of the change from steel–steel to Si_3N_4–steel contacts on debris entrapment and

surface dents. Finally this work aims to develop an understanding of the damage process in order to guide the design and use of debris resistant bearings.

The present study focuses particularly on aerospace applications with Si_3N_4-on-steel contact. Firstly an ideal case, with pure rolling condition within a circular contact is considered. Then different contact configurations with different contacting materials, different geometries and finally different kinematics are analyzed.

In the next chapter, the different numerical and experimental tools developed and used to investigate the particle entrainment phenomenon are presented.

Chapter 2 Numerical model and experimental devices

2.1 Introduction

In the literature, some descriptions of particle entrapment were attempted either analytically or experimentally. Nevertheless more detailed analyses are necessary and that is why a specific dual approach based on numerical simulations and on test rig experimentations is proposed in this study.

Numerical investigations on particle entrapment necessitates to model both the behavior of the fluid and to define the trajectories of the suspended particles. Based on in-house simulation tools for considering EHL problems [29,83], the lubricating contact gap and thus the geometry of the domain where particles are carried is known. By solving the fluid mechanics equations the fluid behavior is then fully described and the trajectories of diluted particles can be derived from the resolution of particles equilibrium.

In parallel, the experimental study of particle entrainment necessitates to use tribological test-rigs commonly called tribometers, with adapted methods and techniques for considering particle entrapment. Many kinds of tribometers, dedicated to EHL studies, exist nowadays and provide different information on EHD contacts with different device architectures (twin-disc machine [31], ball-on-disc tribometer [32] or 1:1 scale test rig [84]).

In this chapter an original numerical model to investigate the fluid flow and particle trajectories is described. Then experimental test rigs with in-house adapted devices to realize particle tracking and to quantify particle entrapment under contaminated lubrication are presented. The solid contamination will be considered here, either numerically or experimentally, with a model of debris-like particles, composed of M50 steel spherical particles with a range from 10 to 40 μm in diameter.

2.2 Numerical model

Particle entrapment in EHL problems results from the transport of solid particles at the contact inlet. As the entrapment phenomenon occurs upstream from the contact zone, as described in prior experimental [56] and numerical studies [21], the numerical fluid domain which is to consider includes the contact inlet. The physical considerations allowing proper simulation of contaminant particles carried by a lubricant are presented here. The assumption of a dilute regime is made [85] which means that the lubricant flow is sparsely contaminated with particles. On this basis, a dual investigation is performed, on one hand on the fluid flow using general fluid mechanics equations and on the other hand on the particles dynamics.

2.2.1 Fluid flow formulation at the EHD contact inlet

2.2.1.1 Geometry calculation

The lubricant layer which separates the contacting solids corresponds to a liquid domain in which particles are moving upstream and towards the EHD contact area. The classical Eulerian description adopted here consists to associate a velocity vector at each node of a specific domain.

Thin film theory is classically assumed near the EHD contact area. In this case, the resolution of the Reynolds equation is coupled with the elasticity of the contacting solids [28,29]. The two paraboloidal shaped surfaces have two equivalent contact radii, $R_{eq,x}$ and $R_{eq,y}$, in the two direction of the contact area (denoted x and y in the following). Figure 2-1 represents the contact between two solids (with $R_{1,x}$, $R_{1,y}$ and $R_{2,x}$, $R_{2,y}$) and the equivalent contact represented with a unique paraboloidal surface over a plane, with the equivalent radii, $R_{eq,x}$ and $R_{eq,y}$:

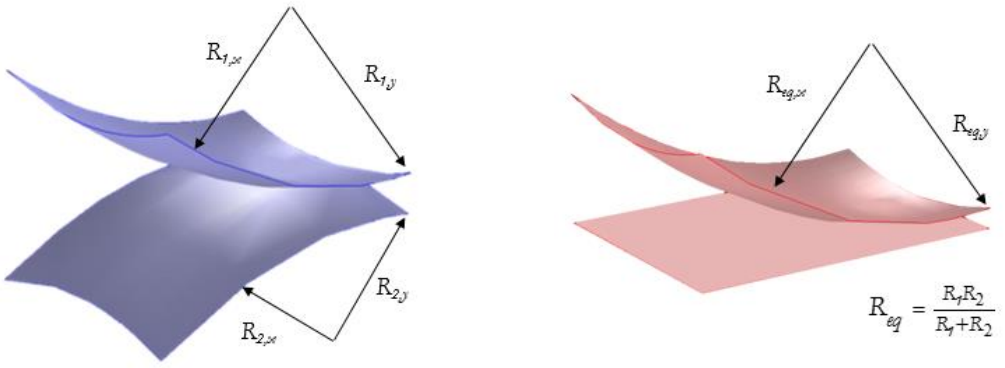

Two bodies Equivalent geometry

Figure 2-1: EHL contact with two-bodies or an equivalent geomerty

Elasticity equations are solved for an equivalent solid submitted to the fluid presuure and characterized by the elasticity parameters E_{eq} and v_{eq} [86]:

$$E_{eq} = \frac{E_1^2 E_2 \left(1+\nu_2\right)^2 + E_2^2 E_1 \left(1+\nu_1\right)^2}{\left[E_1\left(1+\nu_2\right) + E_2\left(1+\nu_1\right)\right]^2} \quad (2\text{-}1)$$

$$\nu_{eq} = \frac{E_1 \nu_2 \left(1+\nu_2\right) + E_2 \nu_1 \left(1+\nu_1\right)}{E_1\left(1+\nu_2\right) + E_2\left(1+\nu_1\right)} \quad (2\text{-}2)$$

with E_1, E_2 the Young's Moduli and ν_1, ν_2 the Poisson ratios of solids, 1 and 2, respectively.

Reynolds equation is then associated with the solid elastic deformation and load balance equations. This allows to calculate simultaneously pressure and film thickness profiles in EHD contacts.

Since the first solution of the EHL problem proposed by Ertel in the 40's [87], various models and simulation methods were developed to describe lubricated contacts. By using dimensionless parameters and a set of EHD cases, Hamrock and Dowson [88] and later Nijenbanning et al. [89] gave analytical formulas to evaluate central and minimum film thicknesses, which are among the key parameters. Multigrid methods, based on iterative schemes, were introduced by Lubrecht [90] and allowed time calculation reduction. The finite element methods (FEM) used for solving EHL problems was introduced in the 70's by Oh et al. [91] and used by many authors to take into consideration more and more physical interactions. Habchi [86] and Doki-Thonon [83] added thermal, non-Newtonian effects. This last approach was adopted in the present study for isothermal problems.

Pressure and film thickness are then known over the mean plane of the lubricant film. Nonetheless, the velocity component across the thickness is missing with this method. The present study, aiming at modeling particle entrapment requires a 3D fluid domain upstream from the contact.

The two parametrized surfaces corresponding to domain boundaries in which entrapment occurs are then defined with respect to the calculated film thickness (classical EHD approach).Within the gap between these two surfaces the complete (3D) velocity field is calculated using the Navier-Stokes equations (2-5). Figure 2-2 recaps the way of proceeding to obtain the fluid domain geometry in which the fluid flow and the particle trajectories will be obtained.

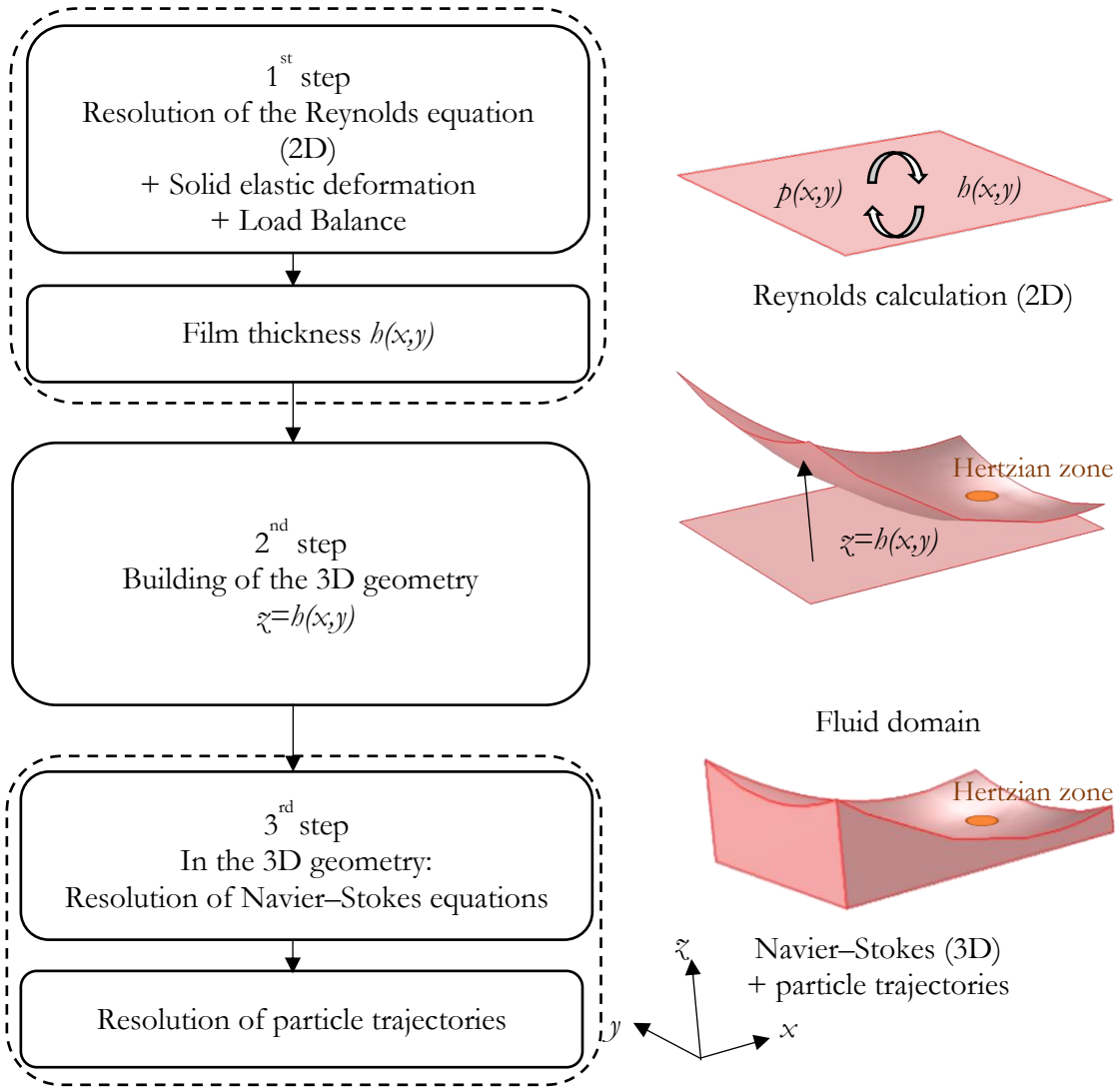

Figure 2-2: Definition of the 3D flow domain

For validation purpose, the pressure and the film thickness profiles obtained from the resolution of the Reynolds equation and the Navier-Stokes ones are compared in Figure 2-3, along the centerline of the contact inlet. The comparison is here performed for a steel–steel circular contact of equivalent radius equals to 17.5 mm, with contact load of 600 N and a mean rolling speed of 22 m/s. The comparison is performed in the contact inlet from -6*a* to -2*a*, in accordance with the size of the fluid domain which is given below in 2.2.1.2

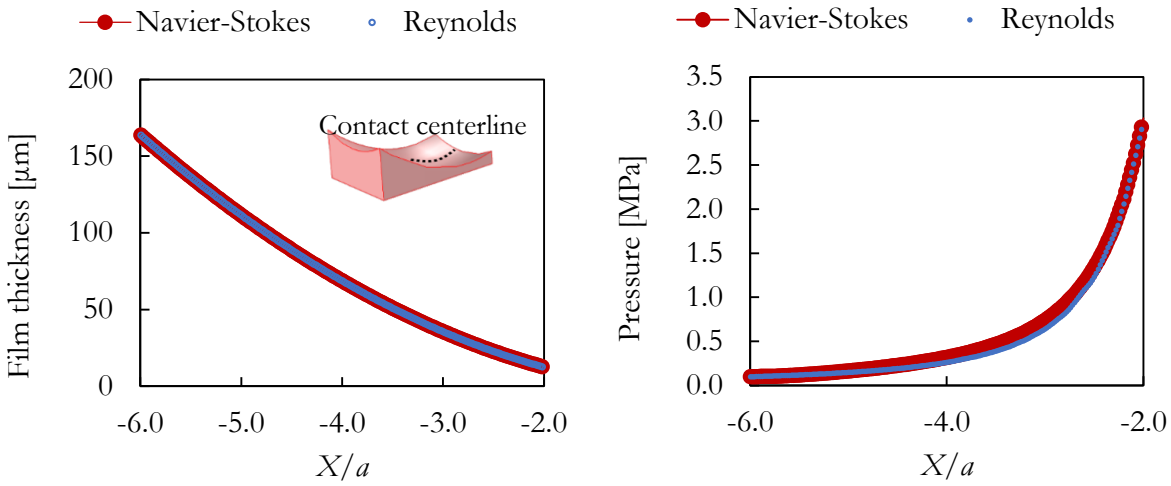

Figure 2-3: Comparison of the film thickness and pressure profiles along the centerline obtained from the resolution of the Reynolds equation and the Navier-Stokes equations for a steel–steel circular contact (600 N – 22 m/s)

The relative mean error between both fields is about 10 % for the pressure and less than 0.02 % for the film thickness. Indeed the pressure profile shows a huge gradient at the contact inlet. Reducing the error for pressure profiles is possible but it necessitates a greater number of elements for the 3D Navier-Stokes calculations which represents a prohibitive time cost. So a compromise of 10 % error on pressure has been accepted for the lubricant flow resolution.

2.2.1.2 Domain definition

The domain definition is directly linked to the type of geometrical configurations (circular, elliptical, etc.) and to the operating conditions. Aerospace applications typically consider a wide range of conditions. In the frame of this study, the following geometries, contact parameters and operating conditions will be considered.

- Curvature radii: 10–20 mm
- Materials: all-steel, Si_3N_4–steel, glass–steel
- Rolling speeds: up to 30 m/s (10^5-10^6 Ndm with R_x = 17.5 mm)
- Hertzian pressures: up to 2 GPa
- Slide-to-Roll Ratios (SRR): 0–12 %

Figure 2-4 reports the size of the fluid domain. It contains a plane of symmetry xx (i) and presents, with a red dotted line in y-direction the inlet boundary (ii) and, the side one in the x-direction (iii). The blue dotted line denotes the outlet boundary (iv). All these boundary positions are defined hereafter. The figure shows also an entrapment line (orange line) which corresponds to the position where the film thickness is equal to the size of the considered solid particle. The boundary conditions applied on the fluid domain are named from (i) to (vi), recalled in 2.2.1.3.

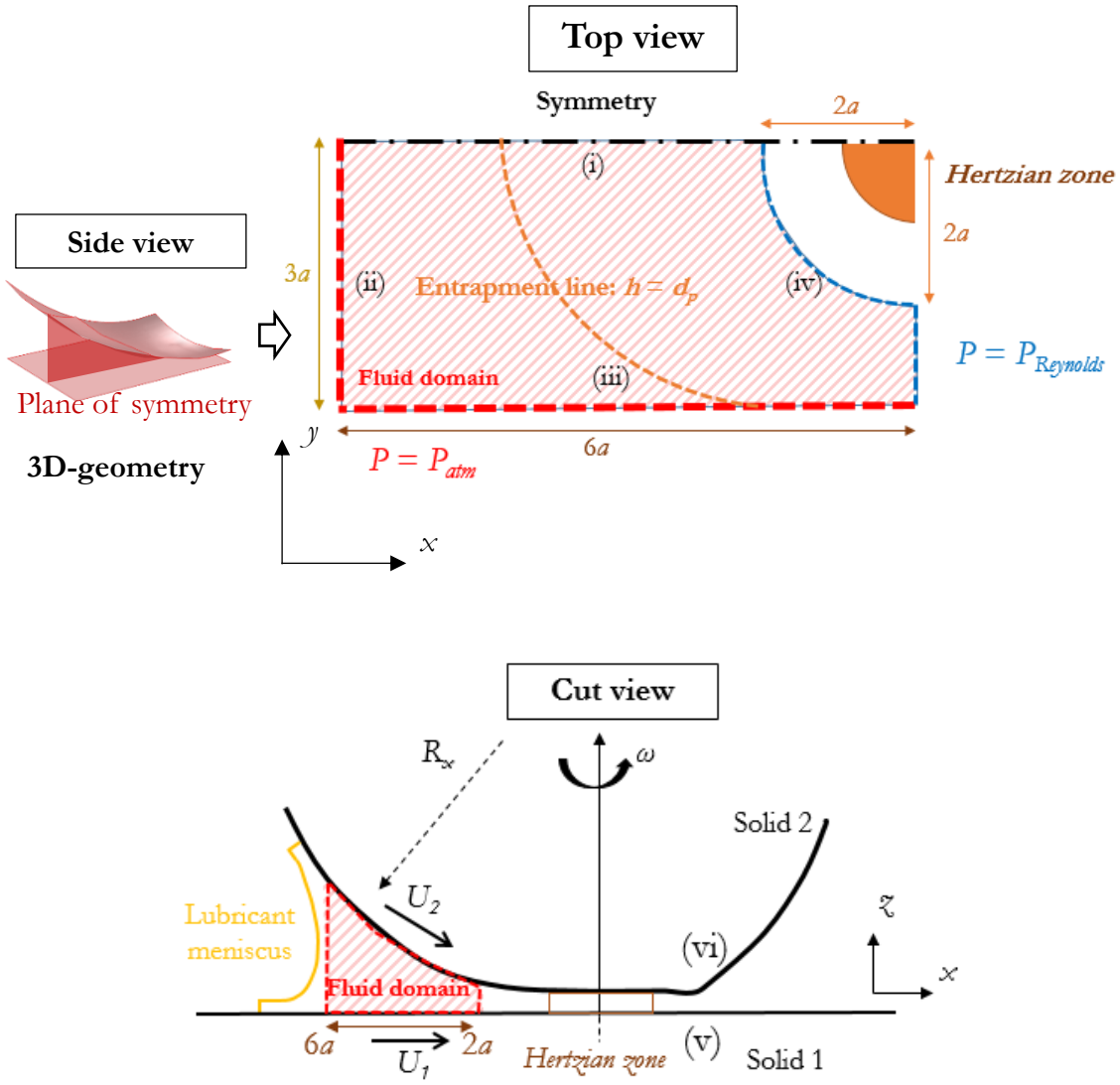

Figure 2-4: Fluid domain and boundary conditions

On Figure 2-4 (cut view) the fluid domain is restricted in *x*-direction between -6*a* and -2*a* and on *z*-direction between a plane (solid 1) and a curved profile (solid 2).

Inlet position

The inlet position was set in accordance with the lubricant meniscus position under fully flooded conditions. The critical meniscus position X_c when the lubrication regime moves from fully-flooded to starved, is given by Hamrock [92]:

$$X_c = -a\left\{1+3.06\left[\left(\frac{R_x}{a}\right)^2\frac{h_c}{R_x}\right]^{0.58}\right\} \qquad (2\text{-}3)$$

where h_c is the central film thickness, R_x the ball radius, and a the Hertzian radius. The critical meniscus position is plotted for a wide range of operating conditions in Figure 2-5 (Mean rolling speed, U_m, from 12 to 22 m/s and normal loads from 100 to 1200 N) in the case of a circular steel–steel contact with R_x = 17.5 mm and a viscosity μ = 12 mPa.s. The dimensionless Moes parameter is used here to take into account these different parameters:

$$M = \frac{W}{E_{eq}R^2}\left(\frac{\mu(U_1+U_2)}{E_{eq}R}\right)^{-3/4} \qquad (2\text{-}4)$$

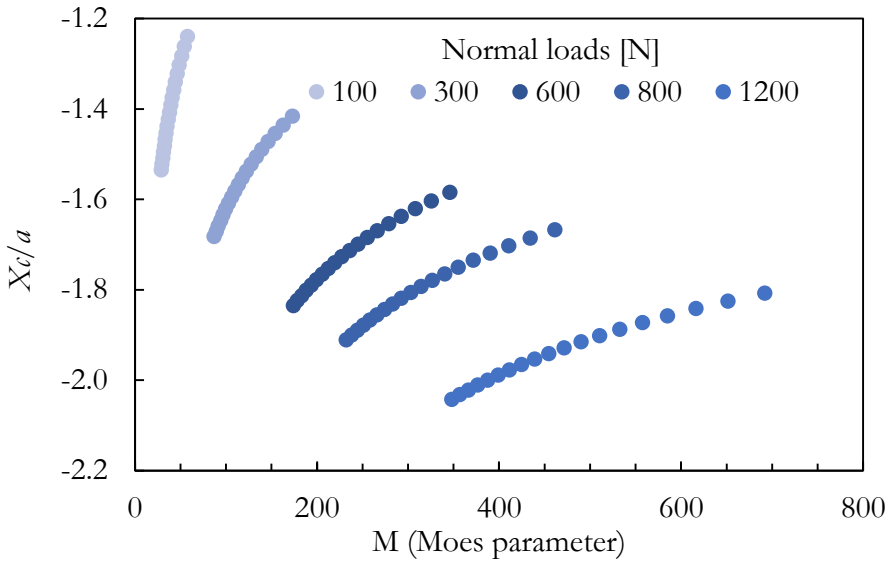

Figure 2-5: Critical meniscus position for different operating conditions for a steel–steel circular contact (R_x = 17.5mm)

The inlet position for this study was set to approximatively two to three times this critical distance to ensure fully-flooded conditions for the different corresponding contact configurations and so is finally fixed to 6*a* upstream from the contact center.

Side boundary

The side boundary was set sufficiently far away from the contact centerline so that the lubricant flow will not be disrupted by the boundary location. Moreover, the location has to be far enough to consider the entrapment of all designated particles. Here, particles were chosen to be in the range between 10 and 40 µm in diameter which corresponds to particles commonly found in aero-engine lubricants.

A further parameter, called entrapment width (EW), defines the width in the contact zone, according *y*, where particles can be entrapped. For example, if the suspended particles are 40 µm of

diameter, the gap will be lower than 40 µm inside the EW. Figure 2-6 reports a representation of EW for 10 and 40 µm contaminants and the Hertzian zone to give an order of magnitude.

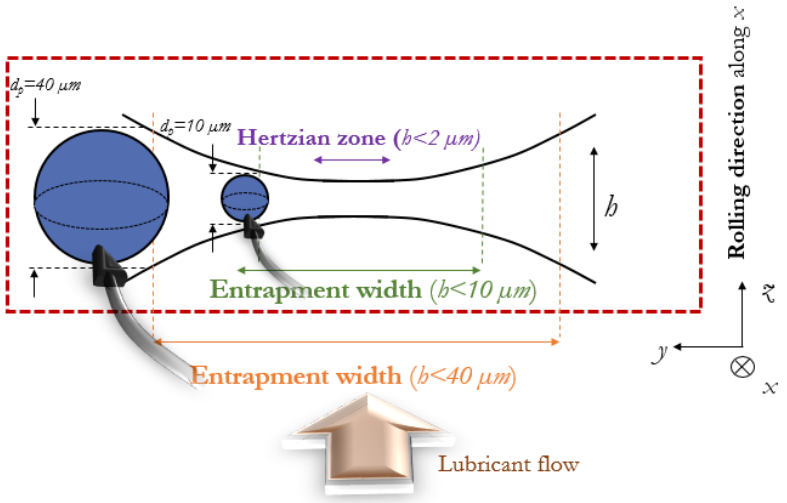

Figure 2-6: Entrapment width (EW) for different spherical particles of 10 and 40 µm

Typical values for dimensionless EW are given in Figure 2-7 for a circular steel–steel contact, with R_x=17.5 mm, μ = 12 mPa.s, U_m = 22 m/s, normal loads from 100 to 1200 N, and solid contaminants from 10 to 40 µm in diameter.

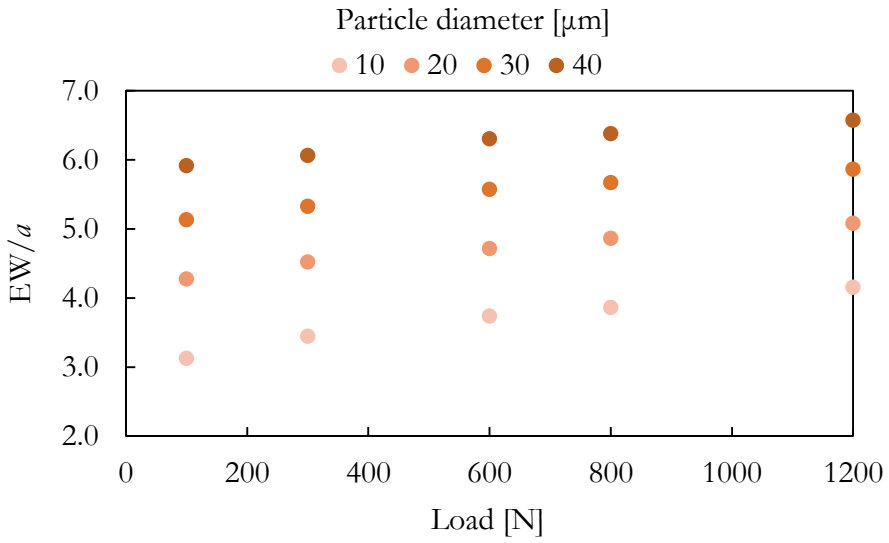

Figure 2-7: Dimensionless EW for different particle sizes: 10, 20, 30 and 40 µm, and different normal loads within a steel-steel circular contact (R_x = 17.5 mm)

Considering the plane of symmetry and the calculated EW for the analyzed EHD contacts, the side boundary will be located 3a away from the symmetry plane.

Outlet boundary

As the solid contaminants are of the order of tens of microns in diameter, and the central oil film thickness of the order of tenths of microns, it was not essential to consider the entire zone around the Hertzian area. Here, not considering an area of radius 2*a*, as represented in Figure 2-4, enabled to save many meshing elements and is not detrimental for the entrapment phenomena which happens upstream from this zone.

2.2.1.3 Equations and boundary conditions

Equations

The mass flow conservation and the momentum one, which describe the confined flow, are assumed by solving the Navier-Stokes equations [93,94]:

$$\nabla \cdot \left(\varrho_f \boldsymbol{U}_f \right) = 0$$
$$\varrho_f \left(\boldsymbol{U}_f \cdot \nabla \right) \boldsymbol{U}_f = -\nabla p + \nabla \cdot \left[\left(-\frac{2}{3} \mu \nabla \cdot \boldsymbol{U}_f \right) \bar{\bar{I}} + \mu \left(\nabla \boldsymbol{U}_f + \nabla \boldsymbol{U}_f^{\mathrm{T}} \right) \right] + \varrho_f \boldsymbol{g} \qquad (2\text{-}5)$$

with $\boldsymbol{U}_f$ the fluid velocity vector, p the fluid pressure, μ the viscosity, ϱ_f the fluid density, $\bar{\bar{I}}$ the identity matrix, $\boldsymbol{g}$ the gravity vector.

In the present study, the lubricant viscosity and density are pressure dependent and follow the William–Landel–Ferry (WLF) rheological law and Dowson–Higginson compressibility law [95,96].

As this study is focused on aeronautical applications, a representative lubricant of this domain was used. The work of Vergne and Nélias [30] on the common aeronautical lubricant MIL-L-23699, gives the parameters for the WLF law, defined as follows:

$$\log \mu = \log \mu_g - \frac{C_1 \left(T - T_g(p) \right) F(p)}{C_2 + \left(T - T_g(p) \right) F(p)}$$
$$T_g(p) = T_g(0) + A_1 \ln\left(1 + A_2 p \right) \qquad (2\text{-}6)$$
$$F(p) = 1 - B_1 \ln\left(1 + B_2 p \right)$$

where μ_g is the glass transition viscosity at $T_g(0)$ and A_1, A_2, B_1, B_2, C_1, C_2 the WLF parameters.

A_1 [°C]	A_2 [1/GPa]	B_1	B_2 [1/GPa]	C_1	C_2 [°C]	$T_g(0)$ [°C]	μ_g [Pa.s]
171.96	0.4294	0.1961	17.434	16.342	29.406	-107.4	10^{12}

Table 2-1: WLF parameter for the MIL-L-23699 lubricant [30]

Boundary conditions

Pressure conditions were set assuming that the environmental pressure is atmospheric (P_{atm}) which is the case on the two boundaries where there is a lubricant-air meniscus: on the inlet boundary and on the side one. On the outlet boundary, the pressure is set equal to the pressure computed by the resolution of the Reynolds equation coupled with the elasticity of the contacting solids. Moreover, a no viscous stress condition is imposed on the inlet and side boundaries [97] as well as a symmetry condition for the velocity field on the plane of symmetry.

Hence, the fluid domain is delimited by a symmetry plane (Figure 2-4, (i)), a fully-flooded condition (Figure 2-4, (ii)), a side boundary (Figure 2-4, (iii)) and an outlet boundary (Figure 2-4, (iv)) :

$$\begin{gathered}\text{(i): } \boldsymbol{U_f}\cdot\boldsymbol{n}=0\\ \text{(ii) and (iii): } P=P_{atm} \text{ and } \left(\nabla\boldsymbol{U_f}+\nabla\boldsymbol{U_f}^{T}\right)\cdot\boldsymbol{n}=0\\ \text{(iv): } P=P_{Reynolds}\\ \text{with } \boldsymbol{n} \text{ the normal vector to the surface}\end{gathered} \quad (2\text{-}7)$$

The upper and lower boundary conditions for the fluid are considered with a no-slip condition:

$$\text{Lower boundary: } \boldsymbol{U_f}=\begin{Bmatrix}u\\v\\w\end{Bmatrix}=\begin{Bmatrix}U_1\\0\\0\end{Bmatrix} \text{ (Figure 2-4, (v))} \quad (2\text{-}8)$$

$$\text{Upper boundary: } \begin{Bmatrix}u\\v\\w\end{Bmatrix}=\begin{Bmatrix}(R_x - z)\omega\\0\\x\omega\end{Bmatrix} \text{ (Figure 2-4, (vi))} \quad (2\text{-}9)$$

where u, v and w are the fluid velocity along x, y and z, respectively, U_1 is the plane speed, while $U_2 = R_x\omega$, R_x is x-radius of the curved surface and ω is the rotating speed of the curved surface.

In this 3D domain, the resolution of the Navier-Stokes equations gives the pressure and velocity fields, as represented for example in Figure 2-8 and Figure 2-9, respectively. A zoom on the fluid velocity field is also given. To follow Doki-Thonon and Habchi's approach [29,83] the same FEM plateform was used to solve these equations with 693846 degrees of freedom (DoF).

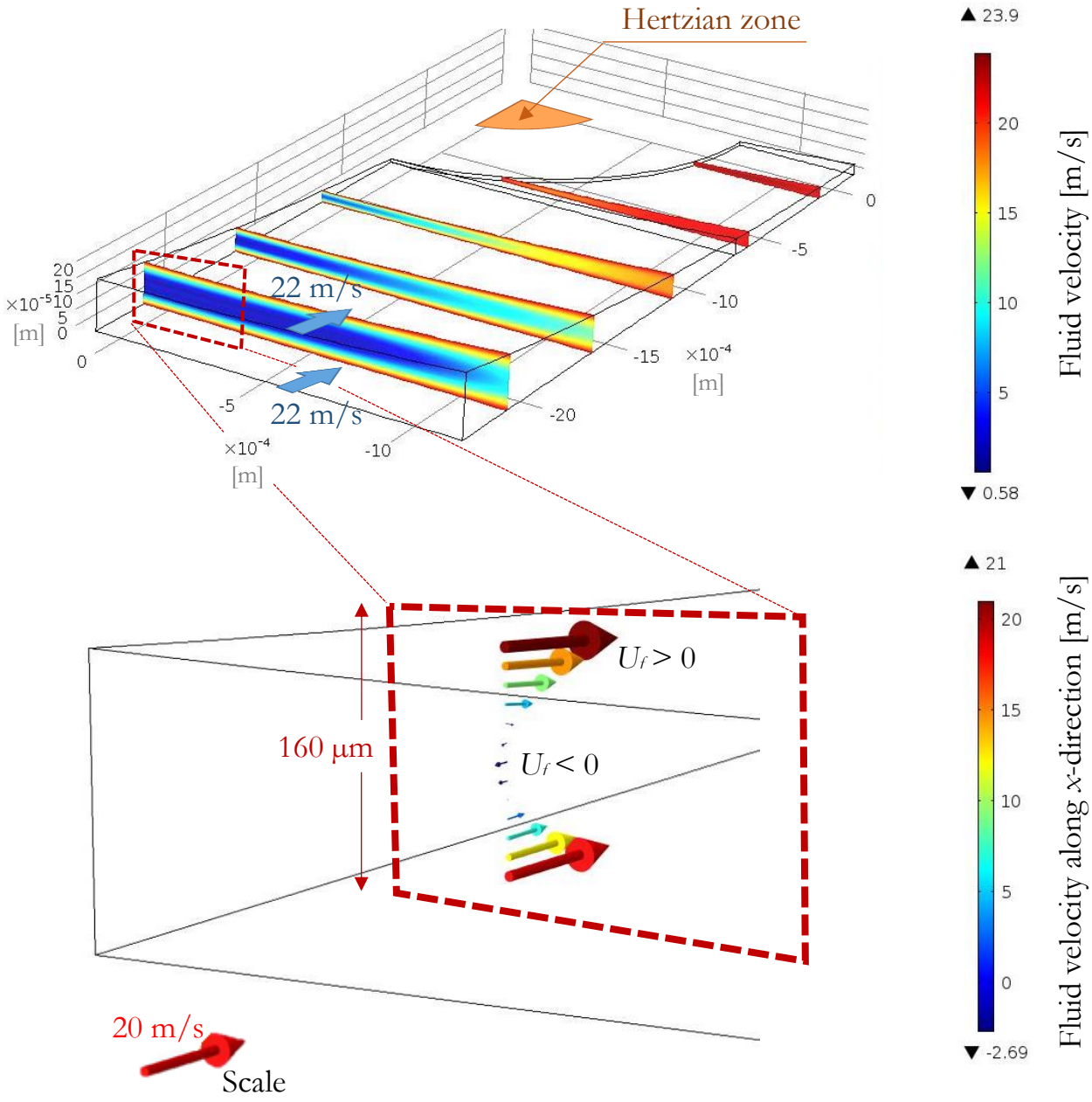

Figure 2-8: Velocity field for a steel–steel contact, equivalent radius of 17.5mm, with EHL parameters: 600 N – 22 m/s – 60 °C

The fluid velocity is mainly governed by the motion of the rolling surfaces guiding the lubricant towards the Hertzian area.

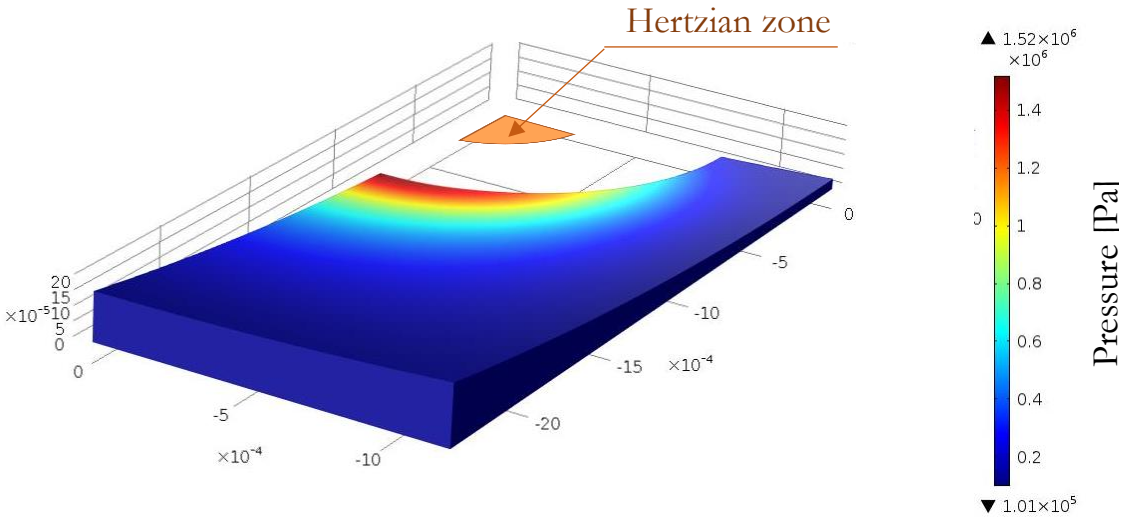

Figure 2-9: Pressure field for a steel–steel contact, equivalent radius of 17.5mm, with EHL parameters: 600 N – 22 m/s – 60 °C

The pressure profile is consistent with an EHD contact inlet. The pressure is ambient on the inlet and side boundaries and increases drastically in the vicinity of the Hertzian zone due to hydrodynamics effects (see also Figure 2-3).

2.2.2 Formalism for the particle motion

In this work, the contaminant particles are considered spherical and well dispersed in the lubricant. Hence, a single contaminant particle will be considered at a time.

2.2.2.1 Brief review

Continuous methods based for example on Finite Element Method (FEM), reproduce easily and accurately the behavior of lubricant. Kumar et al. [98] proposed a model to solve the particle motion using a two-phase flow. Based on a FEM domain with a moving hole simulating the particle and an adaptive mesh process to consider the particle-flow interaction. Isèbe and Nérin [99] also used an adaptive mesh to model the displacement of a single simplified red blood cell. Despite its great accuracy, such calculation is highly time consuming.

The development of discrete numerical methods allowed to solve issues concerning the flow of suspended particles. The sediments transport in rivers [100], the formation of avalanches [101] and the motion of desert sand dunes [102] are problems in which discrete particles motion potentially interacts with a transport medium, either gaseous or liquid.

The different fluid-particle couplings that might be taken into account in numerical models were summarized by Loth et al. [103] (Figure 2-10). Depending on the type of multiplhase flows that have to be considered, different numerical approaches can be foreseen.

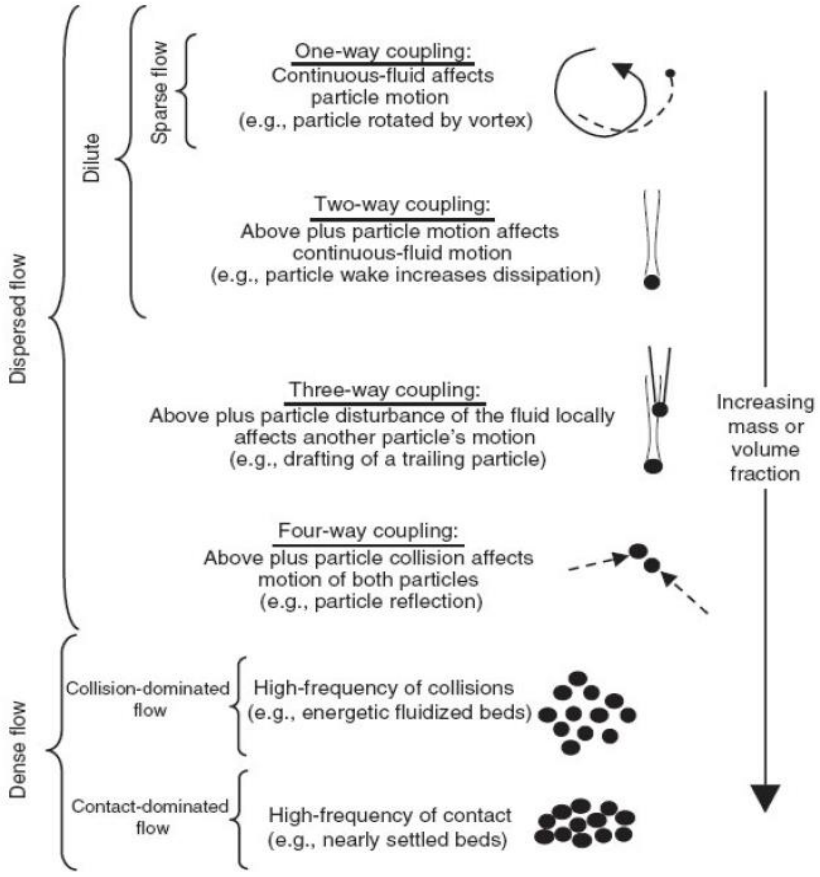

Figure 2-10: Different fluid-particle couplings (inspired by [103])

Rates of contamination found in REBs are reported in the literature. In these studies [18,60], 10 to 150 mg/l of contaminants in solution were considered representative of a realistic state of contamination in operating REBs. For example, with particles of 40 µm in diameter a contamination rate of 75 mg/l means about 28700 particles in 100 ml solution. In a micro-liter oil bath (1 µl = 10^{-9} m^3), as the one presented in Figure 2-4, about only 0.2 particles of volume 10^{-14} m^3 would be in solution. For this reason it is considered that particles enter the fluid domain one by one.

Hence, the present study deals with a sparse flow of particles, with few particles in volume percentage, where particle-particle interactions and perturbation induced by the particles on the lubricant flow can be neglected.

Finally, in his extensive work to simulate particle entrainment in EHD contacts, Nikas [20–23] proposed to consider a one way coupling model with only the effect of the fluid on the particle motion (without effect of the particle on the fluid). On this basis, the next section aims at explaining the one way coupling assumption used through this numerical study.

2.2.2.2 Fluid-particle coupling

The description of the particle motion is based on the resolution of Newton's second law. The forces acting on the particle are computed at each time step in accordance with the fluid and particle state. This consists in solving a set of ordinary differential equations at chosen positions of the particle. The equilibrium equations of a spherical particle, in the case of a rigid non-rotating particle, are summed up hereafter:

$$\begin{aligned} \frac{\mathrm{d}\boldsymbol{x}_p}{\mathrm{d}t} &= \boldsymbol{v}_p \\ m_p \frac{\mathrm{d}\boldsymbol{v}_p}{\mathrm{d}t} &= \sum \boldsymbol{F}_\mathrm{i} \end{aligned} \qquad (2\text{-}10)$$

where m_p is the particle mass, $\mathbf{x_p}$ is the particle position vector, $\mathbf{v_p}$ is the particle velocity vector, and $\mathbf{F_i}$ are the external applied forces. Considering spherical particles, only the diameter and the center of mass will be considered.

2.2.2.3 Acting forces

The gravity, $\boldsymbol{F_G}$, and buoyancy, $\boldsymbol{F_B}$, forces are applied to each particle flowing in the confinement. The formulation of these forces take the following classical forms:

$$\boldsymbol{F_G} + \boldsymbol{F_B} = \left(\varrho_f - \varrho_p\right) V_p \boldsymbol{g} \qquad (2\text{-}11)$$

where $\boldsymbol{g}$ is the gravity vector, V_p the particle volume and ϱ_f and ϱ_p, the density of the fluid and the particle, respectively.

The fluid forces, often called "drag forces" $\boldsymbol{F_D}$, can significantly vary between a laminar regime and a turbulent one. The drag force is directly proportional to the fluid density ϱ_f, to the cross section of the related particle, to the square of the relative particle speed $\boldsymbol{U_r} = \boldsymbol{U_f} - \boldsymbol{v_p}$ and to a drag coefficient C_D, whose definition is given hereafter [104]:

$$\boldsymbol{F_D} = \frac{1}{8} C_D \varrho_f \boldsymbol{U_r}^2 \pi d_p^2 \qquad (2\text{-}12)$$

The use of the Reynolds number (see below) allows to rewrite this drag force:

$$\begin{aligned} \mathrm{R}e &= \frac{U_r d_p \varrho_f}{\mu} \\ \boldsymbol{F_D} &= \frac{1}{8} \mu \mathrm{R}e C_D \boldsymbol{U_r} \pi d_p \end{aligned} \qquad (2\text{-}13)$$

The drag force is directly linked to the flow regime. In creeping or laminar flow ($Re < 1$), the drag coefficient C_D, is determined via shear stress and pressure calculation on a static particle [104]. The value of the drag coefficient in a laminar case is:

$$C_D = \frac{24}{Re} \quad (2\text{-}14)$$

In this kind of flow the viscous effects dominate the inertia ones.

In the transitional regime ($0.2 < Re < 500$), many studies like the one from Ambrosino [105] showed that the drag coefficient is dependent of the Reynolds number:

$$C_D = \mathrm{f}(Re) \quad (2\text{-}15)$$

For larger Reynolds numbers, where the flow is turbulent, a drag coefficient plateau is reached. It is named the Newton's regime and appears for $Re > 1000$ [106]. In this case, drag is due to inertia effects rather than viscous ones and:

$$C_D = 0.44 \quad (2\text{-}16)$$

Figure 2-11 describes the magnitude of the Reynolds number in typical REBs conditions in presence of contamination. The values of the Reynolds number is represented for particles from 10 to 40 µm in diameter. The relative speed is considered in the range 0–30 m/s from a particle moving at the same speed as the fluid (U_r = 0 m/s) to a particle being fixed within a surrounding fluid at the maximal considered rolling speed (U_r = 30 m/s).

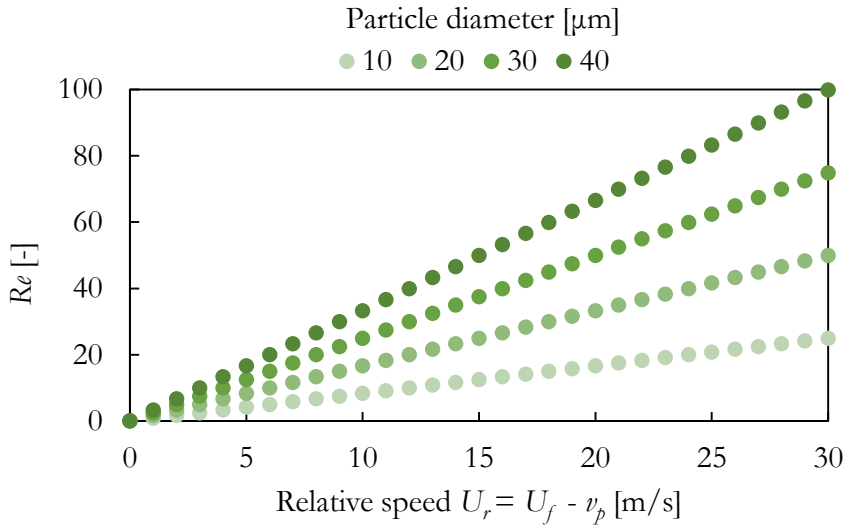

Figure 2-11: Reynolds number function of the relative speed
between the particle and the surrounding fluid velocity for different particle diameters

It appears that the Reynolds number is classically between 1 and 100 which corresponds to the transitional regime.. The values for the drag coefficient are summed up in Figure 2-12 according to the Reynolds number. The red area indicates the range of Re for the present study.

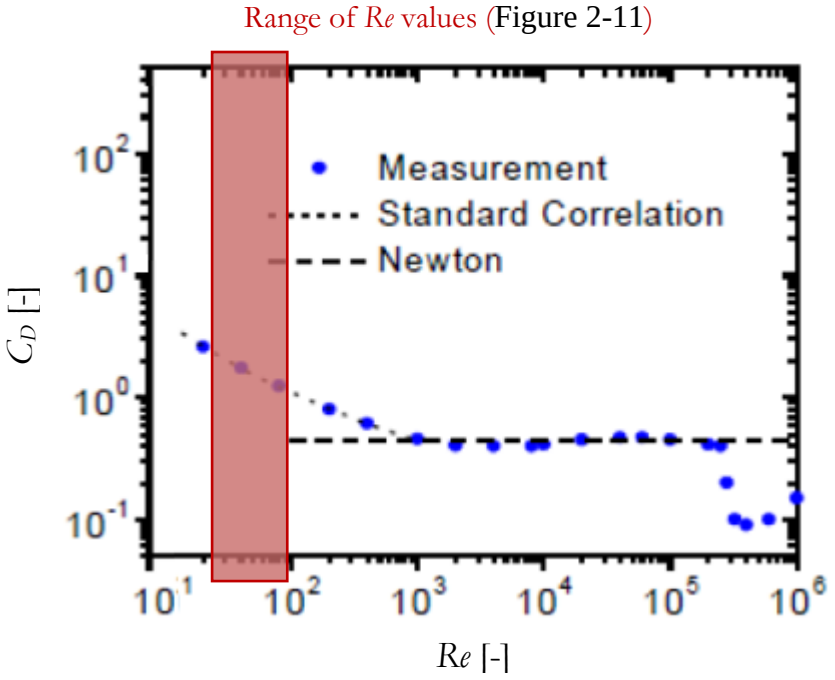

Figure 2-12: Evolution of the drag coefficient with Reynolds number (inspired from [105])

In the current model, the fluid forces are taken into account through the Schiller-Neumann formulation [107], described by the following formulation (2-17). This formulation was chosen as it takes into account the transitional regime and gives an analytical value for the fluid forces:

$$C_D = \frac{24}{Re}\left(1 + 0.15 Re^{0.637}\right) \qquad (2\text{-}17)$$

Some other forces which were here neglected are recalled hereunder [108].

- The virtual added mass and Basset forces [109] correspond to forces linked to the particle trajectory history. Here, these forces can be neglected, due to the small size of the contaminant, the low viscosity of the lubricant and the small particle density ratio [110].
- The lift force which might be induced by a non-uniform velocity field [111]. Here, such a force is of second order in comparison to drag forces as pressure gradient across film thickness is considered negligible.
- The Magnus force which could exist within a rotational velocity field [112] but in the current model the motion of the spherical particles is considered non-rotative.

Figure 2-13 summarizes the forces acting on the particle in the frame of this study:

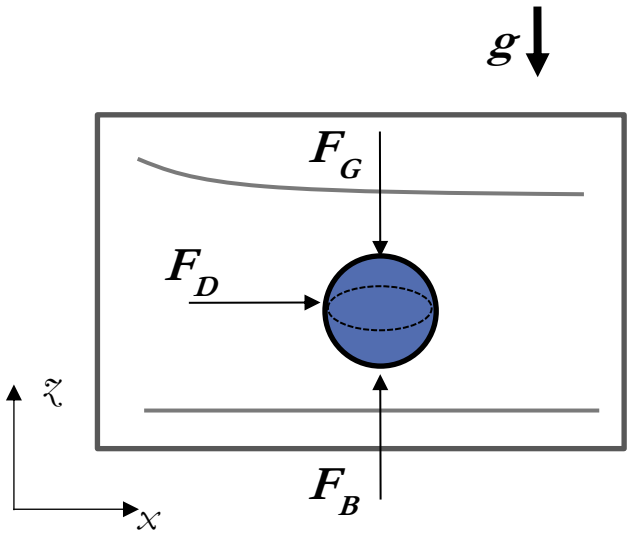

$$\boldsymbol{F_D} = \frac{3\mu Re C_D}{4\varrho_p d_p^2} m_p \left(\boldsymbol{U_f} - \boldsymbol{v_p}\right)$$

$$\boldsymbol{F_G} = -V_p \varrho_p \boldsymbol{g}$$

$$\boldsymbol{F_B} = V_p \varrho_f \boldsymbol{g}$$

Figure 2-13: Sketch of the particle-flow model and the forces at play

2.2.2.4 Wall-particle interaction

A wall-particle interaction has to be defined, to take into account the vicinity of the contacting solids. Here, a simplified interaction model implies that there are no specific friction force at the particle-solid wall interface. Thus, the particles collide on the surfaces with no power loss (Figure 2-14, left). The equation describing this process is the following:

$$\boldsymbol{v'}_{\mathrm{p}} = \boldsymbol{v}_p - 2\left(\boldsymbol{v}_p \cdot \boldsymbol{n}\right) \cdot \boldsymbol{n} \qquad (2\text{-}18)$$

with $\boldsymbol{v'_p}$ and $\boldsymbol{v_p}$, the particle velocity vector after and before the interaction with the wall and $\boldsymbol{n}$ the normal vector to the surface. If a particle touches both surfaces simultaneously, the entrapment criterion "freezes" the particle (Figure 2-14, right). Then, the numerical simulation is stopped and the particle is considered entrapped between the surfaces. In real systems, most of the time, once a particle is caught in the contact inlet, as the traction forces are far larger than the fluid forces, it is drawn by the surfaces into the contact [55,113] and plastic deformation occurs.

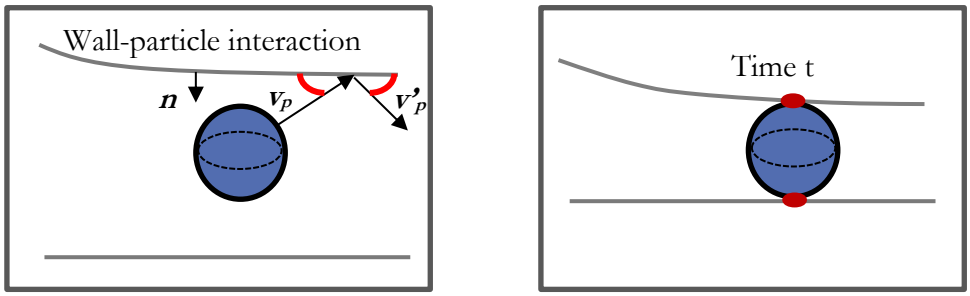

Figure 2-14: Wall particle interaction and entrapment criterion

Finally, it is possible to release particles at different positions, called released position (*RP*), at the inlet boundary (Figure 2-4 - (ii)) of the fluid domain. All particles were considered released with the surrounding fluid velocity $\boldsymbol{U}_f(t=0)$.

$$\boldsymbol{v}_p(t=0)=\boldsymbol{U}_f(t=0) \qquad (2\text{-}19)$$

Then, calculations (implicit scheme / time step: 1 µs) are performed with different conditions leading to either entrapment or rejection. As an example, a top view of the fluid domain, Figure 2-15, represents two 40 µm particles released at different positions, denoted RP_1 and RP_2, upstream from the contact. The two particles are released at the inlet boundary, 20 µm above the lower surface and 5 or 30 µm away from the symmetry plane, respectively.

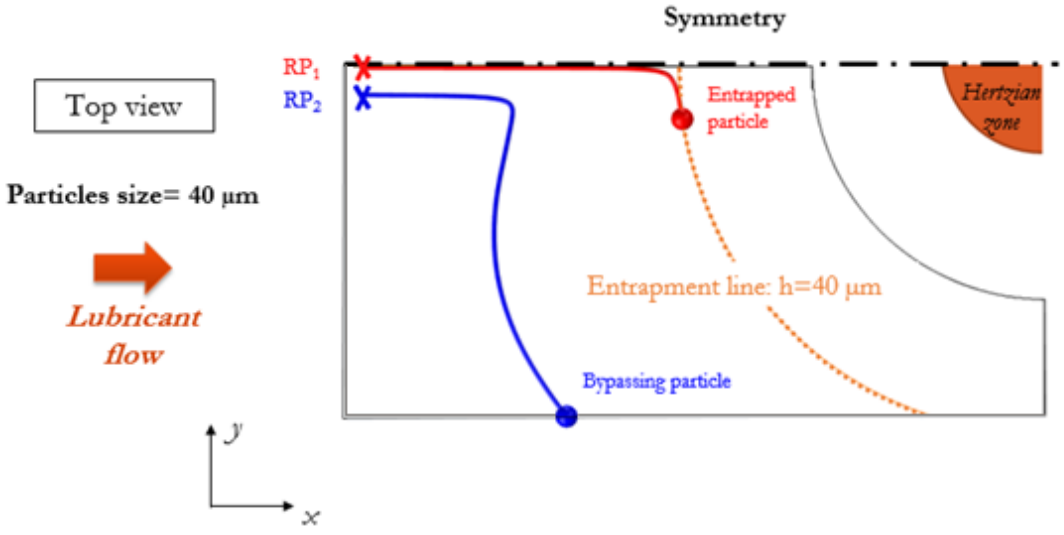

Figure 2-15: Simulations of two released particles, with one entrapped (red) and one bypassing (blue)

On this figure it appears that the particle released at the position RP_1 is entrapped and that the one released at the position RP_2 is bypassing the critical entrapment zone. Following the presentation of the numerical tool and its potential, the next section presents the experimental test-rigs used in the frame of this study.

2.3 Experimental techniques

Here, the two test rigs and their related facilities to observe particle entrapment in EHD contacts are presented. The first one can reproduce highly-loaded lubricated contacts with high rolling speeds in a twin-disc configuration and the second device is a ball-on-disc EHD test-rig, which includes a transparent disc enabling to visualize the lubricant flow penetrating into the convergent area.

2.3.1 Twin-disc machine and contamination test rig

2.3.1.1 Machine and materials

A twin-disc machine [31] aims at reproducing rolling or rolling-sliding highly loaded contacts, thus it consists mainly of two rotating discs with independently controlled speed motors and an applying load system. For this study, the whole test rig (Figure 2-16) consists of the contacting discs and a controlled contamination system.

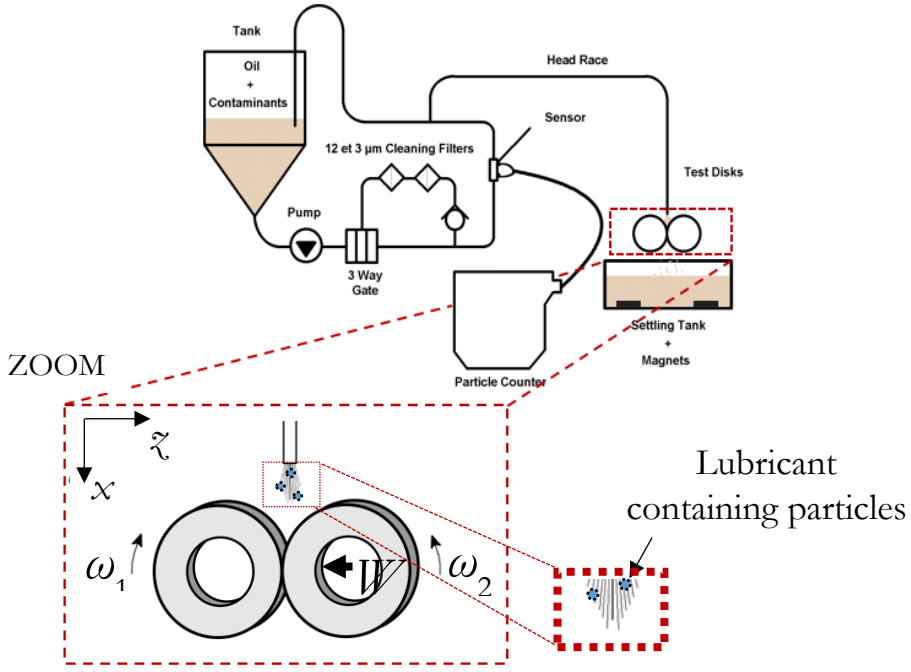

Figure 2-16: Twin-disc machine and device for studying particle entrapment

The two contacting discs are of the same main radius, R_x, of 35 mm, one being cylindrical and the other one being a crowned one with a transverse radius, R_y. To mimic different elliptical contact configurations, R_y was varied from 17.5 mm for the circular case to 35, 70, and 200 mm for the elliptical ones.

The disc specimens were polished to reach a surface roughness down to R_a = 0.05 µm. Different materials were considered for the discs: (i) AISI 52100 steel for the crowned discs with R_y = 17.5 and 200 mm, (ii) AISI M50 steel for the crowned discs R_y = 35 and 70 mm, and (iii) Si_3N_4 ceramic for the cylindrical discs used in the hybrid contacts. The properties of the different discs are summarized in Table 2-2.

	Steels		**Ceramic**
	AISI 52100	AISI M50	Silicon nitride
Young modulus [GPa]	210	210	305
Poisson ratio	0.3	0.3	0.26
Hardness	HRC 64	HRC 62	HV 0.5: 1450 (> HRC 78)
Density [kg/m^3]	7800	7800	3260
R_y [mm]	17.5 200	35 70	∞ (cylindrical)

Table 2-2: Properties of the contacting discs

The different configurations aimed at simulating various type of elliptical EHD contacts occurring between rolling elements and raceways in REBs. Due to different solid geometries, the contact configuration will be either circular when the contact results from a ball-on-plane configuration or elliptical when it results from a barrel-on-plane configuration. Table 2-3 reports the properties of the different contacts obtained with a pair of crowned and cylindrical disc on the twin-disc machine for a constant load equal to 600 N.

Type of contact	**Circular**	**Elliptical**		
R_x [mm]	17.5	17.5	17.5	17.5
R_y [mm]	17.5	35	70	200
W [N]	600	600	600	600
a [µm]	409	362	317	258
b [µm]	409	574	794	1260
k	1.00	1.59	2.50	4.88
P_h [GPa]	1.71	1.38	1.13	0.88

Table 2-3: Different geometries and related parameters resulting for steel-steel contact

Previously MIL-L-23699, was presented for the numerical investigation. It is classicaly used in aerospace applications and fully-characterized. Nevertheless this lubricant is highly toxic and not convenient for experimental tests in labs. That is why a compromise has be found by using a saturated pentaerythritol ester, Nycobase 5750 base oil that presents very close characteristics (see Table 2-4).

Lubricant	Mobil MIL-L-23699	Nycobase 5750
Density (20°C) [kg/m^3]	998	987
Kinematic viscosity (40°C) [cSt]	27.6	24.5
Kinematic viscosity (100°C) [cSt]	5.1	5.1

Table 2-4: Properties of lubricant Nycobase 5750 in comparison to lubricant MIL-L-23699

The controlled contamination system is a closed loop which includes a commercial particle counter device provided by UCC® condition monitoring, which allows a recording of the amount of particles per 100 ml of lubricant by analyzing a sample of the fluid within a bypass channel based on the light absorption principle. According to ISO standards [54], it gives the state of contamination before and after the tests. Finally, two filters in series of range 12 and 3 µm are added to the system to clean the lubricant after the test.

Experimentally, a powder of M50 steel particles, containing particles in the range 5–50 µm was sieved in order to get two well defined ranges of particle diameters, 10–20 µm and 32–40 µm (see Figure 2-17). M50 steel powder is of Hardness 58–61 Rockwell C (HRC) and particles are of spherical shape. Experimentally, contaminants can be composed of larger particles with smaller attached ones which are called satellites.

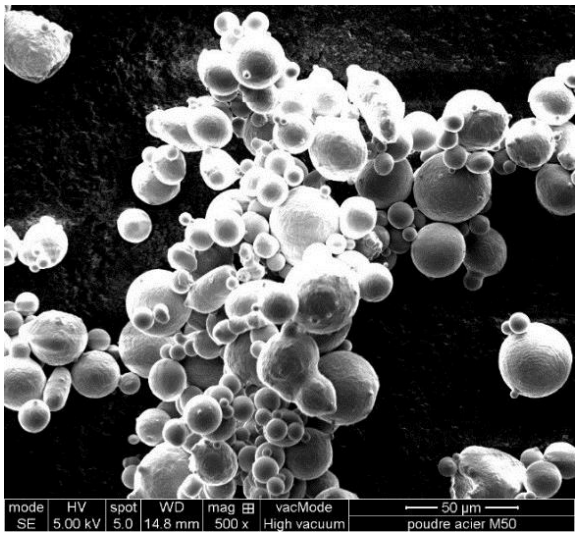

Unsieved powder of M50 steel particles (SEM)

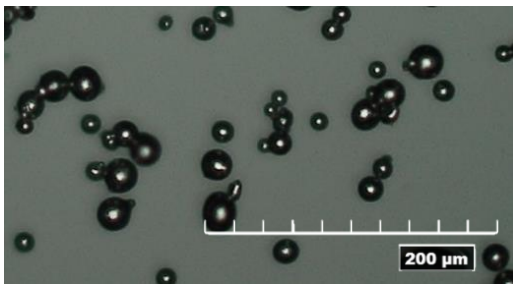

Sieved particles range 10–20 µm

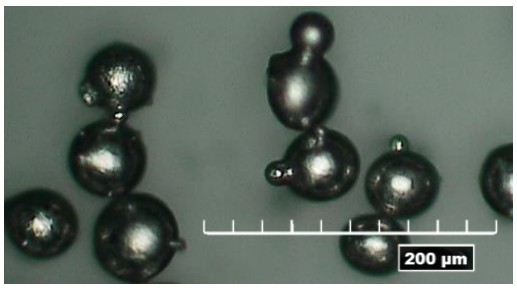

Sieved particles range 32–40 µm

Figure 2-17: (a) Unsieved M50-steel powder observed with SEM, (b) Sieved particles in the range 10–20 µm (c) and in the range 32–40 µm observed with optical microscope

After the presentation of the twin-disc machine and a sum-up on the material which is used for these tests under contaminated lubrication, the next section aims at presenting the procedure of these experimental tests to evaluate particle entrapment.

2.3.1.2 Protocol and methods

The objective of the experimental study on the twin-disc machine was to determine the effective particle entrapment rate under contaminated lubrication for highly loaded contacts. Considering that each entrapped particle is responsible for a single surface dent, this rate is directly linked to the number of dents counted on the disc raceways [18]. It has to be noticed that some particles may be embedded in one of the disc surface and then dent periodically the counterface after repeated rolling cycles. But an entrapped particle will cause only one single time an indentation mark with a characteristic hole in the middle of the dent (see chapter 4, plastic deformation).

Dent count was realized after each test to obtain quantitative comparisons of entrapment rates in different EHD contacts. The count was performed all around the disc but restricted to the entrapment width (EW defined in 2.2.1.2). Figure 2-18 shows a sketch of the twin-disc machine with a contaminated lubrication, a representation of the entrapment width and an image of the dented surface after a test observed with an optical microscope.

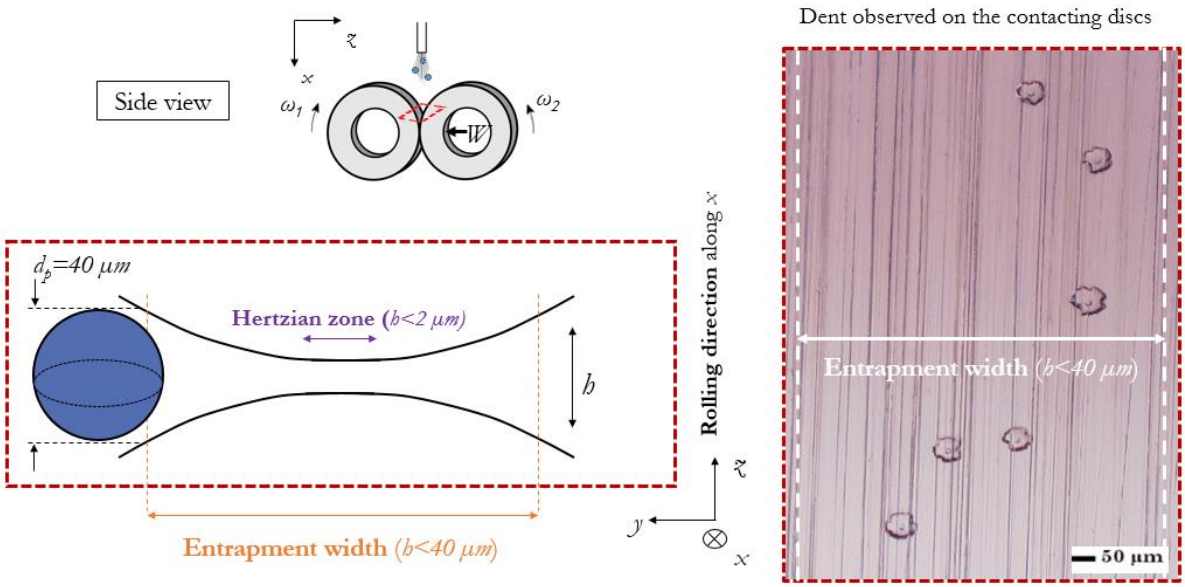

Figure 2-18: Entrapment area and indentation features

The EW defines the domain where particles are trapped and where either indentation of the surfaces or embrittlement of the particle occurs, according to particle/surface hardness ratio.

In the frame of this work, most of the experiments were conducted with ductile particles. Hence, each entrapment led to a dent on each surface for steel–steel contact and to a deformation of the particle. In order to characterize the indentation marks, surface profiles were also obtained using an optical profilometer provided by Sensofar®. Figure 2-19 shows a resulting dent observed on the steel surface and a resulted deformed particle recover in the oil tank.

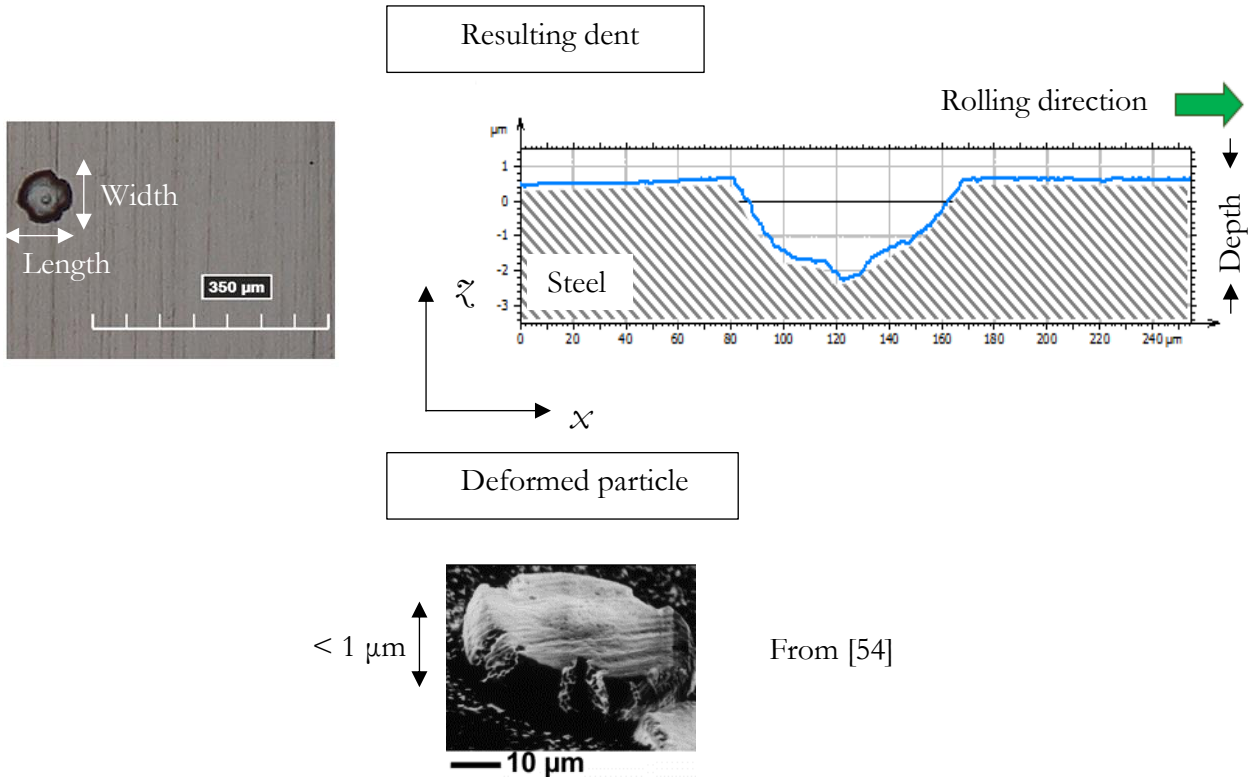

Figure 2-19: Dent on steel surface and related profile in an all-steel case

The dent is characterized by its size, length and width, its depth as well as its slope corresponding to the depth/width ratio. This last parameter is often considered as a key one to quantify the indentation level and thus the risk of premature RCF (see chapter 1), as mentioned by Coulon [114].

2.3.2 Ball-on-disc machine with fluorescence technique

2.3.2.1 Description of the test rig

The ball-on-disc tribometer called "Jerotrib" [32] aimed at reproducing rolling and rolling–sliding contacts within a large rolling speed range (0.005–6 m/s), with different materials (disc and balls in steel, glass, sapphire, etc.) and with different geometries (spherical or barrel samples).

This machine enables friction measurements as well as interferometric measurement of film thickness in the range of 0–800 nm. Figure 2-20 reports a typical film thickness distribution that could be obtained within a dynamical glass–steel contact for the following operating conditions 26 N – 2.5 m/s.

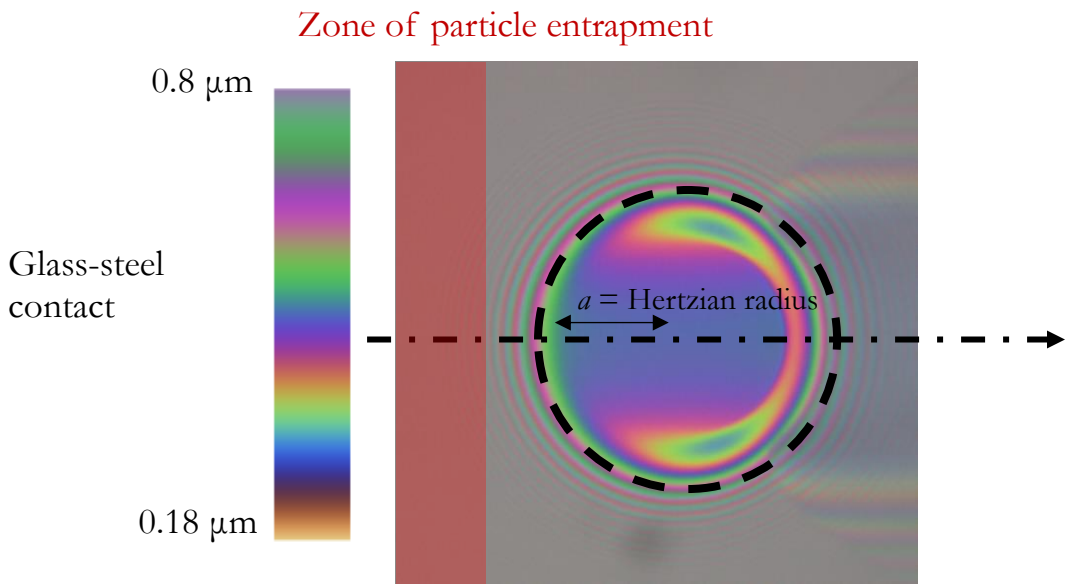

Figure 2-20: Typical film thickness distribution for a steel–glass dynamical contact with a 26N-load and 2.5 m/s rolling speed

The interferometric technique appears not to be appropriate for a direct observation of entrapment phenomenon as the technique enables only to give information for thin films and so in the Hertzian zone. Solid contaminants being particles of tens of microns (10–40 μm), they are caught inevitably further upstream in the contact inlet rather than in the Hertzian zone and another technique is needed.

This test rig stays however a convenient facility to simulate EHD contact and getting in-situ visualization of the lubricant meniscus. As the microscope has a degree of freedom around the $\vec{x}$-axis, it enables the observation of the contact inlet as represented in Figure 2-21.

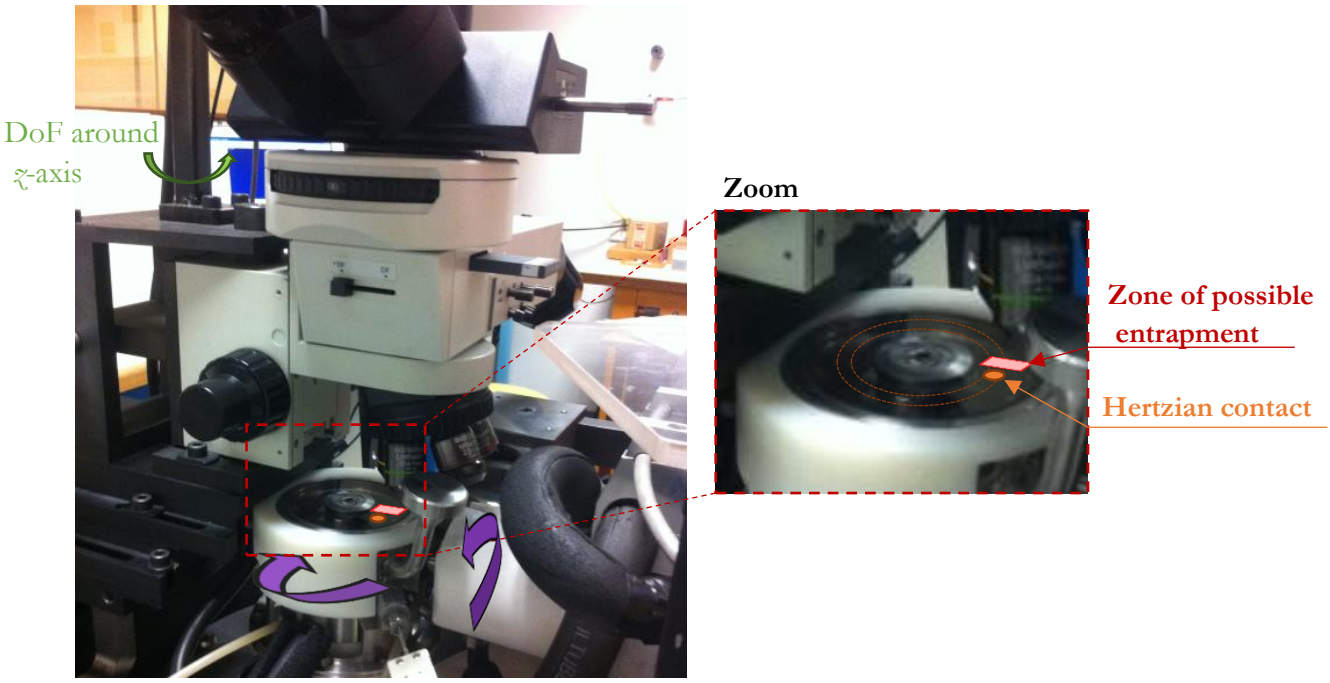

Figure 2-21: Ball-on-disc tribometer composed of tribological part (ball-on-disc device) and an observation device (microscope and related camera)

In-situ methods require a transparent disc and the most common transparent materials are glass or sapphire. In the frame of this study, a PYREX® glass was used. The balls were machined from AISI 52100 steel and are of different shapes. Table 2-5 reports the material properties of the rotating specimens.

	AISI 52100	PYREX®
Young modulus [GPa]	210	64
Poisson ratio	0.3	0.2
Hardness	HRC 64	Knoop Hardness [kg/mm^2] 418
Density [kg/m^3]	7800	2230

Table 2-5: Properties of the rotating counterparts of the ball-on-disc machine

The different geometries of the specimens are presented in Table 2-6, with R_x and R_y the radius along the rolling direction and the transverse one, respectively. These different configurations aimed at reproducing point contacts of different ellipticity ratios.

Type of contact	Circular	Elliptical	
R_x [mm]	12.7	13.1	13
R_y [mm]	12.7	84.2	330
W [N]	10	50	50
a [µm]	124	151	115
b [µm]	124	513	920
k	1.00	3.46	8.02
P_h [MPa]	312	307	226

Table 2-6: Different geometries and related parameters resulting from the contact between a steel ball or a steel barrel and a glass disc

The test rig is lubricated by the ball which dips in a commercial oil, Shell T9. The µ-PIV analysis was performed for qualitative comparison purpose. At room temperature (20 °C) where this test was carried on, the viscosity of Shell T9 presents the same value (12 mPa·s, see [115]) as the Nycobase one at 60 °C where twin-disc tests were run.

2.3.2.2 Fluorescence and µ-PIV technique applied to EHD contacts

For many years Particle Image Velocimetry (PIV) has been a way to measure and control flows in diverse applications [116–118]. To investigate faster flows, flows in smaller channels (µ-PIV), or non-conventional fluids, this technique had to be adapted for each type of fluid applications. For example, Bair [119] using an incandescent source, studied the limiting shear stress phenomenon by observing in the focal plane the motion of glass spheres. With the development of fluorescence microscopes, many studies used fluorescent dye particles to investigate the contact properties. Ponjavic et al. [120] used fluorescence to analyze velocity profiles through the lubricant thickness and Albahrani investigated CdSe Quantum Dots [121] to map pressure and temperature distribution within EHD contact.

The use of fluid mechanics techniques for the investigation of tribological problems enables to get new type of information on oil or grease behaviors as well as a way to observe directly the additives or contamination particles that might be carried within EHD contacts. Horvat and Braun [122] used PIV to study specific flow in hydrostatic bearings. Li et al. [123] obtained the velocity profiles in different restrictions. Reddyhoff et al. [124] used the fluorescence technique for the first time in EHL to catch film thickness variations and to characterize oil starvation risks.

2.3.2.3 Triplet (fluid tracers/light source/recording device) for PIV measurements

Using an adequate triplet of buoyant particles, appropriate lighting source, adapted recording and analyzing device, it becomes possible to track the motion of particle tracers and thus to determine the characteristics of any type of flow.

Fluid tracers

Fluorescent particles were chosen as fluid tracers for this study. They are part of a commercial paint provided by Lefranc & Bourgeois®: the red fire fluo paint. The fluorescent particles are made of rhodamine pigments embedded in a melamine-formaldehyde-sulfomanide copolymer. Rhodamine is known to react inelastically to a laser excitation: for a laser excitation of wavelength at 532 nm, an induced emission is recorded around 570 nm [118,125]. Figure 2-22 gives the size distribution of the particles composing the paint.

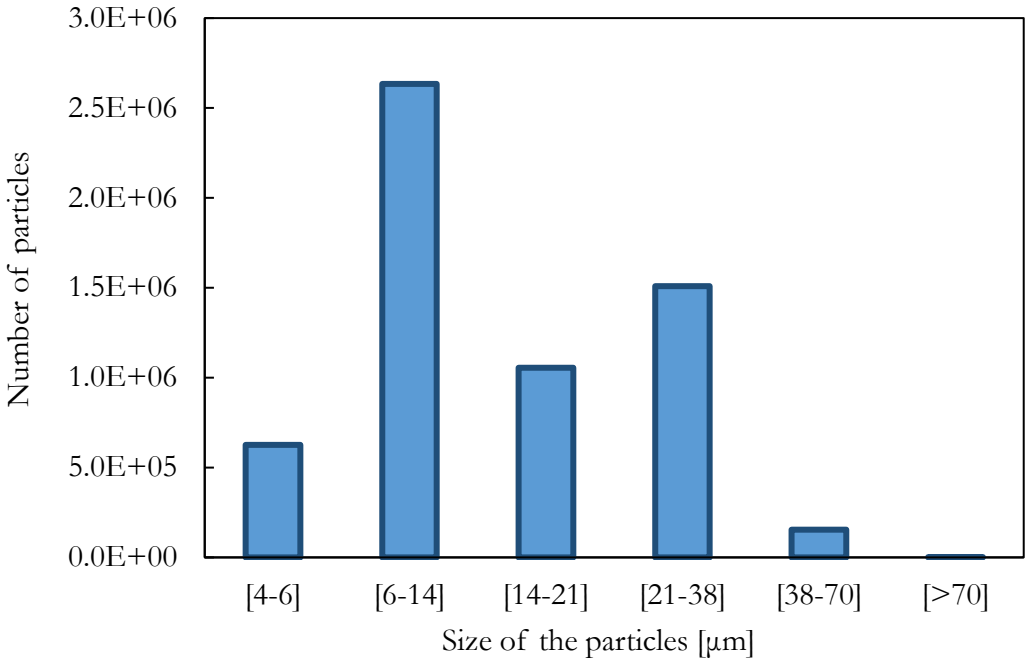

Figure 2-22: Size distribution of the rhodamine tracers composing the red fire fluo paint provided by Lefranc et Bourgeois®

The mean size of the fluorescent particles is 6 µm. The size distribution was obtained by performing a particle counting with a light absorption technique (at Institut de la Filtration et des Techniques Séparatives). The analyzed liquid solution contained 199 ml of lubricant Shell T9, 0.5 ml of diluted red fire fluo paint in 0.5 ml of ethanol.

The density of the paint is 1080 kg/m^3 at 20°C that is why the sedimentation time has to be compared to the other characteristic times of the flow. The steady-state settling velocity is given by Tropea et al. [126]. Assuming seeding particles of 3 µm in mean radius, their settling velocity is 0.3 µm/s. As the range of rolling speeds is 0.005–6 m/s, the particles will have no time to settle and the rhodamine particles can be used as fluid tracers.

Light source

Two pulsed Nd:YAG lasers available from Quantel® (532 nm, 150 mJ) ensure the illumination source and are guided toward the test-rig through an illumination guidance stick, composed of mirrors. Figure 2-23 shows the tribometer test-rig coupled with the PIV system.

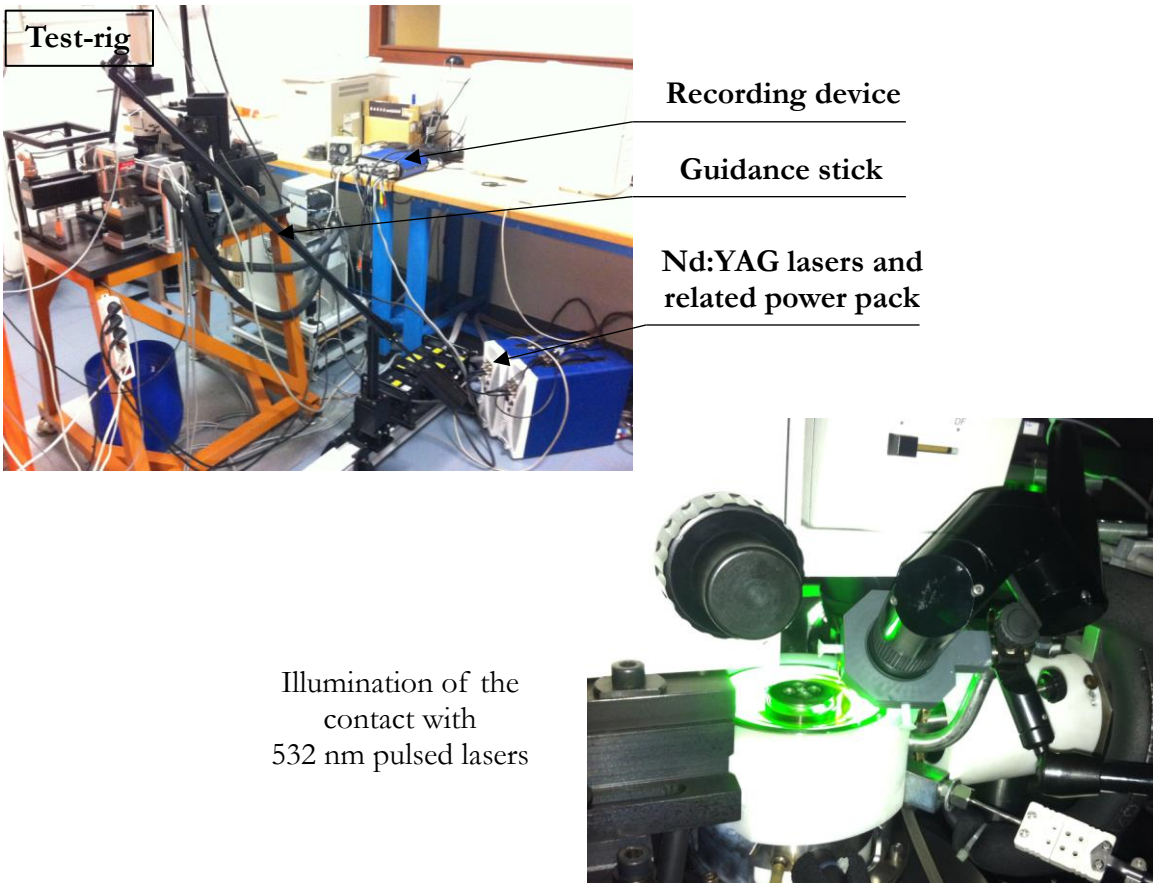

Figure 2-23: Ball-on-disc test-rig coupled with PIV system composed of an illumination source/guidance stick/recording device

The lasers are synchronized together in order to provide one pulse t_0 and a second one $t_0+\Delta t$ (see Figure 2-25) in order to apply PIV analysis on the recorded images.

Recording and analyzing device

A camera (Megaplus ES 1.0) with 1008 x 1018 pixels is used to record microscope pictures. A Davis analyzing system from the LaVision® Company is used to analyze the fluid tracers trajectories. Different optical objectives, provided by Olympus®, were used during the tests. Table 2-7 reports the size of the observed fluid domain according to the selected objective.

Objective	Size [mm]	Depth of focus [µm]
x5	3.610 x 3.640	58.9
x10	1.805 x 1.820 mm	14.7
x20	0.9025 x 0.9100 mm	5.10

Table 2-7: Size of the observed fluid domain with the different microscope objectives

The use of different objectives changes the focus depth of observations. But whatever these objectives are, no clear discrimination could be made across the thickness as the focus depth is thicker than 5 µm. The inlet gap being of 10–100 µm, the observations are made by considering that the system is focused at mid-height of the gap thickness (see Appendix B).

A FB-570-10 band-pass filter (570 nm, FWHM 10 nm) is introduced in the optical path between the illuminated zone and the camera that is focused on the contact, in order to capture the fluorescence lighting only and to ignore the source as well as all others parasitic lightings. Figure 2-24 reports a schematic diagram of the test-rig coupled with the PIV system.

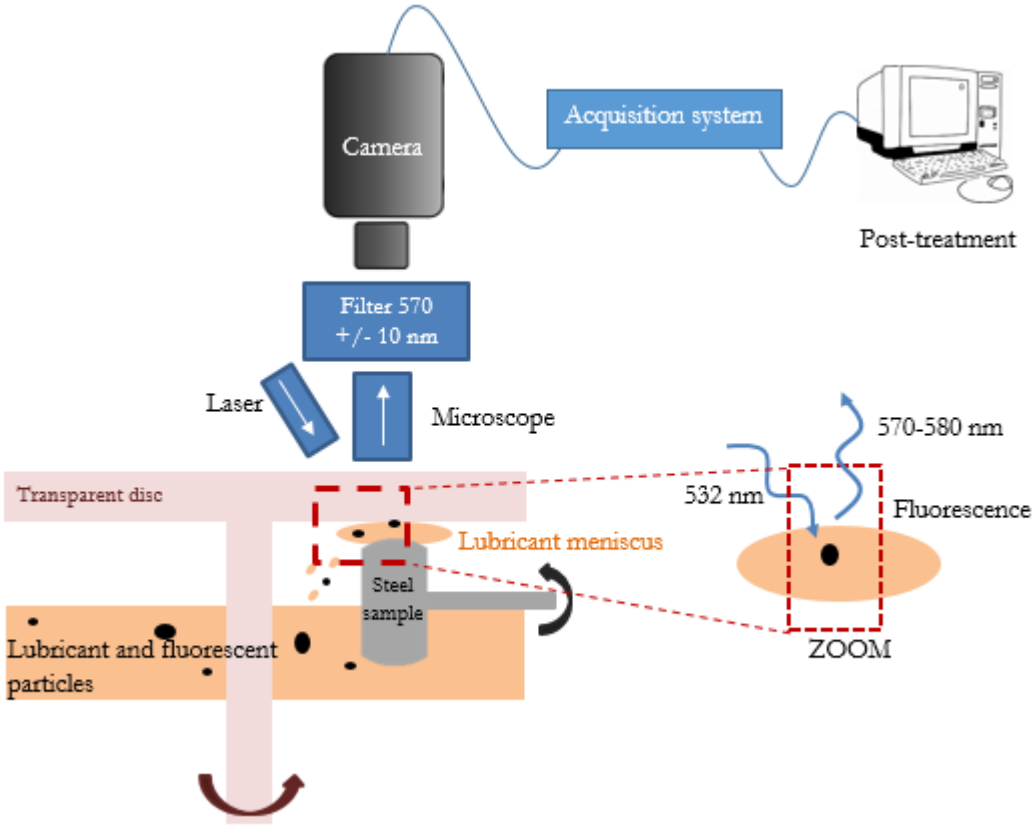

Figure 2-24: Ball-on-disc machine coupled with the PIV system

As depicted previously, the two rotating counterparts composed of a glass disc and a steel sample (ball or barrel) are set in contact and lubricated by the ball which dips in the oil reservoir. As the

fluorescent particles are diluted in the lubricant, once having been entrained in the contact inlet and illuminated by the laser light, from induced fluorescence, particles give information on the fluid flow.

2.3.2.4 Procedure

The lubricating solution introduced in the tribometer is composed of 25 ml of the T9 oil mixed with 1 ml ethanol and 1 g of paint in order to ensure a homogeneous dispersion.

The coupling of two pulsed laser sources provides different possibilities to visualize the flow behavior. The pulsed lasers light sequentially which stimulate the fluorescent particles. The pulses are synchronized together in order to adjust Δt, the time between the two laser pulses (pulse A and pulse B on Figure 2-25) and T_S, related to the sequential frequency of lighting, imposed here by the laser frequency f. Lasers are also synchronized with the CCD camera to capture particle motions on two separate pictures.

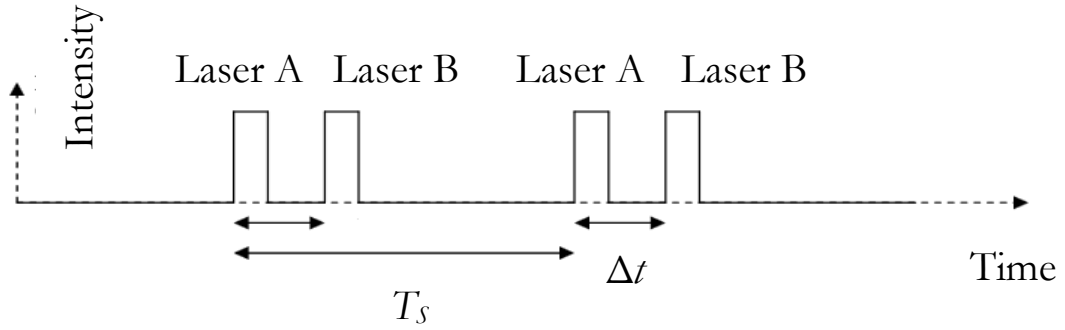

Figure 2-25: Principle of synchronized pulsed lasers

Given the sequential lighting ($T_S = 1/f$), transient observations of the particles' motion, also called particle tracking, can be performed. All along the stay of the particles in the camera frame, if T_S is low enough compared to the velocity time scale, the sequential lasers shots enable to obtain the particle trajectories by tracking the particle positions.

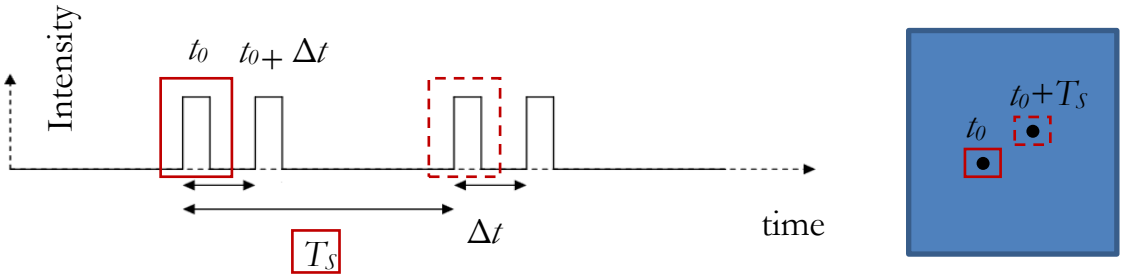

Figure 2-26: Sequential illumination of the fluid domain for performing particle tracking

As laser frequency *f* is linked to their laser charging time, it cannot exceed 15 Hz. Nevertheless, by adapting the synchronization time (Δt) between the two laser pulses in a range varying from some µs to few ms, it allows to establish the velocity field with classical PIV method. A suitable synchronization time, Δt, gives two positions of the seeded particles. If the camera is able to capture each light pulse in separate image frames, using a cross-correlation algorithm on subdivided sections of the recorded images, instantaneous velocity vectors can be plotted. The mesh size gives the spatial resolution of the technique out of the laser sheet thickness. The principle of PIV measurements is recalled in Figure 2-27, provided by the company Dantec Dynamics® [127].

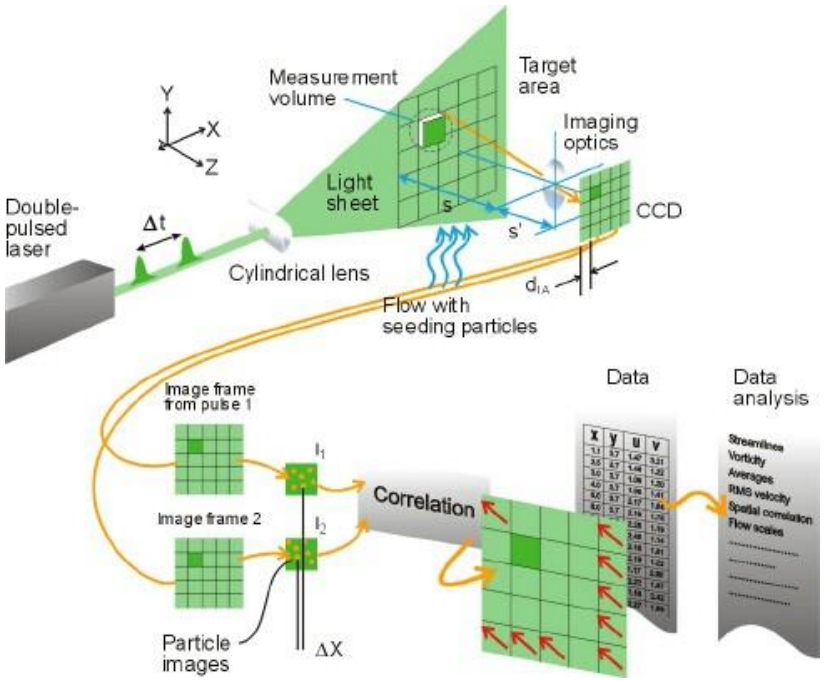

Figure 2-27: Principle of the PIV analysis [127]

This technique relies hence on the synchronization time Δt and on the post-treatment of the particles positions. Considering a mean rolling speed $U_m=U_1+U_2/2$, PIV measurements necessitates the record of a small displacement. In the present study, a displacement over roughly ten pixels (for an analysis mesh size of 32 pixels) is imposed, so that the synchronization time can be defined by (2-20):

$$\Delta t \geq \frac{10\dfrac{\Delta X}{N_{pix,X}}}{U_m} \qquad (2\text{-}20)$$

With ΔX the size of the camera image in the *x*-direction, $N_{pix,X}$ the number of pixels of the camera along the *x*-direction and U_m the mean rolling speed. Table 2-8 reports the correlation between

imposed rolling speeds varying from 0.005 to 3 m/s and synchronization times suitable for allowing PIV analyses.

Rolling Speed [m/s]	0.005	0.01	0.02	0.04	0.1	0.2	1.5	3
Time Δt [µs]	10000	5000	2000	1000	500	200	20	10

Table 2-8: Correlation between rolling speed and synchronization time

According to these synchronization times, the lasers A and B light alternately the lubricant meniscus which enable to determine a mapping of the velocity vectors.

2.4 Conclusion

This chapter presented the different investigation tools that will be used to study particle entrapment mechanisms within EHD contacts. The numerical model with a FEM based resolution enables to describe the lubricant flow. On this basis, trajectories of suspended particles are solved with the resolution of forces equilibrium. The experimental facilities enable to reproduce entrapment condition in highly loaded contacts or to get an in-situ visualization of entrapment in a glass–steel contact, respectively. Hence, a wide number of EHD contact configurations can be reproduced.

The analyses are carried out with dispersed contaminants in solution. It is ensured by few mg/l solid contaminants and numerically with a single contaminant particle considered at a time. Table 2-9 reports the parameters of the EHD contacts that will be analyzed, depending on the simulation numerical/ experimental tools.

Simulation tool	Numerical model	Twin-disc machine	Ball-on-disc machine
Curvature radii [mm]	17.5	17.5	12.7–13.1
Ellipticity ratio	1–2.5	1–4.88	1–8.1
Materials	All-steel / Si_3N_4–steel / glass–steel	All-steel / Si_3N_4–steel	Glass–steel
Rolling speed [m/s]	up to 30	22	up to 3
Hertzian pressure [GPa]	up to 2	up to 2	up to 0.35
SRR [%]	0 / 12	0 / 12	0

Table 2-9: Range of parameters for the EHD contacts simulated with the different numerical/ experimental tools

Simulation outputs will be compared with experimental results to validate numerical assumptions. Moreover, tendencies observed experimentally on the twin-disc machine will be compared to tests carried out on the ball-on-disc machine and analyzed numerically.

In the next chapter, a phenomenological approach on particle entrapment in EHD classical steel–steel contacts is proposed. The use of numerical simulations and tests on the two test-rigs enable an investigation of key parameters leading to entrapment.

Chapter 3 Particle entrapment in circular contacts

3.1 Introduction

Contamination sources are various, as presented in previous chapters. However once in the lubrication medium, the contaminants are likely to travel on their own and be carried wherever the lubricant is spread within REBs.

In this work, it will be assumed that particles enter a single rolling element/ring contact. The goal is to estimate the probability of particles to be entrapped within the contact.

The aim of this chapter is to present a phenomenological approach of particle entrapment within circular contacts. First, the mechanisms leading to entrapment are investigated through in-situ tracking using the fluorescence technique applied to particles entrained in an EHD circular contact. This qualitative approach is completed by a dual analysis which combines numerical simulation tool and experimental tests on the twin-disc machine under contaminated lubrication. It aims at investigating key parameters leading to entrapment, linked either to the critical positions of the particle at the contact inlet or to the intrinsic particle properties (size, material).

3.2 Particle entrapment visualization using fluorescence technique

Occurring at the micrometric scale and within few milliseconds, particle entrapment is a tribological phenomenon which is hard to capture. Many attempts proposed to use the interferometric technique on a ball-on-disc machine to observe particle entrapment (see chapter 1) [17]. However, as explained in chapter 2, this experimental approach does not allow to focus on the contact inlet and thus, is not able to apprehend upstream phenomena such as particle entrapment. Here, a visualization of the process of entrapment is proposed using the fluorescence technique.

3.2.1 Entrapment visualization

The in-house tribometer, is used in a steel-glass configuration under pure rolling conditions. The PYREX® glass disc provides a transparent interface and is in contact with a AISI 52100 steel spherical ball. Table 3-1 reports operating conditions.

Materials	52100 steel / PYREX® glass
Contact	Circular (ball sample)
Load [N]	10
Mean rolling speed [m/s]	0.005

Table 3-1: Contact parameters for particle entrapment tests

Hence, focusing the microscope on the inlet region enables to get a direct insight in upstream phenomena. The aim of this test is to visualize the entrapment of debris-like particles. M50 steel particles, also used in tests under contaminated lubrication on the twin-disc machine, are used for this

purpose: they were mixed with a fluorescent paint to make them observable through the fluorescence technique. Figure 3-1 is a microscope picture of the mixture made with steel particles and fluorescent paint.

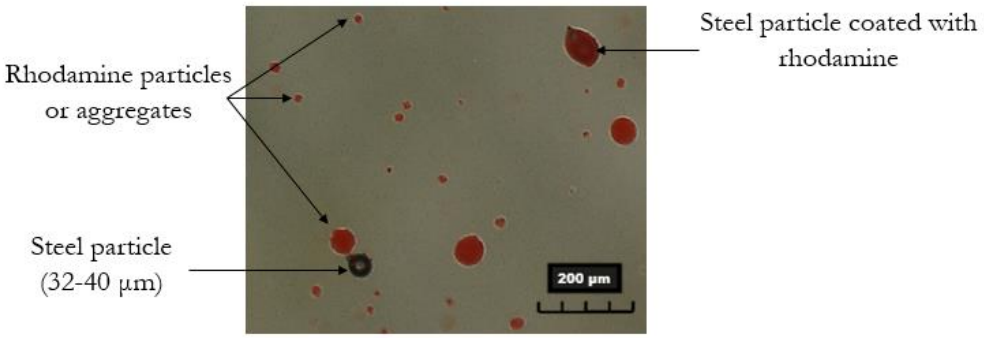

Figure 3-1: Rhodamine particles from Lefranc & Bourgeois® (paint red fire fluo) mixed with sieved M50 steel particles (in the range 32–40 µm) observed with an optical microscope

It appears that some of the spherical steel particles have become "coated" with fluorescent paint which will allow to follow the motion with the fluorescence method, whereas others are simply diluted in the lubricant solution and thus will stay not detectable. By illuminating sequentially the lubricant meniscus upstream the contact inlet, trajectories of coated steel particles are revealed by the fluorescence emission, as soon as they remain in the focus range of the objective.

The use of pulsed lasers allowed to impose a maximum sequential frequency of 15 Hz ($1/f$ = 0.066 s) which forces to use low rolling speed (0.005 m/s in the present work) to perform particle tracking.

Figure 3-2 – (b) represents a series of 6 successive pictures which clearly show the entrapment of a single steel particle. Film thickness indications (dotted lines), calculated using an in-house simulation tool applied to the glass–steel contact [29,83] are plotted (Figure 3-2 – (a)). They correspond to the minimum and maximum steel particle diameters used in this study. The Hertzian zone is represented with a striped circle. A white dotted circle is plotted around the steel particle to improve the tracking.

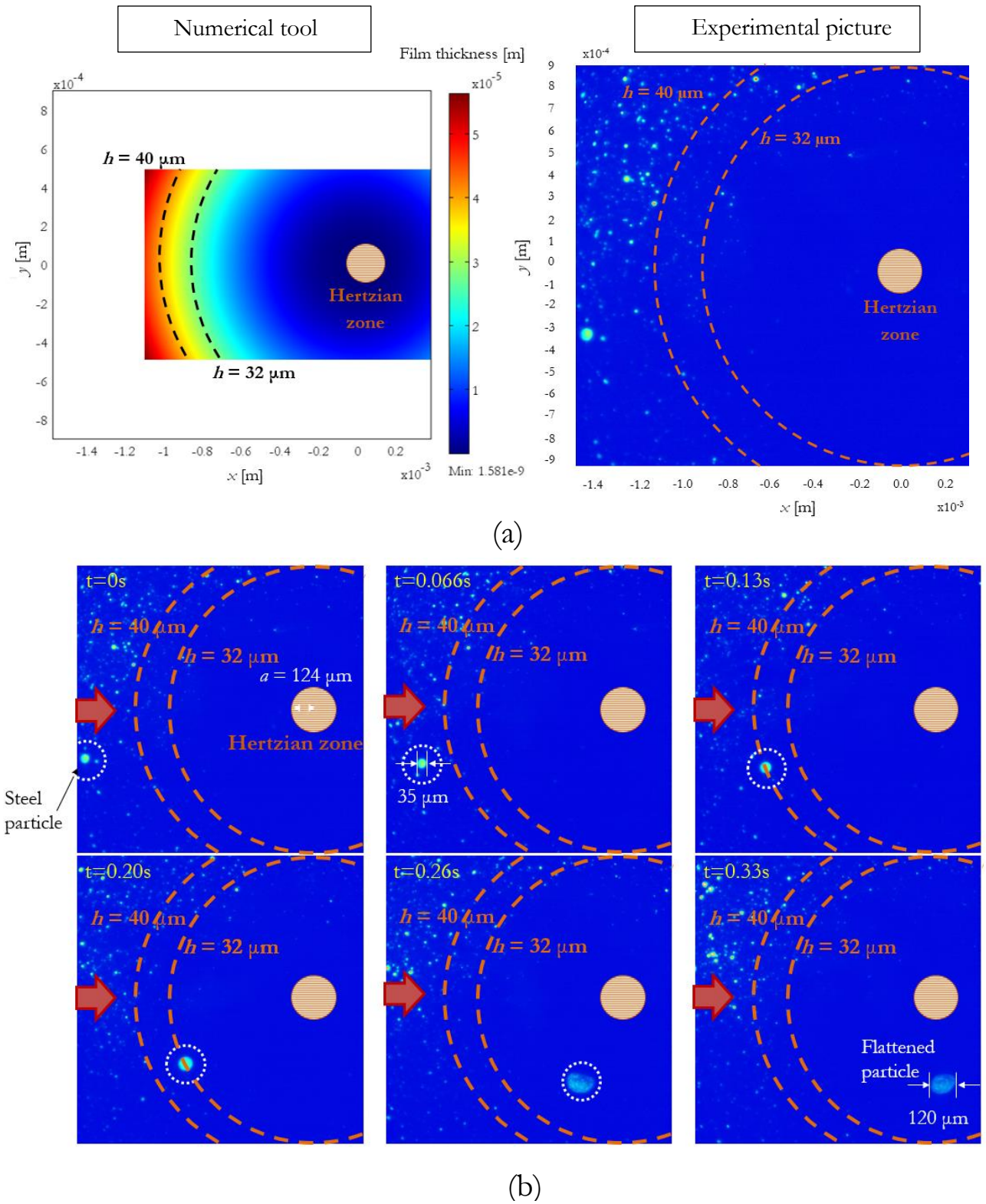

Figure 3-2: Visualization of particle entrapment in a steel-glass contact
(5 mm/s; 10N; optical x10 objective -field size of 1.805 x 1.820 mm):
- (a, left) film thickness distribution obtained with numerical model; (a, right) picture of the contact
- (b) series of 6 successive pictures taken between t = 0 s and t = 0.33 s

Discrimination between steel particles and rhodamine ones clearly appears as the sizes are totally different. The steel ones are in the range from 32 to 40 µm whereas the mean diameter of rhodamine particles contained in the fluorescent paint is 6 µm (see chapter 2).

The process of entrapment follows here an obvious sequence. On the three first pictures of Figure 3-2, the steel particle is carried by the fluid until it reaches a film thickness close to its diameter. Once entrapped, between t=0.13 s (3rd picture) and t=0.20 s (4th picture), the particle is deformed. On the two last pictures, the particle is moving forward, entrained by the friction forces imposed by the contacting surfaces.

As the tracked debris-like particle is made of M50 steel, it is ductile and is deformed in the contact, as explained by Dwyer-Joyce [55]. Hence the process of entrapment and deformation are consistent with the expectations. Moreover, the final size of the particle is roughly elliptical about 120 µm x 100 µm (length x width). Considering that the particle diameter is initially of 35 µm, leading to a volume of $2.24 \cdot 10^{-14}$ m^3, the film thickness at this final particle position at t=0.26 s (400 µm off-axis from the Hertzian contact center) must be of approximately 2 µm, which is consistent with a numerical prediction of the film thickness in the corresponding area.

Finally, this visualization enables to follow in-situ the tracking of one particle, which was critically entrained in the contact inlet as postulated by many authors in the literature [18,22,55] and which can then be entrapped between the two contacting surfaces, as represented in Figure 3-3.

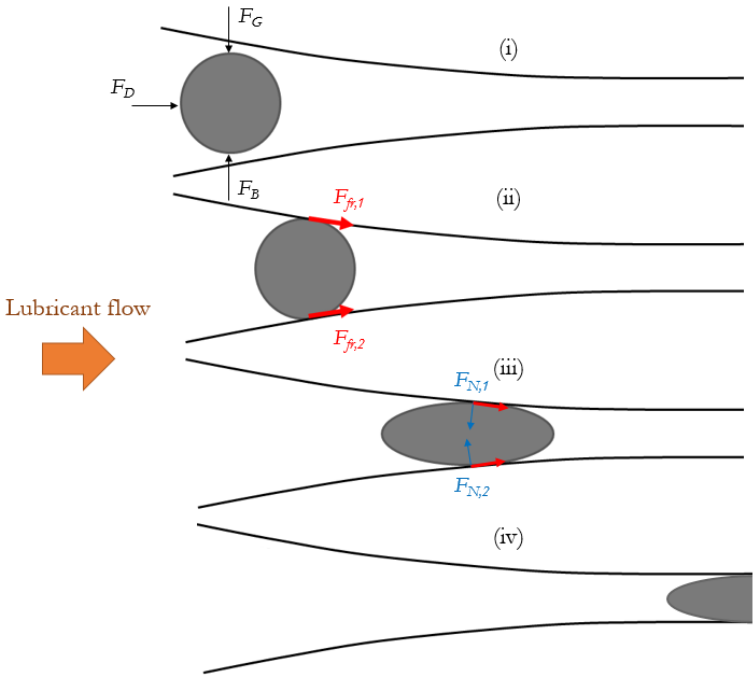

Figure 3-3: Section view of an EHD contact with process leading to particle entrapment

This figure represents the four-step mechanism of particle entrapment phenomenon:

(i) The particle is carried by the fluid within the contact inlet;
(ii) It is trapped within the rolling surfaces and entrained by frictional forces, $F_{fr,i}$;

(iii) It is deformed between contacting surfaces under the effect of the normal forces, $F_{N,i}$;
(iv) The particle is passing through the contact.

Finally, the particle entrapment results from a critical position in the contact inlet. It has to be noticed that entrapment may also occur slightly off-axis of the Hertzian zone as represented in the pictures of Figure 3-2.

The aim of the next section is to understand the critical entrainment of particles in the contact inlet through the analysis of the lubricant velocity field.

3.2.2 Velocity vectors mapping

To obtain a mapping of the velocity vectors in the vicinity of an EHD contact, further tests on the ball-on-disc machine were performed. This time, the lubricant is seeded with only rhodamine particles which allow to follow the fluid flow (see chapter 2). As the lubrication problem is stationary here, by illuminating periodically the lubricant meniscus with two lasers, small displacements of the tracers can be followed. Thus, velocity vectors between successive closed positions can be determined.

The mapping of velocity vectors is obtained by performing a PIV analysis on successive image pairs (related to the synchronized illumination by lasers A and B) recorded by the camera. An average of the velocity field is made over 100 images to obtain a unique mapping of the stationary flow. Figure 3-4 and Figure 3-5 show the mapping obtained for two contacts with two different rolling speeds: 0.005 m/s and 0.5 m/s. The Hertzian contact zone is represented by a striped circle. A black zone around the contact is excluded from the representation as there is too few particles that enter this zone, and thus, a lack of information to perform a proper PIV analysis. Velocity vectors are plotted with white arrows of a length proportional to speed value.

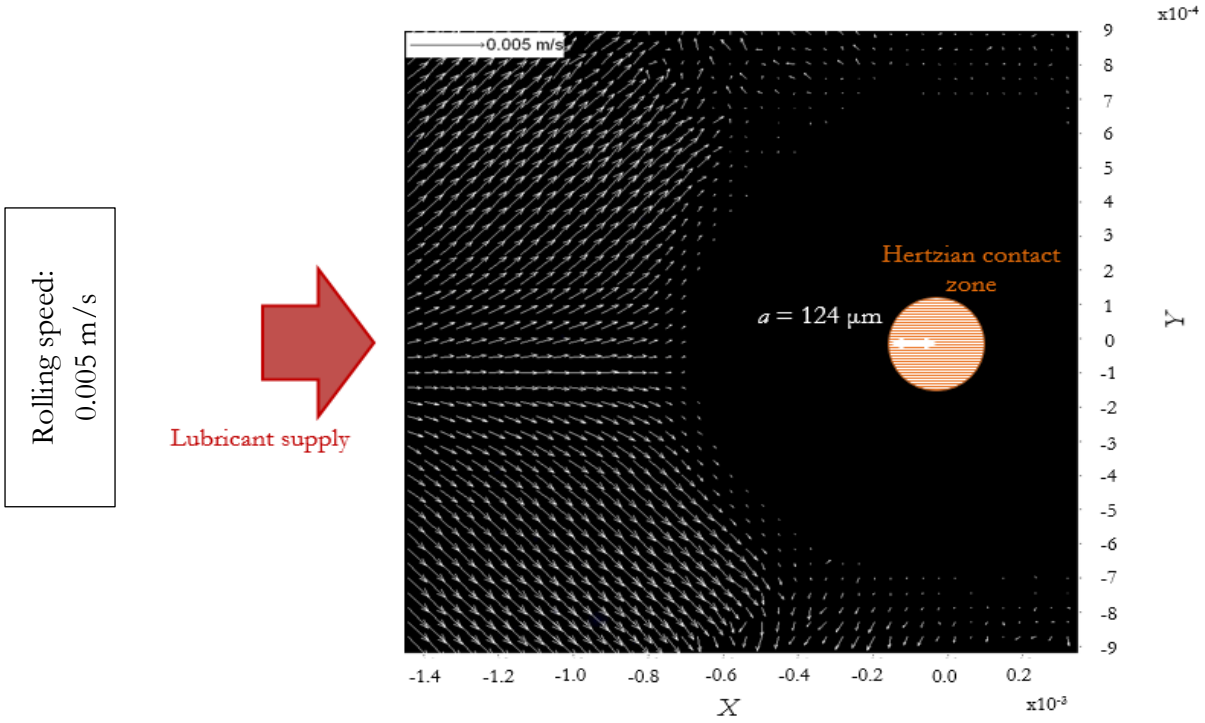

Figure 3-4: Mapping of the mean velocity field from a PIV analysis for a circular steel-glass contact with operating conditions: 0.005 m/s – 10 N

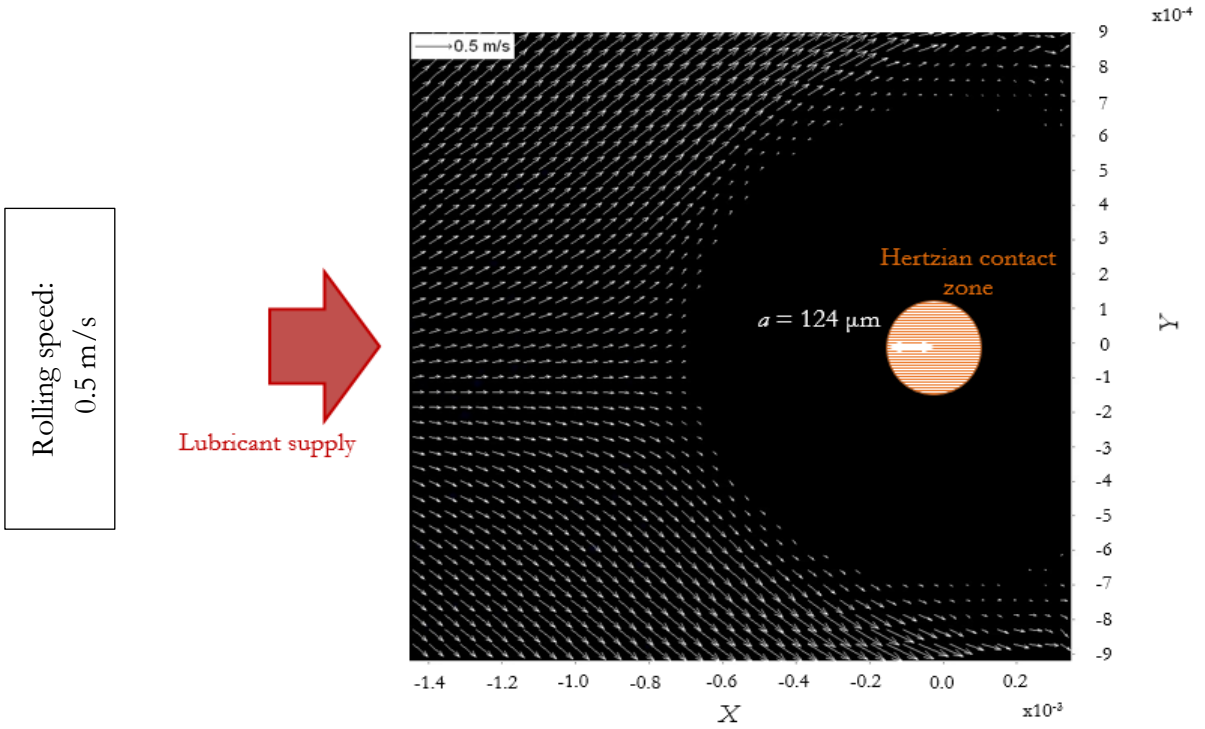

Figure 3-5: Mapping of the mean velocity field from a PIV analysis for a circular steel-glass contact with operating conditions: 0.5 m/s – 10 N

These two velocity vector maps of lubricated contacts submitted to different rolling speeds provide evidence of the feasibility to perform PIV analyses within EHD contacts. Moreover, they can be compared to results from numerical simulations as shown in Appendix B, and thus serve as a qualitative validation step for the numerical model.

It appears that a large amount of lubricant is bypassing the contact. The two figures also show that the lubricant slows down upstream the Hertzian zone, along the contact center and accelerates once located besides the contact. Figures reveal that only a low proportion of lubricant is carried towards the contact, which corresponds in the contact inlet to a very thin section. The mapping obtained at very low rolling speed (0.005 m/s) is noisier than the one at 0.5 m/s, especially downstream, as there are fewer rhodamine particles dragged towards the contact.

This behavior is consistent with Hsiao et al. [128] who proposed a numerical evaluation of the flow in EHD contacts by analyzing streamlines. They underlined the presence of strong side-flows leading to about only 5 % of the lubricant which passes through the Hertzian contact zone.

Hence, a large amount of fluid is bypassing the circular contacts. The important side-flows must inevitably affect the mechanisms of particle entrapment. Thus, in next section, particle positions in the contact inlet are linked to entrapment probability.

3.3 Particle release position and operating conditions influence

Debris-like particles are homogeneously dispersed in the lubricant at the contact inlet. Numerically, it is possible to impose the entry position of an individual particle approaching the EHD contact.

Release position (*RP*) corresponds to the initial location of particle center of mass, when it is released into the fluid flow. As defined previously, particle initial velocity was set equal to the fluid one. Release positions were first considered along the *y*-axis (width) at the distance RP_y to the symmetry plane and at different heights (RP_z) across the inlet film thickness (Figure 3-6). These release positions were given in a $y\tilde{z}$-plane, fixed at the entry of the domain, at $RP_x = -6a$ from the contact center (see 2.2.1.2).

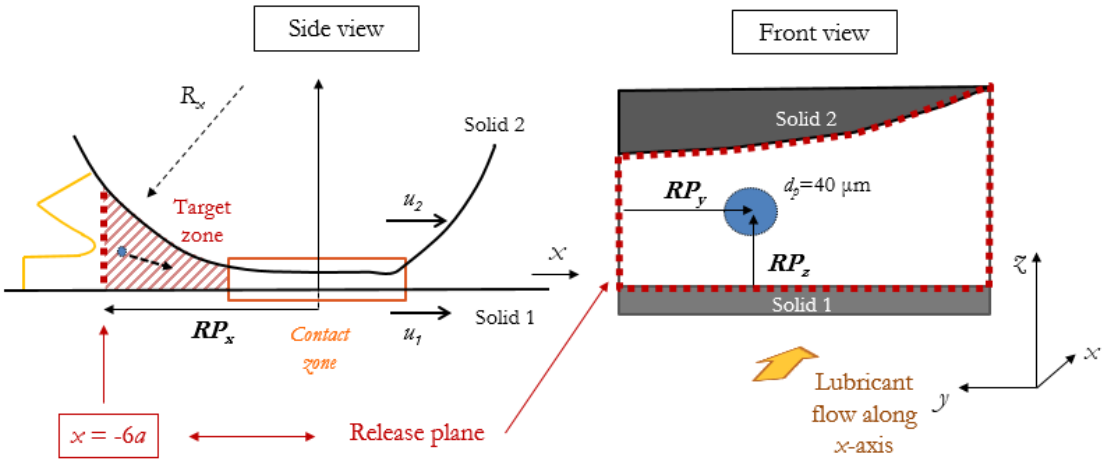

Figure 3-6: a) Side view of the fluid domain (illustration of the numerical fluid domain (striped area)); b) Front view of the release plane at $RP_x = -6a$ (release positions at the inlet boundary)

A first numerical case study [48], using operating conditions defined in Table 3-2, enables to give the release positions in the contact inlet that lead to entrapment.

Parameters	Operating conditions
Ball radius [mm]	17.5
Load [N]	600
Mean rolling speed [m/s] / [r/min]	22 / 6000
Lubricant	Nycobase 5750
Dynamic viscosity at 60°C [Pa·s]	0.012
Piezoviscosity coefficient [GPa^{-1}]	15
Steel Young modulus [GPa]	210
Steel Poisson ratio	0.3
Hertzian radius [µm]	409
Hertzian pressure [GPa]	1.7

Table 3-2: Operating conditions and contact parameters for a steel-steel contact

These operating conditions are representative of an EHD contact met in aeronautical domain (see chapter 2). It is modelled with an equivalent-reduced contact of radius equal to 17.5 mm.

Figure 3-7 reports the effect of different release positions which were tested. Some of them lead to entrapment and positions are represented by striped red circles. In the following figures, the striped red circles represent the farthest positions from the surfaces and the symmetry plane for which the particles are entrapped. It is important to notice that particles are entrapped in a zone, called entrapment area, which corresponds to an area in which film thickness is lower than the diameter of the considered particles (see chapter 2, definition of entrapment width). The Hertzian width is reported with an orange line.

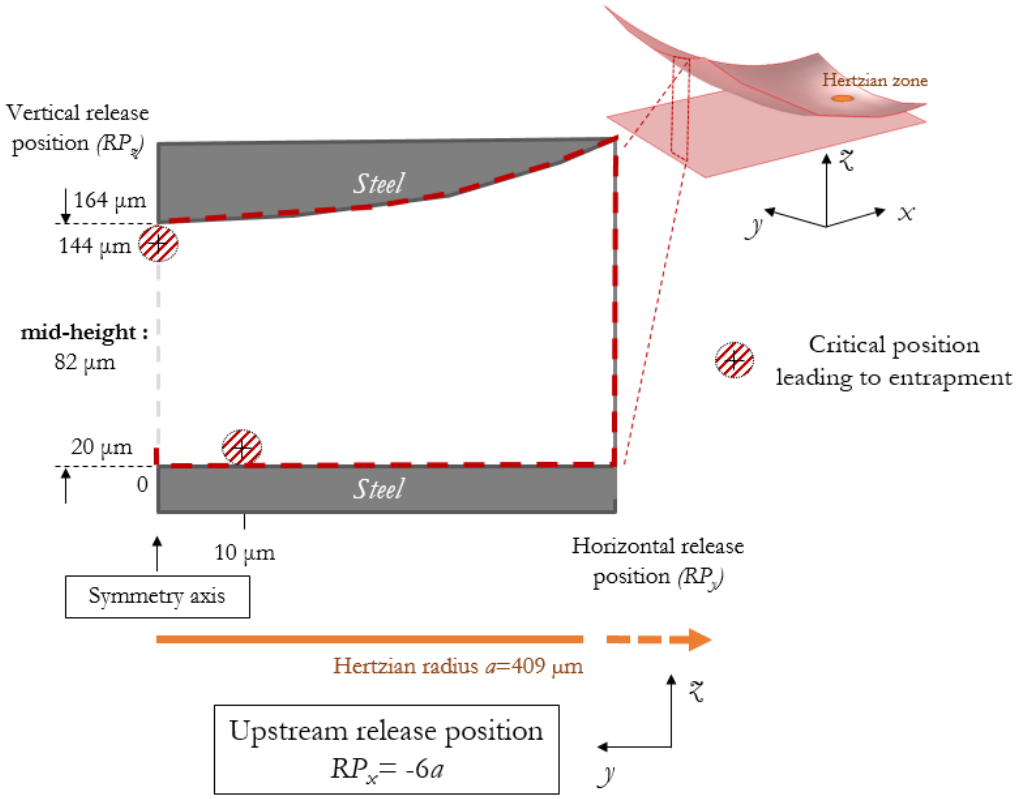

Figure 3-7: Mapping of particle entrapment according to release positions across the film thickness for steel–steel equivalent contact considering a 40 µm particle and using the conditions in Table 3-2 (striped red circles represent the farthest positions from the surfaces and the symmetry plane for which the particles are entrapped)

Particles nearer to the symmetry plane are more likely to be entrapped than other ones. Moreover, particles with an initial released position RP_y larger than 10 µm, inevitably bypassed the entrapment area under these conditions. Such phenomena were experimentally observed by Dwyer-Joyce and Heymer [19] and were explained numerically by Nikas [23], who introduced the concept of unconditionally rejected particles, for the ones approaching the contact area off-axis. It has to be noticed that a particle released at RP_y = 10 µm and RP_z = 144 µm bypasses also the entrapment area whereas for a same RP_y = 10 µm but a RP_z = 20 µm it passes through the contact. It is directly linked to the difference of curvature between the lower and upper surfaces and will be discussed hereafter with the mapping in a two-body symmetrical contact (Figure 3-9). Figure 3-7 also shows how the release position RP_z, across the film thickness, affected the probability for particle entrapment. It appears that for a released position RP_y = 10 µm, a particle in the mid-height of the flow will bypass the entrapment area, whereas particles released nearer to the lower surfaces, would be entrapped. It is due to the lubricant flow across film thickness.

Figure 3-8 represents fluid streamlines across the thickness on a xz-plane at y = -5 µm, close to the plane of symmetry. While the fluid located close to the surfaces is carried towards the contact zone, reverse flow occurred at the fluid mid-height. This feature explains why particles released closer to the surfaces were more likely to be carried towards the contact area.

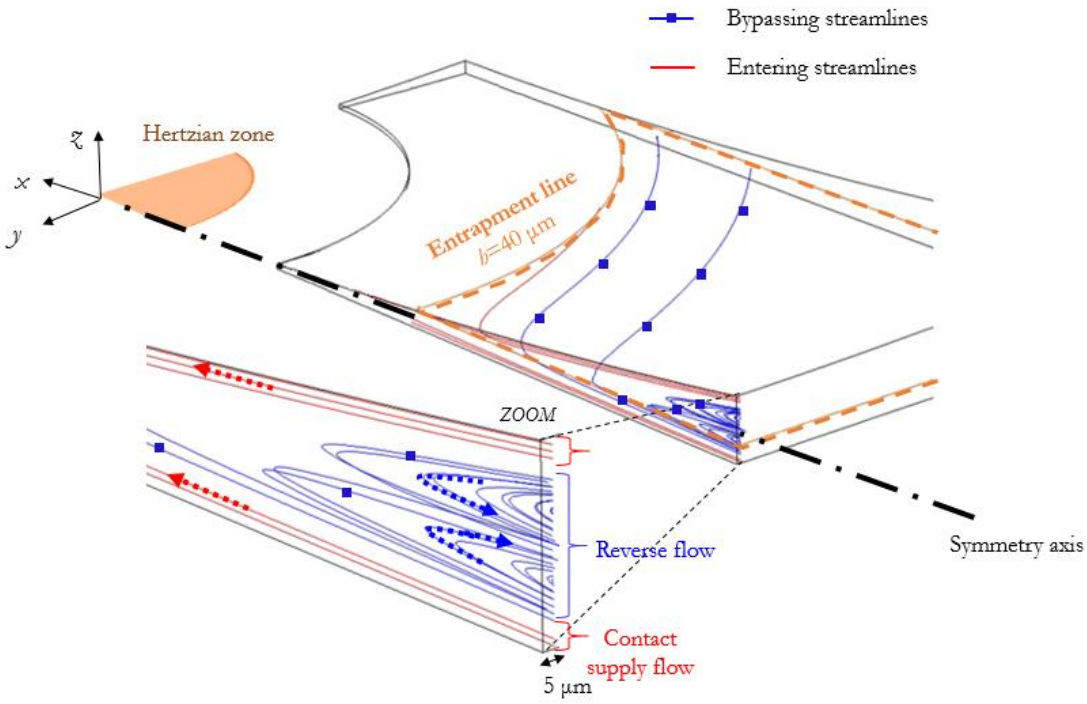

Figure 3-8: Streamlines for a fluid flow entering the domain
at x = -2.4 mm, y =-5 µm and $\Delta z = h_{in}$ = 164 µm (across the film thickness)
upstream from a steel–steel contact
(striped red circles represent the farthest positions from the surfaces and the symmetry plane
for which the particles are entrapped)

Considering the same study but with a two-body symmetrical steel–steel contact instead of an equivalent one (curved surface on plane), a symmetrical mapping is reported (Figure 3-9).

As previously (see Figure 3-7), particles nearer to the plane of symmetry are more likely to be entrapped than the ones released off-axis. In comparison to an equivalent reduced contact configuration, the initial release positions, RP_y, leading to entrapment are shifted towards the symmetry plane (8 µm instead of 10 µm).

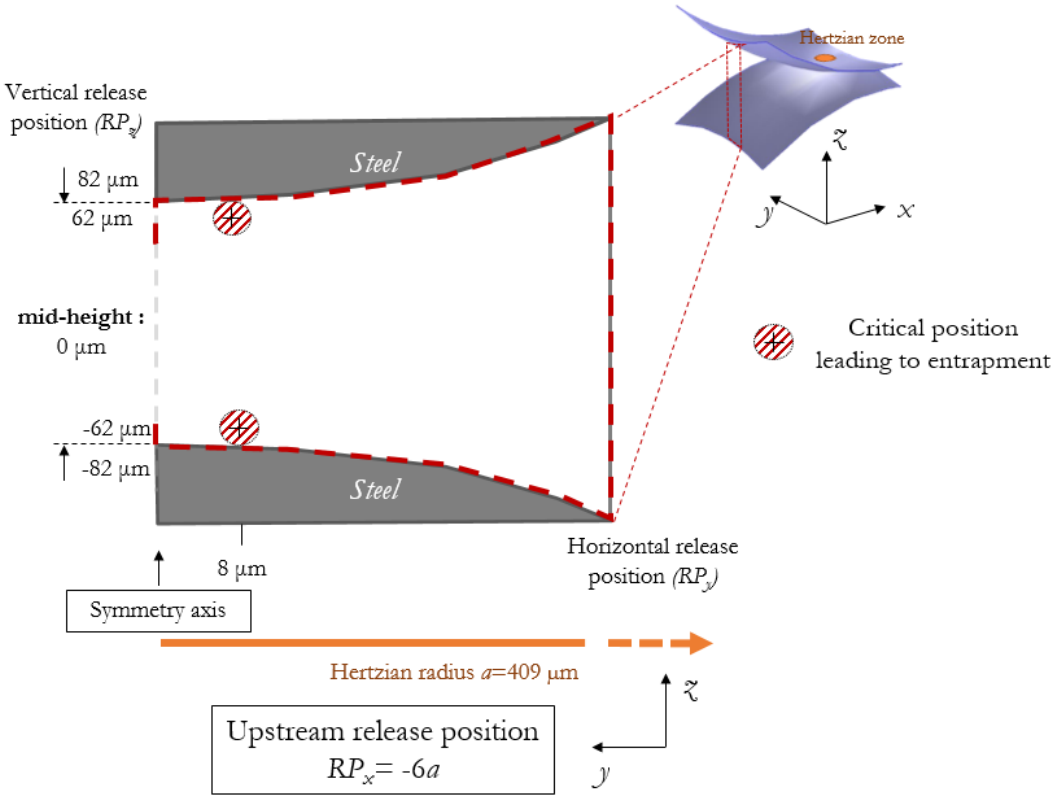

Figure 3-9: Mapping of particle entrapment according to release position across the film thickness for a symmetrical two-body steel–steel contact considering a 40 µm particle and using the conditions in Table 3-2 (striped red circles represent the farthest positions from the surfaces and the symmetry plane for which the particles are entrapped)

3.3.1 Rolling speed influence

To study mean rolling speed influence on particle entrapment, a series of numerical simulations were performed considering the same fluid domain as presented previously, with the same operating conditions given in Table 3-2 and three different mean rolling speeds fixed at 18, 22 and 30 m/s, respectively. Figure 3-10 reports mapping with release positions across the film thickness.

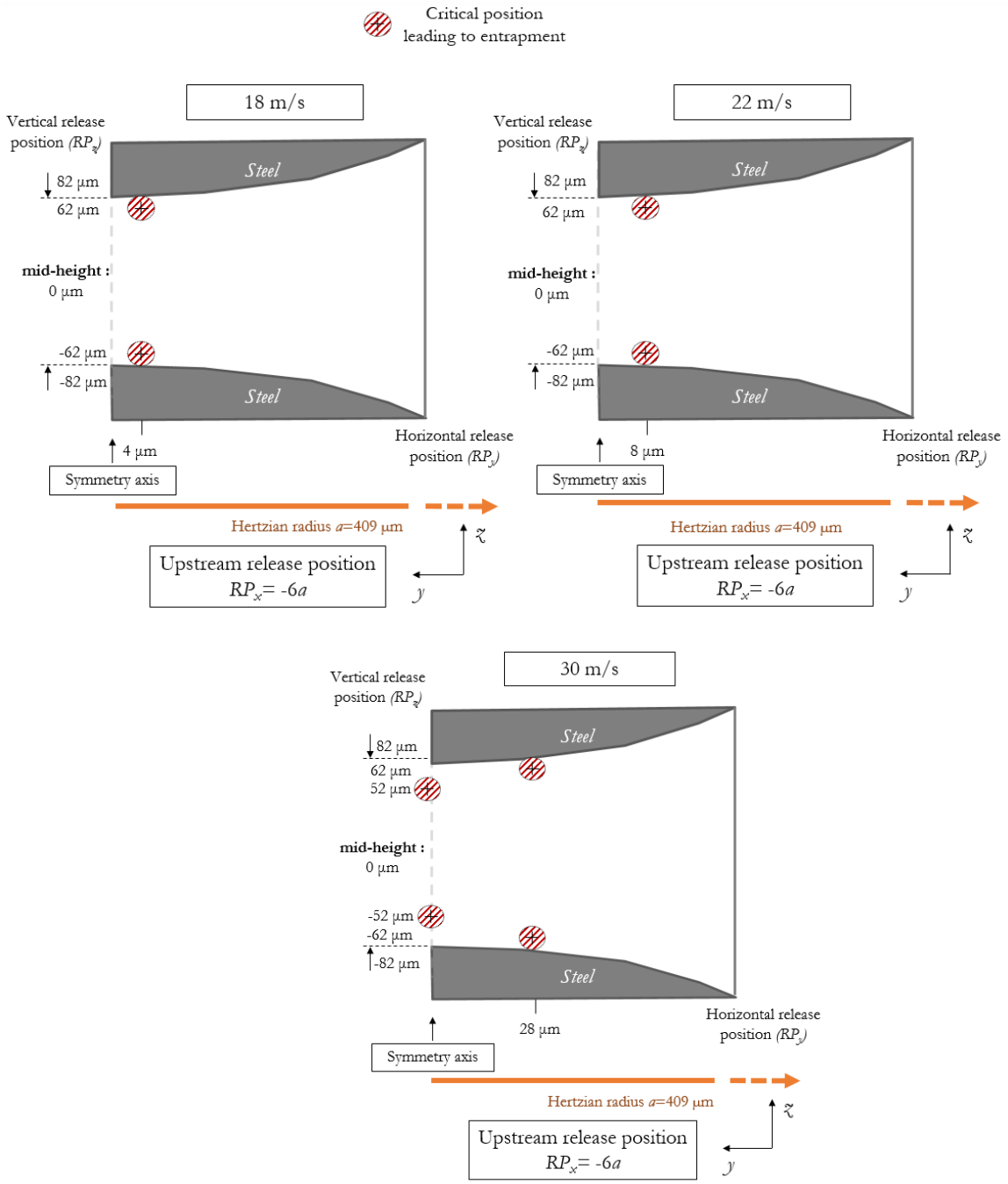

Figure 3-10: Mapping of particle entrapment for different mean rolling speeds (18 – 22 – 30 m/s) within a two-body symmetrical steel–steel contact using the conditions in Table 3-2
(striped red circles represent the farthest positions from the surfaces and the symmetry plane for which the particles are entrapped)

Changing the mean rolling speed affects the location where particles are entrapped. A slower rolling speed caused a smaller probability of particle entrapment. For a mean rolling speed fixed to 18 m/s, particles with initial released positions RP_y larger than 4 µm are bypassing the entrapment area. For a faster rolling speed, the entrapment probability is larger: at 30 m/s, even particles located 30 µm

away from the surfaces on the symmetry plane and the ones located up to 28 µm off-axis if released 20 µm away from the contacting surfaces are entrained in the entrapment area.

Hence, the value of the mean rolling speed affects directly the particle entrapment. As the surfaces carry the lubricant, the higher the mean rolling speed is, the higher the kinetic energy given to the particles for flowing towards the entrapment area is.

3.3.2 Load influence

To study the load influence, different numerical domains have to be considered in order to ensure the fully-flooded condition, as explained in chapter 2. The mean rolling speed was kept constant at 22 m/s and three different loads were considered: 300, 600 and 1200 N. Figure 3-11 represents the size of the fluid domains according the different contact loads.

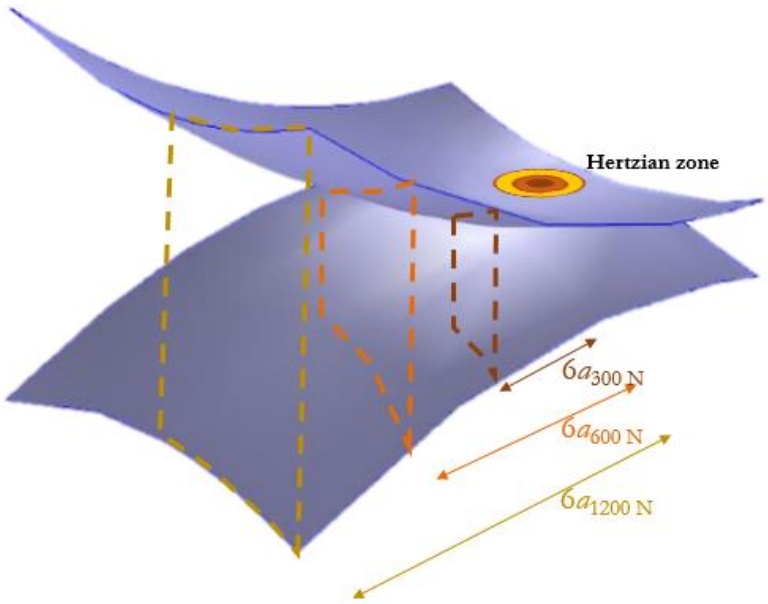

Figure 3-11: Size of the fluid domain for the entrapment calculations using different loads

For the three selected loads, the contact parameters and the entrapment width (EW) for 40 µm particles are given in Table 3-3. As the Hertzian radius is larger, the fully-flooded condition is shifted upstream which is represented by three different inlet surfaces (dotted line) for three different loads.

Normal load [N]	300	600	1200
Hertzian radius [µm]	324	409	515
$6a$ [µm]	1944	2454	3090
$h_{inlet}(6a)$ [µm]	103	164	260
EW/a for particles of 40 µm	6.1	6.4	6.6

Table 3-3: Contact parameters for the simulated contact conditions

Thus, EW is directly affected by the variation of the contact load. For 1200 N it is about 3 % larger than for 600 N and 8 % larger than for 300 N. It means that the entrapment probability of a 40 µm particle should be affected by varying loads. Figure 3-12 reports the mapping of the critical release positions.

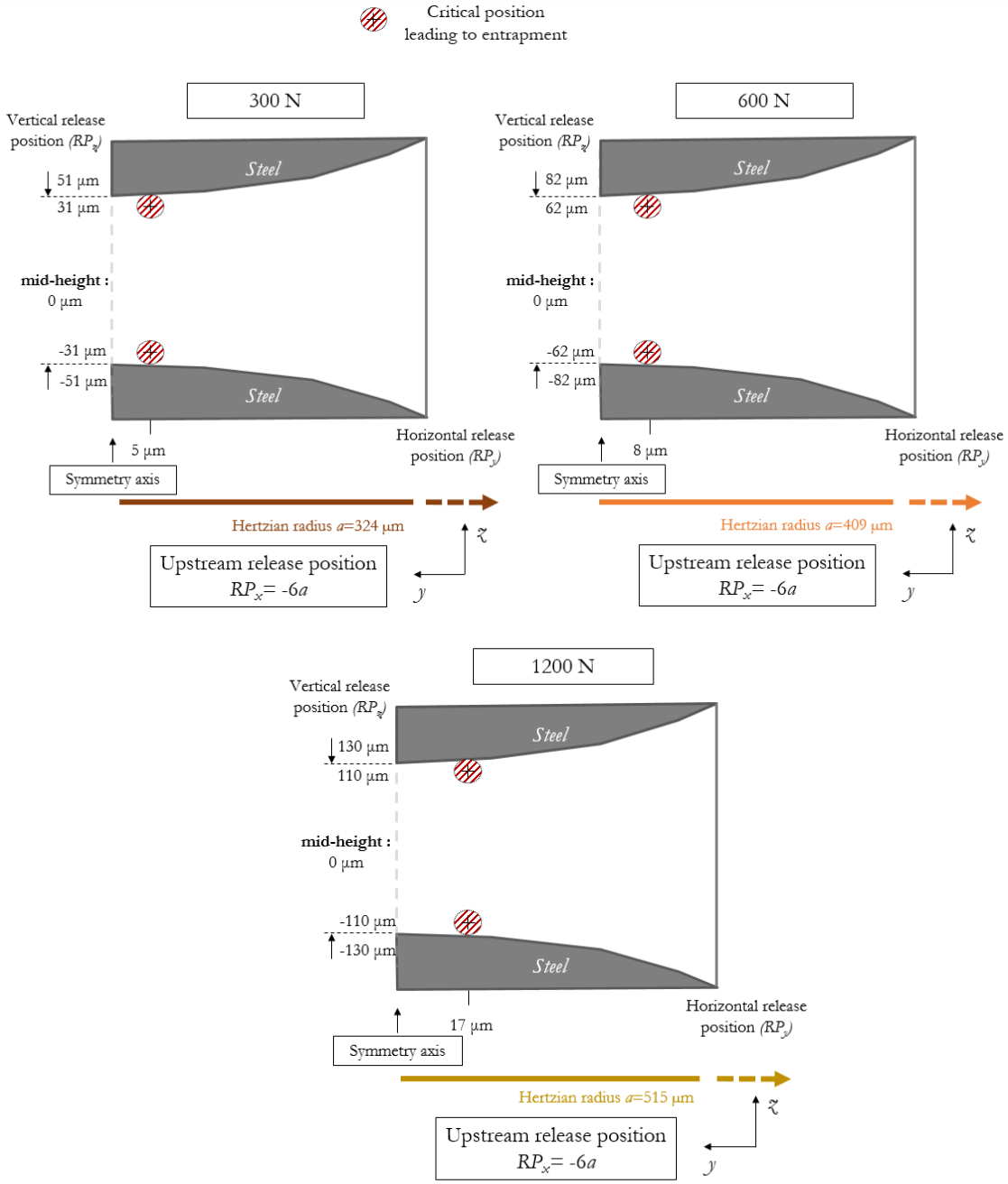

Figure 3-12: Mapping of particle entrapment for different contacting loads (300 – 600 – 1200 N) within a two-body symmetrical steel–steel contacts using the conditions of Table 3-2 (striped red circles represent the farthest positions from the surfaces and the symmetry plane for which the particles are entrapped)

Increasing the contact load causes a higher probability for particle entrapment. For a 300 N contact load, particles located up to RP_y = 5 µm off-axis are entrapped when released sufficiently close to the surfaces (20 µm away), whereas for a 600 N one, this limit is located at RP_y = 8 µm and at 17 µm for 1200 N. Hence, the increase with load of the entrapment probability is consistent with the increase of the EW. A highly loaded contact offers a wider zone for particles to be entrapped and thus causes inevitably a higher particle entrapment probability.

At this point, these observations were related to entrapment of a unique type of particles: spherical steel particle with a diameter of 40 µm. The aim of the next section is to investigate the influence of the intrinsic particle properties, which are its size and nature (material).

3.4 Influence of the particle size and nature

As mentioned previously (chapter 1), the particle size and nature can significantly vary for contaminant debris found in lubricated REBs.

First, considering particles of same nature (same material: steel), and by varying their size, it is possible to highlight a size effect. Figure 3-13 shows the results obtained from two independent numerical simulations which compare the behavior of two steel particles of different diameters, 10 and 40 µm, released at the same position: RP_x = -2.4 mm, RP_y = -5 µm and RP_z = 20 µm.

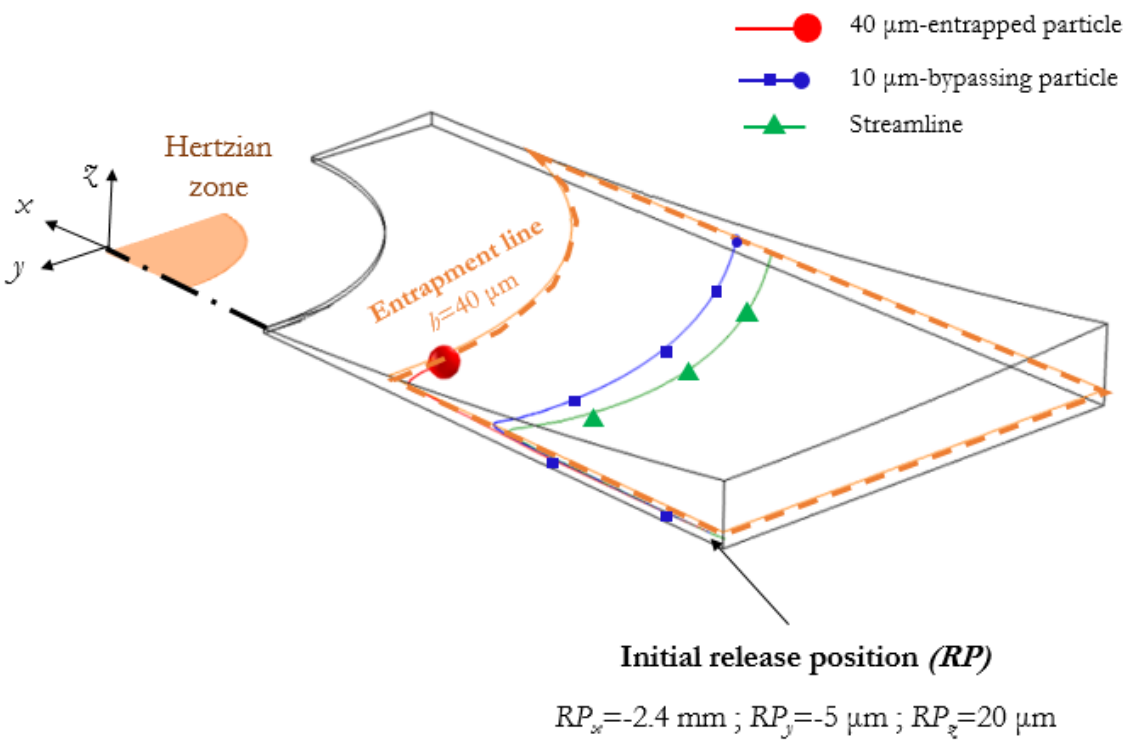

Figure 3-13: Particle-size effect on entrapment with a large particle (40 µm) and a small one (10 µm) within a steel-steel contact (operating conditions in Table 3-2)

Figure 3-13 clearly shows that the trajectories of a small particle (10 µm) and a large one (40 µm) are significantly different. The larger the particles are, the more they will act independently from the flow, represented by the streamlines. In a flow which tends invariably to push particles away from the entrapment area the large particle is entrapped earlier between the surfaces ($d_p \geq h$) than the small one. Using the same operating conditions as previously, it is possible to establish numerically a mapping of release positions leading to entrapment or bypass (Figure 3-14) with particles of different diameters (10, 20 and 40 µm).

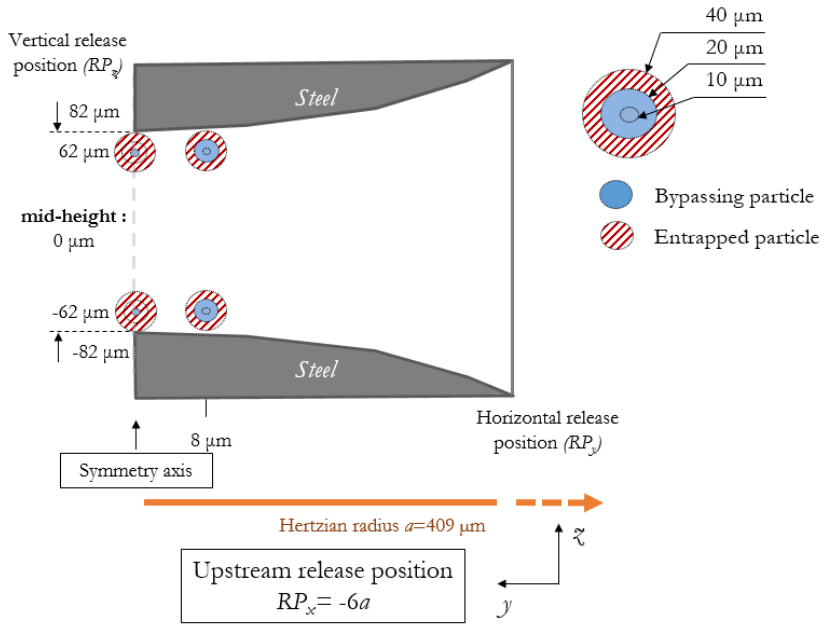

Figure 3-14: Mapping of particle entrapment according to particle size (10, 20 and 40 µm) within a two-body symmetrical steel–steel contacts using the conditions in Table 3-2

It appears that for the same release position along the contact centerline, particles of 20 and 40 µm are entrapped when released 20 µm away from the rolling surfaces (RP_z = -62 µm) whereas a 10 µm-one is bypassing the contact. Similarly, a 40 µm-particle will be entrapped when released 8 µm off-axis and 20 µm away from the steel surfaces, whilst 10 and 20 µm particles bypass the entrapment area. From these numerical observations, two main conclusions can be drawn.

- The particle diameter drives the position of the entrapment line. In other words, the larger the particle is, the further upstream from the contact center the entrapment line is and so the entrapment probability increases.
- An increase of particle diameter for the same type of material induces a heavier particle. Heavier means higher inertia and so particles escape more easily from the flow streamlines to pass through the contact.

In order to validate these numerical observations, experiments were conducted on the twin-disc machine with a controlled level of contaminated lubrication for two ranges of contaminant particles,

small ones (10–20 μm) and large ones (32–40 μm). It allows to quantitatively compare the particle entrapment using the methodology described in chapter 2 (2.3.1.2).

For these experiments, a similar number of suspended particles is used whatever the contaminant size (Table 3-4). To keep this last one constant the concentration of large particles (32–40 μm) is set to 10 mg/l and the one of small particles (10–20 μm) to 0.8 mg/l. The number of small and large dents counted on the discs surfaces (which represents the number of entrapped particles) is given in Table 3-4.

Particle size [μm]		10–20 (Mean diameter: 15 μm)	32–40 (Mean diameter: 35 μm)
Entrapment width [mm] for a steel–steel contact		1.538	2.324
Concentration [mg/l]		0.8	10
Number of particles per 100 ml solution		5804	5710
Number of dents	Test #1	125	252
	Test #2	132	260

Table 3-4: Parameters and results of entrapment tests carried out on the twin-disc tests with particles of different sizes: 10–20 and 32–40 μm

The number of entrapped particles is significantly lower for small particles, with 125–132 small dents against 252–260 large dents. This size effect was already underlined by Dwyer-Joyce and Heymer [19].

Small particles behave like fluid flow tracers and thus bypass much more easily the entrapment area whereas the large ones are trapped between the contacting surfaces and are entrained within the contact. A further experimental test on the twin-disc machine was performed under contaminated lubrication with different range of contaminants in solution, 5 mg/l of particles in the range 32–40 μm mixed with 0.4 mg/l of particles in the range 10–20 μm. This test, performed with a pair of steel–steel contacting discs, aimed at comparing the location of dents left by small and large particles. Figure 3-15 shows an image captured by an optical microscope of the steel disc surface after the test.

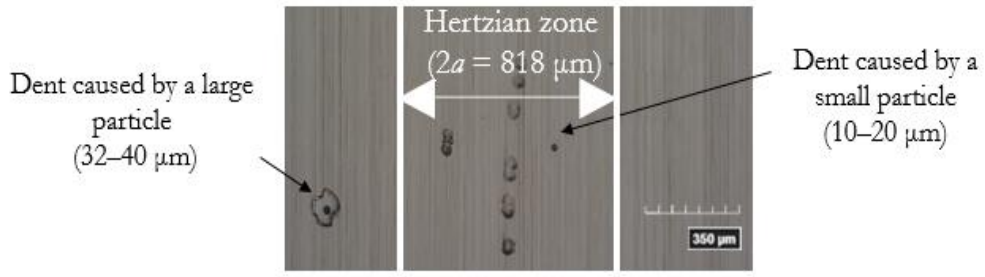

Figure 3-15: Surface of a steel disc after a twin-disc test with a controlled level of contaminants of different sizes (10-20 and 32–40 µm) within a steel-steel contact

It has to be noticed that dents left by small particles are only located within the Hertzian zone contrary to dents left by large particles which are located also above the Hertzian zone. This is due to the entrapment width which is 50 % larger for large particles than for small ones (Table 3-4). Experimental work and numerical simulations show the same trend: large particles are more likely to be entrapped.

To confirm the impact of inertia on particle entrapment, two successive numerical simulations with two particles of same diameter (40 µm), but made from different materials, steel (ρ_{steel}=7800 kg/m^3) and sand (ρ_{sand}=2470 kg/m^3 [129]), are performed. Figure 3-16 shows two independent numerical simulations which compare the behavior of two particles of different natures, steel and sand, released at the same position (RP_x = -2.4 mm, RP_y = -5 µm and RP_z = 20 µm) within a steel–steel contact.

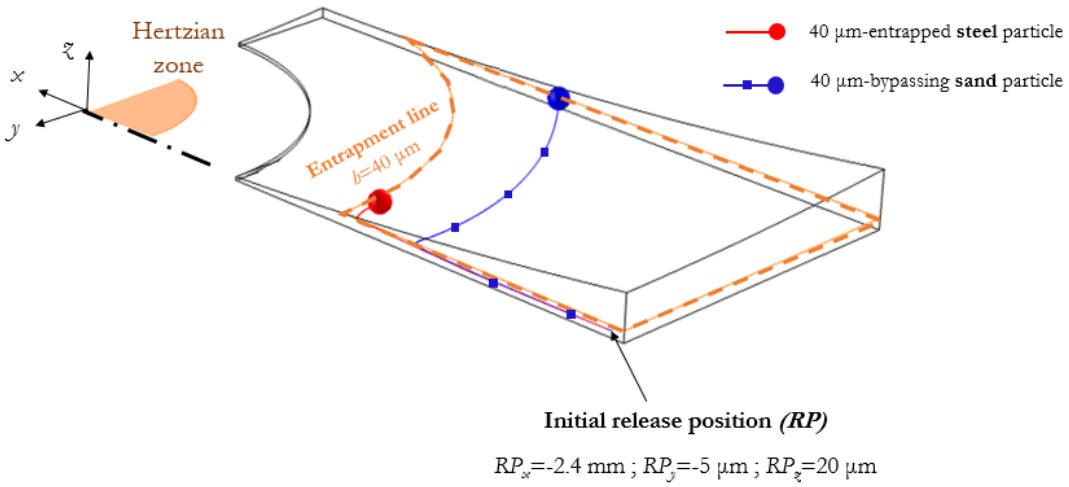

Figure 3-16: Particle-mass effect with a steel and a sand particle released at the same position within a steel-steel contact

The simulations show that the heavier the particle is, the more likely it will be entrapped. Heavy particles are also more subjected to inertia effects and escape more easily the flow streamlines. Finally, an increase of the particle diameter and/or of particle density results in an increase of the entrapment probability.

The dimensionless Stokes number, characterizes the inertia to drag effect ratio:

$$St = \frac{\varrho_p d_p^2 U_r}{18 \mu h} \qquad (3\text{-}1)$$

With ϱ_p the particle density, d_p the particle diameter, $U_r = U_f - v_p$ the relative particle speed, μ the fluid viscosity and h the film thickness. As discussed by Tropea et al. [126], when the Stokes number becomes larger than 0.1, inertia effects tend to affect the particle motion significantly, in other words particles no longer follow streamlines. Figure 3-17 shows the evolution of the Stokes number for several film heights, considering particle diameters varying from 10 to 40 µm, for a fixed viscosity of the fluid (12 mPa·s), a steel density (7800 kg/m^3) for the particles and a constant relative particle speed ($U_r = u_f - v_p$) of 3 m/s.

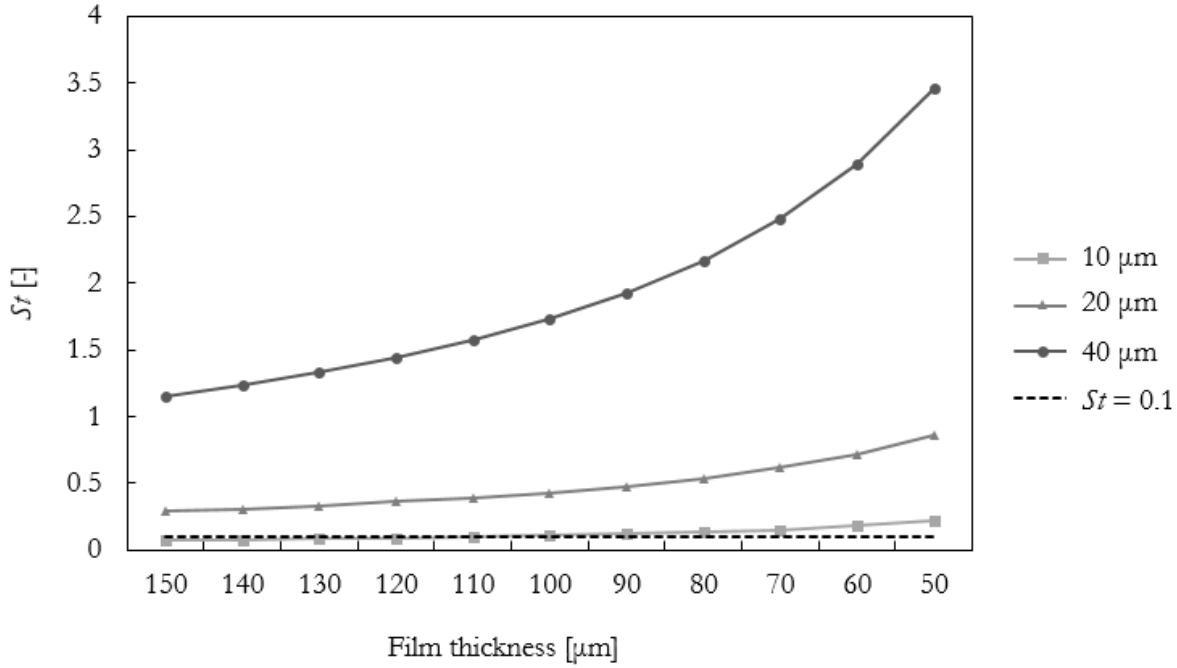

Figure 3-17: Evolution of the Stokes number within confined gaps of various thicknesses considering different steel particles from 10 to 40 µm, for a fixed viscosity of the fluid: 12 mPa·s and constant relative particle speed: 3 m/s

In the different case studies, numerically it has been evaluated that after being released at the same speed than the surrounding fluid velocity (U_r = 0 m/s), the relative particle speed, U_r, varies and becomes possibly much larger than 3 m/s through the fluid transport. Gradually, during the particle entrainment towards the contact, particles are also carried in even thinner contacting gaps. Hence, the Stokes number increases and becomes much higher than 0.1 for large particles (40 µm) or heavy ones, as represented in Figure 3-17. Despite drag effects tending to push particles off-side (see 3.2.2: velocity

vectors mapping), the dominating inertia effects lead large and heavy particles to be entrapped whereas small and light particles bypass more easily the entrapment area.

Finally, regardless the operating conditions and particle intrinsic properties, inlet release positions leading to entrapment are all located close to the symmetry plane. The RP_y distances for which the particles are entrapped are in any case much smaller than the Hertzian radius (see entrapment maps Figure 3-7, 3-9, 3-10, 3-12, 3-14). The next section proposes on this basis an analytical investigation of the velocity profile at the contact inlet, along the symmetry plane.

3.5 Contact inlet analysis

As shown in section 3.4 the critical zone for particle entrapment at contact inlet is located very close to the symmetry plane. Figure 3-18 shows a side view of an EHD contact with a schematic representation of streamlines leading to particle entrapment or bypass according to their positions. A zoom on the flow which passes through the Hertzian contact is also given.

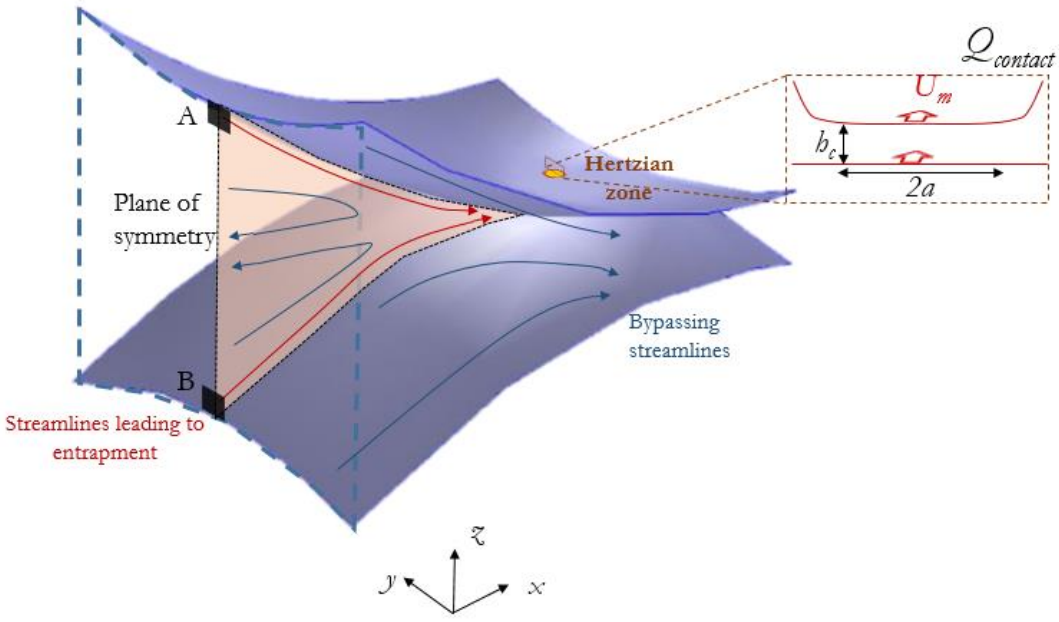

Figure 3-18: Side view of an EHD circular contact with lubricant streamlines leading to particle entrapment or bypass

In this figure it is shown that streamlines oriented towards the contact are only located close to the plane of symmetry (see also Figure 3-8). The lubricant flow passing through the two black squares (A and B) presented in Figure 3-18, is directly supplying the Hertzian contact area. As a consequence particles located in this region upstream from the contact are more likely to be entrapped.

Table 3-5 reports the amount of lubricant that flow through the Hertzian contact zone for three different loads: 300 – 600 – 1200 N. This flow, $Q_{contact}$, is dependent on the Hertzian width, characterized

by the Hertzian radius, the central film thickness and the mean rolling speed, here fixed at 22 m/s. The flow of lubricant passing through sections A and B of Figure 3-18 is calculated according to the results presented in Figure 3-12.

Load [N]	300	600	1200
a [µm]	324	409	515
h_c [µm]	0.84	0.82	0.75
$Q_{contact}$ [µl/s]	12	15	17
Q_{inlet} [µl/s]	4.4	7	14

Table 3-5: Flow of lubricant in the Hertzian contact for three different loads (300 – 600 – 1200 N) using the conditions of Table 3-2

Hence, a flow of some µl/s is driven in the Hertzian contact zone which corresponds to the same lubricant quantity carried from the contact inlet (through the black squares). That is why inlet observations are consistent with the analytical entrapment probability predictions based only on Hertzian zone parameters for example the one proposed by Ville [54].

On this basis, an analytical investigation of the velocity profile is proposed at the contact inlet. From the Navier-Stokes equations, assuming the classical assumptions of thin film theory, the velocity components along the x and y directions are expressed as follows:

$$u(z) = \frac{1}{2\mu}\frac{\partial p}{\partial x}\frac{z}{h}\left(\frac{z}{h}-1\right)h^2 + U_{1,x}\frac{z}{h} + U_{2,x}\left(1-\frac{z}{h}\right) \qquad (3\text{-}2)$$

$$v(z) = \frac{1}{2\mu}\frac{\partial p}{\partial y}\frac{z}{h}\left(\frac{z}{h}-1\right)h^2 + U_{1,y}\frac{z}{h} + U_{2,y}\left(1-\frac{z}{h}\right)$$

Poiseuille Couette

with $\frac{\partial p}{\partial x}$, $\frac{\partial p}{\partial y}$ the pressure gradient along x and y, $\frac{z}{h}$ the dimensionless coordinate across the film thickness and $U_{1,i}$, $U_{2,i}$ the speed of the lower and upper contacting solids.

Considering only the flow in the x-direction, the lubricant is partly carried by the surfaces, through the Couette flow, and partly entrained by the pressure induced gradient through the Poiseuille flow. Figure 3-19 shows a schematic section view of the contact inlet with two zones corresponding to two types of dominated flows, the Couette dominated zone along the surfaces (dark orange), characterized by Δ_C, and the Poiseuille dominated zone characterized by Δ_P in the center (light orange).

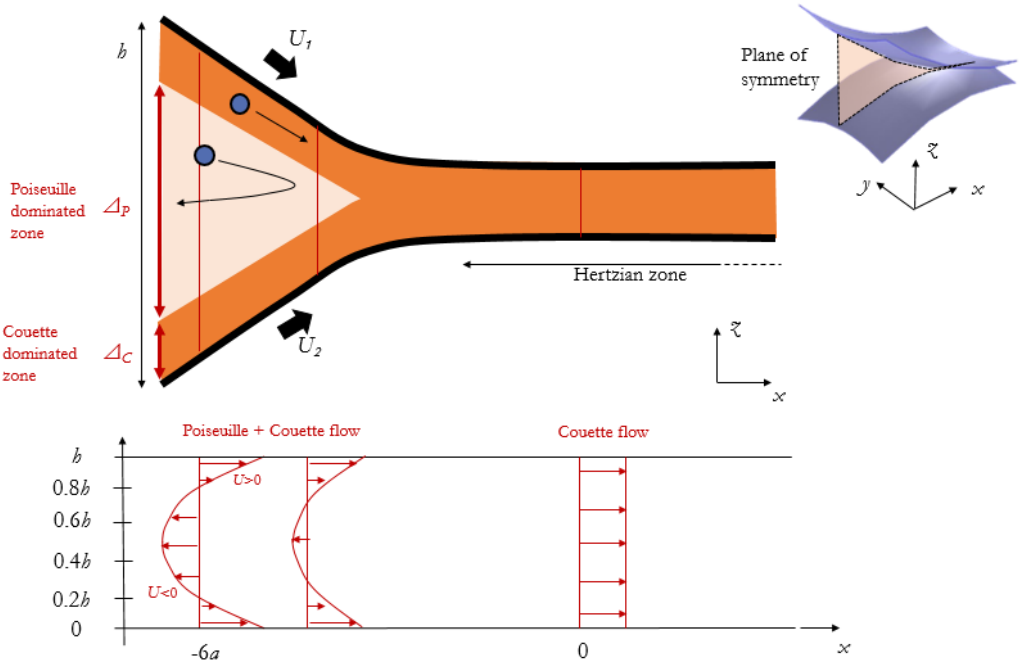

Figure 3-19: Schematic section view of an EHD circular contact with velocity profiles of the lubricant across the film thickness at different abscissa

The Couette flow is oriented downstream and tends to carry the lubricant towards the contact central zone whereas the Poiseuille flow is oriented upstream as the pressure gradient is positive in the contact inlet. The balance between these two flows results in a parabolic profile at the contact inlet, which is presented in Figure 3-19 and following equations given hereafter (see development given in Appendix C).

$$u(Z) = 6U_m Z^2 - 6U_m Z + U_m$$

$$\text{With } Z_{1,2} = \left(\frac{\tilde{z}}{h}\right)_{1,2} = \frac{1}{2} \pm \frac{\sqrt{1/3}}{2} = \begin{cases} 0.21 \\ 0.79 \end{cases} \qquad (3\text{-}3)$$

The velocity profile at the contact inlet ($-6a$) is hence positive from 0 to $0.21h$, then negative between $0.21h$ and $0.79h$ and finally positive from $0.79h$ to h (see Figure 3-20).

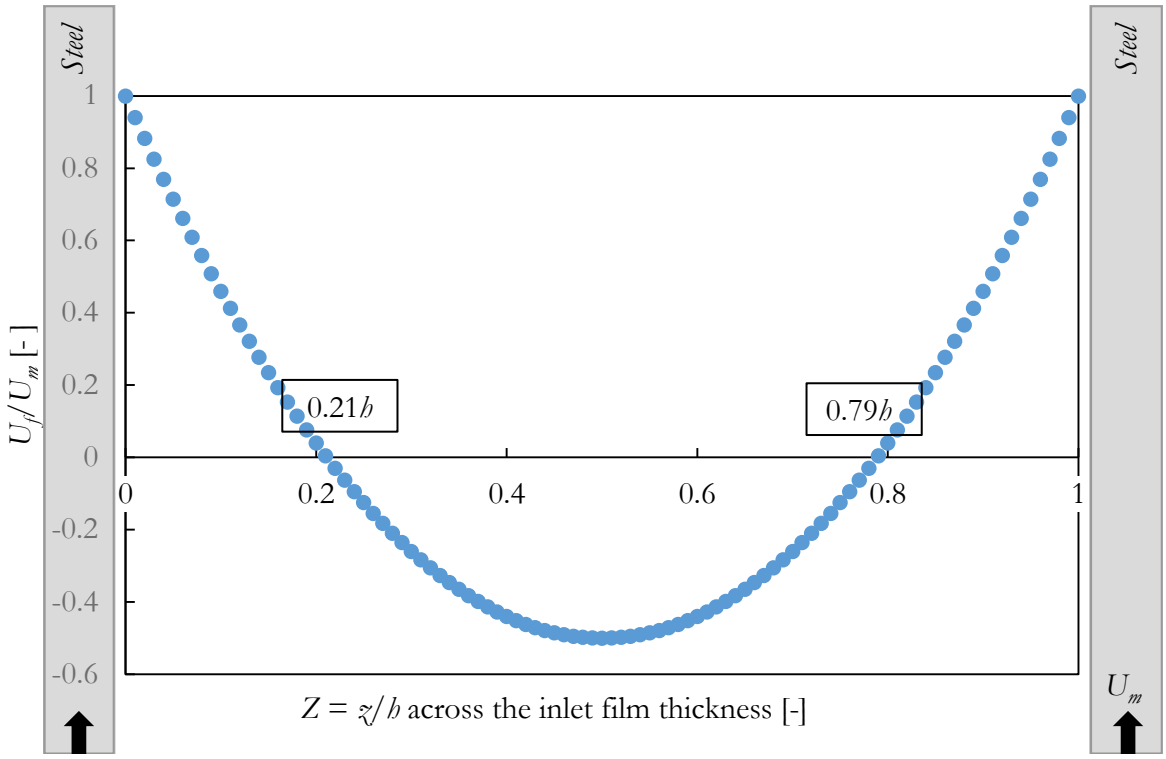

Figure 3-20: Fluid velocity profile across the dimensionless film thickness

It is valid for all EHD contacts only at the contact inlet, along the symmetry plane and for fully-flooded condition.

Entrapment results depicted in Figure 3-10 (mean rolling speed influence) and Figure 3-12 (load influence), can be discussed with the velocity profile at the contact inlet.

- The increase of the mean rolling speed showed to enhance the probability of entrapment and increases the positive fluid velocity, oriented downstream. Indeed the profile being the same, and U_m increasing, particles located in the Couette dominated zone (Figure 3-19) near the surfaces are subjected to a stronger flow. Considering the three configuration presented in Figure 3-10, the size of the inlet film thickness is constant and equal to 164 µm but the velocity profiles are different. Figure 3-21 reports the shape of the velocity profiles at the contact inlet of a steel–steel contact for three different mean rolling speed (18 – 22 – 30 m/s) for a same applied load equal to 600 N.

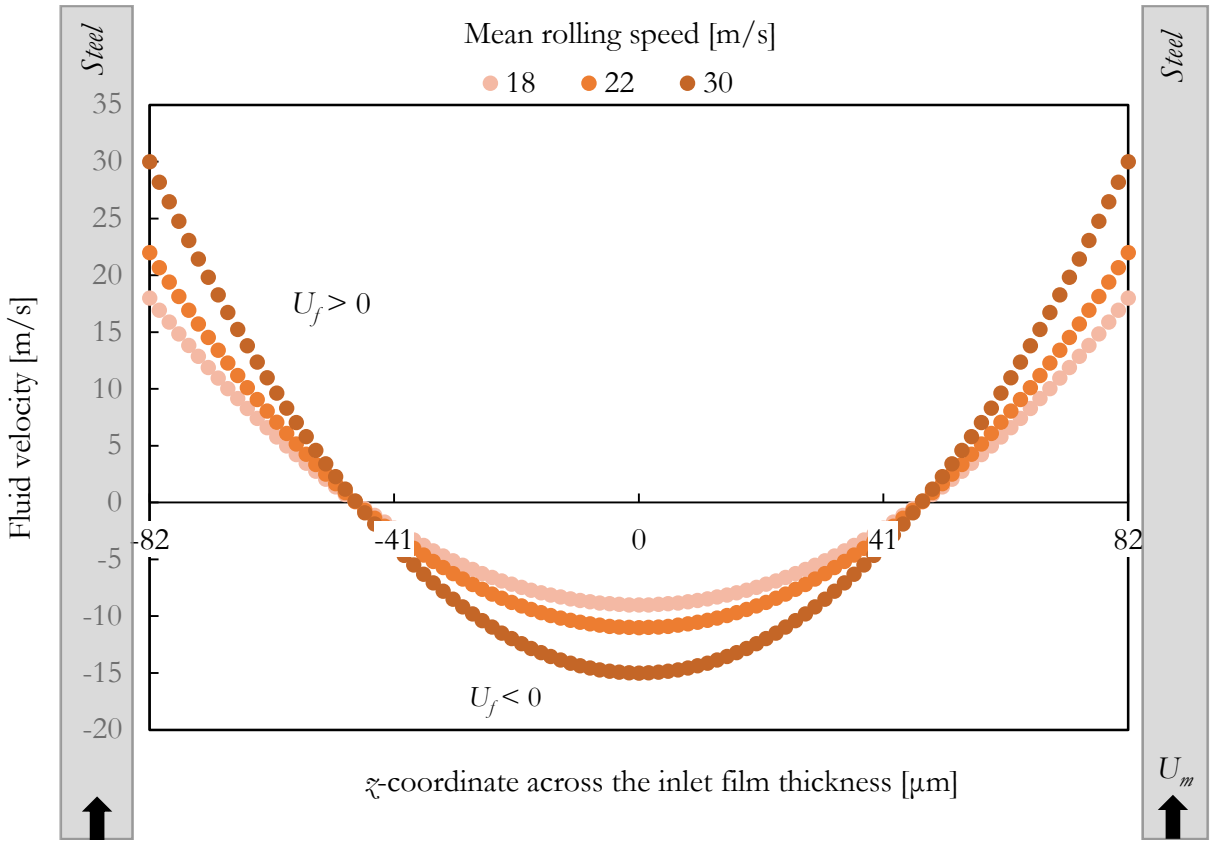

Figure 3-21: Fluid velocity profiles across the film thickness for three different mean rolling speed (18 – 22 – 30 m/s) for a same applied load equal to 600 N

It appears that for these three cases, particles released 20 µm away from the contacting surfaces (as in entrapment mapping of Figure 3-10), at -/+ 62 µm, have a positive speed. The fluid velocity is of 5.8 m/s for the case at U_m = 18 m/s, of 7 m/s at U_m = 22 m/s and of 9.6 m/s at U_m = 30 m/s. It means that particles are guided towards the contact with an increasing inertia linked to the mean rolling speeds. On the contrary, at mid-height ($\bar{z}$ = 0) particles are directly pushed upstream through backflows.

- Increasing the load under fully-flooded condition, the contact meniscus is shifted upstream. Inlet film thickness being larger, the constant velocity profile induces a wider Couette dominated zone. Whatever the load is, the Couette dominated zone is at least 21 µm thick ($\perp_C$ = 21 µm for 300 N, 34 µm for 600 N and 54 µm for 1200 N). In Figure 3-12, all entrapped particles are released 20 µm away from the contacting surfaces (at -/+ 31 µm for 300 N, at -/+ 62 µm for 600 N and at -/+ 110 µm for 1200 N) and thus, particles are transported towards the entrapment area.

3.6 Conclusion

The aim of this chapter was to improve our understanding of the phenomena leading to particle entrapment in circular steel–steel EHD contacts. First, an innovative way to observe particle entrapment was implemented on a ball-on-disc machine by using the fluorescent technique. It enabled to offer a new insight on streamlines and entrapment mechanisms. The use of this technique proved to be adaptable to the study of EHD contacts.

Then, a dual approach, mixing numerical simulations and experimental tests on the twin-disc machine, allowed to study the key parameters which influence particle entrapment.

- The effect of the release position was established numerically, and showed that a particle released close to the symmetry plane (along the y-axis) and in the vicinity of the surfaces (z-axis) is more likely to be entrapped.
- It was shown that an increase of the mean rolling speed induces faster particles which are more likely to enter the entrapment area.
- It was established that increasing the contact load enhances the entrapment width and thus the entrapment probability.
- It was demonstrated numerically and experimentally that large and heavy particles are more likely to be entrapped than small and light ones.

Finally, an analytical analysis on the lubricant velocity profiles at the contact inlet was proposed. Upstream of the contact, critical zones (Couette dominated zones) have been defined and whatever the operating conditions, all the numerical results are explained by the fact that all entrapped particles are released in these critical zones.

In the next chapter, an extension of the entrapment investigations towards more realistic contacts encountered in industrial context is proposed. The influence of different contacting materials, several contacting geometries and rolling–sliding conditions are tested.

Chapter 4 Towards entrapment in more realistic contacts

4.1 Introduction

Contacts between rolling elements and rings vary in terms of materials, contacting geometries and kinematics [130,131]. These parameters should affect particle entrapment.

Current developments towards hybrid REBs impose to update the understanding of entrapment mechanism. The hybrid combination of a Si_3N_4 surface in contact with a steel one is nowadays an industrial-wide-spread solution. It implies new questions in particular in terms of surface indentation resulting from particle entrapment. In this chapter, the focus is made on the influence of the contacting materials on the entrapment phenomena with Si_3N_4–steel pair of contacting discs. It is investigated through twin-disc tests in contaminated regime compared to numerical simulations.

Rolling elements-rings contacts in REBs, are mainly elliptical. The inlet zone is critical for generating hydrodynamic effects and, in turn, to determine whether or not particles are dragged towards the entrapment area. Here, this zone upstream from the contact will be studied both experimentally and numerically, to highlight the effect of the contact configuration on the lubricant flow and thus, on particle entrainment. Beginning with twin-disc tests, the results are compared with those from numerical simulations and validated by visualizations performed on the ball-on-disc machine.

In realistic conditions, the contact is never under pure rolling kinematic condition. The last part of this chapter concerns the influence of rolling–sliding conditions on particle entrapment.

With the twin-disc machine and the ball-on-disc tribometer presented previously, the study of particle entrapment in different conditions was performed for operating conditions defined in Table 4-1.

Experimental device	**Twin-disc machine**	**Ball-on-disc tribometer**
R_x [mm]	17.5	12.7 / 13 / 13.1
R_y [mm]	17.5 / 35 / 70 / 200	12.7 / 84.2 / 330
Load [N]	600	10 / 50
Mean rolling speed [m/s]	22	0.005
Slide-to-roll ratio [%]	0 / 12	0
Contacting materials	Steel–steel / Si_3N_4–steel	Glass–steel

Table 4-1: Operating conditions for tests performed with the twin-disc machine and the ball-on-disc tribometer

This set of parameters enable to reproduce contacts with different configurations, circular to elliptical, all-steel contacting bodies or hybrid ones, as well as pure rolling or rolling-sliding conditions.

4.2 Particle entrapment in hybrid contacts

This section discusses tests carried out on the twin-disc machine to reveal the specificities of the hybrid contacts in terms of particle entrapment. Then, the analyses of both surface topographies give information on the entrapment mechanism itself, by a thorough analysis of dents left by entrapped particles.

4.2.1 Twin-disc tests with hybrid discs

Tests with steel–steel discs or Si_3N_4–steel ones, were performed on the twin-disc machine. The load was kept constant. Due to different elastic properties (Chapter 2, Table 2-2), deformations of contacting bodies are different. Thus, the inlet zone can differ and so, some differences in terms of number of entrapped particles can be expected. Table 4-2 reports the parameters of the two different circular contacts.

Parameters	All-steel	Si_3N_4–steel
Load [N]	600	
Mean rolling speed [m/s]	22	
Hertzian radius [µm]	409	388
Hertzian pressure [GPa]	1.7	1.9
h_c [µm]	0.82	0.79
EW for 32 µm-particles [mm]	2.34	2.26

Table 4-2: Contact parameters for an all-steel contact and a hybrid one (600 N)

Twin-disc tests enable to get a quantitative comparison on the number of entrapped particles using the methodology described in chapter 2 (2.3.1.2). Contamination is composed of M50 steel particles, sieved in the range 32–40 µm, with a concentration of 10 mg/l.

Figure 4-1 reports the number of dents counted all around the discs circumference after tests under contaminated lubrication for an all-steel contact and a hybrid one. The results are compared to the prediction of Ville [54] which postulated that the number of entrapped particles, $n_{ent,part}$ is given by:

$$n_{ent,part} = \frac{10^7 \cdot 6CQ_{contact}t}{\varrho_p V_p} \quad (4\text{-}1)$$

$Q_{contact}=2ah_cU_m$ is the flow which passes through the Hertzian zone (µl/s) (a the Hertzian radius in mm, h_c the central film thickness in µm and U_m the mean rolling speed in m/s), C the concentration of particles in solution (mg/l), t duration of contaminated lubrication (min), ϱ_p the particle density (kg/m^3) and V_p the particle volume (m^3).

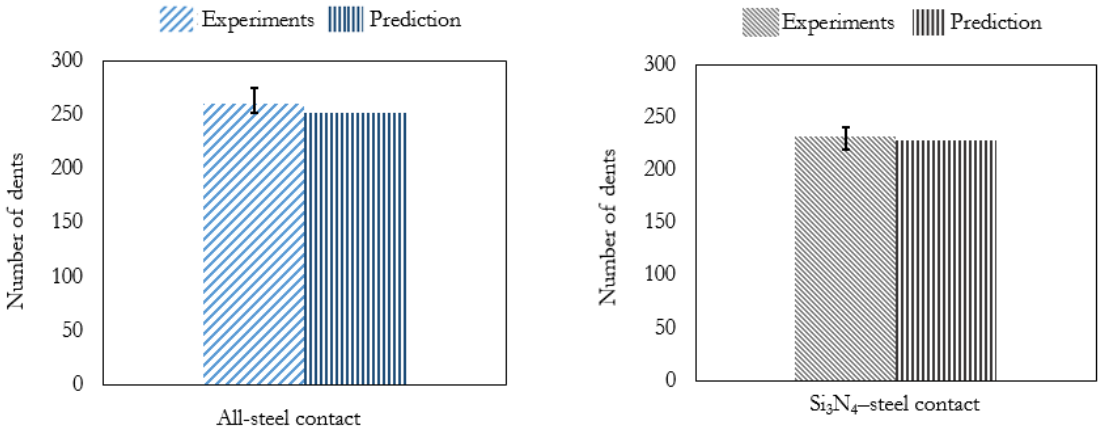

Figure 4-1: Number of dents (corresponding to the number of entrapped particles) for experiments (dispersion established after 3 successive tests) with (left) all-steel and (right) Si_3N_4–steel contacting surfaces using a unique range of contaminants (32–40 µm), see conditions Table 4-1

Ville's formula expects 252 particles to be entrapped, assuming a contaminant mean diameter of 35 µm, a central film thickness of 0.82 µm and a Hertzian radius of 409 µm (Table 4-1). Here, for a circular all-steel contact under pure rolling condition, the mean value of the counted dents is 260. Similarly, the predictions for a hybrid contact is 228 entrapped particles and the mean value of the counted dents is 232. As heavy large particles were used, inertia effects are important and particles are no longer swept around the contact (see chapter 3, 3.4). This is an important condition to use the mentioned formula and that is why predictions are accurate for these cases.

Tests reveal also that there is a slight difference for entrapment ratios between an all-steel contact (260 dents) and a hybrid one (232 dents) for a constant load. It can be attributed to the resulting contact parameters (Table 4-1), particularly the contact width (388 µm for the hybrid contact and 409 µm for an all-steel one). A smaller entrapment width implies a smaller entrapment area and thus a smaller probability for particle entrapment.

Numerical simulations were also performed for both configurations: all-steel and hybrid cases by maintaining a constant load and pure rolling condition (22 m/s). Figure 4-2 reports a comparison of the mapping of release positions leading to entrapment for both cases.

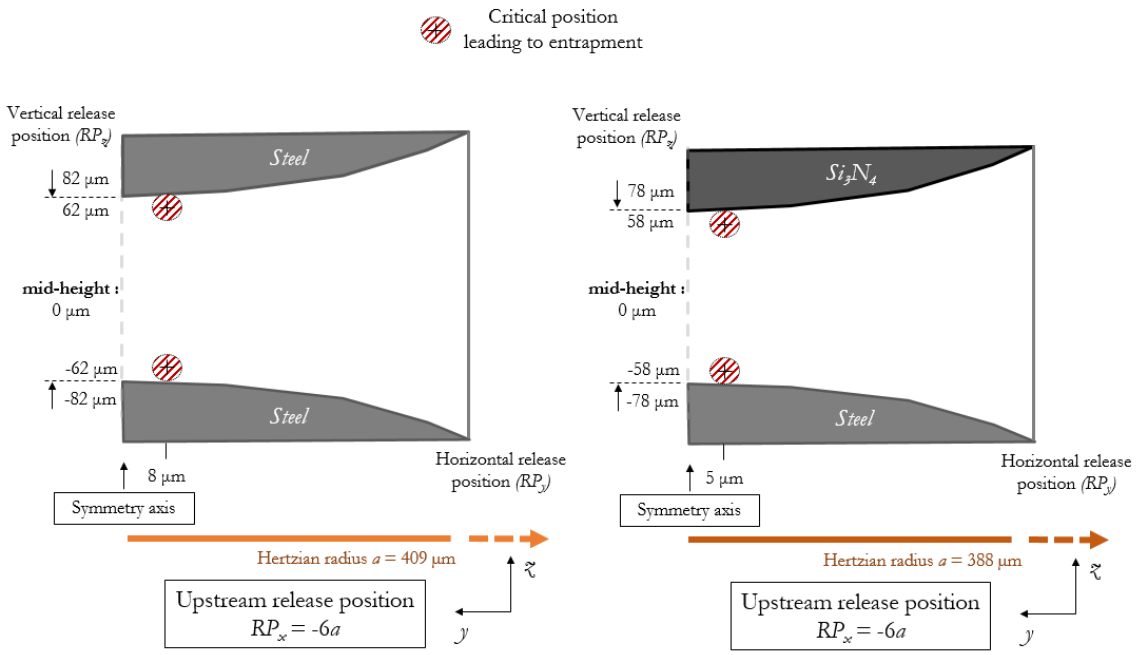

Figure 4-2: Mapping of particle entrapment according to release position across the film thickness for (left) an all-steel contact and (right) a Si_3N_4–steel one considering a 40 µm particle with the conditions in Table 4-2

This comparison shows that the domain of release positions leading to entrapment for a hybrid Si_3N_4–steel contact is slightly more limited than for an all-steel contact. Indeed in an all-steel contact, particles can be released up to $RP_y = 8$ µm off-axis to be entrapped whereas in a hybrid contact particles are entrapped up to $RP_y = 5$ µm off-axis. As described in chapter 3, the release position domain and the Hertzian area are linked. Thus, changing the contact width will change the release position domain and affects the entrapment probability.

To validate that the main cause for the difference is the contact width, more specifically the entrapment width (EW), further tests were performed keeping constant the Hertzian radius and thus adjusting the load (600 N for the all-steel case and 680 N for the hybrid case). Figure 4-3 reports the comparison of the number of dents counted on the discs surfaces after tests at constant load (left) and at constant Hertzian radius (right).

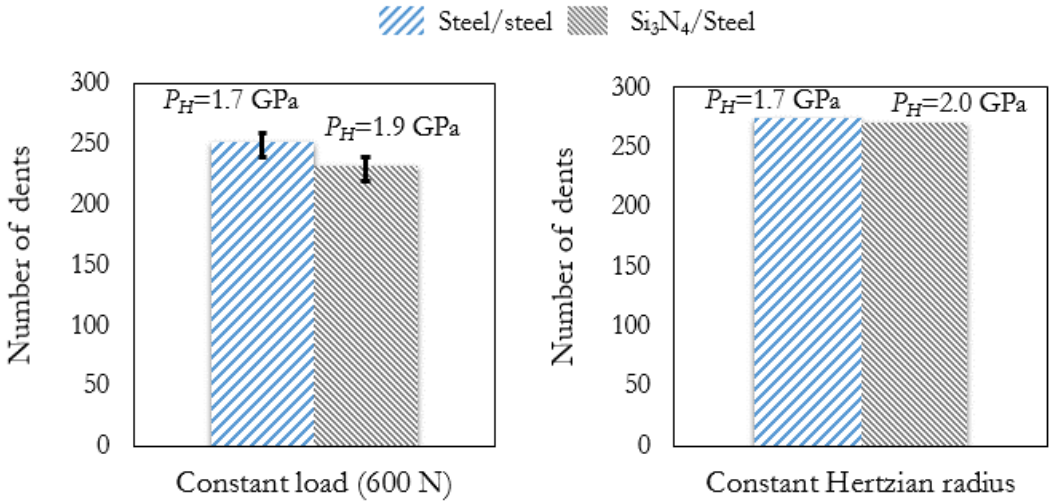

Figure 4-3: Number of dents (corresponding to the number of entrapped particles) for experiments with all-steel contacting surfaces and Si_3N_4–steel ones (left) with a constant load (dispersion established after 3 successive tests) and (right) with a constant Hertzian surface (1 test) using a unique range of contaminants (32–40 µm) with conditions in Table 4-2

Very similar numbers of dents were found on the two tests performed at constant Hertzian radius, 275 dents for the steel–steel contact and 270 for the hybrid one. This result underlines the fact that entrapment is dependent on the size of the Hertzian zone but remains independent on the nature of the contacting materials. This is consistent with the discussion proposed in chapter 3 (3.5) in which the relation existing between the contact inlet geometry and the entrapment probability was shown (see equation (3-2)).

Following the analysis on the number of entrapped particles for steel–steel or Si_3N_4–steel contacts, surfaces were observed to identify the indentation mechanisms.

4.2.2 Surface analysis after tests

Steel particles, once squeezed in the contact inlet, are deformed by the normal forces imposed by the rolling surfaces (see chapter 3). In turn, ductile particles damage the surface and produce smooth rounded dents [55]. Example of dents left on the surfaces are shown in chapter 2 (2.3.1.2). This indentation mark presents a characteristic hole in the middle and a shoulder on the entry side. A scenario is proposed for the mechanism of particle and surface deformations [19,54], which is recalled in Figure 4-4 and explained hereafter.

- First step, the particle is entrapped between the rolling elements (see Figure 3-3 – (ii)) It was postulated that a hole formation (Figure 4-4 – a) precedes the whole dent formation and corresponds to a plastic deformation of the contacting surfaces while the particle stays undeformed.

- Second step, the particle is driven by the surfaces motion through the friction forces, $F_{fr,i}$ and is simultaneously deformed by the normal forces, $F_{N,i}$ to accommodate the very thin gap (see Figure 3-3 – (iii)). The shape of the contact inlet results in normal forces slightly oriented downstream which cause the shoulder formation [54].

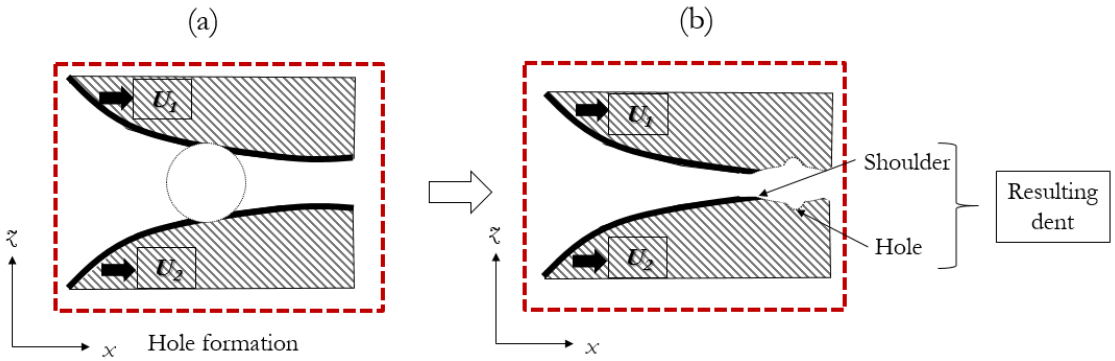

Figure 4-4: Scenario of the particle and surface deformations

Profiles of indentation marks are presented graphically in Figure 4-5 for all-steel configuration and Figure 4-6 for Si_3N_4–steel. The presented dent profiles are representative of a whole set of experiments, whose parameters are given further away in this chapter (see Table 4-5).

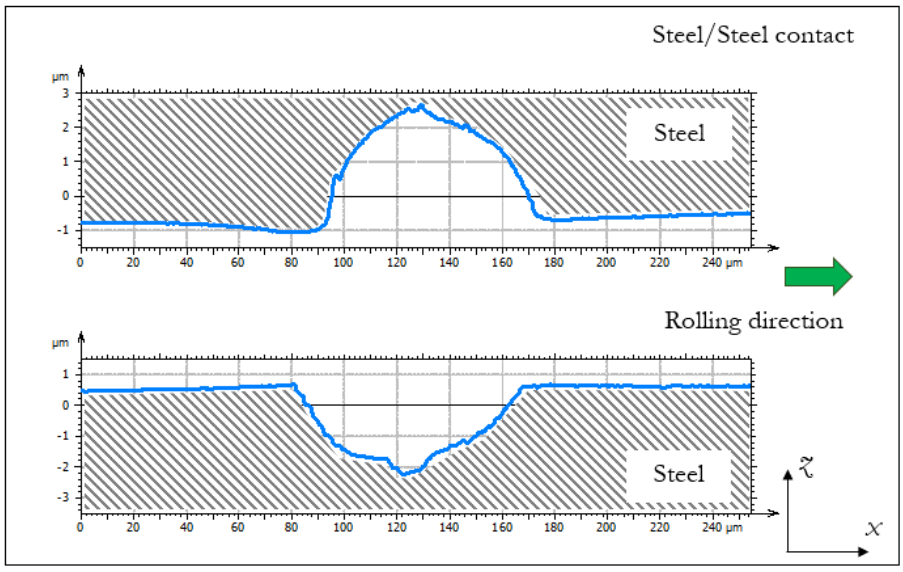

Figure 4-5: Profiles of two representative dents made on all-steel contact by a steel particle in the range 32–40 µm

The dent dimensions made on both surfaces are between 70 and 90 µm in width and between 2 and 3 µm in depth. This corresponds to a slope, depth over width, of 0.028–0.03 which is consistent with the indentation marks found in classical all-steel REBs as underlined in [82].

For a hybrid couple of materials, dents were observed only on the steel surface and not on the ceramic one (Figure 4-6) where no mark was observed. Hence, the undamaged ceramic surface offered a real resistance ability to dent formation.

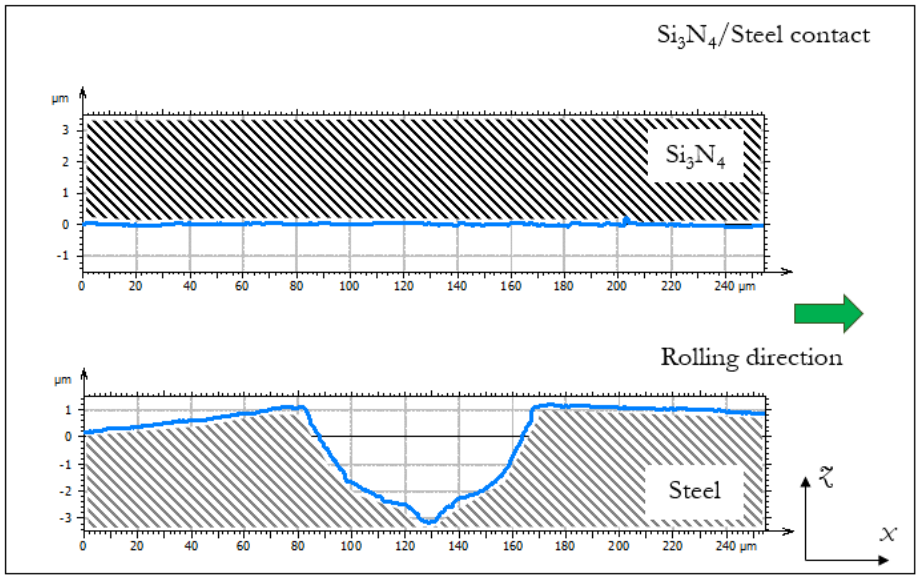

Figure 4-6: Profiles of two representative dents made on a Si_3N_4-steel contact by a steel particle in the range 32–40 µm

Dent features observed on the steel counterface are also of size between 70 and 90 µm in width but deeper, between 4 and 5 µm, which result in slopes varying between 0.055 and 0.057.

Kahlman and Hutchings [24], using a hybrid thrust ball bearing at 2060 r/min with a 3 GPa Hertzian pressure, also showed that no wear or damage occurred on the ceramic balls. As demonstrated by Hamer et al. [132] surface indentation with a ductile particle is strongly governed by the difference between the hardness of the particle and the one of the surface. More recently, it has been shown that if the particle hardness exceeds the contacting surface one, the particle is embedded in one of the rolling surfaces and local plastification takes place inducing a dent [133,134]. Finally, for hybrid contacts, the steel counterface presents a higher risk of spalling than for all-steel contacts, as the dents are deeper.

The aim of the next section is to investigate particle entrapment considering point contacts with various ellipticity ratios.

4.3 Effect of the geometrical configuration

In lubricated REBs, numerous contacts take place simultaneously between the different components in relative motion. However, in the frame of this study, only contacts occurring between rolling elements and inner raceways are considered. Figure 4-7 presents the different parts of REBs that may enter in contact and in the lower part, a zoom-in shows an insight on the type of contacts that are investigated in this study.

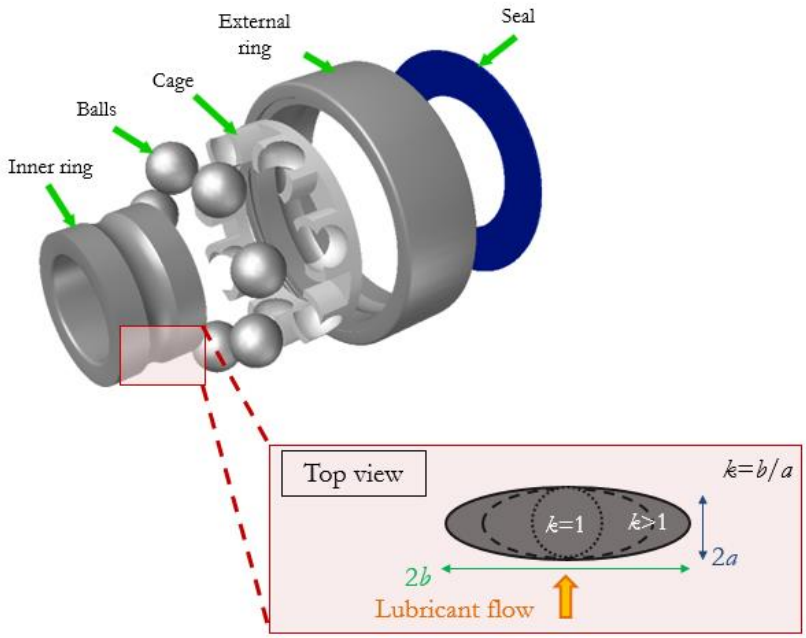

Figure 4-7: Different contacts existing in REBs [135]

Contacts between rolling elements and inner raceways present an elliptical Hertzian area with the main semi-axis perpendicular to the flow direction. This contact is characterized by the ellipticity ratio, $k=b/a$, which is the ratio between the ellipse semi-axis in the perpendicular direction to the flow over the ellipse semi-axis in the direction of the flow. In this section, the aim is to study the influence of the ellipticity ratio k.

4.3.1 Twin-disc tests with elliptical contacts

Previous studies [18,19] have concluded that the number of entrapped particles can be directly obtained by considering a set of parameters that are dependent on particle properties (size and concentration) and operating parameters (rolling speed, film thickness and contact width perpendicular to the lubricant flow).

Tests with the twin-disc machine were performed with steel–steel discs at constant load (600 N) and constant rolling speed (22 m/s) (see Table 4-1), in order to investigate the influence of contact shape. The discs have a constant radius R_x and the different contact configurations were obtained by

using crowned discs of various transverse radii R_y (see Table 4-1). So, the contact width is inevitably larger once passing from a circular to an elliptical configuration and thus, the number of entrapped particles should be affected.

Figure 4-8 shows the geometries of the resulting contact transverse profiles and the size of the entrapment width (see chapter 2) by considering a circular or an elliptical configuration.

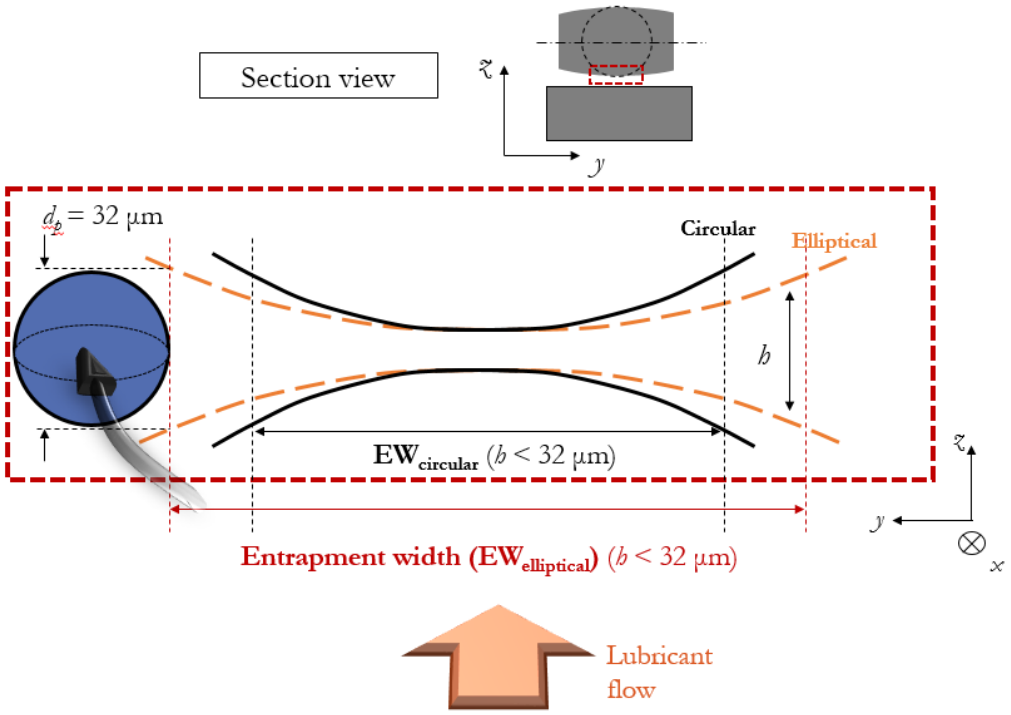

Figure 4-8: Section view and EW for a circular (k = 1) and an elliptical contact configuration (k = 1.6)

The two configurations, i.e. circular and elliptical contacts, lead to contact widths of 409 and 574 µm and EW of 2.34 and 3.28 mm, respectively. The EW is about 30% larger for an elliptical contact than for the circular case. Table 4-3 reports the contact parameters of the different twin-disc configurations for operating conditions in Table 4-1.

Parameters	**Circular**	**Elliptical**		
R_x [mm]	17.5	17.5	17.5	17.5
R_y [mm]	17.5	35	70	200
a [µm]	409	362	317	258
b [µm]	409	574	794	1260
k=b/a	1.00	1.59	2.50	4.88
P_h [GPa]	1.71	1.38	1.13	0.88
h_c [µm]	0.82	0.88	0.96	1.04
EW for 32 µm-particles [mm]	2.34	3.28	4.6	7.58

Table 4-3: Parameters for the different contact configurations tested on the twin-disc machine for operating conditions in Table 4-1

The contact width and the EW increase hence proportionally with the ellipticity ratio k. The EW is about two times larger than a circular contact for k = 2.5 and about three times larger for k = 4.9. Simultaneously, the central film thickness (computed with the resolution of the Reynolds equation coupled with the elasticity of the neighboring solids) increases from 0.82 to 1.04 µm (Table 4-3), but remains much smaller than the size of the considered particles (32–40 µm). Hence, assuming a similar entrapment mechanism as in circular contacts, a larger number of entrapped particles would be expected in the elliptical configuration.

Figure 4-9 reports the number of dents counted on the discs surfaces after the tests carried out with a contaminated lubricant, for the four different configurations listed in Table 4-3. The number of counted dents is compared with the predictions given by [54]. Three successive tests were performed for the circular configuration and two for the elliptical ones.

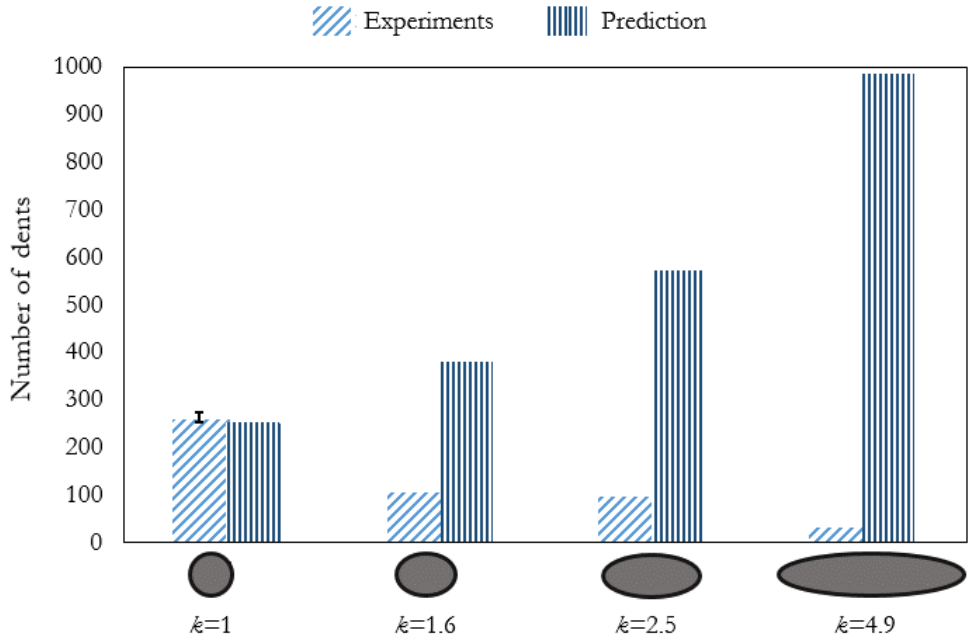

Figure 4-9: Number of dents (corresponding to the number of entrapped particles) in different contacts for steel–steel contacts under pure rolling condition with 10 mg/l contamination (particles 32–40 µm) and conditions of Table 4-1

Very surprisingly, tests revealed a significant decrease in the number of entrapped particles as k increases, a trend that was just opposite to the predictions from Ville's model [54]. Considering the number of entrapped particles found in a circular steel–steel contact as a reference (100 % and Figure 4-9 – k = 1), it appears that for the same contaminated lubricant, the same load and the same mean rolling speed:

- 40% of the particles entered an elliptical contact when k = 1.6;
- About 35% of the particles entered an elliptical contact when k = 2.5;
- And only about 15% of the particles entered an elliptical contact when k = 4.9.

This trend was observed for the entrapment tests whatever the materials of surfaces (see Appendix D).

This decrease of the number of entrapped particles can arise from a geometrical effect. Canzi et al. [136] and Brewe et al. [137] described this one for different geometrical configurations mainly through modifications of the pressure distribution which affect the film thickness formation. More recently, Wheeler et al. [115] showed that in elliptical contacts the geometry of the contact shape affects the lubricant flow, which in turns, impacts the oil film generation. They demonstrated, by analyzing incoming and outgoing flows, that wide elliptical contacts present important backflows. Particle motion being affected by the lubricant flow, a link between backflows and drop of entrapment is assumed.

To offer a more detailed insight on the effect of the contact configuration, numerical simulations were used to evaluate the extent to which the particle trajectories upstream of the contact region were altered by the resulting inlet geometry. Figure 4-10, 4-11 and 4-12 show the lubricant streamlines, in the absence of particles, for the three configurations k = 1, 1.6 and 2.5. These three configurations were numerically parametrized to be representative of the previous twin-disc tests. The streamlines were restricted to those entering the domain in a line defined by a height of 10 µm above the lower surface, x = -2.4 mm, and a width of 200 µm beginning from y = 0.

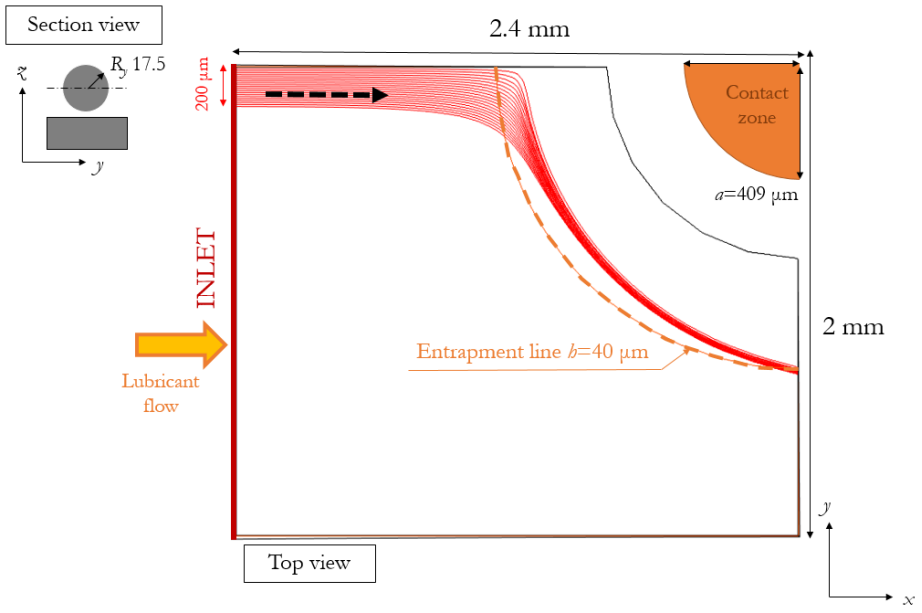

Figure 4-10: Streamlines for a fluid line entering the domain at x = -2.4 mm, Δy = 200 µm, z = 10 µm, for a circular contact (k = 1) and conditions of Table 4-1

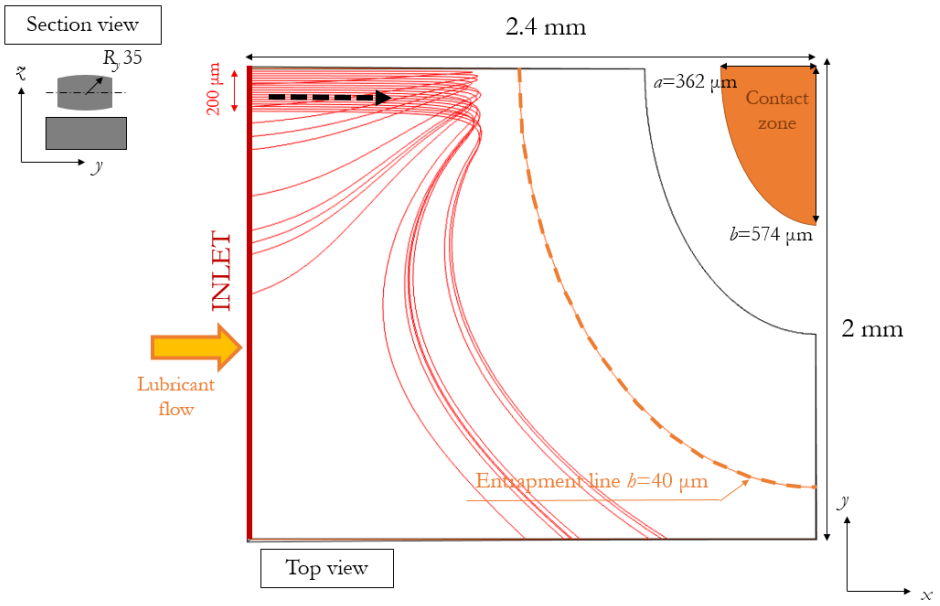

Figure 4-11: Streamlines for a fluid line entering the domain at x = -2.4 mm, Δy = 200 µm, z = 10 µm, for an elliptical contact (k = 1.6) and conditions of Table 4-1

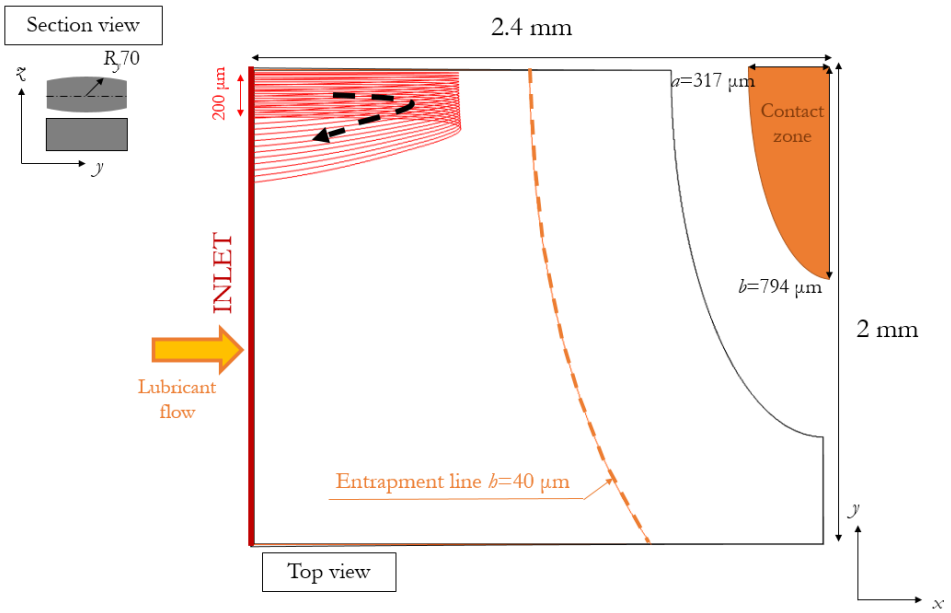

Figure 4-12: Streamlines for a fluid line entering the domain at x = -2.4 mm, Δy = 200 µm, z = 10 µm, for an elliptical contact (k = 2.5) and conditions of Table 4-1

In the circular case (k = 1), streamlines are directed downstream, towards the contact whereas in the elliptical cases (k = 1.6 and 2.5) backflows clearly occur. The larger the elliptical contact width is, the stronger the backflows are. As the particle trajectories are mainly governed by hydrodynamic effects upstream from the contact area, a decrease in the entrapment probability can be expected with increasing ellipticity.

Numerical simulations were performed with a 40 µm particle entering the fluid region. The particle was released near the contact centerline (RP_y = -10 µm) and close to a carrying surface, to be entrapped. A particle released at the same released position (*RP*): RP_x = -2400 µm, RP_y = -10 µm, RP_z = 20 µm is entrapped in the case of a circular configuration (k = 1) whereas it bypasses the elliptical contact (k = 1.6), subjected to important backflows (Figure 4-13).

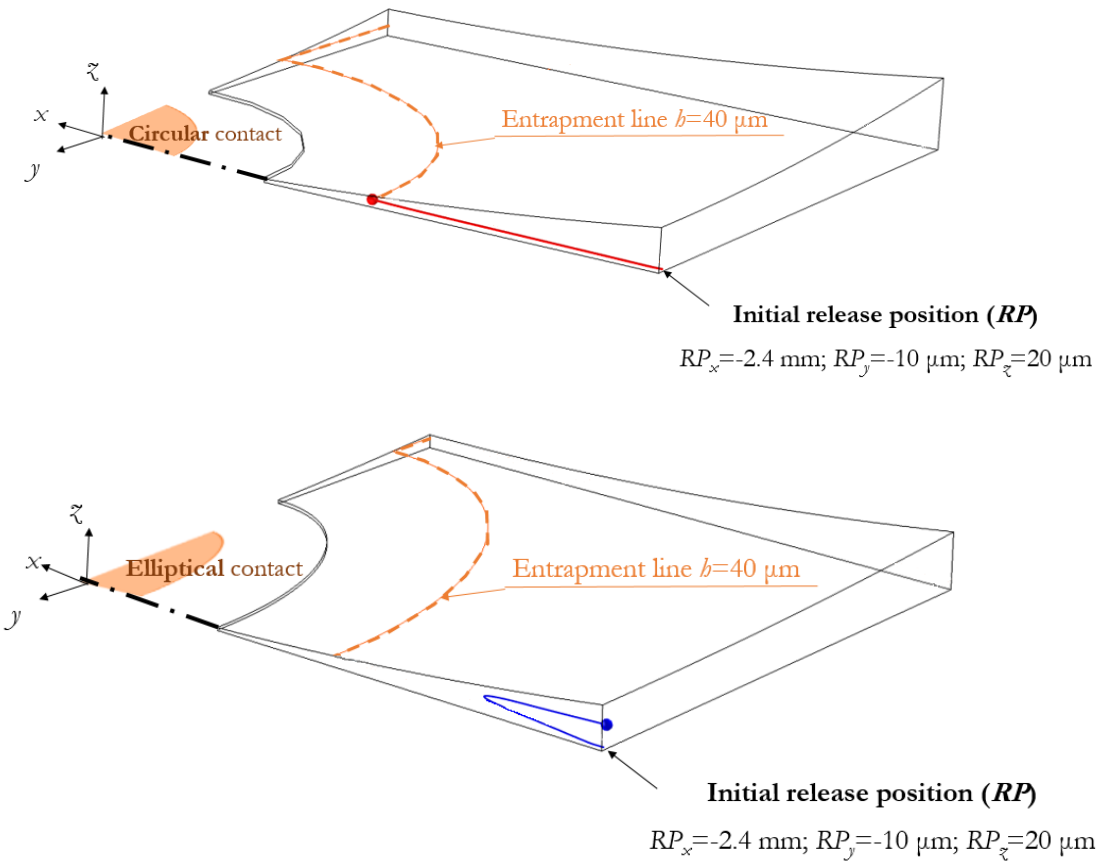

Figure 4-13: Particle trajectories within a circular contact (top) and an elliptical one (bottom) for the same upstream release position: RP_x = -2400 µm, RP_y = -10 µm and RP_z = 20 µm

As discussed by Nikas [22], the presence of backflows does not automatically mean "no entrapment". However, taking place upstream from the theoretical entrapment line in the case of elliptical contacts, these backflows represent a barrier that hinder particles to approach the contact zone. The geometrical configurations of the EHD contact affect directly the entrapment probability, as shown experimentally [138]. The use of numerical simulations allowed to confirm the generation of backflows in elliptical contacts. An experimental evidence of the phenomenon of backflow is proposed in the next section for which a ball or barrel-on-disc machine was combined with a PIV visualization device.

4.3.2 Visualization of lubricant flows in elliptical EHD contacts

The objective is to compare the lubricant flow approaching a circular EHD contact and an elliptical one and to observe the lubricant streamlines, by means of buoyant florescent particles. The experimental visualization was done using a ball or barrel-on-disc set-up and the particle tracking, as exposed in chapter 2.

Different contact parameters (10 or 50 N – 0.005 m/s) were used to validate the link that exists between the formation of backflows and elliptical configurations.

Table 4-4 reports the dimensions of the ball and barrels and related contacting parameters.

Parameters	**Circular**	**Elliptical**	
R_x [mm]	12.7	13.1	13
R_y [mm]	12.7	84.2	330
W [N]	10	50	50
a [µm]	124	151	115
b [µm]	124	513	920
k	1.00	3.46	8.02
P_h [MPa]	312	307	226

Table 4-4: Contact parameters obtained with a steel ball or steel barrel and a glass disc on the ball-on-disc machine

Figure 4-14, 4-15 and 4-16 represent visualizations of upstream flows for a circular and elliptical configurations with a mean rolling speed fixed at 0.005 m/s and an applied load of 10 and 50 N, respectively, to keep a similar Hertzian pressure whatever the geometrical configuration. As in chapter 3 (3.2.1), a sequential lighting with a pulsed laser of 15 Hz-frequency and an optical lens x10 enables a tracking of rhodamine particles that appear like white light spots. The film thickness indication, h = 6 µm (dotted line) which correspond to the mean size of rhodamine particles, is plotted. The Hertzian zone is represented with a striped circle or ellipse. White dotted circles are plotted around some rhodamine particles distributed in the whole contact inlet. At each time step the new position of the tracked particle is spotted and thus, the complete trajectory is summarized in the final picture at t = 0.33s and highlighted with white arrows.

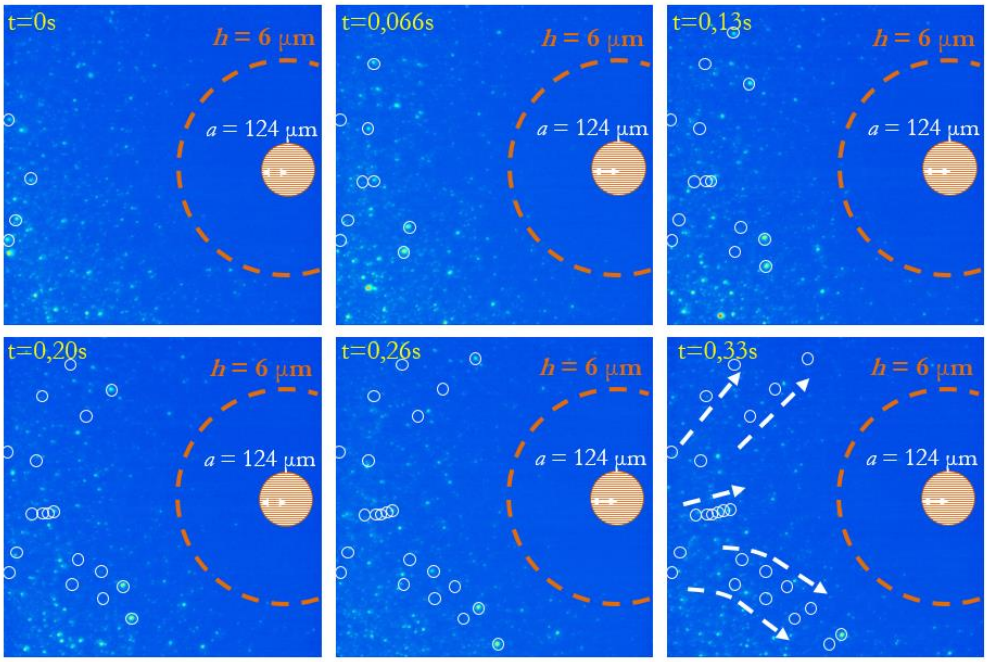

Figure 4-14: Visualization of the fluid flow upstream a steel–glass circular contact with k = 1 (5 mm/s – 10 N)

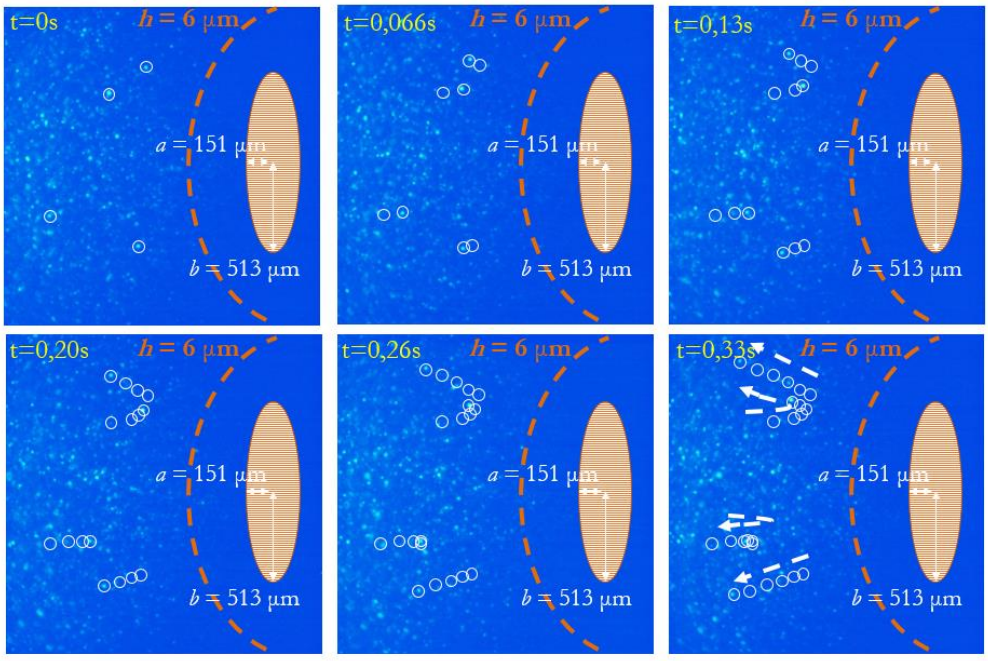

Figure 4-15: Visualization of the fluid flow upstream a steel–glass elliptical contact with k = 3.5 (5 mm/s – 50 N)

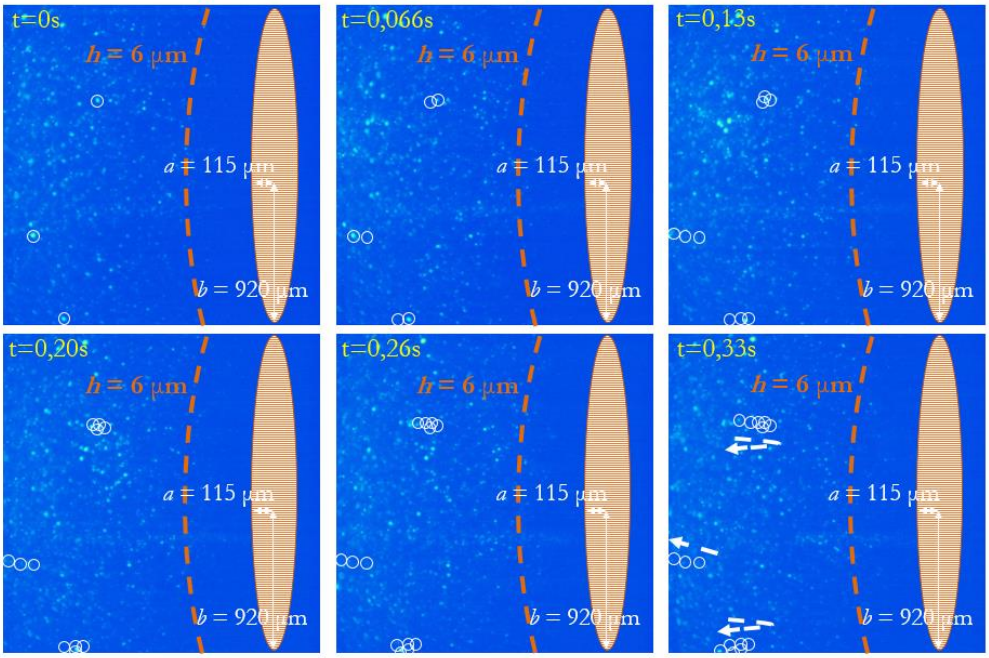

Figure 4-16: Visualization of the fluid flow upstream a steel–glass elliptical contact with k = 8 (5 mm/s – 50 N)

For a circular contact, a large amount of lubricant is bypassing the contact zone but the general motion of the lubricant is oriented towards the contact zone and no backflows are observed. On the contrary, upstream from an elliptical contact, either for k = 3.4 or 8, most of the lubricant is clearly subjected to backflows.

These tests performed with ellipticity ratios equal to 1, 3.4 and 8 can be qualitatively compared with the ones performed on a twin-disc machine with ellipticity ratios equal to k = 1, 1.6, 2.5 and 4.9 (see Figure 4-9). The experiments validate that at the contact inlet of elliptical contacts, strong reverse flows take place and strongly limit the transport of solid contaminant through the contact, as shown numerically in Figure 4-13 and experimentally in Figure 4-15 and Figure 4-16.

After focusing on geometry influence, the aim of the next section is to analyze the influence of the kinematics on entrapment phenomena.

4.4 Effect of Slide-to-Roll ratio

Some studies in the literature have characterized entrapment under rolling–sliding conditions. Ville and Nélias [18], dealing with ductile particles and circular contacts, showed that the particle entrapment probability was only slightly affected by a non-zero SRR, whereas the indentation process remained highly dependent on the value of the SRR.

In the present study, the effect of the SRR will be mainly investigated by testing different contact configurations on the twin-disc machine with different pairs of contacting materials. Figure 4-17 reports observations of entrapment features observed on steel discs for a steel–steel configuration under rolling–sliding condition, for a fixed SRR (12 %).

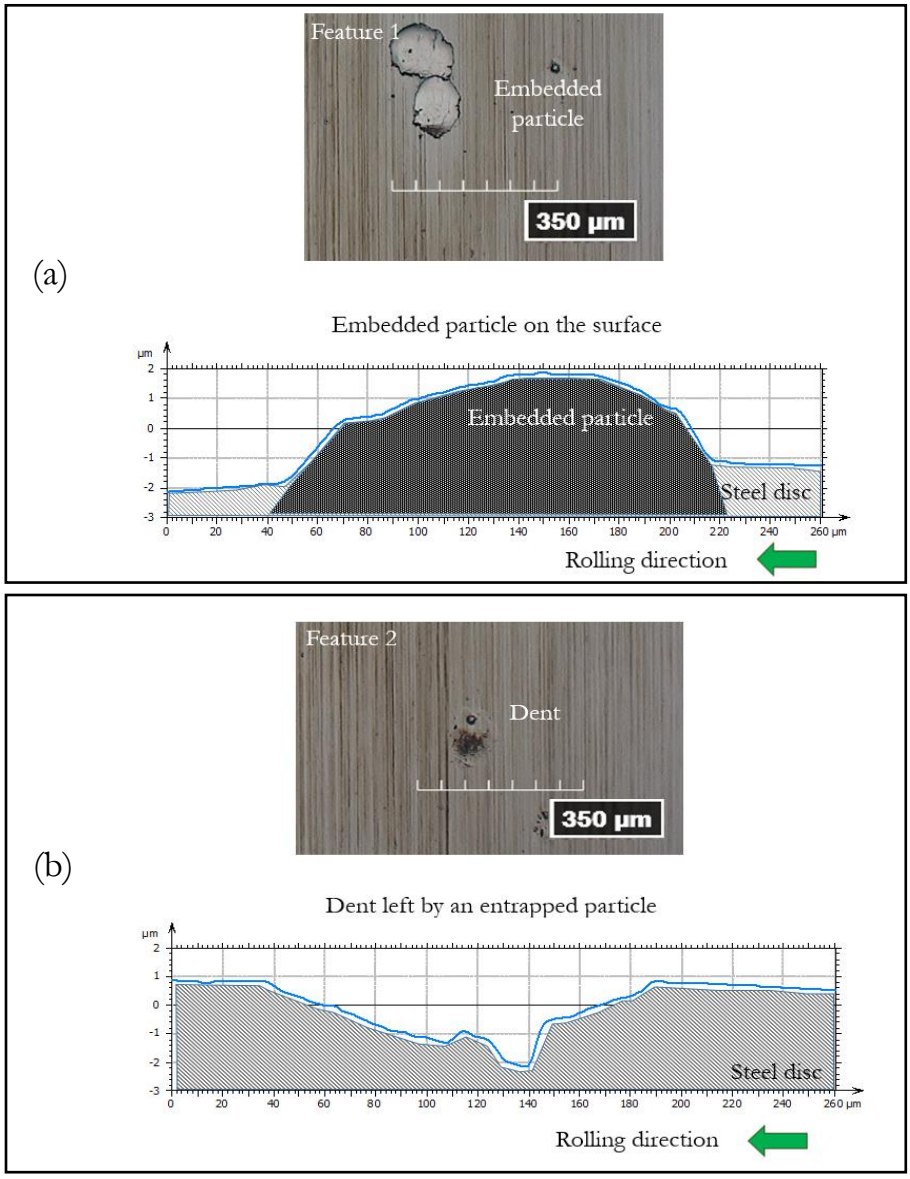

Figure 4-17: Entrapment features after rolling–sliding tests in the steel–steel configuration (600N – 22 m/s – SRR=12%) (a): embedded particles, (b): dents left by entrapped particles

Two types of dent features were observed on the surface of the steel contacting discs. They are different from the ones observed under pure rolling conditions (see Figure 4-5) and can be described as follows: embedded/ flattened particles (Figure 4-17, a) and elongated dents left on the surface (Figure 4-17, b). These features are related to two different stages of the same entrapment mechanism. The first one corresponds to an earlier stage of entrapment, after the particle has been trapped (Figure 4-18, (A)) it is squeezed and sheared (Figure 4-18, (B)) within the contact. And the second feature is the dent left by the particle after being expelled from the contact (Figure 4-18, (C)).

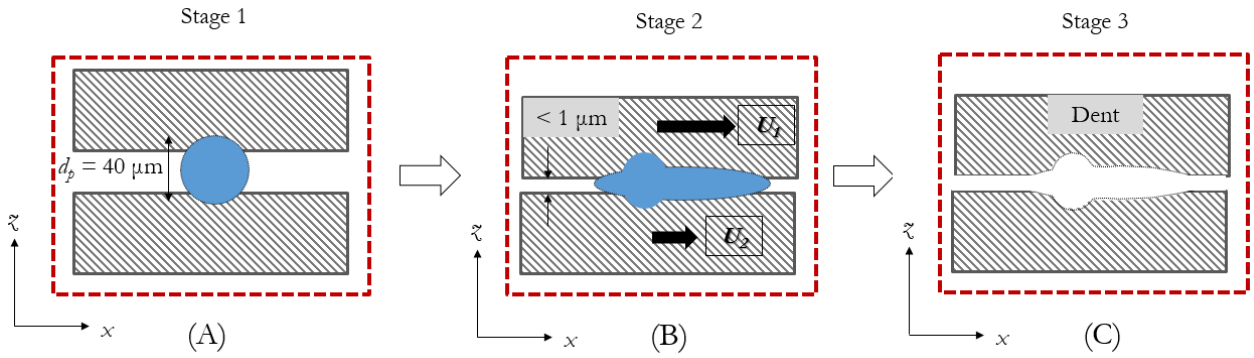

Figure 4-18: Stages of the indentation process during a rolling–sliding test: (A) the particle is trapped between the surfaces, (B) the particle is squeezed and sheared in the contact, (C) the particle is expelled from the contact and the dents caused by entrapment remains on the discs surfaces

This three-stage scenario of entrapment is consistent with previous studies [54,55]. The elongation phenomenon directly affects the dent size. This last one is reported in Table 4-5 (over a sample of 25 dents) revealed by tests in pure rolling and rolling–sliding conditions for all-steel and Si_3N_4–steel contact configurations.

Parameters	**Pure rolling**		**Rolling–sliding**	
Materials	All-steel	Hybrid	All-steel	Hybrid
Size [µm]	70–90	70–90	Length: 110–130 Width: 90–100	Length: 110–140 Width: 90–100
Depth [µm]	2–3	4–5	1–2	2–3
Slope (depth/width)	0.028–0.033	0.055–0.057	0.009–0.015	0.018–0.021

Table 4-5: Dent dimensions (in pure rolling and rolling–sliding conditions) for steel–steel and Si_3N_4–steel contacts with conditions of Table 4-1

Dents found after the pure rolling tests had typically a diameter of 70–90 µm and a depth of 2–3 µm for all-steel contacts and 4–5 µm for Si_3N_4–steel contacts. The rolling–sliding tests induced larger and more elongated dents, with an elliptical shape of length between 110–140 µm, of width between 90–100 µm and depth of 1–2 µm for all-steel contacts and 2–3 µm for Si_3N_4–steel ones. In brief, rolling–sliding conditions cause shallower and more elongated dents. However, the materials effect is

consistent with observations made from pure rolling tests with deeper dents on the steel surfaces of hybrid contact.

Twin-disc tests with a contaminated lubricant and rolling–sliding conditions were carried out to investigate the influence of the kinematics on particle entrapment. Figure 4-19 reports the number of dents counted after the tests with a contaminated lubrication (10 mg/l of 32–40 µm particles) carried out for three elliptical configurations (k = 1, 1.6 and 2.5) in pure rolling and rolling–sliding conditions.

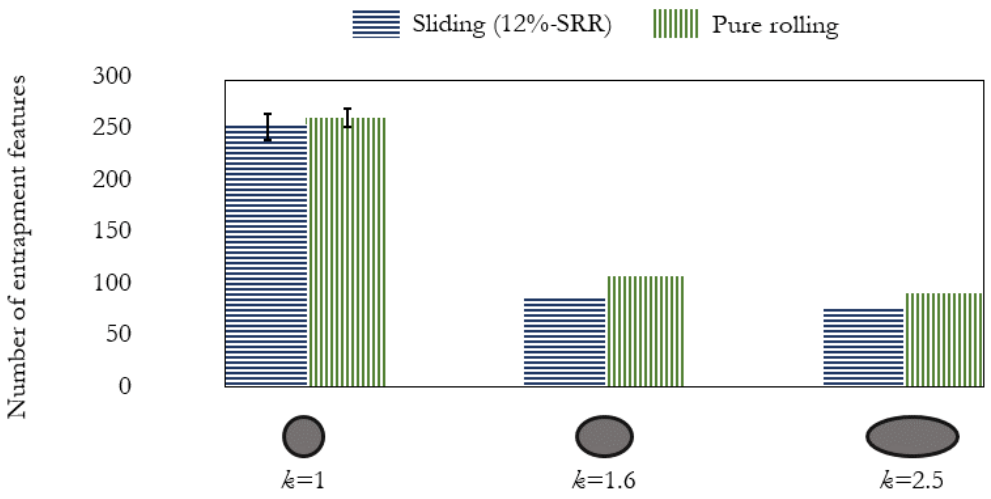

Figure 4-19: Number of dents for different steel–steel twin-disc experiments in pure rolling and in rolling–sliding conditions (SRR=12%) for different configurations: circular (k=1) and elliptical (k=1.6 and 2.5) contacts with conditions of Table 4-1

The figure reports similar numbers of counted dents, which means similar numbers of entrapped particles in pure rolling and rolling–sliding conditions for the different configurations. These tests carried out on elliptical contacts revealed that there was an important effect of the ellipticity ratio as mentioned earlier but no significant effect of the SRR on the number of entrapped particles.

It should be noticed that former numerical [139] and experimental [16,140] studies reported some accumulation of particles at the contact inlet under rolling–sliding conditions. In the present work, no particle accumulation or cluster formation was observed. This was probably due to the high rolling speeds (approximately 22 m/s instead of 0.01-1 m/s in [16,140]), and the lubricant supply through a nozzle located above the contacting discs, leading to a top-down lubrication. The falling of the lubricant may have contributed to limit the particles concentration upstream of the contact.

In hybrid contacts and under rolling–sliding conditions, the faster disc can be either the steel one or the Si_3N_4 one. Figure 4-20 reports the number of entrapment features (see Figure 4-17) revealed after tests with hybrid materials under contaminated lubrication: faster disc is the steel one on the left side of the figure and the Si_3N_4 disc on the right side. It is important to notice that the dents and embedded particles were counted only on the steel surfaces, as the Si_3N_4 remained unmarked. The contamination was composed of 11 mg/l of contaminants in solution (32–40 µm).

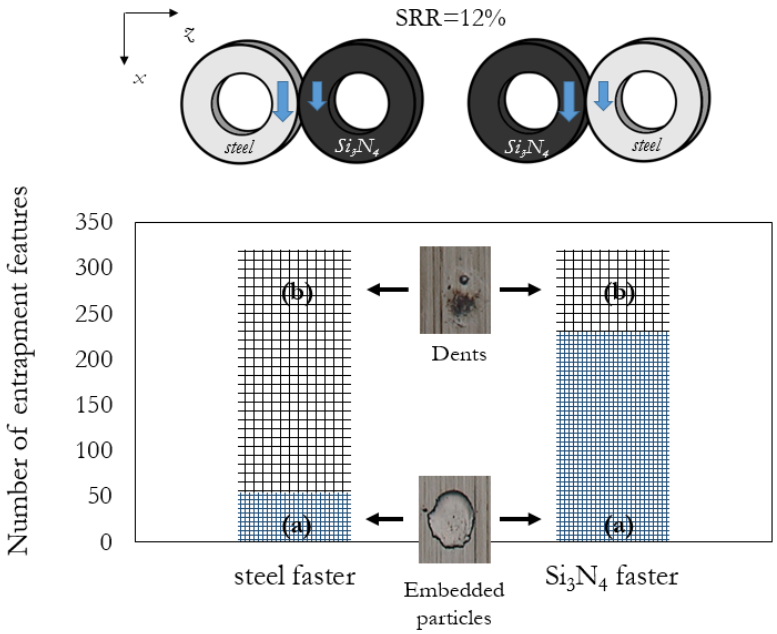

Figure 4-20: Number of dents on the steel disc for two different twin-disc experiments with SRR = 12 % within a hybrid Si_3N_4–steel circular contact with the steel disc moving faster and (left) with the Si_3N_4 disc moving faster (right) with conditions of Table 4-1 with 11 mg/l of contaminants

The figure shows that the number of entrapment features are the same in both cases, with about 320 and 315 dents and embedded particles observed. It suggests that the entrapment probability is not dependent on the material of the faster surface. However, depending on the material of the faster disc, the figure shows that the proportion of dents and embedded particles is different.

When the steel disc moves slower than the ceramic one (Figure 4-20, right), a larger number of particles were found embedded on the surface (72% of feature a) and fewer dents were observed (28% of feature b). In the case of a faster steel disc (Figure 4-20, left), many more dents (83% of feature b) than embedded particles (17% of feature a) were found.

Because of the lower friction properties expected with Si_3N_4 surfaces [1], the number of entrapped particles could be different by using a hybrid pair of discs instead of a pair of steel discs. However, with this further experimental test configuration the results revealed no major differences in terms of the number of entrapped particles, but differences in dent features.

It is also important to notice that the disc surfaces showed morphological differences when considering a hybrid or an all-steel pair of materials. For steel–steel contacts, a worn track appeared on both steel surfaces, as shown on the left of Figure 4-21, whereas for Si_3N_4–steel contacts, no wear track appeared on either the steel or the Si_3N_4 discs (Figure 4-21, right).

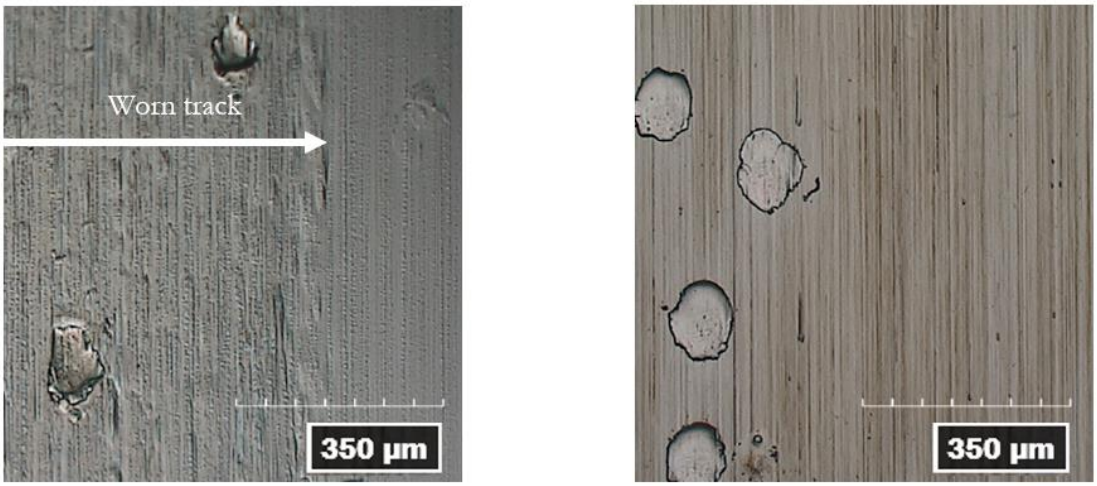

Figure 4-21: Resulting steel disc surfaces with embedded particles observed in both steel–steel and Si_3N_4–steel contacts with SRR=12% with conditions of Table 4-1 with 11 mg/l of contaminants

Worn tracks which appeared on steel surfaces of steel–steel contacts are characterized by small parallel ridges all along the Hertzian zone which did not appeared in Si_3N_4–steel contacts. Some authors have found a tendency toward lower adhesion of hybrid materials compared with an all-steel configuration [1,141]. As explained by Wang et al. [44] using REBs of an air cycle machine, a hybrid pair of materials exhibits no smearing damage, in contrast to a steel–steel pair. Brizmer et al. [142] recently showed that even under poor lubrication condition, Si_3N_4 surfaces lead to lower friction coefficients and smoother counterfaces compared with steel surfaces. Thus, a steel disc paired with a Si_3N_4 disc is unlikely to favor adhesion.

Finally, compared with pure rolling experiments, these tests revealed some alterations of the ceramic surfaces. While Si_3N_4 surfaces suffered no damage or wear under pure rolling, white marks appeared in the rolling–sliding tests. Figure 4-22 reports a picture of a Si_3N_4 surface after a rolling–sliding test with a contaminated lubricant.

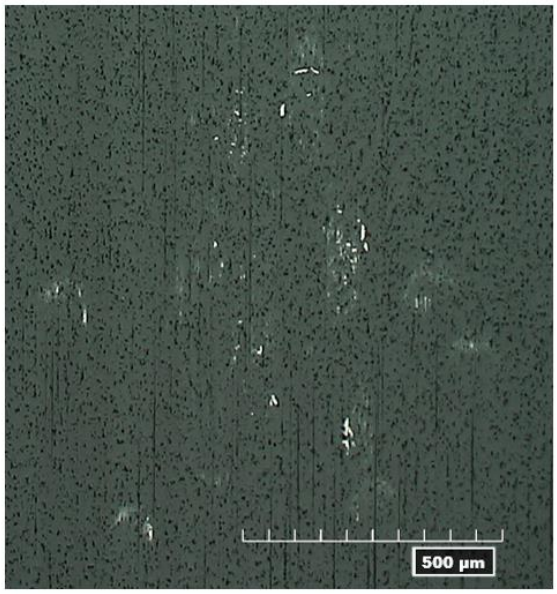

Si_3N_4 surface

Figure 4-22: Marks observed on a Si_3N_4 disc after a rolling-sliding test within a hybrid Si_3N_4–steel contact (600N – SRR=12% – 60°C – 5min)

Some iron oxide from the steel particles might be transferred onto the Si_3N_4 disc, as observed and reported by Sutor in sliding tests [143] with silicon nitride and steel counterfaces. The observed marks are typically between 50 and 100 µm in size, which corresponds to the size of the flattened particles. Dwyer-Joyce [60] focusing on abrasive wear, underlined that ductile particles cannot be treated equivalently to brittle particles that typically present a rigid body behavior. Nevertheless, he reported that with rolling–sliding conditions, the harder of two contacting surfaces will endure the higher rate of wear damage. As steel particles are of smaller hardness than Si_3N_4 discs, these particles are embedded in the steel counterface. Contrary to pure rolling condition, it will periodically rub the Si_3N_4 counterface as long as particles stick the surfaces, leading possibly to material transfer from the embedded steel particles to the ceramic surface.

4.5 Conclusion

Different contacting materials (steel–steel and Si_3N_4–steel), contact configurations (ellipticity ratio of k = 1, 1.6, 2.5, and 4.9 on the twin-disc machine and k = 1, 3.4 and 8 on ball-on-disc machine) and kinematic conditions (pure rolling and rolling–sliding) were considered. Tests with these parameters allowed to highlight specific behaviors related to either particle entrapment probability or particle entrapment mechanism. The following conclusions can be drawn.

- Entrapment probability is not affected by changing steel–steel contacts with Si_3N_4–steel contacts.

- It was established that silicon nitride surfaces have a real ability to resist to indentation by ductile contaminant particles, based on the fact that successive experiments in pure rolling conditions did not affect the silicon nitride discs surfaces. However deeper dents are observed on the steel counterfaces, which increase the risk of crack initiation and justify further research on harder steels, compatible with silicon nitride rolling elements.
- An increase in the contact ellipticity ratio leads to a decrease in the number of entrapped particles, mostly due to stronger backflows occurring upstream the elliptical contacts.
- The effect of the ellipticity ratio dominates over the other effects (kinematics condition or different materials).
- Rolling–sliding conditions do not change the entrapment probability but affect the entrapment mechanism. Dents are found shallower and elongated compared to the ones under pure rolling condition. With Si_3N_4–steel, the dents are found to be deeper, as in pure rolling. Depending on the contacting materials and the kinematics, either more dents or embedded particles are found.

General Conclusions and Prospects

General Conclusions

The phenomenon of particle entrapment within elastohydrodynamic (EHD) contacts, occurring in rolling element bearings (REBs) of aerospace applications is investigated in this work. This study proposes a new insight on the mechanisms leading to entrapment supported by a numerical modelling together with twin-disc and ball-on-disc experiments under contaminated lubrication. An original analysis was introduced using the Particle Image Velocimetry (PIV) technique.

A state of the art is exposed in **chapter 1**, depicting researches focused on entrapment in EHD contacts. Early works aimed at establishing the consequences of entrapment by observing the damages left by entrapped particles on the contacting surfaces. Later, studies investigated single ideal contacts and parameters leading to entrapment. The current trend is to model even more realistic contacts to establish the impact of the new REB design including new type of contacting materials, like hybrid Si_3N_4–steel or the wide ranges of encountered REB geometries.

Chapter 2 is dedicated to the presentation of the numerical model and of the experimental devices available at laboratory and developed during this study. Assuming entrapment is highly related to the flow of lubricant in the contact inlet, the numerical model combines both the resolution of the lubricant flow through the fluid mechanics theory and the consideration of the particle trajectories by solving Newton's law. Concerning experiments, a twin-disc machine combined with a contamination control device enabled to perform quantitative entrapment tests: knowing the nature and concentration of the suspended particles, a direct correlation between the indentation marks left by solid contaminants on the contacting discs and the number of entrapped particles is made. A ball-on-disc machine was used in a glass–steel configuration to get an in-situ visualization of the EHD contact and its vicinity. The direct observation of particle entrapment is possible using a fluorescent "paint" in combination with the PIV technique.

In **chapter 3** a phenomenological approach of entrapment is proposed. An innovative method using PIV technique allows to track steel rhodamine-coated particles during their entrainment in the contact inlet, their entrapment and their passing through the contact itself. Then, the confrontation of results from numerical simulations and observations from twin-disc experiments enables to study particle entrapment within a wide number of different EHD contacts. This draws the following conclusions on the behavior of entrained contaminants within steel–steel contacts.

- Particle entrainment is linked to its entry position. If released close to the symmetry plane (along the y-axis) and in the vicinity of the surface (z-axis) particles are more likely to be entrapped.
- Large and heavy particles are more likely to be entrapped. In the framework of this study, steel particles larger than 15 µm are more likely to be entrapped than sand or volcano ash ones smaller than 15 µm.
- Increasing rolling speeds enhance the chance to capture particles.
- Particle entrapment increases with increasing load.

An analytical formulation of the lubricant flow at the contact inlet enables to synthesize these statements.

After proposing a new point of view on particle entrapment in idealized steel–steel circular contacts the work focused on more realistic EHD contacts encountered in REBs in the framework of aerospace applications. This work is presented in **chapter 4**, and the main conclusions are the following.

- Entrapment probability is not affected by changing steel–steel contacts with Si_3N_4–steel contacts but silicon nitride surfaces show a real ability to resist to indentation by ductile particles.
- Under rolling–sliding conditions, the number of entrapped particles is similar to that in the pure rolling case but the dents left on the surfaces are found to be more elongated. With a Si_3N_4–steel contact under rolling–sliding conditions, the damage typology is clearly affected by the nature of the faster surface.
- Geometrical configuration influences strongly the number of entrapped particles. Within wide elliptical contacts a severe drop of the number of entrapped particles was observed which is due to backflows occurring in the contact inlet. The ellipticity effect dominates over other effects (kinematics, material of contacting surfaces).

The complementarity of the three numerical and experimental approaches is underlined on this last point concerning the effect of the geometrical configuration.

i) Twin-disc experiments revealed an important decrease of the number of entrapped particles in elliptical contacts in comparison to circular ones.
ii) Numerical simulations enabled to validate the assumptions of backflows occurring within elliptical EHD contacts that hinder particle entrainment.
iii) The use of the PIV technique on the ball-on-disc machine with specific barrel samples allowed to observe the reverse flows existing in elliptical contacts.

Prospects

Phenomena leading to particle entrapment can be widely studied experimentally and numerically.

Experimental techniques showed to be limited by the test-rig characteristics. The twin-disc machine enables to reproduce highly loaded contacts with important mean rolling speeds but gives no in-situ visualization. On the contrary, the ball-on-disc test rig in glass–steel configuration offers a convenient facility to get a visualization of the lubricant meniscus but for less severe contact conditions and at least one transparent surface. Hence, further investigations on alternative common tribometer architectures may offer possibilities to reproduce typical aeronautical contacts (high loads and mean rolling speeds) and to get in-situ information using transparent materials. Moreover, the use of PIV technique with high-speed cameras, continuous lasers and objectives with thinner depths of focus will allow to track particles, even for high mean rolling speeds.

Numerically, the current model allows to consider particle contaminants, one by one which is inconsistent with advanced stages of contamination. First, particle-particle interactions model could allow to investigate the formation of particle clusters at the contact inlet. It may then be possible to reproduce particle accumulation leading to oil starvation for extreme cases. Then, using moving mesh method, a more accurate physical description of entrapment could be obtained considering the particle-fluid and particle-surface interactions.

From another point of view, entrapment is only the first step to predict contact fatigue life under contaminated lubrication. Even if nowadays the link between dent geometry and life reduction is established, further development seems necessary for hybrid contacts. In fact, it was shown, in the present study, that Si_3N_4 surfaces present a high resistance to indentation which induces deeper dents on the steel counterfaces. This last point should lead to premature failure of steel surfaces compared to steel–steel contacts and must lead to the development of new materials such as NiTi proposed recently by the NASA [144].

Finally, considering REBs the main prospects concern:

- the design of new REBs: from a geometrical point of view deducted from the observed backflows in wide elliptical contacts which may drastically reduce the number of entrapped particles;
- the understanding of lubricant flows inside REBs: to complete the present study focused on the contact inlet, it is necessary to describe the general lubricant motion with CFD simulations on a whole REB for example. Moreover, more complex REB geometries like the ones in contacts between tapered rollers end and flanges must be analyzed;
- the analyse of the impact of lubrication regimes: in most of applications, starvation could occur leading to worst contact conditions with particles possibly entrained in the direct vicinity of entrapment area.

All these prospects may have to be confirmed on a full-scale test rig for aeronautical applications, in terms of component sizes and operating conditions, with a controlled contaminated lubrication.

Appendices

Appendix A **Entrapment of volcano ashes**

Entrapment of volcano ashes can possibly occur in aeronautical REBs. The recent volcanic eruption in Iceland of the Eyjafjallajökull volcano (2010) disrupted the european air traffic for more than two weeks. That is why investigations on the consequences of the entrapment of volcano ashes in EHD contacts, were carried out. This should help to evaluate the damage risk followed by the intake of such particles in the turbofan, and so within REBs through the lubrication system. An experimental work on the twin-disc machine with a mixture of oil and ashes, allowed to investigate the effects of such phenomenon. Comparisons hereafter were performed for different EHD contacts made of steel–steel or Si_3N_4–steel pairs of discs.

These tests are of interest as the NASA recently published a report [145] on full-scale tests with airplane engines fed with volcano particles, as represented on Figure A-1.

Figure A-1: Full-scale test of volcano particle intake performed by NASA [145]

It was clearly demonstrated that the primary risk is on turbine blades, however REB damage should be taken into account.

In the present study, two types of volcano ashes were observed with scanning electron microscope (SEM), one from El Misti volcano, Peru and another one from Fuji Mount, Japan (Figure A-2).

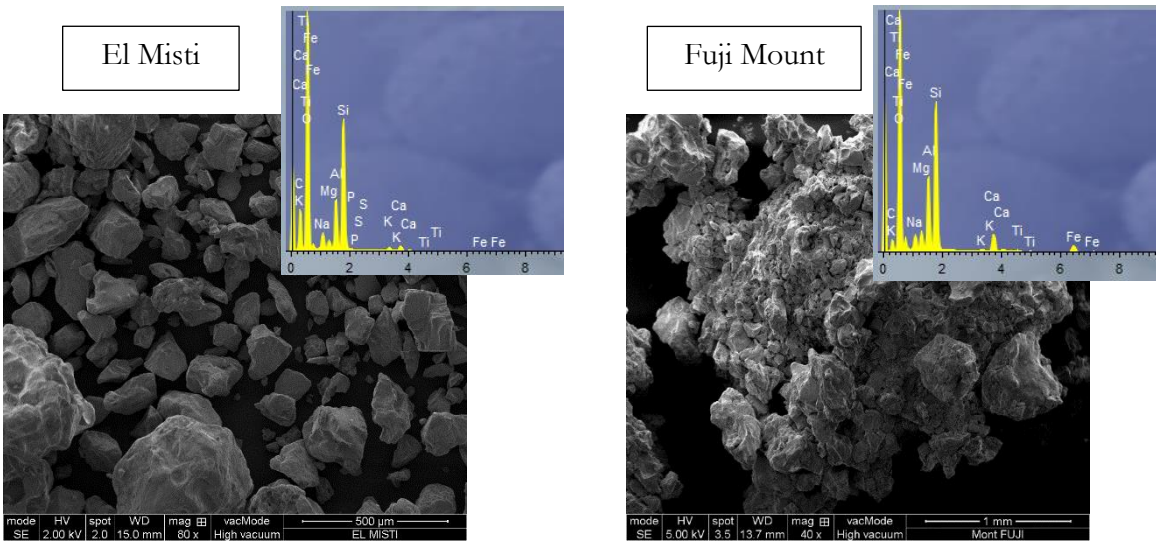

Figure A-2: SEM pictures of the volcano ashes (from El Misti volcano, Peru and from Fuji Mount, Japan) and Energy-dispersive X-ray spectroscopy (EDX) analysis revealing the ash compositions

The composition of both ashes is very similar with the presence of silicium (Si), potassium (K), iron (Fe), sodium (Na), magnesium (Mg) and some traces of titanium (Ti). The ash particles were dried to avoid any further oxidation but not sieved. Hence, the size spectrum is large, varying from some microns to several hundreds of microns. As there were many more particle clusters in the ashes from the Fuji Mount, only tests with the El Misti ashes were performed.

Table A-1 reports twin-disc tests performed with the following operating conditions: 600 N – 22 m/s – 60 °C – 5 min, using steel–steel contacts or Si_3N_4–steel ones and circular or elliptical contacts.

Cylindrical disc	Crowned disc	Ellipticity ratio
M50 steel	AISI 52100 steel with R_y 17.5	1
Si_3N_4	AISI 52100 steel with R_y 17.5	1
M50 steel	M50 steel with R_y 35	1.6
M50 steel	M50 steel with R_y 70	2.5

Table A-1: Pair of contacting materials for twin-disc tests performed with volcano ashes with the following operating conditions: 600 N – 22 m/s – 60 °C – 5 min

Tests with different type of contact configurations enabled to compare the entrapment mechanism, especially by studying the kind of damages that results from the entrapment of these brittle particles. Brittle particles are known to be crushed into many thin and tough micrometric particles that cause abrasive wear [55] and cause small indentation marks [54]. Figure A-3 shows indentation marks left on a steel surface caused by the entrapment of volcano ash particles.

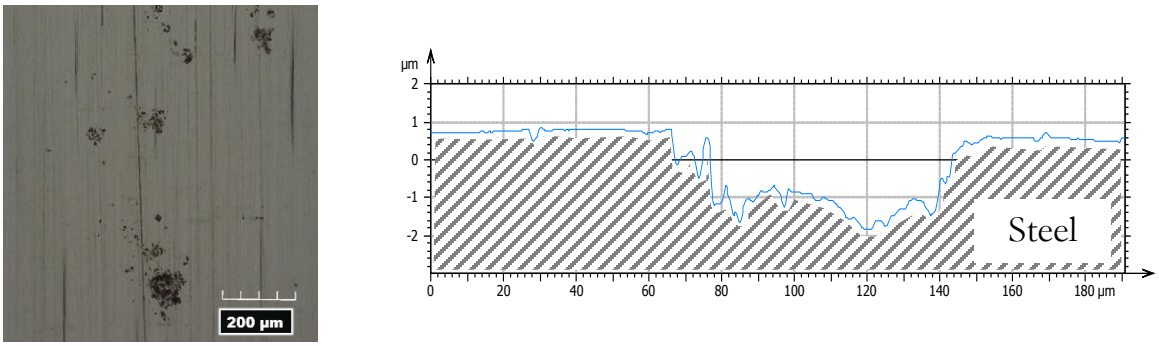

Figure A-3: Indentation marks left on the steel surface after a twin-disc test with a steel–steel contact with the operating conditions: 600 N – 22 m/s – 60 °C – 5 min

The damage feature is consistent with those from similar tests performed with brittle particles. They crushed in the contact in many tough fragments and severely damaged the surface. For a not sieved ash powder with a large size spectrum, the indentation marks are about 3 µm deep, and about 20–80 µm large.

The same features are observed on the steel counterfaces of steel–steel or Si_3N_4–steel contact. However, the Si_3N_4 suffers from no damage similarly as with M50 steel particles entrapment, which underlined the ability of silicon nitride to also resist to indentations made by brittle particles.

A comparison with boron carbide particles for similar operating conditions and assuming similar mechanical properties to ashes (in terms of fracture toughness and hardness), revealed similar damage features, as shown in Figure A-4.

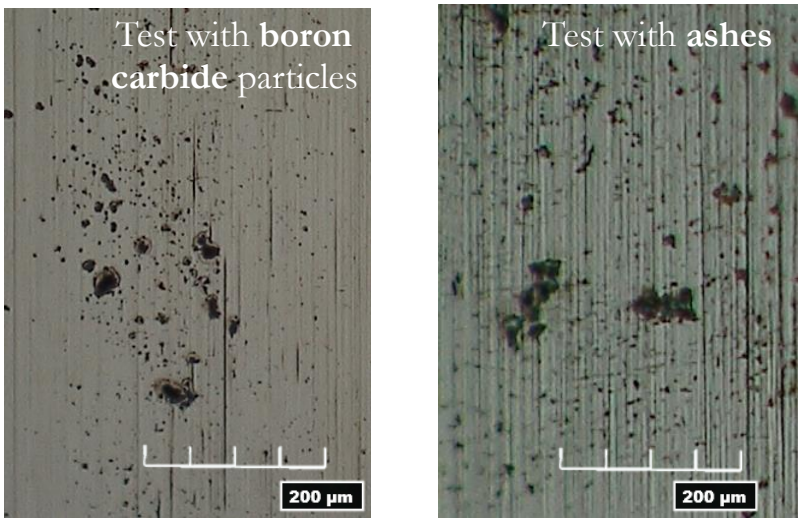

Figure A-4: Indentation marks left on steel counterfaces after two different twin-disc tests with a hybrid Si_3N_4–steel couple of contacting materials with the operating conditions: 600 N – 22 m/s – 60 °C – 5 min and two types of particles dispersed in the lubricant (boron carbide – left and El Misti volcano ashes – right)

Finally, by performing entrapment tests with the twin-disc machine and elliptical contact configurations, it was not possible to underline a specific effect of the ellipticity. The fracture of the ashes in tiny fragments made difficult any quantitative counts.

Appendix B **Mapping of the velocity vectors**

The fluorescence technique enables to perform PIV analyses, as presented in chapter 3 for circular contacts. After a sequential lighting by two synchronized pulses (lasers A and B), the camera is recording two separate image frames and the mapping of the velocity vectors is obtained by cross-correlation (chapter 2). Figure B-1 shows the way to obtain the mapping of the velocity vectors using the experimental ball-on-disc machine combined with a PIV analysis set-up. The microscope is focused on an upstream zone of the lubricant meniscus. The light emitted by the fluorescent particles, which are within the objective depth of focus, are captured by the microscope. In the case of the performed PIV measurements, the depth of focus are too thick, 5–60 µm for the different objectives (see chapter 2, 2.3.2.4), to discriminate flow phenomena across the film thickness. However, a 2D-visualization of the fluid flow is possible.

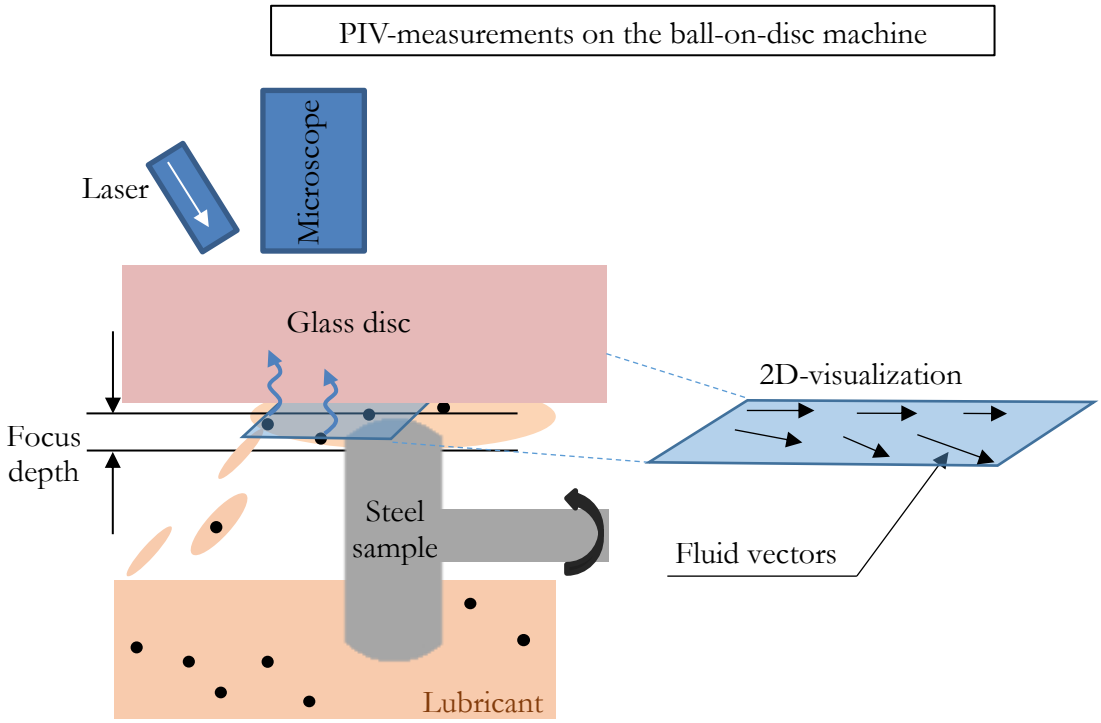

Figure B-1: Mapping of the velocity vectors using the experimental ball-on-disc set-up with a PIV analysis

This mapping of the velocity vectors, obtained experimentally for glass–steel circular contacts with rolling speed varying between 0.005 and 3 m/s and applied load from 10 to 50 N, can be compared to velocity vectors obtained with the numerical simulations. Figure B-2 reports the way to get a mapping of the fluid velocity vectors using the numerical modelling. Once the Navier-Stokes equations are solved, fluid velocity vectors can be simply described on different height sections across the fluid domain. Here, the mapping of the fluid vectors is defined on a mean section across the fluid domain.

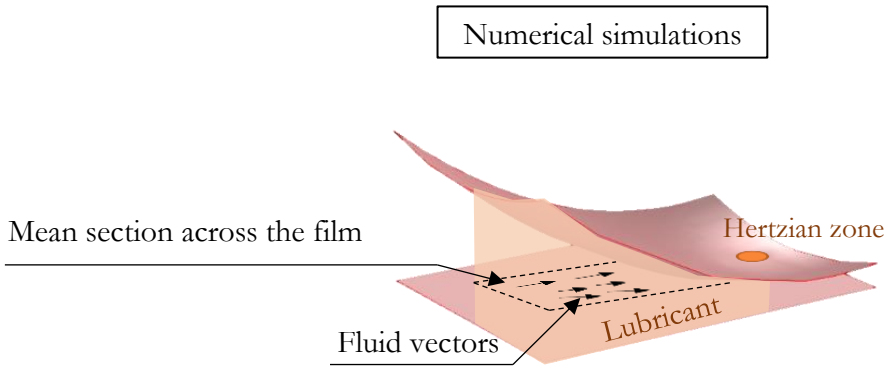

Figure B-2: Mapping of the velocity vectors using the numerical simulations

Fluid vectors obtained numerically on eleven different section heights are averaged to be compared to experimental measurements. Figure B-3 reports the comparison between the mapping of velocity vectors obtained with a PIV analysis and the mapping of the velocity vectors obtained numerically for a glass–steel contact with 0.5 m/s-mean rolling speed and 10 N-load.

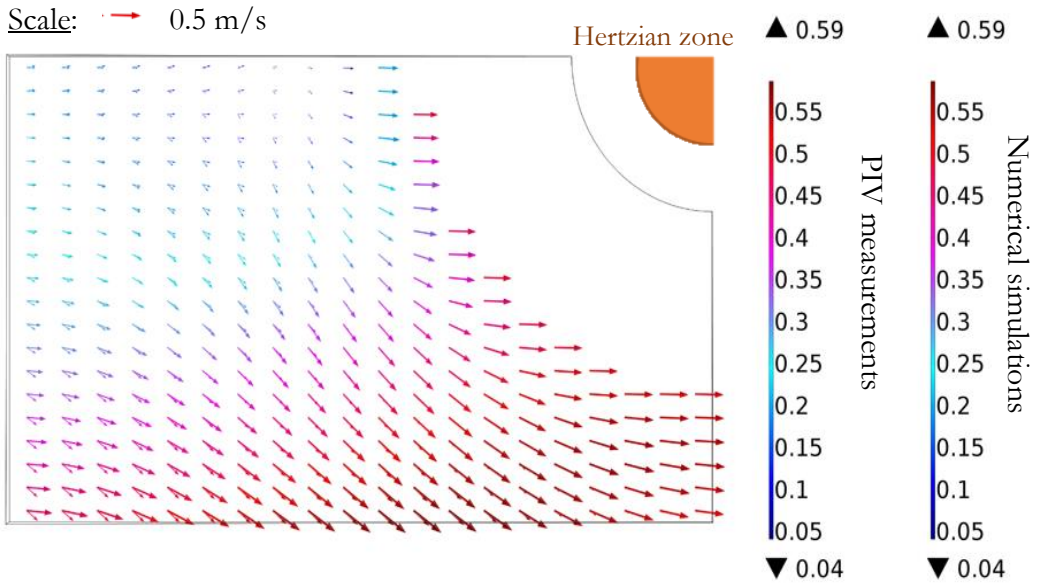

Figure B-3: Comparison of the velocity vector mapping for the experimental ball-on-disc machine and using the numerical simulation for a circular glass–steel contact
with following operating conditions: 10 N applied load and 0.5 m/s rolling speed

Some discrepancies appear between the two resulting mappings of the velocity vectors (near the left bottom edge), but general trends are in agreement. These discrepancies are mainly due to the lack of precision on the experimental mapping.

Appendix C **Velocity profile at the contact inlet**

The velocity profile at the contact inlet along the symmetry plane and for fully-flooded condition is derived from the velocity component along *x*:

$$u(z)=\frac{1}{2\mu}\frac{\partial p}{\partial x}\frac{z}{h}\left(\frac{z}{h}-1\right)h^2+U_{1,x}\frac{z}{h}+U_{2,x}\left(1-\frac{z}{h}\right) \quad (C\text{-}1)$$

Poiseuille Couette

Simplifying the velocity equation, with $Z=\frac{z}{h}$, $K_1=\frac{1}{2\mu}\frac{\partial p}{\partial x}h^2$ and $U_{1,x}=U_{2,x}=U_m$, it is possible to solve a 2nd order equation:

$$K_1Z^2-K_1Z+U_m=0 \quad (C\text{-}2)$$

As long as the fully-flooded condition is respected, the flow at the contact inlet is a combination of both Couette and Poiseuille contributions as commonly assumed [146]. Hence, there are two solutions for this problem and the discriminant $\Delta=K_1^2-4K_1U_m$ is positive which results in two solutions that can be expressed as follows:

$$Z_{1,2}=\frac{1}{2}\pm\frac{\sqrt{1-\frac{4U_m}{K_1}}}{2} \quad (C\text{-}3)$$

The heights, $Z_{1,2}$, where an equilibrium between the Couette and Poiseuille flows occur, are functions of the rolling speed, U_m, the pressure gradient $\frac{\partial p}{\partial x}$, the viscosity, μ, and the film thickness, h. Assuming that the pressure gradient can be derived from the one dimensional Reynolds equation and by neglecting the compressibility effects, it is possible to write:

$$\frac{\partial}{\partial x}\left(\frac{h^3}{12\mu}\frac{\partial p}{\partial x}\right)=\frac{12\mu}{h^3}U_m\frac{\partial h}{\partial x} \quad (C\text{-}4)$$

Integrating once, the pressure gradient can be expressed in relation with the central film thickness h_c:

$$\frac{\partial p}{\partial x}=12\mu U_m\frac{h-h_c}{h^3} \quad (C\text{-}5)$$

Then, the film thickness in the contact, h_c (tenths of microns) is neglected compared to the film thickness in the contact inlet, h (hundreds of microns) and the pressure gradient can be approximated by $\frac{\partial p}{\partial x} = \frac{12\mu U_m}{h^2}$. The pressure-dependent constant, $K_1 = \frac{1}{2\mu}\frac{\partial p}{\partial x}h^2$ can be then expressed: $K_1 = \frac{1}{2\mu}\frac{12\mu U_m}{h^2}h^2 = 6U_m$. Finally, in the contact inlet, it appears that the velocity profile can be described as a parabolic profile, whose equation is:

$$u(Z) = 6U_m Z^2 - 6U_m Z + U_m$$

$$\text{With } Z_{1,2} = \left(\frac{z}{h}\right)_{1,2} = \frac{1}{2} \pm \frac{\sqrt{1/3}}{2} \qquad \text{(C-6)}$$

Appendix D **Entrapment results for hybrid elliptical contacts**

Twin-disc tests were performed with hybrid Si_3N_4–steel contacts and three elliptical configurations: k = 1, 1.6 and 2.5. As it was demonstrated in chapter 4 (4.2) for circular contacts under pure rolling, the number of entrapped particles is not much affected by the nature of the contacting materials when $E_1 \approx E_2$.

Figure D-1 reports the number of dents counted on the disc surfaces after the tests with a contaminated lubricant, for three different contact configurations with Si_3N_4–steel discs under pure rolling condition and with a constant load.

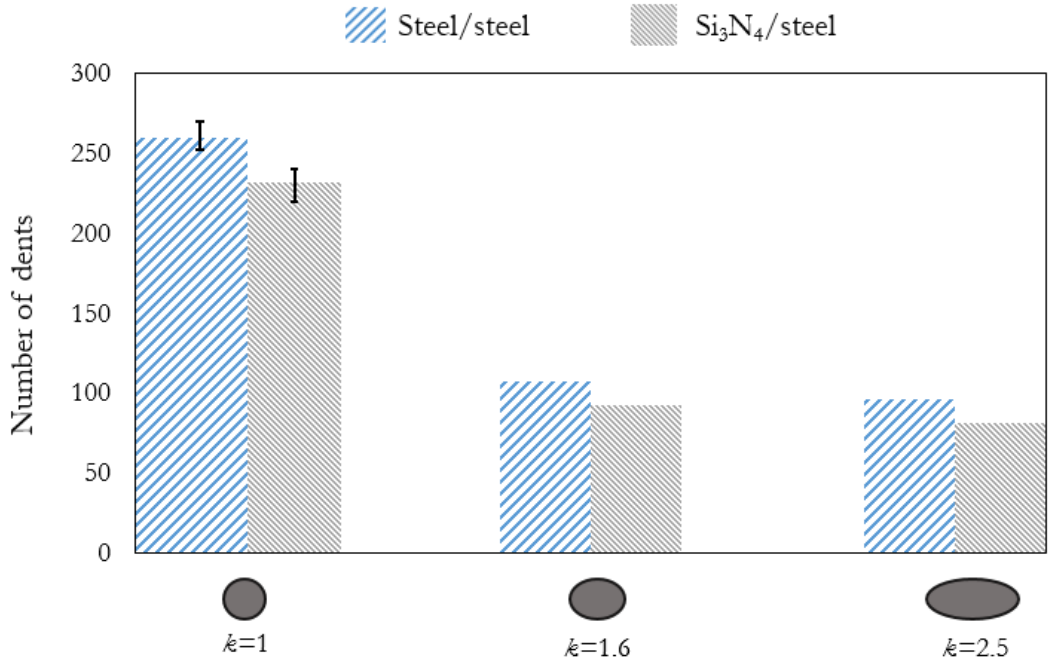

Figure D-1: Number of dents (corresponding to the number of entrapped particles) for different pure rolling experiments, with steel–steel and Si_3N_4–steel contacting discs for different contact configurations: k=1, k=1.6 and 2.5 with 10 mg/l contamination and conditions of Table 4-1

Figure D-1 shows that particles are much less entrapped in elliptical contacts than in circular ones whatever the materials of surfaces. The tendency of a lower entrapment within elliptical contacts is in agreement with the previous observations. The small difference, observed between all-steel and Si_3N_4–steel cases, is consistent with the changes in terms of contact geometry and with the slightly smaller EW observed in the hybrid cases compared with the all-steel ones.

References

[1] Tonicello, E., Girodin, D., Sidoroff, C., Fazekas, A., and Perez, M., 2012, "Rolling bearing applications: some trends in materials and heat treatments," Materials Science and Technology, **28**(1), pp. 23–26.

[2] Wang, W., Wong, P. L., He, F., and Wan, G. T. Y., 2007, "Experimental study of the smoothing effect of a ceramic rolling element on a bearing raceway in contaminated lubrication," Tribology Letters, **28**(1), pp. 89–97.

[3] Sawaguchi, A., Toda, K., and Niihara, K., 1991, "Mechanical and electrical properties of silicon nitride--silicon carbide nanocomposite material," Journal of the American Ceramic Society, **74**(5), pp. 1142–1144.

[4] Niizeki, S., 2000, "Ceramic bearing for special environments," NSK J. Motion Control, (8), pp. 17–22.

[5] Kaneta, M., Yang, P., Krupka, I., and Hartl, M., 2014, "Fundamentals of thermal elastohydrodynamic lubrication in Si3N4 and steel circular contacts," Proceedings of the Institution of Mechanical Engineers, Part J: Journal of Engineering Tribology, **229**(8), pp. 929–939.

[6] Savio, D., Fillot, N., Vergne, P., Hetzler, H., Seemann, W., and Espejel, G. E. M., 2015, "A Multiscale Study on the Wall Slip Effect in a Ceramic--Steel Contact With Nanometer-Thick Lubricant Film by a Nano-to-Elastohydrodynamic Lubrication Approach," Journal of Tribology, **137**(3), pp. 1–13.

[7] Lakshminarayanan, R., Chao, L. Y., Iyer, N., and Shetty, D. K., 1997, "Wear of steel in rolling contact with silicon nitride," Wear, **210**(1), pp. 278–286.

[8] Kalin, M., Vižintin, J., Novak, S., and Dražič, G., 1997, "Wear mechanisms in oil-lubricated and dry fretting of silicon nitride against bearing steel contacts," Wear, **210**(1), pp. 27–38.

[9] Novak, S., Dražič, G., Kalin, M., and Vižintin, J., 1999, "Interactions in silicon nitride ceramics vs. steel contact under fretting conditions," Wear, **225**, pp. 1276–1283.

[10] Chao, L.-Y., Lakshminarayanan, R., Iyer, N., Lin, G.-Y., and Shetty, D. K., 1998, "Transient wear of silicon nitride in lubricated rolling contact," Wear, **223**(1), pp. 58–65.

[11] Leng, J. A., and Davies, J. E., 1988, "Ferrographic examination of unused lubricants for diesel engines," Wear, **122**(1), pp. 115–119.

[12] Stachowiak, G. W., Kirk, T. B., and Stachowiak, G. B., 1991, "Ferrography and fractal analysis of contamination particles in unused lubricating oils," Tribology International, **24**(6), pp. 329–334.

[13] Akl, E. Y., Khalifa, S. E., Flamand, L., and Berthe, D., 1987, "Investigation of wear debris associated with different stages of operation in EHD contact," Second ASAT Conférence, Caire, pp. 671–687.

[14] Nélias, D., 1989, "Etude du glissement dans les roulements a billes grande vitesse de turbomachines: influence de la pollution," Thèse de Doctorat, INSA-Lyon, Villeurbanne, n° ordre 1989-ISAL-0083, 292 p.

[15] Fitzsimmons, B., and Clevenger, H. D., 1977, "Contaminated lubricants and tapered roller bearing wear," ASLE Transactions, **20**(2), pp. 97–107.

[16] Wan, G. T. Y., and Spikes, H. A., 1988, "The behavior of suspended solid particles in rolling and sliding elastohydrodynamic contacts," STLE Transactions, **31**(1), pp. 12–21.

[17] Cann, P. M., Sayles, R. S., Spikes, H. A., Ioannides, E., and Hamer, J. C., 1996, "Direct observation of particle entry and deformation in a rolling EHD contact," Proceedings of the 22nd Leeds–Lyon Symposium on Tribology, Elsevier Tribology and Interface Engineering Series 31, Dowson, et al. (Eds.), pp. 127–134.

[18] Ville, F., and Nelias, D., 1999, "An Experimental Study on the Concentration and Shape of Dents Caused by Spherical Metallic Particles in EHL Contacts," Tribology Transactions, **42**(1), pp. 231–240.

[19] Dwyer-Joyce, R. S., and Heymer, J., 1996, "The entrainment of solid particles into rolling elastohydrodynamic contacts," Proceedings of the 22nd Leeds–Lyon Symposium on Tribology, Elsevier Tribology and Interface Engineering Series 31, Dowson, et al. (Eds.), pp 135–140.

[20] Nikas, G., 1999, "Theoretical modelling of the entrainment and thermomechanical effects of contamination particles in elastohydrodynamic contacts," PhD Thesis, University of London, London, 342 p.

[21] Nikas, G. K., 2001, "Mathematical analysis of the entrapment of solid spherical particles in non-conformal contacts," Journal of Tribology, **123**(1), pp. 83–93.

[22] Nikas, G. K., 2002, "Particle entrainment in elastohydrodynamic point contacts and related risks of oil starvation and surface indentation," ASME Transactions Journal of Tribology, **124**(3), pp. 461–467.

[23] Nikas, G. K., 2006, "A mechanistic model of spherical particle entrapment in elliptical contacts," Proceedings of the Institution of Mechanical Engineers, Part J: Journal of Engineering Tribology, **220**(6), pp. 507–522.

[24] Kahlman, L., and Hutchings, I. M., 1999, "Effect of particulate contamination in grease-lubricated hybrid rolling bearings," Tribology Transactions, **42**(4), pp. 842–850.

[25] Lundberg, G., and Palmgren, A., 1949, "Dynamic Capacity of Rolling Bearing," Journal of Applied Mechanics, **16**(2), pp. 165–172.

[26] Harris, T. A., and Mindel, M. H., 1973, "Rolling element bearing dynamics," Wear, **23**(3), pp. 311–337.

[27] Zaretsky, E. V, Poplawski, J. V, and Miller, C. R., 2000, "Rolling bearing life prediction-past, present, and future," Proceedings International Tribology Conference, Nagasaki 2000, pp. 101–107.

[28] Venner, C. H., and Lubrecht, A. A., 2000, "Multigrid techniques: a fast and efficient method for the numerical simulation of elastohydrodynamically lubricated point contact problems," Proceedings of the Institution of Mechanical Engineers, Part J: Journal of Engineering Tribology, **214**(1), pp. 43–62.

[29] Habchi, W., Demirci, I., Eyheramendy, D., Morales-Espejel, G. E., and Vergne, P., 2007, "A Finite Element Approach of Thin Film Lubrication in Circular EHD Contacts," Tribology International, pp. 1466–1473.

[30] Vergne, P., and Nélias, D., 1995, "Tribological and rheological properties of a MIL-L-23699 lubricant," Proceedings of the International Tribology Conference, Yokohama, Japan, pp. 691–696.

[31] Ville, F., Nélias, D., Tourlonias, G., Flamand, L., and Sainsot, P., 2001, "On the two-disc machine: A polyvalent and powerful tool to study fundamental and industrial problems related to elastohydrodynamic lubrication," Proceedings of the 27th Leeds–Lyon Symposium on Tribology, Tribology Research: From Model Experiment to Industrial Problem: A Century of Efforts in Mechanics, Material Science and Physico-Chemistry, Elsevier Tribology Series 39, D. Dowson, et al. (Eds.), pp 393–402.

[32] Molimard, J., Querry, M., and Vergne, P., 1999, "New tools for the experimental study of EDH and limit lubrications," Proceedings of the 25th Leeds–Lyon Symposium on Tribology, In Thinning Films and Tribological Interface, Elsevier Tribology Series 36, Dowson, D. et al. (Eds.), pp 717-726.

[33] Jacq, C., 2001, "Limite d'endurance et durée de vie en fatigue de roulement du 32CrMoV13 nitruré en présence d'indentations," Thèse de Doctorat, INSA-Lyon, Villeurbanne, n° ordre 2001-ISAL-0085, 241 p.

[34] Bamberger, E. N., Zaretsky, E. V, and Signer, H., 1976, "Endurance and Failure Characteristic of Main-Shaft Jet Engine Bearing at 3 times 10^6 DN," Journal of Lubrication Technology, **98**(4), pp. 580–585.

[35] Booser, E. R., 1993, CRC Handbook of Lubrication and Tribology, Volume III: Monitoring, materials, synthetic lubricants, and applications, CRC Press, Boca Raton, Florida, 640 p.

[36] Ebert, F.-J., 2010, "Fundamentals of design and technology of rolling element bearings," Chinese Journal of Aeronautics, **23**(1), pp. 123–136.

[37] Miner, J. R., Dell, J., Galbato, A. T., and Ragen, M. A., 1996, "F117-PW-100 hybrid ball bearing ceramic technology insertion," Journal of Engineering Gas Turbines and Power, **118**(2), pp. 434–442.

[38] Aramaki, H., Shoda, Y., Morishita, Y., and Sawamoto, T., 1988, "The performance of ball bearings with silicon nitride ceramic balls in high speed spindles for machine tools," Journal of Tribology, **110**(4), pp. 693–698.

[39] Paleu, V., and Nelias, D., 2007, "On kerosene lubrication of hybrid ball bearings," International Conference on Diagnosis and Prediction in Mechanical Engineering Systems, pp. 50–56.

[40] Zaretsky, E. V, Chiu, Y. P., and Tallian, T. E., 1989, "Ceramic bearings for use in gas turbine engines," Journal of Material Engineering, **11**(3), pp. 237–253.

[41] Misada, Y., Takebayashi, H., Matsuyama, H., Tomotaka, Y., and Noguchi, S., 2015, "A study on application of zirconia ceramic balls to rolling bearings," Proceedings of the International Tribology Conference Tokyo, Japan pp. 357-358.

[42] Scott, D., and Blackwell, J., 1973, "Hot pressed silicon nitride as a rolling bearing material-a preliminary assessment," Wear, **24**(1), pp. 61–67.

[43] Katz, R. N., 1994, "Ceramic materials for rolling element bearing applications," Technical report US Research Army, pp. 313–328.

[44] Wang, L., Snidle, R. W., and Gu, L., 2000, "Rolling contact silicon nitride bearing technology: a review of recent research," Wear, **246**(1), pp. 159–173.

[45] Reddecliff, J. M., and Valori, R., 1976, "The performance of a high-speed ball thrust bearing using silicon nitride balls," Journal of Lubrication Technology, **98**(4), pp. 553–558.

[46] Shoda, Y., Ijuin, S., Aramaki, H., Yui, H., and Toma, K., 1997, "The performance of a hybrid ceramic ball bearing under high speed conditions with the under-race lubrication method," Tribology Transactions, **40**(4), pp. 676–684.

[47] Azeggagh, N., Joly-Pottuz, L., Chevalier, J., Omori, M., Hashida, T., and Nélias, D., 2015, "Indentation strength of silicon nitride ceramics processed by spark plasma sintering technique," Materials Science Engineering A, **644**, pp. 159–170.

[48] Strubel, V., Fillot, N., Ville, F., Cavoret, J., Vergne, P., Mondelin, A., and Maheo, Y., 2015, "Particle Entrapment in Hybrid Lubricated Point Contacts," Tribology Transactions, **59**(4), 768-779.

[49] Dwyer-Joyce, R. S., Hamer, J. C., Sayles, R. S., and Ioannides, E., 1992, "Paper II (iv) Lubricant Screening for Debris Effects to Improve Fatigue and Wear Life," Proceedings of the 18th Leeds–Lyon Symposium on Tribology, *Wear Particles: From the Cradle to the Grave,* Elsevier Tribology Series 21, Dowson, D. et al. (Eds.), pp. 57–63.

[50] Hadfield, M., and Stolarski, T. A., 1995, "The effect of the test machine on the failure mode in lubricated rolling contact of silicon nitride," Tribology International, **28**(6), pp. 377–382.

[51] Hadfield, M., 1998, "Failure of silicon nitride rolling elements with ring crack defects," Ceramics International, **24**(5), pp. 379–386.

[52] Khonsari, M. M., and Booser, E. R., 2008, Applied tribology: bearing design and lubrication, Second Edition, John Wiley & Sons, 578 p.

[53] Hunt, T. M., 1993, Handbook of wear debris analysis and particle detection in liquids, Springer Netherlands, 488 p.

[54] Ville, F., 1998, "Pollution solide des lubrifiants, indentation et fatigue des surfaces." Thèse de Doctorat, INSA-Lyon, Villeurbanne, n° ordre 1998-ISAL-0085, 163 p.

[55] Dwyer-Joyce, R. S., 2005, "The life cycle of a debris particle," Proceedings of the 31st Leeds–Lyon Symposium on Tribology, Life Cycle Tribology, Elsevier Tribology and Interface Engineering Series 48, Dowson, et al. (Eds.), pp. 681–690.

[56] Cusano, C., and Sliney, H. E., 1982, "Dynamics of Solid Dispersions in Oil During the Lubrication of Point Contacts, Part I-Graphite," ASLE Transactions, **25**(2), pp. 183–189.

[57] Cusano, C., and Sliney, H. E., 1982, "Dynamics of Solid Dispersions in Oil During the Lubrication of Point Contacts, Part II-Molybdenum Disulfide," ASLE Transactions, **25**(2), pp. 190–197.

[58] Kirk, M. T., 1962, "Hydrodynamic lubrication of perspex," Nature, **194**, pp. 965–966.

[59] Gohar, R., and Cameron, A., 1963, "Optical measurement of oil film thickness under elasto-hydrodynamic lubrication," Nature, **200**, pp. 458–459.

[60] Dwyer-Joyce, R. S., 1999, "Predicting the abrasive wear of ball bearings by lubricant debris," Wear, **233**, pp. 692–701.

[61] Underwood, R. J., 2008, "The tribological effects of contamination in rolling element bearings," PhD Thesis, Imperial College London, London, 284 p.

[62] Kang, Y. S., Ai, X., and Sadeghi, F., 2000, "Debris effects on EHL contact," Journal of Tribology, **122**(4), pp. 711–720.

[63] Twist, C. P., 2013, "Tribological Interfaces and Fluid Flows Containing Particles and Chemically Designed Additives," PhD Thesis, Northwestern University, Evanston, 167 p.

[64] Kaneta, M., Kanada, T., and Nishikawa, H., 1997, "Optical interferometric observations of the effects of a moving dent on point contact EHL," Proceedings of the 23rd Leeds–Lyon Symposium on Tribology, *Fundamentals and Applications in Lubrication and Traction,* Tribology Series 32, , Dowson, et al. (Eds.), pp. 69–79.

[65] Nixon, H. P., and Zantopulos, H., 1995, "Fatigue life performance comparisons of tapered roller bearings with debris-damaged raceways," Lubrication Engineering, **51**(9), pp. 732–736.

[66] Cusano, C., and Wedeven, L. D., 1983, "The influence of surface dents and grooves on traction in sliding EHD point contacts," ASLE Transactions, **26**(3), pp. 306–310.

[67] Kang, Y. S., Sadeghi, F., and Hoeprich, M. R., 2004, "A finite element model for spherical debris denting in heavily loaded contacts," Journal of Tribology, **126**(1), pp. 71–80.

[68] Sun, J., Wood, R. J. K., Wang, L., Care, I., and Powrie, H. E. G., 2005, "Wear monitoring of bearing steel using electrostatic and acoustic emission techniques," Wear, **259**(7), pp. 1482–1489.

[69] Hebrard, Y., 2013, "Bearing, housing including a set of bearings, associated method and computer program," Brevet EP2730898 A, 14/05/2014.

[70] Maru, M. M., Castillo, R. S., and Padovese, L. R., 2007, "Study of solid contamination in ball bearings through vibration and wear analyses," Tribology International, **40**(3), pp. 433–440.

[71] Martin, P., 2016, "Online-Monitoring of Particles, Bubbles and Droplets in Lubricants of Engines and Gears," Proceedings of the 20th International Colloquium Tribology Esslingen, p. 164.

[72] Harvey, T. J., Wood, R. J. K., and Powrie, H. E. G., 2007, "Electrostatic wear monitoring of rolling element bearings," Wear, **263**(7), pp. 1492–1501.

[73] Ioannides, E., and Harris, T. A., 1985, "A new fatigue life model for rolling bearings," Journal of Tribology, **107**(3), pp. 367–377.

[74] Loewenthal, S. H., and Moyer, D. W., 1979, "Filtration effects on ball bearing life and condition in a contaminated lubricant," Journal of Tribology, **101**(2), pp. 171–176.

[75] Totten, G. E., Wills, D. K., and Feldmann, D. G., 2001, Hydraulic Failure Analysis: Fluids, Components, and System Effects, ASTM International, 601 p.

[76] Mitamura, N., and Murakami, Y., 2000, "Development of NSJ2 Bearing Steel," NSK Journal of Motion Control, (8), pp. 27–34.

[77] Sayles, R. S., Hamer, J. C., and Ioannides, E., 1990, "The effects of particulate contamination in rolling bearings-A state of the art review," Proc. Inst. Mech. Eng. Part G J. Aerosp. Eng., **204**(1), pp. 29–36.

[78] Coulon, S., Ville, F., and Lubrecht, A. A., 2005, "Experimental investigations of rolling contact fatigue of dented surfaces using artificial defects," Proceedings of the 31st Leeds–Lyon Symposium on Tribology, Life Cycle Tribology, Elsevier Tribology and Interface Engineering Series 48, Dowson, et al. (Eds.), pp. 691–702.

[79] Biboulet, N., 2008, "Influence of Indentations on Rolling Bearing Life." Thèse de Doctorat, INSA-Lyon, Villeurbanne, n° ordre 2008-ISAL-0054, 129 p.

[80] Ai, X., 2001, "Effect of debris contamination on the fatigue life of roller bearings," Proceedings of the Institution of Mechanical Engineers, Part J: Journal of Engineering Tribology, **215**(6), pp. 563–575.

[81] Morales-Espejel, G. E., and Gabelli, A., 2016, "Particle entrapment and indentation process in rolling bearings," Proceedings of the Institution of Mechanical Engineers, Part J: Journal of Engineering Tribology, DOI: 10.1177/1350650116641018.

[82] Ai, X., and Hager, C., 2016, "Forensic Analysis of Surface Indentations in Rolling Contact," Journal of Tribology, **138**(1), DOI: 10.1115/1.4030713.

[83] Doki-Thonon, T., 2012, "Thermal effects in elastohydrodynamic spinning circular contacts," Thèse de Doctorat, INSA-Lyon, Villeurbanne, n° ordre 2012-ISAL-0058, 133 p.

[84] Dormois, H., Fillot, N., Vergne, P., Dalmaz, G., Querry, M., Ioannides, E., and Morales-Espejel, G. E., 2009, "First traction results of high spinning large-size circular EHD contacts from a new test rig: tribogyr," Tribology Transactions, **52**(2), pp. 171–179.

[85] Yang, W., 2003, Handbook of fluidization and fluid-particle systems, CRC Press, New York, 1868 p.

[86] Habchi, W., 2008, "A full-system finite element approach to elastohydrodynamic lubrication problems: application to ultra-low-viscosity fluids." Thèse de Doctorat, INSA-Lyon, Villeurbanne, n° ordre 2008-ISAL-0038, 155 p.

[87] Ertel, A. M., 1939, "Hydrodynamic lubrication based on new principles," Proceedings of the USSR Academy of Sciences, Prikladnaya Matematika i Mekhanika, **3**(2), pp. 41–52.

[88] Hamrock, B. J., and Dowson, D., 1976, "Isothermal Elastohydrodynamic Lubrication of Point Contacts: Part II: Ellipticity Parameter Results," Journal of Tribology, **98**(3), pp. 375–381.

[89] Nijenbanning, G., Venner, C. H., and Moes, H., 1994, "Film thickness in elastohydrodynamically lubricated elliptic contacts," Wear, **176**(2), pp. 217–229.

[90] Lubrecht, A. A., Ten Napel, W. E., and Bosma, R., 1986, "Multigrid, an alternative method for calculating film thickness and pressure profiles in elastohydrodynamically lubricated line contacts," Journal of Tribology, **108**(4), pp. 551–556.

[91] Oh, K. P., and Rhode, S. M., 1975, "A Unified Treatment of Thick and Thin Film Elastohydrodynamic Problems by Using Higher Order Elements," Proc. Royal Soc. London A, pp. 315–331.

[92] Hamrock, B. J., and Dowson, D., 1977, "Isothermal Elastohydrodynamic Lubrication of Point Contacts: Part III-Fully Flooded Results," Journal of Lubrication Technology, **99**(2), pp. 264–275.

[93] Gence, J.-N., 2007, Mécanique des fluides: les écoulements de fluides newtoniens: principaux mécanismes associes aux mouvements des fluides, Ellipses, 382 p.

[94] Bruyère, V., 2012, "Une modélisation multi-physique et multi-phasique du contact lubrifié," Thèse de Doctorat, INSA-Lyon, Villeurbanne, n° ordre 2012-ISAL-0110, 175 p.

[95] Yasutomi, S., Bair, S., and Winer, W. O., 1984, "An application of a free volume model to lubricant rheology I-dependence of viscosity on temperature and pressure," Journal of Tribology, **106**(2), pp. 291–302.

[96] Dowson, D., and Higginson, G. R., 1966, Elastohydrodynamic lubrication, the fundamentals of roller and gear lubrication, Pergamon, Oxford, 235 p.

[97] Gresho, P. M., Sani, R. L., and Engelman, M. S., 1998, Incompressible flow and the finite element method: advection-diffusion and isothermal laminar flow, Wiley, New York, 480 p.

[98] Kumar, A., R Schmid, S., and Wilson, W. R. D., 1997, "Particle behavior in two-phased lubrication," Wear, **206**(1), pp. 130–135.

[99] Isèbe, D., and Nérin, P., 2013, "Numerical simulation of particle dynamics in an orifice--electrode system. Application to counting and sizing by impedance measurement," International Journal for Numerical Methods in Biomedical Engineering, **29**, pp.462–475.

[100] Van Rijn, L. C., 1993, Principles of sediment transport in rivers, estuaries and coastal seas, Part 1, Aqua Publications, Amsterdam, 700 p.

[101] Savage, S. B., and Hutter, K., 1991, "The dynamics of avalanches of granular materials from initiation to runout. Part I: Analysis," Acta Mechanica, **86**(1-4), pp. 201–223.

[102] Bishop, S. R., Momiji, H., Carretero-González, R., and Warren, A., 2002, "Modelling desert dune fields based on discrete dynamics," Discrete Dynamics in Nature and Society, **7**(1), pp. 7–17.

[103] Loth, E., Tryggvason, G., Tsuji, Y., Elghobashi, S., Crowe, C., Berlemont, A., Reeks, M., Simonin, O., Frank, T., Onishi, Y., Wachem, B., 2005, Multiphase Flow Handbook, Modeling, In: Crowe, C. (Ed.), 1st ed. CRC, London, 1156 p.

[104] Stokes, G. G., 1846, "Report on recent researches in hydrodynamics," Report for the British Association for the Advancement of Science, **1**, pp. 1–20.

[105] Ambrosino, F., 2011, "Wall effects in particle-laden flows." PhD Thesis, Universita' Degli Studi Di Napoli "Federico II", Napoli, 105 p.

[106] Du, W., Bao, X., Xu, J., and Wei, W., 2006, "Computational fluid dynamics (CFD) modeling of spouted bed: Assessment of drag coefficient correlations," Chemical Engineering Science, **61**(5), pp. 1401–1420.

[107] Schiller, L., and Neumann, A., 1933, "Fundamental calculations in gravitational processing," Zeitschrift Des Vereines Deutscher Ingenieure, **77**, pp. 318–320.

[108] Salari, A., Karmozdi, M., Maddahian, R., and Firoozabadi, B., 2013, "Analytical study of single particle tracking in both free and forced vortices," Scientia Iranica, **20**(2), pp. 351–358.

[109] Sebesta, C. J., 2012, "Modeling the effect of particle diameter and density on dispersion in an axisymmetric turbulent jet," Master Thesis, Virginia Polytechnic Institute and State University, 70 p.

[110] Johnson, R. W., 2016, Handbook of fluid dynamics, CRC Press, Boca Raton, Florida, 1952 p.

[111] Zeng, L., Balachandar, S., and Fischer, P., 2005, "Wall-induced forces on a rigid sphere at finite Reynolds number," J. Fluid Mech., **536**, pp. 1–25.

[112] Bigillon, F., 2001, "Etude du mouvement bidimensionnel d'une particule dans un courant d'eau sur forte pente," Thèse de Doctorat, Grenoble 1, Grenoble, n° ordre 2001-GRE1-0148, 217 p.

[113] Nikas, G. K., Sayles, R. S., and Ionnides, E., 1998, "Effects of debris particles in sliding/rolling elastohydrodynamic contacts," Proceedings of the Institution of Mechanical Engineers, Part J: Journal of Engineering Tribology, **212**(5), pp. 333–343.

[114] Coulon, S., 2001, "Prédiction de la durée de vie des contacts ponctuels lubrifiés en présence d'indentations," Thèse de Doctorat, INSA-Lyon, Villeurbanne, n° ordre 2001-ISAL-0038, 202 p.

[115] Wheeler, J.-D., Fillot, N., Vergne, P., Philippon, D., and Morales Espejel, G., 2016, "On the Crucial Role of Ellipticity on EHD Film Thickness and Friction," Journal of Engineering Tribology, DOI: 10.1177/1350650116637583.

[116] Grant, I., 1997, "Particle image velocimetry: a review," Proceedings of the Institution of Mechanical Engineers, Part C: Journal of Mechanical Engineering Science, **211**(1), pp. 55–76.

[117] Santiago, J. G., Wereley, S. T., Meinhart, C. D., Beebe, D. J., and Adrian, R. J., 1998, "A particle image velocimetry system for microfluidics," Experiments in Fluids, **25**(4), pp. 316–319.

[118] Nogueira, S., Sousa, R. G., Pinto, A., Riethmuller, M. L., and Campos, J., 2003, "Simultaneous PIV and pulsed shadow technique in slug flow: a solution for optical problems," Experiments in Fluids, **35**(6), pp. 598–609.

[119] Bair, S., Qureshi, F., and Winer, W. O., 1993, "Observations of shear localization in liquid lubricants under pressure," Journal of Tribology, **115**(3), pp. 507–513.

[120] Ponjavic, A., Chennaoui, M., and Wong, J. S. S., 2013, "Through-thickness velocity profile measurements in an elastohydrodynamic contact," Tribology Letters, **50**(2), pp. 261–277.

[121] Albahrani, S. M. B., 2016, "Photoluminescent CdSe/CdS/ZnS Quantum Dots for Temperature and Pressure Sensing in Elastohydrodynamic Contacts," Thèse de Doctorat, Université de Lyon, Insa-Lyon, Villeurbanne, n° ordre 2016-LYSEI-016, 176 p.

[122] Horvat, F. E., and Braun, M. J., 2011, "Comparative experimental and numerical analysis of flow and pressure fields inside deep and shallow pockets for a hydrostatic bearing," Tribology Transactions, **54**(4), pp. 548–567.

[123] Li, J. X., Höglund, E., Westerberg, L. G., Green, T. M., Lundström, T. S., Lugt, P. M., and Baart, P., 2012, "μPIV measurement of grease velocity profiles in channels with two different types of flow restrictions," Tribology International, **54**, pp. 94–99.

[124] Reddyhoff, T., Choo, J. H., Spikes, H. A., and Glovnea, R. P., 2010, "Lubricant flow in an elastohydrodynamic contact using fluorescence," Tribology Letters, **38**(3), pp. 207–215.

[125] Reiss, P., and Chandezon, F., 2004, "Nanocristaux semi-conducteurs fluorescents," Tech. l'Ingénieur, **2**(030), pp. 1–15.

[126] Tropea, C., Yarin, A. L., and Foss, J. F., 2007, Springer handbook of experimental fluid mechanics, Springer Science & Business Media, Berlin, 1557 p.

[127] Dantec Dynamics, "Measurement Principles of PIV," [en ligne], Disponible sur : <http://www.dantecdynamics.com/measurement-principles-of-piv> (consulté le 20.05.2016).

[128] Hsiao, H.-S. S., Hamrock, B. J., and Tripp, J. H., 2001, "Stream functions and streamlines for visualizing and quantifying side flows in EHL of elliptical contacts," Journal of Tribology, **123**(3), pp. 603–607.

[129] Berruti, F., Liden, A. G., and Scott, D. S., 1988, "Measuring and modelling residence time distribution of low density solids in a fluidized bed reactor of sand particles," Chemical Engineering Science, **43**(4), pp. 739–748.

[130] Gupta, P. K., 1979, "Dynamics of rolling-element bearings—part iii: Ball bearing analysis," Journal of Tribology, **101**(3), pp. 312–318.

[131] Thorp, N., and Gohar, R., 1972, "Oil film thickness and shape for a ball sliding in a grooved raceway," Journal of Tribology, **94**(3), pp. 199–208.

[132] Hamer, J. C., Sayles, R. S., and Ioannides, E., 1989, "Particle deformation and counterface damage when relatively soft particles are squashed between hard anvils," Tribology Transactions, **32**(3), pp. 281–288.

[133] Chao, K. K., Saba, C. S., and Centers, P. W., 1996, "Effects of lubricant borne solid debris in rolling surface contacts," Tribology Transactions, **39**(1), pp. 13–22.

[134] Nikas, G. K., 2012, "An experimentally validated numerical model of indentation and abrasion by debris particles in machine-element contacts considering micro-hardness effects," Proceedings of the Institution of Mechanical Engineers, Part J: Journal of Engineering Tribology, **226**(5), pp. 406–438.

[135] Bearings RMD, "Angular Contact Ball Bearings." [en ligne] Disponible sur : <http://http://www.rmdbearing.com> (consulté le 12.03.2016).

[136] Canzi, A., Venner, C. H., and Lubrecht, A. A., 2010, "Film thickness prediction in elastohydrodynamically lubricated elliptical contacts," Proceedings of the Institution of Mechanical Engineers, Part J: Journal of Engineering Tribology, **224**(9), pp. 917–923.

[137] Brewe, D. E., Hamrock, B. J., and Taylor, C. M., 1979, "Effect of geometry on hydrodynamic film thickness," Journal of Tribology, **101**(2), pp. 231–237.

[138] Strubel, V., Fillot, N., Ville, F., Cavoret, J., Vergne, P., Mondelin, A., and Maheo, Y., 2016, "Particle Entrapment in Rolling Element Bearings: the Effect of Ellipticity, Nature of Materials and Sliding," Tribology Transactions, DOI: 10.1080/10402004.2016.1168901.

[139] Nikas, G. K., 2007, "Effects of operating conditions and friction on the entrapment of spherical debris particles in elliptical contacts," Proceedings of the Institution of Mechanical Engineers, Part J: Journal of Engineering Tribology, **221**(6), pp. 727–741.

[140] Sliney, H. E., 1978, "Dynamics of solid lubrication as observed by optical microscopy," ASLE Transactions, **21**(2), pp. 109–117.

[141] Popp, M., and Sternagel, R., 1999, "Hybrid ceramic and all ceramic anti friction bearings," ESA Publications, **438**, pp. 105–110.

[142] Brizmer, V., Gabelli, A., Vieillard, C., and Morales-Espejel, G. E., 2015, "An Experimental and Theoretical Study of Hybrid Bearing Micropitting Performance under Reduced Lubrication," Tribology Transactions, **58**(5), pp. 829–835.

[143] Sutor, P. A., 1984, "Tribology of silicon-nitride silicon-nitride and silicon-nitride steel sliding pairs," Proceedings of the 8th Annual Conference on Composites and Advanced Ceramic Materials: Ceramic Engineering and Science Proceedings, Vol. 5, pp. 461-469.

[144] DellaCorte, C., Noebe, R.D., Stanford, M. K. and Padula, S. A., 2012, "Resilient and Corrosion-Proof Rolling Element Bearings Made From Superelastic Ni-Ti Alloys for Aerospace Mechanism Applications," NASA/TM-2011-217105, 24 p.

[145] Levine, J., "NASA, Partners Test Engine Health Monitoring System," [en ligne], Disponible sur <http://www.nasa.gov/centers/armstrong/features/engine_health_monitoring.html> (consulté le 14.06.2016).

[146] Chinas-Castillo, F., and Spikes, H. A., 2003, "Mechanism of action of colloidal solid dispersions," Journal of Tribology, **125**(3), pp. 552–557.

Scientific contributions

List of Publications

- Strubel, V., Fillot, N., Ville, F., Cavoret, J., Vergne, P., Mondelin, A., and Maheo, Y., (2016), "Particle Entrapment in Rolling Element Bearings: the Effect of Ellipticity, Nature of Materials and Sliding," *Tribology Transactions*, (accepted 14/03/2016), DOI: 10.1080/10402004.2016.1168901.

- Strubel, V., Fillot, N., Ville, F., Cavoret, J., Vergne, P., Mondelin, A., and Maheo, Y., (2015), "Particle Entrapment in Hybrid Lubricated Point Contacts," *Tribology Transactions*, **59**(4), 768-779.

List of Oral presentations

- Strubel, V., Fillot, N., Ville, F., Vergne, P., Mondelin, A., and Maheo, Y., (2016), "Vizualisation of debris entrapment in EHL contacts using μ-PIV technique", STLE 71st Annual Meeting, Las Vegas, USA, 14-19/05/2016.

- Strubel, V., Fillot, N., Ville, F., Vergne, P., Mondelin, A., and Maheo, Y., (2016), "Debris Entrapment in Hybrid Rolling Element Bearings", 20th International Colloquium Tribology, Esslingen, Germany, 12-14/01/2016.

- Strubel, V., Simoens, S., Fillot, N., Ville, F., Vergne, P., Devaux, N., El Hajem, M., (2015), "Utilisation d'un dispositif micro-PIV pour la visualisation d'un micro-écoulement confiné et de son voisinage non confiné", 16ème Congrès Français du club FLUVISU, Lannion, France, 16-20/11/2015.

- Strubel, V., Fillot, N., Ville, F., Vergne, P., Mondelin, A., and Maheo, Y., (2015), "Debris Entrapment in Elliptical EHD Contacts", International Tribology Conference, Tokyo, Japan, 16-20/09/2015.

- Strubel, V., Fillot, N., Ville, F., Vergne, P., Mondelin, A., and Maheo, Y., (2015), "Etude du piégeage de contaminants solides dans des contacts EHD", 22ème Congrès Français de Mécanique, Lyon, France, 24-28/08/2015.

- Strubel, V., Fillot, N., Ville, F., Vergne, P., Mondelin, A., and Maheo, Y., (2015), "Analysis of Particle Entrapment in Hybrid Lubricated Bearings", STLE 70th Annual Meeting, Dallas, USA, 17-21/05/2015.

- Strubel, V., Fillot, N., Ville, F., Vergne, P., Mondelin, A., and Maheo, Y., (2014), "Numerical Simulation of Particle Entrapment in Hybrid Lubricated Bearings", 1st Tribology Frontiers Conference, Chicago, USA, 25-27/10/2014.

- Strubel, V., Fillot, N., Ville, F., Vergne, P., Mondelin, A., and Maheo, Y., (2014), "Ingestion de particules solides dans un roulement hybride", 26ème Journées Internationales Francophones de Tribologie, Mulhouse, France, 26-28/05/2014.

List of Posters

- Strubel, V., Fillot, N., Ville, F., Devaux, N., Vergne, P., Simoens, S., El Hajem, M., Mondelin, A., and Maheo, Y., (2016), "Large Elliptical EHL Contacts for Reducing Particle Entrapment", STLE 71st Annual Meeting, Las Vegas, USA, 14-19/05/2016.

- Strubel, V., Fillot, N., Ville, F., Vergne, P., Mondelin, A., and Maheo, Y., (2015), "Hybrid Rolling Element Bearings: a New Answer Facing the Problem of Debris Entrapment", STLE 70th Annual Meeting, Dallas, USA, 17-21/05/2015.

FOLIO ADMINISTRATIF

THESE DE L'UNIVERSITE DE LYON OPEREE AU SEIN DE L'INSA LYON

NOM : STRUBEL DATE de SOUTENANCE : 21/10/2016

Prénoms : Vincent

TITRE : Particle Entrapment in EHD Contacts – Aerospace Applications

NATURE : Doctorat Numéro d'ordre : 2016LYSEI098

Ecole doctorale : Mécanique, Energétique, Génie Civil, Acoustique

Spécialité : Génie Mécanique

RESUME : Une lubrification suffisante est essentielle au bon fonctionnement des mécanismes et/ou composants comme, par exemple, les paliers à roulement. Par contre, les lubrifiants contiennent souvent des débris d'usure ou des polluants extérieurs. Ces particules micrométriques peuvent pénétrer des contacts d'épaisseur inférieure au micromètre induisant des empreintes ou indents pouvant conduire à des endommagements irréversibles pour les surfaces en contact. L'objet de ce travail est l'étude du piégeage de polluants solides à l'aide de particules sphériques d'acier, d'un point de vue numérique et expérimental. Dans un premier temps, une étude phénoménologique a été proposée à l'aide d'une nouvelle méthode expérimentale basée sur la technique PIV combinée à un tribomètre bille/disque. Les trajectoires des polluants à l'entrée du contact ont pu ainsi être identifiées. En parallèle, un modèle numérique d'écoulement du lubrifiant a été développé pour permettre l'évaluation des conditions menant au piégeage ou non de particules. Finalement, des expériences sur une machine bi-disques en conditions de lubrification polluée contrôlée ont permis de valider les tendances observées pour le piégeage. Une première série de résultats a montré que le piégeage de contaminants est fortement dépendant du profil de vitesse du lubrifiant. Un taux de piégeage très hétérogène a été observé sur des contacts avec une ellipticité transverse à l'écoulement variable. De manière surprenante, malgré une augmentation de la largeur de contact, une forte diminution du nombre de particules piégées a été observée dans des contacts elliptiques. Il a été démontré que cette diminution peut être imputée à la présence d'importants reflux de lubrifiant dans les contacts elliptiques larges. L'étude de contacts hybrides, nitrure de silicium–acier, a montré une bonne résistance à l'indentation du nitrure de silicium. Enfin, il est à noter que les contacts hybrides présentent des niveaux de piégeage similaire à un contact tout acier.

MOTS-CLÉS : Piégeage de polluants, contacts elliptiques, nitrure de silicium–acier, modèle numériques, machine bi-disques, tribomètre bille/disque, technique PIV

Laboratoire de recherche : Laboratoire de Mécanique des Contacts et des Structures

Directeurs de thèse: FILLOT Nicolas et VILLE Fabrice

Présidente de jury : TANGUY Anne

Composition du jury : DELLACORTE Christopher, DWYER-JOYCE Rob, FILLOT Nicolas, MONDELIN Alexandre, TANGUY Anne, VILLE Fabrice